High target utilisation sputtering for the development of advanced materials for magnetic data storage applications

Submitted by Denh Tran to the University of Exeter as a thesis for the degree of Doctor of Philosophy in Engineering, June 2012

This thesis is available for Library use on the understanding that it is copyright material and that no quotation from the thesis may be published without proper acknowledgement.

I certify that all material in this thesis which is not my own work has been identified and that no material has previously been submitted and approved for the award of a degree by this or any other University.

(signature)..

Abstract

High target utilisation sputtering (HiTUS) is a relatively new thin film deposition technique that generates a high density plasma remotely from the sputter target. This method has been employed firstly to investigate FePt and FePtN thin films for high density data storage media applications and secondly to investigate the production of a GMR/PZT hybrid structure (multi-ferroism) for improvements to magneto-resistive read-sensor devices in hard disk drives and potentially for other novel multi-ferroic applications.

The magnetic and structural properties of FePt and FePtN films, prepared by the HiTUS method, on both silicon and glass substrates have been investigated before and after annealing at temperatures in the range of 300 to 800 °C. It is shown that during thermal annealing there is a degradation in magnetic properties of the FePt films at around 400 °C due to the formation of silicides as the thermal processing promotes the reaction of the film with the substrate. However, in the FePtN samples coercivity values continue to rise with annealing temperatures above 400 °C. XRD analysis confirms that silicide formation is suppressed in films containing nitrogen up to 800 °C. Using the HiTUS technique, there is evidence that $L1_0$ ordering of FePt has occured at annealing temperature of 400 °C with in plane and out of plane coercivities of 7180 Oe and 6300 Oe respectively.

Finally, it is shown that HiTUS is capable of depositing ultra thin multilayer GMR structures onto a variety of substrates; silicon, glass, flexible kapton film and PZT. It is interesting to find that the GMR ratio obtained on kapton film (14.39 %) is almost as high as that on silicon (16.15 %), with much scope for improvement. Multi-ferroic composite films consisting of the GMR multilayer structure $[\mathrm{Co}(8\ \text{Å})/\mathrm{Cu}(21\ \text{Å})]_{\times 20}/\mathrm{Co}(12\ \text{Å})$ on PZT substrates were fabricated and magneto-electric coupling effects explored. It was found that AC voltages applied across the composite GMR/PZT structure produced a marked decrease in the coercivity of the GMR layer. However, DC voltages did not produce any measurable magnetic effects. Careful investigation revealed that the reduction in coercivity observed during AC measurements was, in fact, due to sample heating effects.

Contents

1 Introduction **12**

1.1 Overview of thesis 14

2 Thin film fabrication **16**

2.1 Introduction 16

2.2 Vacuum Evaporation 18

2.3 Sputtering 19

2.3.1 Glow discharges 20

2.3.2 DC cathode sputtering 22

2.3.3 Magnetron sputtering 24

2.4 High target utilisation sputtering 27

2.4.1 System overview 29

2.4.2 Plasma generation and HiTUS process 30

2.4.3 Sputtering of magnetic materials 39

3 Magnetic materials **45**

3.1 Magnetism 45

3.2 Classification of magnetic materials 46

3.3 Characteristics of ferromagnetic materials 48

3.3.1 Ferromagnetic domains 48

3.3.2 Magnetostatic energy 49

3.3.3 Magnetic anisotropy 50

3.3.4 Magnetocrystalline anisotropy 51

3.3.5 Stress anisotropy 53

3.3.6 Domain walls 54

3.3.7 Shape anisotropy and inter-particle interactions 55

3.3.8 Hysteresis loops 56

4 Magnetic data storage **58**

4.1 The basic hard disk drive 58

4.1.1 The recording process 58

4.2 Data read out 61

4.2.1 Magneto-resistive Effect 61

4.2.2 Giant Magneto-resistive Effect 62

4.2.3 Giant magneto-resistance in multilayers 63

4.2.4 Basic principles of the reading process using GMR spin valves 63

4.3 Exchange coupling 65

4.4 Magnetic Tunnel Junctions 66

4.5 Data storage media 68

4.5.1 Important magnetic properties of magnetic recording media . 71

4.5.2 Recording media challenges 72

4.6 High K_u materials 74

4.7 Crystal structures 76

4.7.1 Miller System 78

4.8 $L1_0$ FePt structure and phases 79

4.9 Challenges for FePt 81

4.9.1 Controlling the easy axis 81

4.9.2 Reduction of ordering temperature 84

4.9.3 Reduction of grain size 85

5 Multi-ferroism **86**

5.1 Ferroelectricity 86

5.2 Ferroelasticity 88

5.3 The piezoelectric effect 90

5.4 Lead zirconate titanate 92

5.5 Combining ferromagnetism and ferroelectricity 94

5.6 Magneto-electric coupling mechanisms 97

5.6.1 Interface charge mediated coupling 97

5.6.2 Exchange bias mediated coupling 97

5.6.3 Strain mediated coupling 98

6 Characterisation techniques **100**

6.1 Vibrating sample magnetometry . . . 100

6.1.1 Theory of VSM . . . 101

6.2 Magneto-optical Kerr effect magnetometry . . . 103

6.2.1 Magneto-optic effect . . . 103

6.2.2 Magneto-optic Kerr effect . . . 104

6.2.3 Operating geometries . . . 105

6.3 X-ray diffractometry . . . 107

6.3.1 Theory . . . 107

6.3.2 Diffraction measurements . . . 110

6.3.3 Crystallite size . . . 111

6.4 Atomic force microscopy . . . 112

6.4.1 Optical lever detection . . . 112

6.4.2 AFM modes . . . 113

6.5 Magneto-resistivity measurements . . . 115

7 Fabrication and characterisation of annealed FePt thin films **118**

7.1 Introduction . . . 118

7.2 Sputtering with nitrogen . . . 119

7.2.1 Silicon nitride . . . 121

7.3 Project Introduction . . . 123

7.4 Experimental . . . 124

7.5 Results . . . 126

7.5.1 Magnetic properties . . . 126

7.5.2 X-Ray diffractometry . . . 134

7.5.3 Electrical properties . . . 143

7.5.4 Surface morphology . . . 146

7.5.5 Crystallite size . . . 147

7.5.6 High coercivity FePt . . . 147

7.6 Summary and conclusions . . . 153

8 Multi-ferroics for future data read sensors **156**

8.1 ME for data storage read out applications . . . 157

8.2 The GMR effect on ferroelectric PZT . . . 159

8.2.1 Introduction 159
8.2.2 Co/Cu GMR multilayers 160
8.3 Preliminary experiments 163
8.3.1 Experimental 163
8.3.2 Results 164
8.3.3 Observations 169
8.4 Combining GMR and PZT 172
8.4.1 Experimental 172
8.4.2 Results 173
8.4.3 Additional experimental results 178
8.5 Summary and conclusions 186

9 Concluding remarks 188

Appendix A Magnetic data for FePt films deposited under different conditions 192

Appendix B Surface roughness of Co and Cu films sputtered at different process pressures 194

Appendix C Journal articles published as a result of the work of this thesis 195

List of Figures

2.1 A typical thermal evaporation system. 18

2.2 An illustration of the sputtering process. 19

2.3 Initiation of a glow discharge between parallel plate electrodes. 20

2.4 Uniform glow discharge between parallel plate electrodes. 21

2.5 Regions within the glow discharge at sufficiently low pressures. 21

2.6 Typical DC diode type arrangement. 23

2.7 Schematic showing typical magnetron sputtering system. 25

2.8 Image showing racetrack formation in a copper target sputtered using a magnetron system (photograph of an actual target taken at PQL). . 27

2.9 Diagram of a typical HiTUS system showing visible plasma path (chamber door removed for clarity), used with permission from PQL. 30

2.10 PL intensity for HiTUS deposited ZnS:Mn films prepared at ambient temperature using target power of 200 W. As deposited and post deposition annealed ZnS:Mn films prepared by RF magnetron sputtering are shown for comparison [1]. 35

2.11 Variation of refractive index with wavelength for titania and hafnia deposited by HiTUS. 37

2.12 Spectral transmittance characteristics of HiTUS deposited titania and hafnia. The transmission of the uncoated substrate is also shown for comparison. 37

2.13 Magnetic target reduces vacuum magnetic field through confinement in target material. 39

2.14 Thin magnetic target allows magnetic field to penetrate vacuum. . . . 40

2.15 Photograph showing the HiTUS system used for the deposition of the coatings in this work. 41

2.16 Schematic view of the HiTUS system: (1) process chamber, (2) roughing valve, (3) low vacuum (LV) rotary pump, (4) backing valve, (5) turbomolecular high vacuum (HV) pump, (6) cryogenic HV pump, (7) HV pump gate valves, (8) substrate holder assembly, (9) substrate shutter, (10) inlet for reactive gas, (11) MFC isolation valve, (12) Mass flow controllers (MFCs), (13) reactive gas supply, (14) Penning HV gauge, (15) capacitance manometer (CM) gauge, (16) Pirani LV gauge, (17) target electromagnet, (18) plasma source (PLS) electromagnet, (19) remote plasma source (PLS), (20) DC power supply, (21) sputter target, (22) dark shield, (23) inlet for process gas, (24) process gas supply, (25)RF impedance matching network, (26) RF power supply. 42

3.1 The motion of an electron within an atom. 46
3.2 Domain formation in ferromagnetic materials. 49
3.3 Magnetisation curve for a ferromagnetic single crystal with the field applied along the easy and hard axes. 51
3.4 Definition of the θ and ϕ angles in the tetragonal symmetry. 52
3.5 Interparticle interactions. 56
3.6 Typical M–H hysteresis loop. 57

4.1 Schematic of the basic hard disk drive. 59
4.2 Longitudinal recording principle. 60
4.3 Perpendicular recording using the stronger “gap fields” for writing. . 61
4.4 NiFe/Cu/NiFe GMR structure. 64
4.5 Simple GMR spin valve. 65
4.6 Exchange coupling in ferromagnetic/anti-ferromagnetic heterostructures. 67
4.7 Basic TMR structure and electron spin tunneling. 69
4.8 Magnetic hysteresis loop indicating certain properties important for media materials. 71
4.9 Ideal hysteresis loops of a magnetic uniaxial sample. 72
4.10 Energy barrier for magnetisation reversal. 73
4.11 The edge lengths (a, b, c) and axial angles (α, β, γ) of a unit cell. . 76
4.12 The cubic crystal class, (a) primitive, (b) bcc and (c) fcc. 77

4.13 The tetragonal crystal class, (a) primitive, (b) fcc and (c) fct. 78
4.14 Miller indices (h, k, l) and example crystallographic direction, represented by the blue arrow. 79
4.15 Miller indices (h, k, l) and three equivalent planes are shown for a cubic unit cell. 80
4.16 Two main crystal structures of equiatomic FePt. 80
4.17 Tilting of the [100] axis for fct FePt. 82

5.1 (a) A non-polar crystal structure displaying a centre of symmetry. (b) Cation displacement resulting in polarization; the red arrow shows movement of the cation possessing a charge of 4^{-}. 87
5.2 Characteristic P-E hysteresis loop for a ferroelectric material. 88
5.3 Stress induced strain on austenite (A), resulting in two phases of marstenite (+M and -M). 89
5.4 Defined symmetry axes for a piezoelectric crystal. 92
5.5 (a) The cubic perovskite structure, (b) arrows to show the six equivalent $\langle 100 \rangle$ directions that results in the tetragonal crystalline phase, (c) arrows to show the eight equivalent $\langle 111 \rangle$ directions that results in the rhombohedral crystalline phase. 93
5.6 Carrier mediated mechanism. 98

6.1 Schematic of a vibrating sample magnetometer. 101
6.2 Principle of the magneto-optic Kerr effect. 104
6.3 Longitudinal, transverse and polar MOKE geometries. 106
6.4 Schematic of MOKE measurement setup. 106
6.5 Diffraction of x-rays by planes of atoms. The blue circles represent atoms. 108
6.6 Bragg Brentano focusing geometry of the diffractometer. 110
6.7 Concept of AFM and optical lever detection. 113
6.8 Four point probe setup. 116
6.9 GMR measurement setup at NPL. 117

7.1 In plane VSM magnetic hysteresis loops for FePt at various temperatures. 127

7.2 Perpendicular VSM magnetic hysteresis loops for FePt at various temperatures. . . . 127
7.3 In plane VSM magnetic hysteresis loops for FePtN at various temperatures. . . . 128
7.4 Perpendicular VSM magnetic hysteresis loops for FePtN at various temperatures. . . . 128
7.5 Coercivity of 250 Å of FePt and FePtN on Si. . . . 130
7.6 Saturation magnetisation of 250 Å of FePt and FePtN on Si. . . . 131
7.7 Remanence of 250 Å of FePt and FePtN on Si. . . . 132
7.8 X-ray diffraction patterns of FePt for different anneal temperatures (deposited onto Silicon). . . . 136
7.9 X-ray diffraction patterns of FePt for different anneal temperatures (deposited onto glass). . . . 138
7.10 coercivity of 250 Å of FePt on glass. . . . 139
7.11 X-ray diffraction patterns of FePtN for different anneal temperatures (deposited onto Silicon). . . . 141
7.12 Example graph showing measured voltages at various applied currents. 144
7.13 Specific resitivity data for 250 Å FePt and FePtN deposited onto Si. . . 145
7.14 RMS roughness of FePt and FePtN on Si measured using AFM. . . . 147
7.15 Crystallite size of FePt and FePtN on Si measured using XRD. . . . 148
7.16 Hysteresis loops, produced using VSM, for 250 Å of FePt deposited onto naturally oxidised Si. . . . 149
7.17 X-ray diffraction pattern of 250 Å FePt deposited onto naturally oxidised Si. . . . 152

8.1 Proposed GMR/PZT hybrid. . . . 160
8.2 An illustration of a Co/Cu multilayer system. . . . 161
8.3 Magneto-resistance versus Cu spacer layer thickness for a series of Co/Cu multilayers, adapted from [2]. . . . 162
8.4 Measured GMR ratios with varying Cu thickness on (a) silicon, (b) glass and (c) kapton film. . . . 165
8.5 STEM image of [Co(18 Å)/Cu(48 Å)]/[Co(8 Å)/Cu(21 Å)]$_{\times 20}$/Co(12 Å) deposited on glass. . . . 170
8.6 Magneto-resistive measurements with applied voltages. . . . 173

8.7 Magneto-resistance measurements for hybrid structure PZT/[Co(18 Å)/Cu(48 Å)]/[Co(8 Å)/Cu(21 Å)]$_{\times 20}$/Co(12 Å). 174
8.8 Magneto-resistance measurements for different DC applied voltages. . 175
8.9 (a) Changes in magneto-resistance with applied AC voltages and (b) a closer view of these changes for the circled area in (a). 176
8.10 MOKE measurements with applied voltages. 179
8.11 Normalised hysteresis loops for (a) Co and (b) CoFe with different applied DC voltages, measured using MOKE. 180
8.12 MO loops for 100 nm Co film, with applied AC voltages at 117 Hz. . 182
8.13 MO loops for 100 nm CoFe, with applied AC voltages at 117 Hz. . . . 182
8.14 MO loops for 100 nm Co, with applied AC voltages at 1777 Hz. . . . 183
8.15 MO loops for 100 nm CoFe, with applied AC voltages at 1777 Hz. . . 183
8.16 Decrease in coercive field for (a) Co and (b) CoFe on application of AC voltages to PZT. 184
8.17 Coercive field and inverse of measured temperature as a function of applied voltage at (a) frequency = 117 Hz and (b) frequency = 1777 Hz. 185

List of Tables

4.1 Magnetic properties of $L1_0$ and other ferromagnetic alloys, (from [3]). 75

4.2 The seven unit cell categories. 77

7.1 Enthalpy of formation values. 143

7.2 Room temperature resistivities of likely compounds. 145

7.3 Properties of both samples A and B annealed at 400 °C. The properties of un-annealed FePt are also shown. 151

8.1 Second anti-ferromagnetic coupling GMR values, from literature. . . . 166

8.2 Effect of changing Co thickness on GMR. 168

8.3 GMR ratio of [Co(8 Å)/Cu(21 Å)]$_{\times 20}$/Co(12 Å) on different buffers using glass and silicon substrates. 169

8.4 Temperature of ferromagnet/PZT on applying AC voltages. 181

A.1 Summary of some magnetic information extracted from hysteresis loops on FePt samples deposited under different RF power and target voltages. By changing these two parameters the magnetic properties change, as is particularly evident by the coercivity and squareness (SQR) values. 193

B.1 The reduction in film roughness as process pressure is reduced 194

Acknowledgments

This work was supported by Plasma Quest Limited (PQL) and the University of Exeter. I am grateful to both parties for giving me the opportunity to learn about such an interesting topic; the whole experience has been an enjoyable one.

I would particularly like to thank Mike and Annette for their kindness, support and generosity over the years - I don't know where I'd be now without them both! A massive thank you to Pete for providing useful knowledge (technical and non-technical) and wonderful pictorial based tutorials. Stuart has always made time to lend a helping hand no matter how busy he is - so thanks to him also.

I could not have wished for better or nicer supervisors; Prof. David Wright and Dr. Mustafa Aziz have been fantastic. I am thankful to them for their guidance, encouragement and never-ending patience, it has been a pleasure to have been under their supervision. There are too many colleagues to thank individually at the university and at PQL but the help that I have received at both sites has been invaluable and is greatly appreciated.

Prof. Tom Thomson and Dr. Chris Morrision deserve a special thank you as they have welcomed me into their department on many occasions. As well as offering me advice and guidance they let me loose on their valuable equipment, for which I am most grateful.

I am eternally grateful to my family for their love and support, particularly my mother who is the biggest support there can ever be. Lastly an especially big big thank you (the biggest thank you one can ever imagine) to Steve and Fu - could not have done this without you guys!

Chapter 1

Introduction

Thin films are an essential part of today's technological applications. In this thesis it is assumed that a thin film is a layer of material that is less than 1000 nm thick formed onto a substrate. Thin film devices and coatings surround us in various forms, for example anti-reflective coatings on eye glasses, optical and infra-red equipment, corrosion protection coatings, microelectronic devices, semiconductor devices, barrier layers, magnetic sensors, capacitors and electrodes to name a few. The rapid advances in vacuum technology, the phenomenal growth of surface science and applications, together with continued development of high resolution analytical techniques have allowed the field of thin films to become an advanced field of science [4][5]. Each one of these areas must be continually improved and developed in order for thin film science, and therefore devices and industries relying on thin films, to further advance.

The technology by which thin films are prepared is key to the structural evolution of the films. The general process of thin film formation, consisting of atomic adsorption, diffusion, combination, nucleation and growth, are controlled by the thin film preparation parameters [6]. Therefore, the thin film deposition process plays a significant role, in addition to film composition of course, in determining the final properties of the deposited layers [7].

A recent development for thin film preparation is the HiTUS technique. The acronym "HiTUS" stands for High Target Utilisation Sputtering. It is a thin film deposition technique, designed and patented by Plasma Quest Ltd (PQL). The basic

principles regarding this technique and its advantages are reviewed in Chapter 2 of this thesis. HiTUS is different to conventional sputtering techniques in that the gas plasma required for sputtering to take place is generated remotely. One major advantage to this is that independent control of ion density and ion energy is possible, permitting an extra avenue for 'tailoring' the structure of thin films. The HiTUS technique is used at PQL for contract research and development purposes, and also by a number of academic institutions and thin film manufacturers. High quality thin film coatings and material performance with this deposition technology have been achieved. The full potential of HiTUS is yet to be realised. Many materials remain to be investigated using this innovative technology, including those used by the data storage industry; one important industry that has greatly benefited from the improvements in thin film deposition technology.

The work contained in this thesis concentrates on using the HiTUS sputtering technique as a means of investigating potential future materials for magnetic data storage. Magnetic data storage is widely used in stationary and mobile applications for example mobile phones, MP3 players and corporate storage systems. The developments in this industry since 1956, when the first digital magnetic disk drive - the Random Access Method of Accounting and Control (RAMAC), was introduced by IBM have been astonishing. The areal density of RAMAC was 2000 bit/in^2. Fifty 24 inch diameter disks were needed to hold 5 MB of data and its size was comparable to a large filing cabinet. Storage capacity was often leased to companies rather than purchased [8]. In 2002 three or four 2.5 inch hard disks held 60 GB of data at a cost of about $100 (close to 1 cent per MB). In 2007 one terabyte of data could be purchased on a single 3.5 inch disk drive for less than $399 [9]. Today a one terabyte HDD can be purchased for as little as $100. The hard disk drive (HDD) constitutes the main form of data storage and retrieval in present day computer and data processing systems. The market for 3.5 inch HDDs is growing at an annual rate of 9 %, and for 2.5 inch HDDs growth rate is over 20 % [10]. The growth of bit areal density (the number of bits per unit area of disk surface) has on average been about 40 % per year [10]. The fastest pace in bit areal density progress occurred in the 1990s, with the invention of the giant magnetoresistance read head, coupled with improvements in thin film sputtered media and advancements in digital recording channels, enabling over 60 % compounded growth [11].

Disk drives are increasingly smaller, lighter, faster and bought for a fraction of the cost of IBM's first HDD. The pursuit of higher areal densities for data storage is on-going, with the continual search for new materials and improved methods of storing and retrieving data. This project is in collaboration with PQL, to investigate the use of the HiTUS technology to fabricate materials for magnetic recording and contribute to the continuous research within this industry.

1.1 Overview of thesis

This project uses the relatively new High Target Utilisation Sputtering (HiTUS) technology to grow magnetic thin films for data storage applications. There are two aims to this project, both relating to the development of ultra high density hard disk drives. The first aim is to investigate the fabrication of iron platinum (FePt), which has been attracting a lot of attention for use as future data storage media. A particular phase of FePt, known as the $L1_0$ phase, has a high anisotropy constant which means it has a higher resilience to thermal switching of magnetisation in small grains than materials currently used; this renders it an attractive material for future magnetic media, enabling higher storage densities. The second aim of this project is to improve upon current magneto-resistive read sensors employed in hard disk drives by using multi-ferroism – a new term coined to describe the multi-functionality of a system which in our study is the combination of ferroelectricity and ferromagnetism.

The following chapters begin with an introduction to the most common thin film deposition methods, namely DC diode and magnetron sputtering (Chapter 2). The HiTUS system and the advantages associated with this sputtering technique are also discussed in Chapter 2. Chapter 3 reviews the basic concepts in magnetism and the important properties associated with magnetic materials. Chapter 4 provides background information on magnetic data storage and the $L1_0$ phase of FePt, highlighting the interest in this material. Chapter 5 introduces the topic of multiferroic materials; materials that display multiple functionalities, and their potential contribution to data storage devices. Chapter 6 describes the characterisation techniques used throughout this work which include Vibrating sample magnetometry,

Magneto-optic kerr magnetometry, X-ray diffractometry, Atomic force microscopy and a 4-point probe technique for magneto-resistance measurements.

Chapter 7 concentrates work that has been undertaken on FePt thin films deposited by HiTUS. FePt is a material of great interest and the research into creating high quality FePt of the correct structural order via an easy, non expensive route is extensive. In this work an alternative method for producing FePt is also studied; by a reactive sputtering process nitrogen can be incorporated into FePt films producing FePtN. When the nitrogen is released from the film during annealing it is hopeful that this can improve the structural order of FePt. Key findings are reported and a conclusion is found at the end of this chapter.

Multi-ferroic materials are regarded as having great importance in future technologies and applications such as magnetic field sensors, current sensors, transformers and gyrators and microwave devices. Chapter 8 is concerned with how combining the functionality of ferroelectricity and ferromagnetism can lead to improved performance in practical devices - for our studies, potential multi-ferroic read head sensors are of most interest. The possibility of using voltage to control magnetism and vice versa can open many areas of research. In magneto-resistive read devices a constant current is required for reading data, in a multi-ferroic read device there would be no need for this current, this is attractive as thermal issues can be greatly improved and power consumption reduced; these are very important aspects for small portable devices. The experimental work and results in chapter 8 explore the phenomenon of multi-ferroism for improving present day read head devices.

Chapter 2

Thin film fabrication

The rapid developments in thin film deposition processes over the past few decades have lead to the production of thin films with improved film characteristics and superior film qualities. The improvements in thin film fabrication processes have been partly responsible for the advances made in the data storage industry. There are numerous ways of producing thin films. The most common methods of thin film fabrication involving electro-deposition and vacuum techniques are discussed in this chapter, with a stronger emphasis on sputtering and in particular, the high target utilization sputtering (HiTUS) technique.

2.1 Introduction

Electro-deposition, or electroplating, provides a means of depositing metal films from an ionic solution (electrolyte) of the metal [12]. In the solution the constituent ions interact so weakly they are virtually free. A substrate that is to be coated is placed into the solution and a negative charge is applied to the substrate to which the positive metal ions in the solution are attracted. The equipment required is simple, deposition is rapid, therefore this method is used due to its cost effective nature. However, the resulting films are often impure and it is difficult to achieve dense and defect free films. Vacuum methods are preferred and more common in the data storage industry since better quality films are possible.

Vacuum methods rely on some method of vaporizing of solid materials and transporting the material to the substrate all within an evacuated chamber. There are several ways that vaporization can be achieved: by heat (as in evaporation), by

a focused energetic beam of electrons (as in electron beam evaporation), by irradiation with a laser beam (as in laser ablation), or by the bombardment of positive ions (as in sputtering) to name a few [13][14].

The most widely used vacuum methods are Chemical Vapor Deposition (CVD) and Physical Vapor Deposition (PVD). Here, only the most commonly used vacuum methods will be described, with a stronger focus on the PVD group, particularly DC cathode and planar magnetron sputtering. It is from these two techniques that the "High Target Utilisation Sputtering" (HiTUS), used in this project, is based.

In CVD processes solid materials are created directly from chemical reactions [15]. The source material is supplied as a gas or as an evaporating liquid having sufficient vapour pressure to be transported at moderate temperatures. Even solids that have been chemically converted to vapors are categorized as CVD. A carrier gas is also often used. The constituents can react on a hot surface to deposit a solid film. Gaseous compounds can decompose on a hot surface, for example, graphite can be produced from methane (CH_4) at a substrate temperature of 2200 °C. Hydrogen can be used in reduction reactions, for example silicon tetrachloride is reduced to deposit silicon at 1000 °C [16]. Aside from decomposition and reduction reactions on substrate surfaces other possible reactions including oxidation, nitridation and carbidization can occur. A variety of elements and compounds of high purity can be deposited this way. The main disadvantages of CVD are related to safety issues and contamination. Some hydrides and carbonyls are poisonous. Metalorganics are pyrophoric (ignite spontaneously if exposed to air) [17]. An extensive amount of chemical toxic waste is produced which is also expensive to dispose of. Some elements are difficult to obtain in compounds of high purity at reasonable cost.

In PVD processes the material deposited is physically moved onto the substrate. There is no chemical reaction which forms the material on the substrate as in CVD. The two main branches that fall within the PVD group are evaporation and sputtering.

2.2 Vacuum Evaporation

The basic set-up for vacuum evaporation is shown in Fig. 2.1.

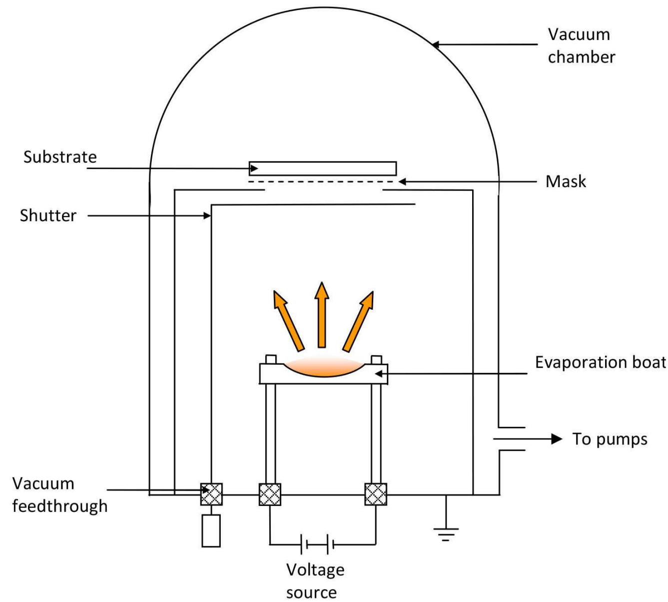

Figure 2.1: A typical thermal evaporation system.

The basic set-up for evaporation comprises of a chamber connected to suitable vacuum equipment, and a crucible containing the solid or liquid to be deposited (the evaporant). If the evaporant is heated to sufficiently high temperatures it will evaporate and the evaporated atoms will condense onto any suitable substrate in their path. Methods of heating the evaporant include resistive heating, eddy current heating, electron beam heating, and by the use of a focused high power laser beam [18].

Due to the substrate being cooler than the evaporant, the evaporated material travels with thermal velocities in a straight line (line of sight deposition), provided the chamber has been sufficiently evacuated. At pressures of 10^{-5} mmHg about 99 % of the evaporant leaving in the direction towards the substrate would reach a substrate 10 cm away without collision [6].

Though high purity and high quality films are obtainable using this technique there are some disadvantages using evaporation.

- High temperatures may be required to heat the evaporant [19].

- It is difficult to maintain high rates for long periods since large quantities of evaporant are not easy to heat, it is also difficult to control the deposition rate [20].
- Some evaporants are highly reactive at high temperatures which may pose problems and not all materials can be evaporated [18].
- Films are often not uniform, the depositing atoms have low energies (about 0.1 eV) so films of low adhesion and low density are produced. Much more uniform, denser and better adhered films are also easier to obtain by sputter deposition [19].

2.3 Sputtering

Sputtering is defined as the erosion of solid surfaces during ion bombardment [21]. The solid surface is usually the material that is to be deposited, known as the *target*, and the ions used to strike the target material are energetic positive inert gas ions [22]. During ion bombardment a cascade of atomic collisions is created in the bulk of the material and if enough momentum is transferred to the atoms that are in the surface, one or more atoms are freed, scatter in all directions and collect onto a substrate to form a film. This is "sputter deposition" [23]. This is shown schematically in Fig. 2.2.

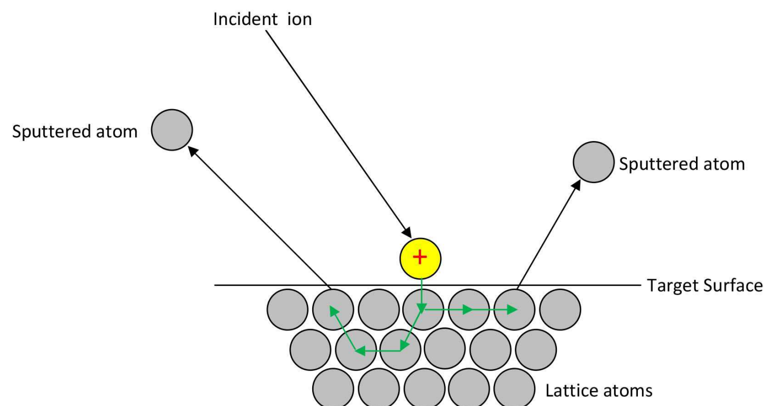

Figure 2.2: An illustration of the sputtering process.

In order to produce sputtered atoms a practical approach is by generating electrical discharges known as *plasma* or *glow discharge* in an inert gas atmosphere.

Argon, Ar, is a commonly used gas. Plasma can be considered as the fourth state of matter - when a material is energised beyond its gaseous state at least one of the outer shell electrons is stripped away, producing a mixture of gas atoms, gas ions and free electrons [24][25]. Near equal concentrations of positive ions and negative particles (electrons and negative ions) are found in plasmas [26]. A glow discharge is a specific form of plasma containing regions of net positive and regions of net negative charges, but overall it must remain globally neutral [26]. Glow discharge processes are often associated with electrode based sputtering systems. The terms plasma and glow discharge are often used interchangeably as many of the physical principles are the same. Both DC and RF discharges are used [22].

2.3.1 Glow discharges

In the simplest form, the electrical discharge is initiated between two parallel plate electrodes, one is the cathode (C), the other is the anode (A). A quartz tube is evacuated and filled with an inert gas. Without the application of a potential between the electrodes, the gas molecules are electrically neutral, though there are a few free electrons around that are emitted by the cathode (via thermal emission, field emission, photoemission) or random collisions may have occurred with the release of free electrons (Fig. 2.3).

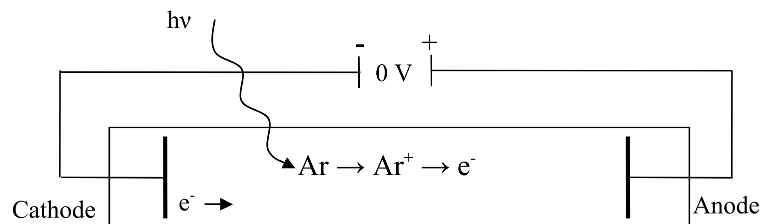

Figure 2.3: Initiation of a glow discharge between parallel plate electrodes.

When the pressure in the tube is reduced further to a few centimetres of mercury (1cm Hg = 13.33 mbar) and a sufficient potential difference is applied across the electrodes, a uniform glow is obtained throughout the tube as it becomes filled with positive and negative particles throughout (Fig. 2.4).

If the pressure is reduced further to a few millimetres of mercury (1mm Hg =

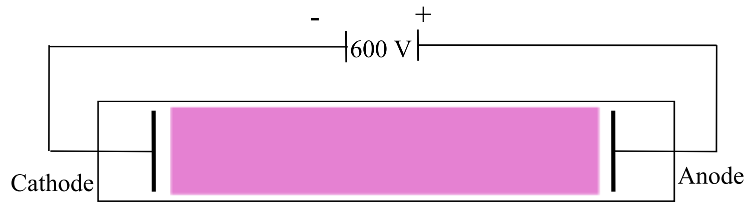

Figure 2.4: Uniform glow discharge between parallel plate electrodes.

1.333 mbar), a series of dark zones cross the glow discharge (Fig. 2.5) [27]. With sufficient voltage any free/secondary electrons leave the cathode area quickly and accelerate towards the anode. On their journey they first cross a 'cathode dark space' (region 1), attaining high velocities (and so high kinetic energies) due to their low mass. The mass of an electron is 9.11 x 10^{-31} kg, so is very light compared to the mass of Ar which is 6.64 x 10^{-20} kg. The cathode dark space is a region of the discharge where the electrical potential drops drastically, it is also known as the cathode fall [24]. It is dark here because the glow intensity depends on the number density and energy of the excited electrons, and here there has not yet been enough inelastic collisions with molecules for the glow from their excited states to be visible [27].

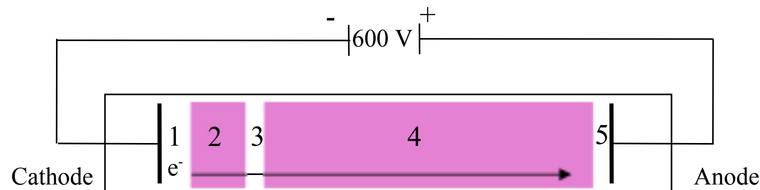

Figure 2.5: Regions within the glow discharge at sufficiently low pressures.

The electrons then pass through the 'negative glow' (region 2) where they collide with the gas molecules, ionizing and exciting them as well as losing their directionality by scattering [24]. This region is the most luminous of all gas discharge regions due to the high density of equal negative and positive charged particles (resulting in charge neutrality, i.e field free). Here, the electrons carry almost all the electrical current due to their high mobility. By the time the electrons reach the end of the negative glow region they have lost most of their energy, excitation and ionization of the gas is drastically reduced. A Faraday dark space (region 3) may exist after the negative glow, where the electron energy is very low [26].

Beyond the negative glow is the positive column (region 4), where the charge density is low, the electric field is very small but enough for it to be luminous and maintain some ionization until the electron reaches the anode. The positive column acts as a conducting path between the negative glow and the anode.

The electrons accelerate across the anode dark space (region 5), a region that has a negative space charge (electrons out number the positive ions) and the electric field is higher than in the positive column. Upon striking the anode the electrons lose the energy that they are carrying.

Meanwhile, positive ions in the negative glow region are accelerated towards the cathode by the electric field in the cathode fall. These high energy ions collide with the cathode surface producing secondary electrons, which in turn accelerate out towards the cathode fall, attaining high energies, transferring their energies via inelastic collisions (excitation, dissociation, ionization) creating extra charge carriers. This occurs mainly in the cathode fall and negative glow regions. This cascade of events continue, sustaining the discharge [27].

2.3.2 DC cathode sputtering

The application of a DC voltage across the electrodes within the plasma chamber is the simplest form of sputtering, known as cathode sputtering, see Fig. 2.6.

A chamber is evacuated and filled with an inert gas, such as Ar to pressures between between 3 Pa to 300 Pa (0.03 to 3 mbar) [28]. The target (the material to be sputtered) acts as the cathode and the substrate the anode. A DC potential of several kilovolts is applied between the electrodes [28].

The positive ions of the gas created by the discharge are accelerated by the electric field toward the target. These bombarding ions gain energies of a few eV in the cathode fall region (high compared to those created during evaporation with energies of 0.1 eV) [16]. These energies are by far enough to break chemical bonds. The electrons are accelerated across the cathode dark space and strike the target.

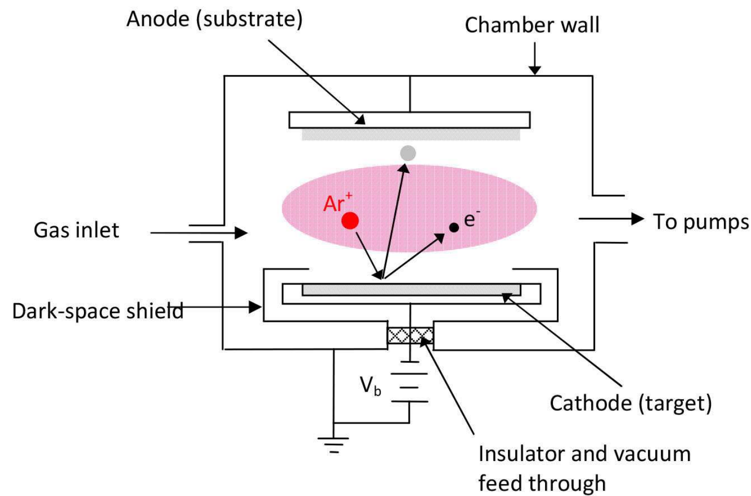

Figure 2.6: Typical DC diode type arrangement.

On striking the target atoms the displacement of lattice atoms, the formation of defects and the surface sputtering of the target material occurs. Material is sputtered mostly as neutral atoms but some will also take the form of ions. The sputtered material condenses onto surrounding areas, including the substrate.

The bombarding positive ions can also excite target surface atoms to an excited state with the emission of a secondary electron. The small number of secondary electrons that are created this way at the target accelerate towards the anode and serve to maintain the glow discharge.

The rate of material sputtered, Q, under constant conditions is inversely proportional to the gas pressure, p and anode-cathode distance, d [16]. It can be assumed that the amount sputtered will be proportional to the positive ion current, i_+, flowing to the cathode [29],

$$Q = \frac{kVi_+}{pd} \tag{2.1}$$

where k is the constant of proportionality that is a function of the voltage, V. However, the rate of sputtering also depends on the sputtering yield (the number of atoms ejected per incident ion), which is in turn a function of the ion energy, mass of the ion, target material and target - substrate geometry [21].

The main advantages of this technique are [30][31]:

- Most vacuum compatible materials can be deposited.
- No heating of the target material is required so materials which are difficult to evaporate are easily sputtered.
- Sputtering takes place from the whole of the target surface which means a uniform film can be deposited over a large area.
- It is a controllable process since the sputtering rate is proportional to the current flowing between the electrodes.

The main disadvantage of this technique is the slow deposition rates. A typical deposition rate is 0.1 nm s^{-1}. The DC parallel plate glow discharge technique operates at relatively high pressures, in the 3 to 300 Pa range (depending on gas composition and electrode spacing) and relatively high voltages of about 1000 to 2000 V [28]. If the operating pressure is too low, electrons from the cathode would not undergo enough ionizing collisions with the working gas to sustain the plasma before reaching the anode (where it is lost). At too higher pressures, the sputtered atoms would undergo too many collisions to reach the substrate [28].

Positive ion bombardment of insulating targets would soon lead to a charge up on a target, subsequently shielding the electric field. The ion current would die off and sputtering would stop. The solution to sputtering non-conductive target materials is by applying an alternating voltage at radio frequency so that the targets are periodically charged and then discharged - this is RF sputtering [22].

2.3.3 Magnetron sputtering

The planar magnetron system is a slight adaptation of the DC cathode parallel plate system, with the addition of magnets (either permanent or electromagnets) behind the cathode (the target) [32]. This is shown in Fig. 2.7.

The glow discharge is ignited the same way to that in a DC cathode system, i.e free electrons are accelerated by the electric field in the cathode fall, but their

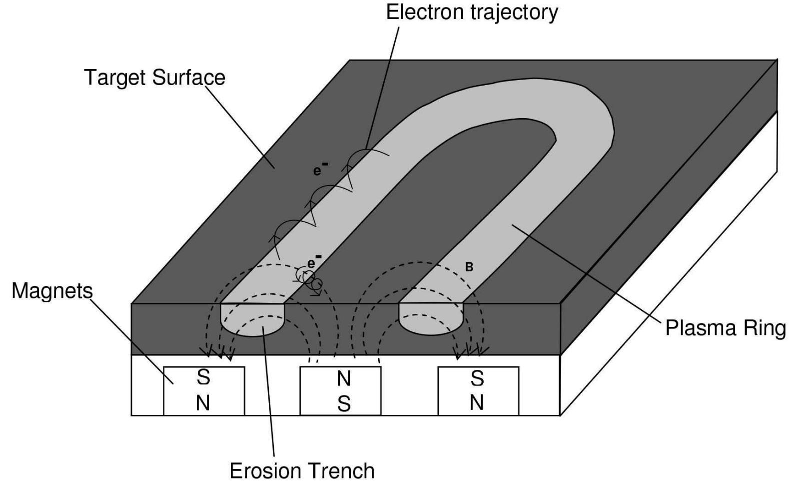

Figure 2.7: Schematic showing typical magnetron sputtering system.

subsequent journey is different.

In the presence of only a magnetic field the typical motion of an electron is circular around the field lines. This orbiting motion around field lines is known as 'Larmor rotation' [33]. The frequency (the number of revolutions per second) at which an electron orbits the field lines is known as the 'cyclotron frequency,' ω, and is given by $\omega = eB/m$ where B is the magnetic field strength (Gauss), e the elementary charge and m the mass of an electron. The radius of the orbit is the 'Larmor radius,' R_L. The Larmor radius is given by equation 2.2 and is dependent on the kinetic energy of the electron (therefore electric field) perpendicular to the magnetic field,

$$R_L = \frac{mv}{eB} \tag{2.2}$$

where v is the velocity of an electron perpendicular to the magnetic field.

Electrons, whether emitted from the target or created by ionization in the sheath field experience forces from both the electric field (**E**), that is generated by applying a negative voltage to the target, and the magnetic field strength (**B**). The force which describes the force on a charged particle due to electromagnetic fields is the Lorentz force (**F**) which is given by:

$$\mathbf{F} = q[\mathbf{E} + (\mathbf{v} \times \mathbf{B})] \tag{2.3}$$

where **B** is the magnetic field vector (tesla), **E** the electric field vector (volts per meter). **F** is the force (Newtons), q is charge of particle (in Coulombs), **v** is particle velocity and $\times$ represents the vector cross product. The emitted electrons are accelerated vertically by **E** but at the same time are forced sideways by **B**.

Another motion that the electrons perform is one in which they spiral along the magnetic field lines bouncing back and forth between the magnetic poles due to the magnetic mirror effect [34]. The magnetic mirror effect can be simply defined to say that charged particles are reflected in the zones of with higher density magnetic force lines to the zones of lower density of the same lines.

The electron density (and so the number of ions generated) is highest where the **B** field is parallel to the substrate, causing the sputter yield to be highest directly below this region. This electron trajectory is responsible for the non-uniform erosion of the targets in a magnetron system [28]. A trench or 'racetrack' forms in areas where ionization has been the strongest. A non-uniform target can result in non-uniform films.

Magnets in the range 100 to 500 G are used, so that only the motion of electrons are significantly affected, Ar ions are too massive to be affected with these strengths. Imposing a magnetic field effectively increases the electron path length, which in turn increases the ionization rate (and subsequently the sputtering rate). Due to this increase in dwelling time of the electrons, a magnetron sputtering system can sustain a plasma with a pressure as low as 0.1 Pa (0.001 mbar), whereas a typical minimum pressure required by a DC cathode system is 3 Pa (0.03 mbar). By increasing the efficiency of electron usage, a lower voltage (typically 500 V) is required to sustain a plasma of given density [28].

Another advantage to using magnetic fields is that electrons, along with the tremendous energy they carry, can be deflected away from the substrate. Where in

DC cathode sputtering, the substrate is an electrode, the energy dissipated by the electrons could have detrimental effects on the growing film. Excess heating can cause distortion, recrystallisation and even evaporation of the film material.

The magnetron sputtering process is the same as in cathodic sputtering, i.e. the establishment and maintenance of a glow discharge and the positive ion bombardment of a negatively biased target material. As in DC cathode sputtering, RF excitation can be used for sputtering insulating targets. With the addition of an active gas (e.g O_2, N_2, H_2S) to the working gas new compounds with controllable stoichiometry can be deposited. The active gas would react with the target material, either at target surface or in the gas phase. This is 'reactive sputtering.'

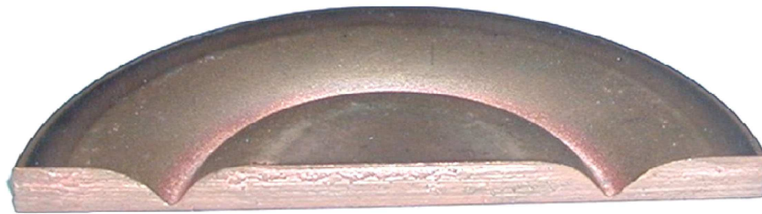

Figure 2.8: Image showing racetrack formation in a copper target sputtered using a magnetron system (photograph of an actual target taken at PQL).

The racetrack effect of a magnetron system limits the lifetime of a target material. Sometimes only 10 to 30 % of a target is used before it has to be recycled [32]. Fig. 2.8 above shows this racetrack effect on a copper target sputtered using a magnetron system. Much effort has been put into improving target utilization whilst maintaining the high deposition rates and low pressures used in magnetron sputtering. One such design is the High Target Utilisation Sputtering (HiTUS) technique designed by Plasma Quest Ltd.

2.4 High target utilisation sputtering

The High target utilisation sputtering (HiTUS) system is a variant of conventional vacuum sputtering systems. Originally, the intention of its design was to enable high rate sputtering from the full exposed surface of a target material (a limitation of earlier conventional sputtering systems). However, experience with the development

and use of the HiTUS sputter technique has shown that improved quality coatings and coating performance are also delivered; this is now considered the main benefit associated with HiTUS. The benefits of HiTUS include:

- The ability to sputter thick ferromagnetic targets
- $>$ 95 % target utilization with uniform target erosion
- Easy control of film stress
- The ability to perform high rate, stable reactive sputtering processes
- High coating rates with low thermal load

A HiTUS system deposits materials by the sputtering process - it therefore shares many similarities with other sputter coating technologies. This includes the mechanisms by which energetic atoms or ions 'sputter' the target material, the transfer of that material to a substrate, and the formation of a thin film coating. However, the manner in which the plasma required for the sputter process is generated and the impact of that on system operation and process behaviour leads to substantial operational and capability improvements. Thus HiTUS is not just a derivative of conventional sputter systems; to fully realise the technology's potential, it is usually important to explore the range of different process parameter settings provided by the technology.

The mechanisms by which the plasma containing the energetic atoms or ions that cause sputtering is produced and the manner in which the coating growth is additionally influenced by this plasma differ from usual sputtering. This has been found by PQL and others to bring significant and beneficial changes to the structure and properties of the deposited materials, the conditions under which they can be deposited in their preferred forms and the capability to achieve these benefits with commercially viable processes.

Thus whilst it is appropriate to use much of the established thin film deposition theory when considering sputtering and film growth fundamentals, it is not appropriate to use most of the usual operational theories, results and practice without careful consideration of the differences that might result from the HiTUS technique.

2.4.1 System overview

A standard HiTUS coating system is shown in Fig. 2.9. As in conventional sputter coating systems (such as DC cathode and magnetron), a HiTUS system comprises a high vacuum chamber and associated vacuum components, a sputter target assembly and associated power supply, and a substrate holder positioned to receive material sputtered from the active target. In addition, the system includes PQL's proprietary design remote 'side arm' plasma source (PLS) to generate the high density plasma needed for the sputter process. Therefore, a HiTUS sputter deposition system essentially differs from a conventional sputter deposition system in that the target is not itself required to generate the gas plasma needed for the sputtering process to occur. This permits a far wider 'process space' to be explored and used.

Rather than the target producing the sputter plasma, the attached remote PLS separately generates the plasma, which is guided to the target by a shaped constant magnetic field produced by DC powered electromagnets. The PLS is able to generate plasma over a wide process pressure range independently of the target condition or type, and so a very wide range of process options and target materials are able to be used.

The PLS unit comprises a Radio Frequency (RF) induction coil antenna (run at 13.56MHz as standard) positioned around a quartz tube; the tube diameter is typically 8cm to 15cm. An annular electromagnet is fitted at one end of the quartz tube and defines the exit of the plasma source; it is this end that attaches to the process chamber. A second similar electromagnet is placed beneath the target position and, in conjunction with the plasma source electromagnet produces a magnetic field profile that directs the plasma to the target surface. Magnetic field strengths in the range 30 G to 300 G are used. Substrates are placed on a floating or grounded (as required) substrate table above the target. The chamber is evacuated to the base pressure required for the process (typically $<5 \times 10^{-5}$ mbar) and then fed with a controlled flow of Ar gas to achieve a dynamic flow/pump rate balance process pressure, typically 3×10^{-3} mbar. As with conventional sputter processes, argon is the primary gas used. Other gases such as oxygen, nitrogen, hydrogen, helium, carbon tetrafluoride and silane can also be used.

Visually, the plasma source appears to produce a 'tube' of brightly glowing gas plasma of colour and intensity dependent on the process gases used and the PLS power - typically bright purple-blue for high power operation with argon gas. This is usually 'directed' over the sputter target area using DC electromagnets as shown in Fig. 2.9.

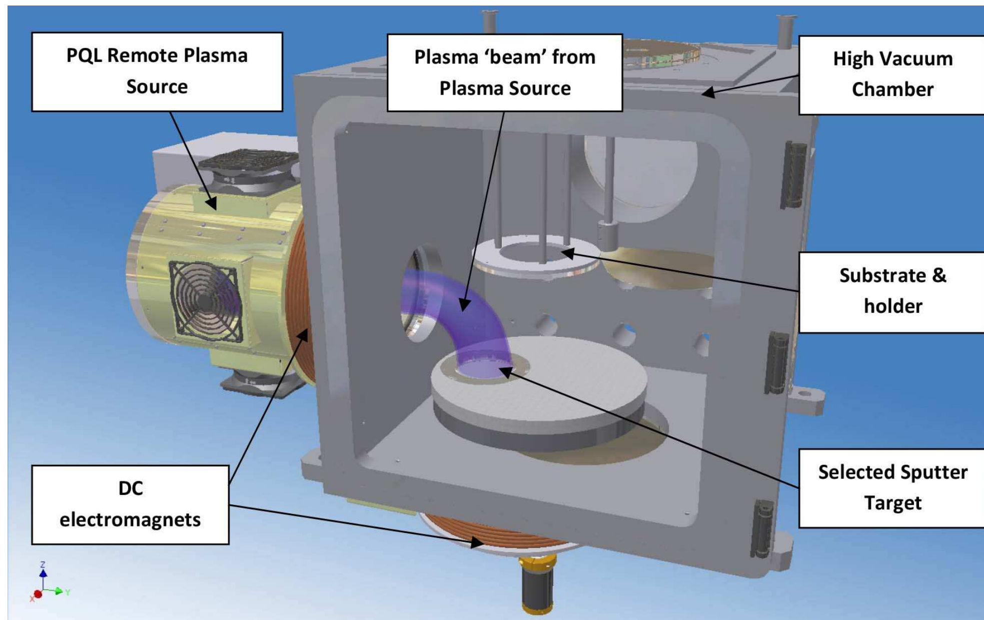

Figure 2.9: Diagram of a typical HiTUS system showing visible plasma path (chamber door removed for clarity), used with permission from PQL.

2.4.2 Plasma generation and HiTUS process

The exact manner in which the PQL plasma source operates is still the subject of research at PQL. It has been confirmed that it is not a simpler version of the well known Helicon plasma source, despite apparent engineering similarity. The following therefore describes PQL's (largely unproven) theories on which their (successful) plasma source development is based at the time of writing.

The application of RF power to the plasma source antenna inductively couples energy to the process gas, causing free electrons to oscillate and collide with the gas atoms, resulting in ionization with the ejection of secondary electrons which themselves are energised to continue the ionization process. This is the basis of any

standard Inductively Coupled Plasma (ICP) system.

With the PQL plasma source the presence of the magnetic field produced by the plasma source electromagnet is expected to greatly enhance plasma generation effectiveness. Within the vacuum gas environment, recombination of Ar ions and electrons is possible but is greatest at the walls of the quartz tube; however, the plasma source electromagnet serves to create a field that 'traps' the electrons, so keeping them away from the walls of the tube and increasing their average path length. An initial low density plasma of at least 10^{10} cm^{-3}, probably more than 10^{11} cm^{-3}, is produced [35].

Between the RF antenna and the plasma source electromagnet optical emission spectrometry (OES) shows that the combined RF field of the plasma source antenna and static magnetic field of the electromagnet(s) result in an order of magnitude or greater increase in the localised plasma density. The means by which this occurs is unknown.

As a result, at the sidearm exit plasma densities in excess of 10^{13} cm^{-3} can be achieved. This high density plasma generation region continues to be guided to the target by the magnetic field of the combined plasma source and target electromagnets, it is believed by an ionization 'cascade' process driven by the RF field from the plasma source. Under optimised processing conditions, where the cascade of ion production is sustained, plasma densities of typically 10^{13} cm^{-3} arrive at the target surface (as evidenced by measured target currents in excess of 30 mAcm^{-3}).

An important factor in considering the operation of the HiTUS is to appreciate the impact of the static magnetic field. In a traditional plasma, the electron density and ion density are, on average, equal except very close to the electrodes. In a HiTUS plasma, electrons are confined to a tubular path (initiated by the annular ICP generation of the RF antenna) that 'bends' from the plasma source exit to the target (see Fig. 2.9). However, the higher mass ions are not effectively confined and a high ion density is therefore present throughout the process chamber volume. These ions do not evidence a 'glow' as there are no energetic electrons nearby to excite such behaviour; their presence is only shown by positive charging of electrically

isolated features within the process chamber away from the visible plasma region. Thus when considering the impact of the plasma on the substrate, it is important to remember that the substrate need not be near or in the visible plasma; it is, in fact, highly destructive if it is too close due to the high flux of energetic electrons.

A major benefit arises from the use of the remote plasma source in that the target is not required to generate or sustain the plasma. As the PLS does not itself impart any substantial kinetic energy to the plasma ions, the target must be negatively biased. This is identical to standard planar diode and magnetron sputtering and in principle therefore, the extensive literature covering these techniques and the general knowledge regarding material sputter yields, angular distribution of sputtered material, etc. can be used to assist process development. Effective sputtering can generally be obtained for negative bias voltages as low as 50 to 80 V. Essentially, the target acts as a collector plate for the remotely generated plasma ions and, above about 100 V negative bias, the target current is essentially independent of bias voltage, being set by the remote plasma RF power and system operating pressure. This contributes both to a stable sputtering process and greatly increases the range of process parameters that can be used to sputter. For example, a low target voltage can be used with a high sputter current (plasma density, hence plasma source RF power dependent) to provide a high arrival rate of sputtered material without the high and potentially disrupting kinetic energy that would result from DC or magnetron sputter techniques.

The HiTUS sputter process itself (the mechanism by which material is released from the target surface) is believed to be identical to that of other sputter techniques. Energetic gas ions impacting the target surface impart a proportion of their kinetic energy to the surface (or near surface) atoms, resulting in emission of these atoms if the ion energy and/or density is sufficient to overcome the local bonding energy.

Process gas pressures of 3×10^{-3} mbar and RF powers of 1 to 2 kW are typically used to strike a plasma. However, plasma generation using the remote PLS can also occur at pressures as low as 3×10^{-4} mbar. The system may also be successfully operated with RF power levels from less than 100 W up to 5 kW. A wide range in

sputter target current densities is attainable by varying the gas pressures and RF power alone.

The HiTUS system is capable of sputtering a wide range of materials, either single element or of compound formation, and additionally reacting these with appropriate added gas(es). Target materials can be metallic, semiconducting or insulating. As with most other sputtering methods, insulating materials require the use of an AC bias supply, usually at RF frequency. In general, the use of magnetic target materials has little or no impact on the sputter or coating processes with HiTUS and those factors relevant to single or multiple element conductive targets are appropriate.

The sputter targets are usually circular planar, typically 5cm to 20cm in diameter and 6mm thickness. Multiple targets can be mounted on a single, rotatable circular planar holder and individually indexed into an aperture in a dark shield that otherwise blocks the plasma and thereby prevents sputtering from the non-selected targets, whether they are powered or not.

The remote plasma system is capable of providing a uniformly high plasma density over the full target area. When the target is biased, the entire exposed target is subject to sputtering and for an optimally designed system, erosion of up to 95 % of the target surface area may be achieved. This has several major process benefits. Firstly, very high sputter rates are achievable. An ion current density of up to 100 mA/cm^2 is possible, as in magnetron sputtering, however, in HiTUS this is over the full target surface, not just locally; for DC cathode sputtering ion current densities are usually in the range 0.1 - 2.0 mA/cm^2. *Ion current density* is defined as the number of ions (e.g ionized Ar atoms) hitting the target per unit area. A high ion current density leads to a high sputter rate. Sputter rate is generally a linear function of the target power. Hence increased voltage or, independently if required, current both increase the deposition rate though with potentially different effects on the thin film surface growth kinetics. High sputter rates permit high deposition rates to be maintained at wide target to substrate separations (e.g. 20 - 30cm). Combined with process optimisation, this substantially reduces the heat load on the substrates and it is therefore possible to deposit a range of high quality

thin films at high rates onto even traditionally 'heat sensitive' plastic sheets such as PET and PEN. Compatibility with other organic based structures, e.g. OLED, is also possible.

In addition, the very uniform and extensive target erosion minimises target "poisoning" by reactive gases present in the process, and allows compound targets to be used without stoichiometric changes as the target erodes. The absence of racetrack formation combined with the independence of the plasma on the target state leads to excellent process stability and reliable reproducibility for reactive processes.

The remote plasma also facilitates the traditionally 'difficult' process of reactive sputtering and high rate sputtering of ferromagnetic materials. For example, it is possible to deposit very high quality dielectric films at high deposition rates, typically 100-200 nm/min, using inherently stable reactive sputter processes. Examples of dielectric films produced using the remote plasma include alumina, silica, titania, tantala, niobia, silicon nitride, titanium nitride and aluminium nitride. Typically, these films show very low stress (essentially zero in most cases for optimised processes), excellent adhesion and refractive index near bulk values.

The remote plasma source enables the HiTUS technique to provide a wide process range. This allows increased control of the growing thin film microstructure, both due to an ability to 'customise' the precise target sputter conditions (e.g. the same target sputter rate can be obtained using a wide range of target voltage and plasma densities without changing sputter pressure) and through using the plasma itself to 'modify' the film as it deposits. The remote source allows independent control of ion density (set by the RF power) and ion energy (set by the target bias). Metallic, insulating and semiconducting thin films have routinely been prepared at PQL with low stress, near ideal material optical properties, excellent electrical conductivity, good magnetic properties and high dielectric breakdown strengths.

The HiTUS process has been applied to a wide range of coatings by PQL and other users; examples include:

- Zinc sulphide doped with manganese (ZnS:Mn), indium tin oxide (ITO) and alumina
- Hafnium oxide (HfO_x)
- Zinc oxide (ZnO) and indium zinc oxide (IZO)

- Niobium pentoxide (Nb_2O_5)
- Titania and hafnia

Wakeham et al. [1] have used the HiTUS method for producing electroluminescent (EL) devices. The three main materials used for these devices are ZnS:Mn, alumina and ITO. The ZnS:Mn acts as the phosphor layer, and initial studies involved fabricating this layer using HiTUS and incorporating it into a complete device. These devices were compared directly with devices incorporating ZnS:Mn produced using RF magnetron sputtering. The photoluminescence (PL) of RF magnetron and HiTUS deposited ZnS:Mn films were independently measured and the results are shown in Fig. 2.10. As can be seen, ZnS:Mn films produced using HiTUS exhibit significantly higher luminance than equivalent coatings deposited using RF magnetron sputtering. Even following post deposition annealing of the RF magnetron films at 500 °C, the brightness is still less than as deposited HiTUS coatings of equivalent thickness. Since the publication of this paper, complete EL devices have been fabricated using HiTUS technology comprising ZnS:Mn, hafnia, alumina and ITO. The high dielectric constant of the HiTUS hafnia and excellent breakdown properties of the alumina yield stable devices with a low threshold voltage.

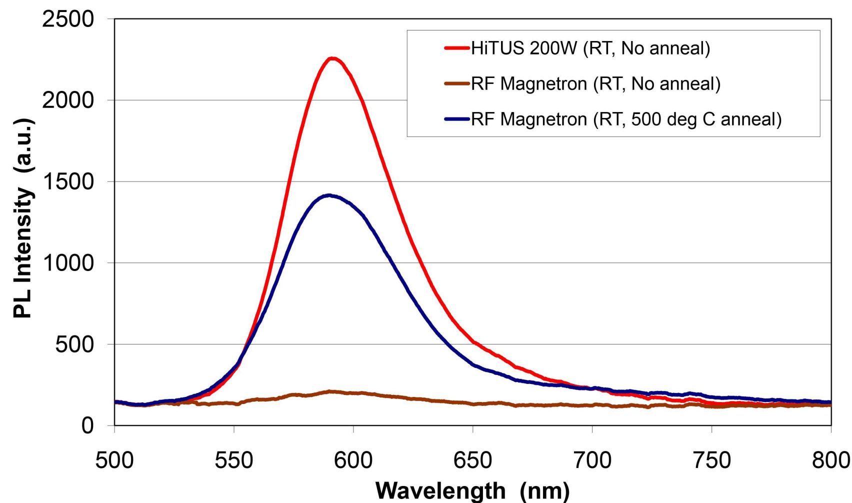

Figure 2.10: PL intensity for HiTUS deposited ZnS:Mn films prepared at ambient temperature using target power of 200 W. As deposited and post deposition annealed ZnS:Mn films prepared by RF magnetron sputtering are shown for comparison [1].

Flewitt et al. [36] have shown that the HiTUS system can deliver high deposition rates ($\sim$ 50 nm/min) of the metal oxide semiconductors ZnO and IZO with

material properties, such as field effect mobility, that are comparable with films deposited by other techniques. Although techniques such as pulsed laser deposition, atomic layer deposition and RF magnetron sputtering are known to produce good quality materials, the deposition rates are relatively low, for example RF magnetron sputtering offers a deposition rate of $\sim$ 5 nm/min. Higher deposition rates are possible using RF magnetron sputtering but higher deposition rates also increase ion bombardment of the substrate leading to deterioration of film properties.

Li et al. [37] have also reported on the advantages of high deposition rates using HiTUS. In addition, the separate control of ion density and ion energy using the HiTUS system has enabled Li et al. to produce amorphous HfO_x with a high dielectric constant (k = 30) using high deposition rates of over 25 nm/min at room temperature. Good dielectric properties, such as high electrical resistivity, high breakdown strength and wide optical band gap, were observed in the HfO_x films. The ability to produce HfO_x as an amorphous material with a high dielectric constant is a property that appears to be unique to HiTUS. These films are currently being investigated for TFT applications.

The metal oxide Nb_2O_5 has been fabricated by Chow et al. [38] using the HiTUS technique. This group showed that Nb_2O_5 films produced by HiTUS possess higher refractive indices than those prepared by ion-beam sputtering, DC magnetron sputtering and electron beam deposition. High refractive indices observed in materials are amongst the many advantages of HiTUS that have been independently corroborated by third party organizations but remain unpublished. Titania and hafnia for example have been deposited at room temperature, with high deposition rates, low absorption and high refractive indices. Measured transmission and dispersion data for titania and hafnia films produced by the HiTUS technique are shown in Figs. 2.11 and 2.12. It is clear that the transmission of the HiTUS films peak at the same level as that of the uncoated substrate (fused silica). The difference in the refractive indices of these materials is evident from the different amplitudes of the interference fringes. It should also be noted that the overall transmission is below that of the substrate only because the refractive index of both materials is higher than that of the fused silica. Hence, a reduction in transmission indicates increased reflectance, not absorption. The electronic absorption edge of the titania

and hafnia is indicated by the rapid drop in transmission in the short wave visible and long wave UV. The deposition rate of titania was 26 nm/min for a target power density of 19.1 W/cm^2 (from a 4 inch sputter target with a bias of 1.5 kW) and that of hafnia was 60 nm/min for a power density of 15.3 W/cm^2. These results compare favourably with results achieved using other high energy deposition techniques.

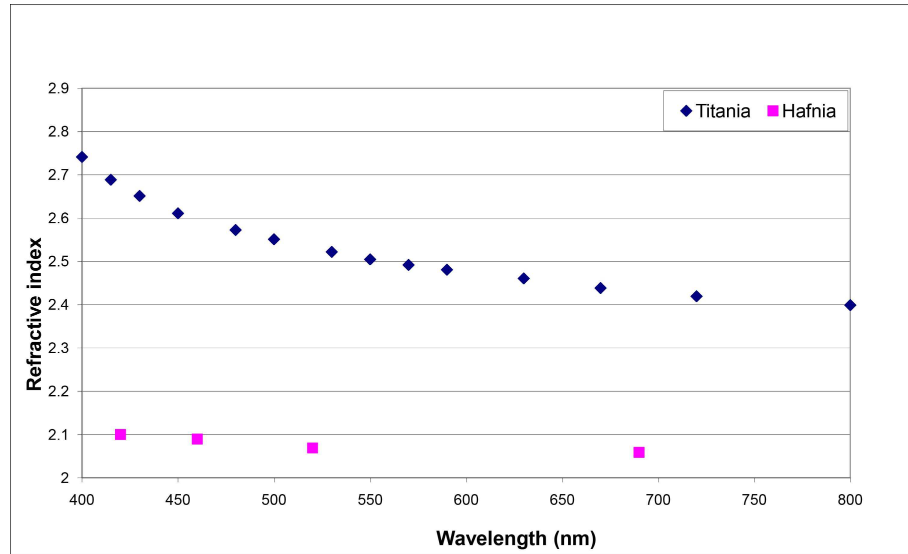

Figure 2.11: Variation of refractive index with wavelength for titania and hafnia deposited by HiTUS.

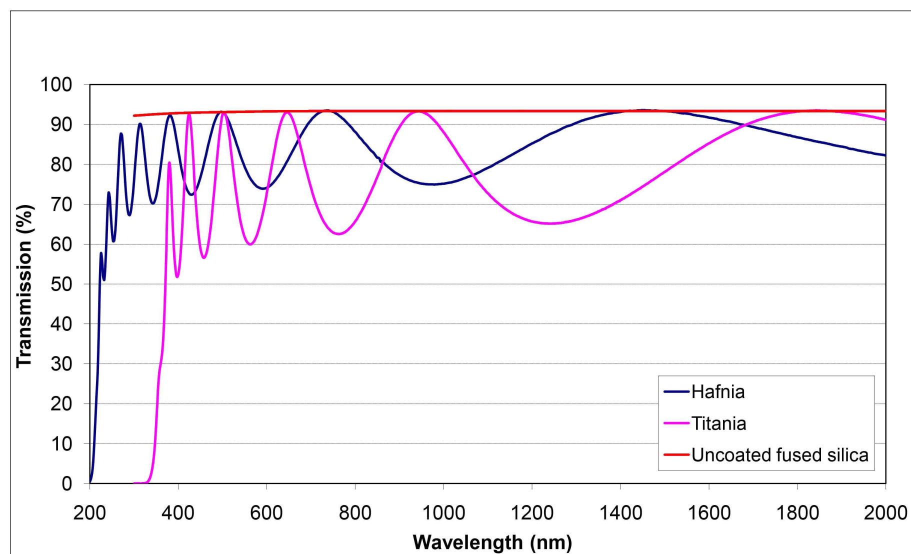

Figure 2.12: Spectral transmittance characteristics of HiTUS deposited titania and hafnia. The transmission of the uncoated substrate is also shown for comparison.

For a general idea of how titania deposited by HiTUS compares with titania

films prepared by other methods a brief comparison is summarized here. Hasan et al. [39] achieved a refractive index of 2.31 at 550 nm and an average visible transmission of greater than 75 % (presumably referenced to air) using RF reactive magnetron sputtering and room temperature deposition. For films deposited at 200 °C , a higher refractive index of 2.37 at 550 nm was observed. Krishna et al. [40] have used the electron beam evaporation technique and at a substrate temperature of 100 °C have obtained a refractive index of about 2.3 with a deposition rate of 12 nm/min. Kuo et al. [41] deposited titania at 200 °C using RF magnetron sputtering at a deposition rate of 4 nm/min. A refractive index of 2.4 at 633 nm was obtained (from Fig.2.11, HiTUS room temperature prepared titania has a refractive index of 2.46 at 630 nm) and a peak transmission of nearly 100 % when referenced to the uncoated substrate. Ion beam assisted electron beam evaporation has been used by Yang et al. [42] to prepare titania films. The substrate temperature was 300 °C and following deposition the films were annealed for 1 hour at 450 °C. A refractive index of 2.29 was calculated at 550 nm and the peak transmission for material deposited with minimal substrate heating was less than 65 % after post deposition annealing at 450 °C. This transmission was seen to improve with increasing deposition temperature but is still significantly lower than that attainable for HiTUS deposited films.

For HiTUS deposited hafnia, the refractive index is 2.07 at 520 nm. Fig. 2.12 shows the optical transmission of HiTUS deposited hafnia. A refractive index of 2.08 at 550 nm achieved by Pervak et al. [43] (using plasma assisted reactive magnetron sputtering) is similar to that obtained using HiTUS. The peak transmission obtained by Pervak et al. is also excellent but their deposition rate is significantly lower than that achieved using HiTUS, at 18 nm/min. Bright et al. [44] have used DC magnetron sputtering to deposit hafnia; the substrate temperature was maintained at 300 °C during deposition. A refractive index of about 2.01 was achieved with a deposition rate of 1.0 nm/min. Laser assisted electron beam evaporation has been used by Schmidt et al. [45] for hafnia fabrication. During deposition (at rates $\leq$ 20 nm/min) the substrate was irradiated with a laser power of 40 W and so heating effects contributed to film formation. A refractive index of less than 2.00 was obtained at 550 nm. With the rapid growth of the plastic electronics industry, the ability to deposit high quality thin films at low temperature onto polymeric

substrates is of huge importance. This is an area where HiTUS could prove to be of immense benefit.

2.4.3 Sputtering of magnetic materials

One of the advantages of HiTUS that is directly related to the work in this thesis is its ability to sputter thick magnetic materials without compromising the deposition rate. Magnetron sputtering is a commonly used method in the magnetics industry [46][47]. Magnetic materials are usually difficult to sputter with this method. This is due to the weakening of the magnetron vacuum component of the magnetic field as it is largely channeled through the material and therefore plasma generation is weakened (Fig. 2.13).

One solution is to use very thin targets and high field strength magnets to enable the magnetic field to extend back out into the plasma generation area (Fig. 2.14) and re-establish magnetron sputtering. The main disadvantage of this is the short life-time of a target due to rapid racetrack wear, and so it is not an ideal solution, particularly for use in industry.

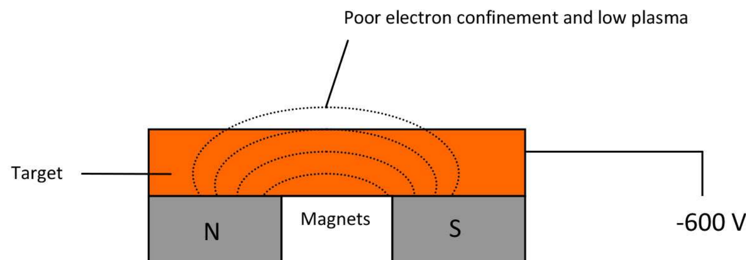

Figure 2.13: Magnetic target reduces vacuum magnetic field through confinement in target material.

When a ferromagnetic target is used in a HiTUS system there is no adverse effect on the plasma in part because the target is not required to initiate nor sustain the plasma but primarily because the magnetic field from the electromagnets is mainly orthogonal to the target surface at the target, therefore any magnetic confinement produced by a magnetic target merely assists in guiding the plasma to the target surface, potentially enhancing the local plasma density through its 'focusing' effect. This allows thick targets, up to 15 mm, to be sputtered resulting in high coating

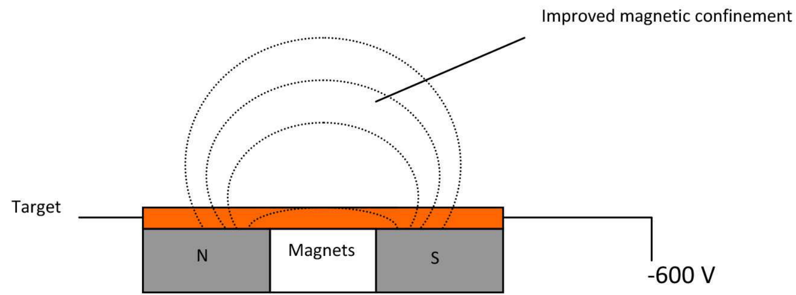

Figure 2.14: Thin magnetic target allows magnetic field to penetrate vacuum.

rates (typically 50 nm/min or more) onto substrates at distances of 100mm or more.

By experience, the remote plasma also appears to aid with beneficial densification of the growing thin film. This is evidenced by the lack of process gas inclusion and higher film densities (both physical and optical) than achieved by other sputter processes. Thus HiTUS has the potential to reduce or eliminate poor intergrain boundaries or voids within the film. It is also possible that the energies provided by the plasma could reduce the temperatures for processes requiring post deposition annealing treatments or in-situ substrate heating during deposition [48][49]. The control of grain size for ferromagnetic CoFe has been demonstrated using HiTUS by controlling the process parameters [50]. These qualities of HiTUS, combined with its other assets such as stress control and stable reactive sputtering processes renders it an interesting tool for investigating the properties of selected ferromagnetic materials for data storage applications.

The actual HiTUS system used for this project is an in-house design and is shown in Fig. 2.15. All the main components can be seen, including the remote side arm plasma generation unit, the sputtering chamber, the vacuum pumps, the DC and the RF power supplies.

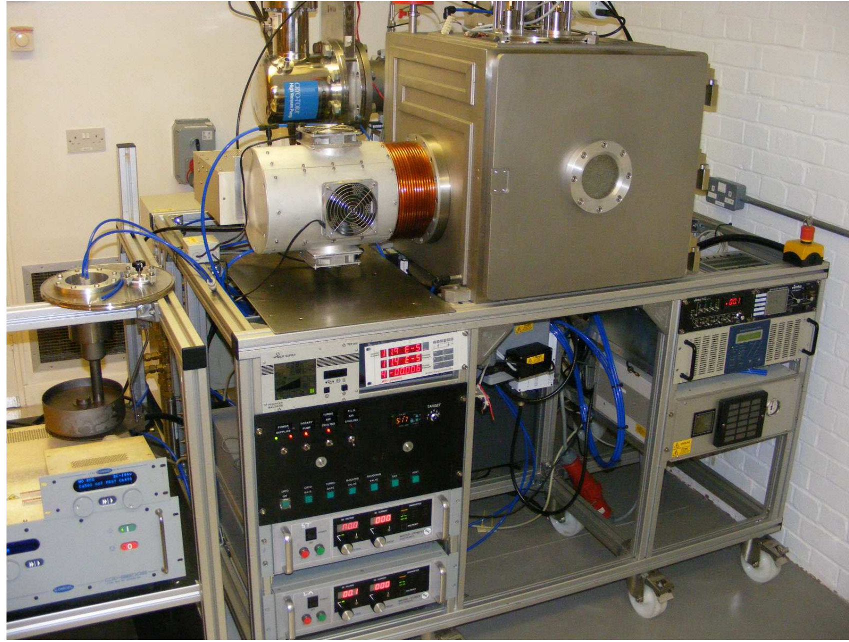

Figure 2.15: Photograph showing the HiTUS system used for the deposition of the coatings in this work.

A schematic view of the HiTUS system used for this work is shown in Fig. 2.16. The vacuum chamber is a 50 cm x 50 cm x 50 cm stainless steel chamber, with Viton O-ring sealed commercial fittings and pipework and a large access door on one side (also Viton o-ring sealed when closed). The remote plasma source (PLS) is a PQL custom made unit mounted to the chamber side on an ISO160 flange. A 520 l/s turbomolecular (turbo) pump is mounted on a flange with a gate valve separating it from the chamber. In addition, a cryogenic (cryo) pump (Cryo-Torr model 8F) is mounted on another flange with a gate valve separating it from the chamber. The gases and vapors captured by the cryo pump can be released via the turbo pump when the cryo pump is shut down. The combination of turbo and cryo pumps is ideal, with the turbo pump providing high pumping speeds for most gases and the cryo pump delivering very high pump speeds for water vapour (4000 l/s by specification). More importantly, the cryo pump provides an option for running a process with minimal risk of oil vapour contamination.

Typically, the system is rough pumped to $\sim 10^{-2}$ mbar with the rotary pump, and then further pumped to $<8 \times 10^{-7}$ mbar with the turbo and cryo pumps. The Pirani gauges are accurate for pressure readings down to about 1×10^{-2} mbar, therefore a reading from this gauge is used to guide the switching over from rotary

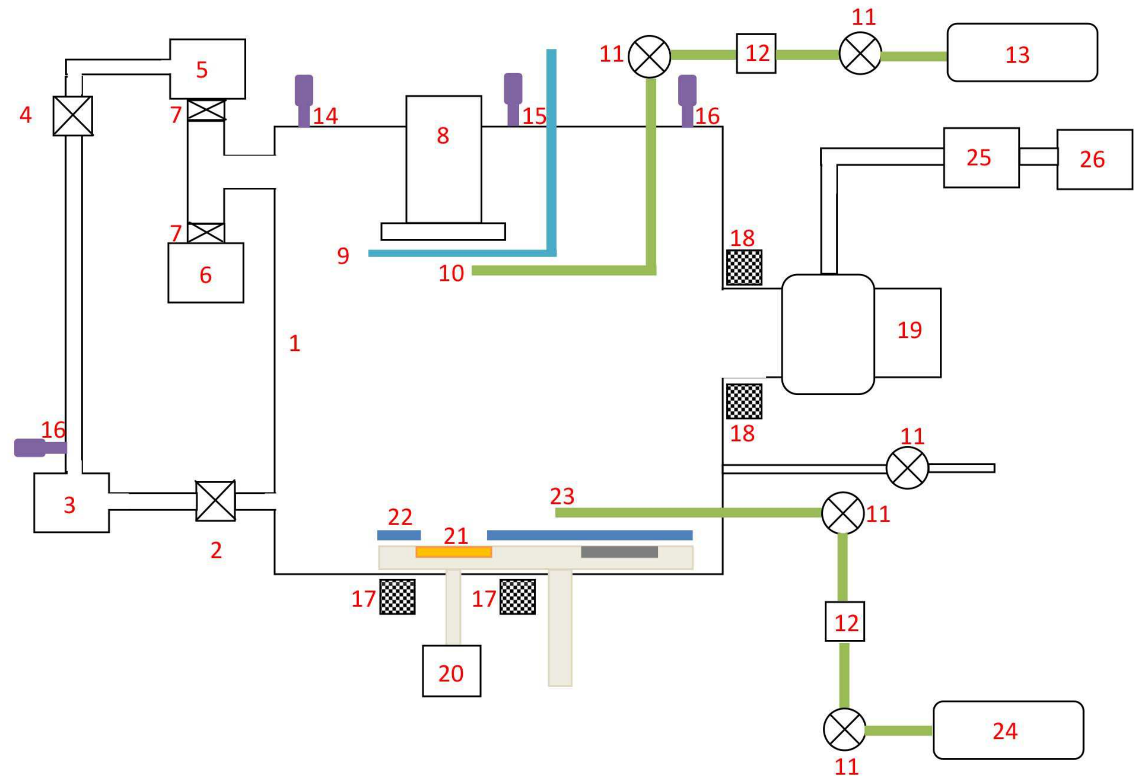

Figure 2.16: Schematic view of the HiTUS system: (1) process chamber, (2) roughing valve, (3) low vacuum (LV) rotary pump, (4) backing valve, (5) turbomolecular high vacuum (HV) pump, (6) cryogenic HV pump, (7) HV pump gate valves, (8) substrate holder assembly, (9) substrate shutter, (10) inlet for reactive gas, (11) MFC isolation valve, (12) Mass flow controllers (MFCs), (13) reactive gas supply, (14) Penning HV gauge, (15) capacitance manometer (CM) gauge, (16) Pirani LV gauge, (17) target electromagnet, (18) plasma source (PLS) electromagnet, (19) remote plasma source (PLS), (20) DC power supply, (21) sputter target, (22) dark shield, (23) inlet for process gas, (24) process gas supply, (25)RF impedance matching network, (26) RF power supply.

to turbo and cryo pumps. A Penning gauge reading is then used for pressure readings during high vacuum pumping.

The HiTUS sputtering process is very similar to conventional sputtering. Sputtering gas is flowed into the process chamber (which is still being pumped) to provide the required pressure of sputter gas, typically between 1 x 10^{-3} and 1 x 10^{-2} mbar. The two electromagnets are turned on to set current values (previously established for the system during commissioning) and the PLS RF power applied, typically at 1 to 2 kW. With the plasma present, a (negative) DC bias is then applied to the target to promote sputtering.

The sputtering gas is typically high purity (99.99 % or better) argon supplied from a cylinder via dedicated clean stainless steel gas lines. Additional gases, such as nitrogen used in this project, are also supplied from cylinders of high purity gas via independent clean stainless steel gas lines. During sputtering the pressure in the chamber is read by a capacitance manometer gauge, as the HV Penning gauge is unsuitable for use at the process pressures used and the Pirani gauge is inadequately accurate or reproducible. The pressure is held constant by fixing the gas flow using individual gas mass flow controllers (MFCs) for each gas; these are typically accurate to 3 % and no feedback pressure control is required; for critical applications (e.g. multi-layer optical stacks) any small variation in process pressure can be compensated in the HiTUS process itself by running the target in 'constant power' mode.

To maintain steady sputtering rates, the PLS RF power and voltage to the target are kept constant. Target current is determined by the plasma density, itself a function of the PLS RF power, electromagnet currents and process pressure; in practice only a 3 - 5 % variation is seen in the target current, primarily resulting from process pressure variation. As target voltage is usually very accurately controlled (less than 1 % variation), the process itself can usually be accurately reproduced within a few percent run to run.

Substrates are positioned 27 cm from the sputter target. The substrates are mounted onto a custom stainless steel or aluminium substrate holder that is then attached to the substrate table, thereby clamping the substrates in place. The sub-

strate table is itself directly water cooled. The HiTUS system used in this work used the 'sputter up' configuration, i.e. the substrate was inverted, to minimise debris contamination.

Sputtering targets are circular planar, 10 cm in diameter and 6mm thick. In this particular system, a water cooled target 'carousel' holding four targets was fitted, with the target selected for sputtering being positioned under the plasma through rotational positioning of the target carousel; the other targets were essentially shielded from the plasma by the target assembly construction and therefore did not sputter (even though biased with the selected target).

The system is capable of sputtering metallic, semiconducting or insulating targets (an AC bias supply is required for the latter, usually RF but pulsed DC is also effective). Materials may be single elements or alloys, compounds and multiple material 'segments'. The ability to uniformly sputter a target surface at high rate and moderate process pressure using the remote plasma technique allows use to be made of 'constructed' multi-element targets as in this work.

Chapter 3

Magnetic materials

The basic concepts in magnetism and important properties associated with magnetic materials, predominantly ferromagnets, are reviewed in this chapter. This should provide a foundation to the discussions on magnetic materials and structures presented in this thesis.

3.1 Magnetism

Magnetism is a property that arises from the motion of electrons within atoms. The electron in an atom has two separate motions [51]. First the electron orbits the nucleus, just like the earth orbits the sun. Secondly, the electron spins on its own axis, just like the earth does (Fig. 3.1). Any motion of an electron produces an electric current, whether in a wire or in an atom. As a result the orbital motion gives rise to an orbital magnetic moment and the spinning motion causes an electron spin magnetic moment [52]. Each atom is essentially a tiny permanent magnet. Any magnet can be considered to be made up of a number of dipoles; the total moment of the magnet is the sum of the moments (called dipole moments) of its constituent dipoles [53].

The magnetic moment (m) is defined as the strength of the magnet (p) multiplied by the length of the magnet (l), $m = pl$. The magnetisation, M, describes the degree to which the magnets are magnetised and is defined as the magnetic moment per unit volume, $M = m/V$. When a magnetic field, H, is applied to a material, lines of magnetic flux are produced and the total number of lines per cm^2 is called the magnetic flux density or magnetic induction, B. The equation relating B, H and M

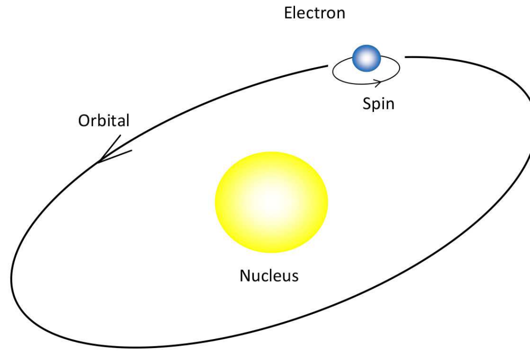

Figure 3.1: The motion of an electron within an atom.

in cgs units (G) is

$$B = H + 4\pi M. \tag{3.1}$$

In SI units (T) the relationship between B, H and M relates also to the permeability of free space, μ_0 and is given by

$$B = \mu_0(H + M). \tag{3.2}$$

In this thesis, cgs units are used. The cgs unit of magnetisation, M, is the emu/cm^3 and the cgs unit of magnetic field, H, is the oersted (Oe) [51].

3.2 Classification of magnetic materials

All materials can be classified into five magnetic behaviour basic groups depending on their bulk magnetic susceptibility. Magnetic susceptibility describes how magnetisation, M varies with an applied magnetic field, H. The ratio of M to H is called the susceptibility, $\chi = M/H$.

The five magnetic behaviour groups are diamagnetism, paramagnetism, ferromagnetism, anti-ferromagnetism and ferrimagnetism. Diamagnetism and paramagnetism are the most common types of magnetism in the periodic table of elements at room temperature, and materials exhibiting only diamagnetism or paramagnetism are usually referred to as non-magnetic. Those which usually are referred to as

magnetic are actually ferromagnetic. The only other type of magnetism observed in elements at room temperature is anti-ferromagnetism. Ferrimagnetism is not observed in single elements but can only be found in compounds, such as mixed oxides and rare-earth/transition metal alloys [54].

The five categories of magnetism will be briefly described. Since ferromagnetism is a central topic in this thesis a discussion on ferromagnetic materials and some of the important characteristics associated with ferromagnetism will continue in the next section.

Diamagnetism

A diamagnetic substance is one with a small and negative magnetic susceptibility. The atoms have no net magnetic moment when there is no applied field. Under the influence of an applied field the spinning electrons precess generating electric currents in the molecule in an opposing direction to that of the applied magnetic field. The result is that all substances have a diamagnetic contribution to their total magnetic susceptibility but is often masked by a large paramagnetic or ferromagnetic contribution.

Paramagnetism

A paramagnetic substance is one with a small and positive magnetic susceptibility. In a paramagnetic material, the electron spins are aligned at random in the absence of an applied magnetic field. In an applied magnetic field, there is a slight alignment of the atomic magnetic moments in the direction of the field. Paramagnetism is normally due to the presence of unpaired electron spins.

Ferromagnetism

A ferromagnetic substance is one in which atoms have parallel aligned magnetic moments. The susceptibility is large and positive. Ferromagnetism occurs when atoms are arranged in a lattice and the atomic magnetic moments can interact by way of exchange forces to align parallel to each other. The substances that form a ferromagnetic phase do so below a critical temperature called the Curie Temperature, T_c, above which the material becomes paramagnetic. A more detailed

description of ferromagnetic characteristics is given in Section 3.3.

Anti-ferromagnetism

In an anti-ferromagnetic material, adjacent atoms have their magnetic moments locked together in an antiparallel array. Above a transition temperature anti-ferromagnetic materials become paramagnetic. This temperature is known as the Néel temperature, T_n [52]. Both ferromagnetic and anti-ferromagnetic arrangements can remain in the absence of an applied field.

Ferrimagnetism

A ferrimagnetic material is observed in compounds with complex crystal structures. Like ferromagnets, the magnetic susceptibility is large and positive and at some crystal sites the exchange interaction leads to parallel alignment of moments. At other crystal sites the moments are locked together like those in an anti-ferromagnetic material. Alternating moments have different magnitudes and the net moment of the sample is non-zero.

3.3 Characteristics of ferromagnetic materials

3.3.1 Ferromagnetic domains

A property of ferromagnetic materials is the existence of ferromagnetic domains. These are small regions within which all the magnetic dipoles are aligned parallel to each other [55]. When there is no external field applied, the magnetisation vectors in different domains have different orientations and the direction of the domain alignment across a large volume of a ferromagnetic material is more or less random and so the total magnetisation averages to zero. Magnetisation is the process that causes the domains to re-orientate.

Heisenberg and Dirac showed that ferromagnetism is a quantum mechanical effect that fundamentally arises from Coulomb (electric) interaction [56]. The Pauli exclusion principle states that when electron spins are aligned the Coulomb repulsion energy is lowered and so aligning their magnetic dipole moments parallel to each other is favoured. This exchange interaction (or exchange energy) provides a

strong driving force for parallel alignment, therefore one single domain would minimize exchange energy [54]. Ferromagnetic materials do not, however, consist of one single domain as other energy contributions towards the *total* magnetic energy of a ferromagnet need to be taken into account [57].

Other energy contributions to the total magnetic energy include magnetostatic energy (which is the principle driving force for domain formation), the magnetocrystalline and magnetostrictive energies (which influence the size and shape of the domains).

3.3.2 Magnetostatic energy

A magnetised ferromagnetic material containing a single domain has a large magnetostatic energy associated with it which causes it to behave as a magnet (see Fig. 3.2(a)). Whilst the magnetisation points from south (S) to north (N), the direction of the magnetic field points from N to S. This is the 'demagnetising field,' H_d, which acts to magnetise the block in the opposite direction from its own magnetisation.

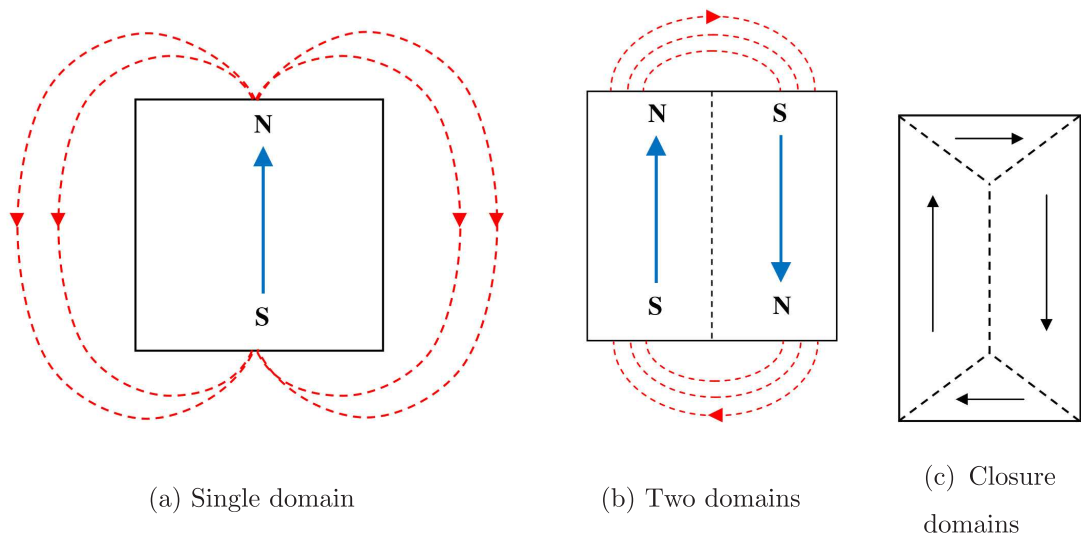

(a) Single domain (b) Two domains (c) Closure domains

Figure 3.2: Domain formation in ferromagnetic materials.

The demagnetising field, H_d, causes a magnetostatic energy which is dependent on the geometry and magnetisation of the sample. If one large domain is divided into two domains (Fig. 3.2(b)) the magnetostatic energy can be lowered. By lowering the external field, magnetostatic energy is lowered. As the magnetic moments at

the boundary between the two domains are not able to align parallel the formation of domains increases the exchange energy of the block [54].

Fig. 3.2(c) shows a closure domain where the magnetostatic energy is zero, however this is only possible for materials that do not have a strong uniaxial anisotropy. Uniaxial anisotropy refers to the existence of only one easy direction [51] – please see the following section (3.3.3) for a review on anisotropy. The horizontal domains at the top and bottom of the block are called 'domains of closure' since there are no magnetic poles at the surface and so minimal magnetostatic energy.

3.3.3 Magnetic anisotropy

In crystalline magnetic materials the magnetic properties vary depending on the direction in which they are measured, that is, dependent on the crystallographic direction in which the magnetic dipoles are aligned. This is referred to as *magnetic anisotropy* [57][58]. In ferromagnetic crystals the magnetisation tends to align along certain preferred crystallographic directions, called the 'easy' axes since the magnetisation can be easily saturated if the magnetic field is applied in this direction. On the contrary, if the magnetic field is applied along other crystallographic directions, the magnetisation reaches saturation at higher fields. These axes are called 'hard' axes of magnetisation [57] (see Fig. 3.3). A material may contain more than one easy and hard axis. Magnetic materials that show a preferential direction for the alignment of magnetisation (that is, it attempts to align its magnetic moment with one of the easy axes) are said to be *magnetically anisotropic*. When a material has a single easy and hard axis, the material is said to be *uniaxially anisotropic* [51].

Since ferromagnetic crystals exhibit 'easy' and 'hard' directions of magnetisation the energy required to magnetise a crystal depends on the direction of the applied field relative to the crystal axes [59]. For technological applications this magnetic anisotropy is one of the most important properties of magnetic materials since the magnitude and type of magnetic anisotropy affect properties such as magnetisation and hysteresis curves in magnetic materials [59]. Magnetic anisotropy is, therefore, an important factor in determining the suitability of a magnetic material for a particular application.

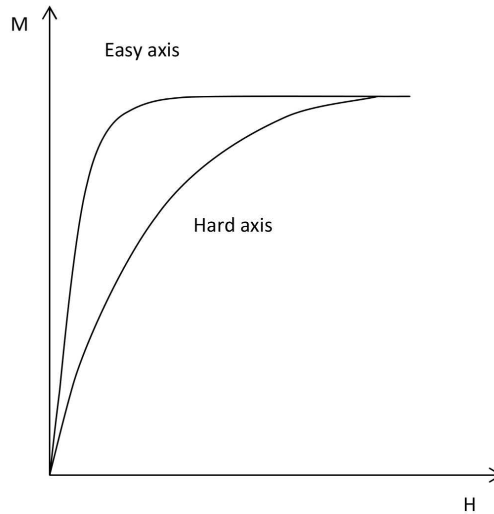

Figure 3.3: Magnetisation curve for a ferromagnetic single crystal with the field applied along the easy and hard axes.

There are several types of magnetic anisotropy. These include magnetocrystalline anisotropy, stress anisotropy and shape anisotropy. Of these only magnetocrystalline anisotropy is intrinsic to the material, as a result of its crystal chemistry and the other two may be induced by processing methods such as annealing [51].

There are two main origins of the magnetic anisotropy. These are the spin-orbit interaction (the interaction between the electron-spin and the orbital angular momentum) and the magnetic dipolar interaction (dipole-dipole interaction that can lead to ferromagnetic long-range order on some crystal lattices) [60][61]. Spin-orbit interactions are responsible for magnetocrystalline anisotropy and stress anisotropy. Dipolar interactions are responsible for shape anisotropy [59].

A discussion on magnetocrystalline, stress and shape anisotropies are included in the following sub-sections. For this thesis the magnetocrystalline anisotropy is of the most interest as FePt, a material with a high high uniaxial magnetocrystalline anisotropy, is investigated for ultra high density magnetic recording applications.

3.3.4 Magnetocrystalline anisotropy

Coupling exists between the electron spin and the orbital [62]. Electron orbits are in turn coupled to the crystallographic lattice, and by their interaction with the spins

they make the spins prefer to align along well-defined crystallographic axes (along the easy direction). In the easy direction of magnetisation the coupling electron orbitals to the lattice is such that the electron orbitals are in the lowest energy state. So when an applied magnetic field tries to rotate the electron spin, the strong coupling to the lattice resists the spin rotation [51]. Forcing the spins to align in the direction of the applied external field leads to an energetically unfavourable crystal arrangement. Magnetocrystalline anisotropy may be regarded as a force which holds the magnetisation in certain equivalent crystallographic directions and resists the rotation of spins away from the easy axis [51]. A part of the total energy in the system therefore depends on the direction of magnetisation with respect to the different crystallographic directions and is called the Magnetocrystalline anisotropy.

The crystal is higher in energy when the magnetisation points along the hard direction than along the easy direction [57]. A measure of this energy difference is the magnetocrystalline anisotropy constant, K. Magnetocrystalline anisotropy energy is the energy required per unit volume to rotate the magnetic moments from the easy to the hard direction [63]. Magnetocrystalline anisotropy energy, E is usually expressed in terms of sine and cosine functions where θ is the angle between the direction of easy magnetisation and the vector of magnetisation and ϕ is the angle between the projection of the magnetisation vector in the basal plane of the crystal and one of the other axes, see Fig. 3.4.

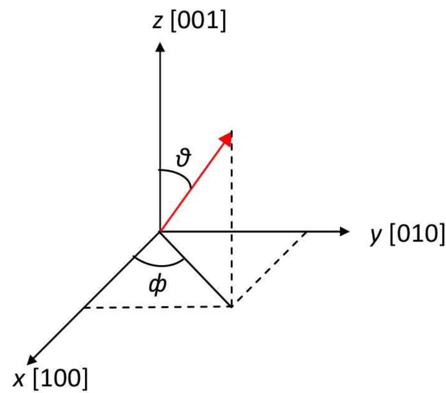

Figure 3.4: Definition of the θ and ϕ angles in the tetragonal symmetry.

The expression for magnetocrystalline anisotropy energy for tetragonal crystals is as follows; where K_1, K_2, and K_3 are the coefficients of anisotropy [64][65]:

$$E = K_1 \sin^2\theta + K_2 \sin^4\theta + K_3 \sin^4\theta \cos 4\phi + ... \tag{3.3}$$

For uniaxial systems, the anisotropy energy depends only on a single angle and so the first order magnetocrystalline anisotropy constant K_1 becomes K_u and the anisotropy energy becomes:

$$E = K_u \sin^2\theta. \tag{3.4}$$

Materials that have high uniaxial magnetocrystalline anisotropy (strong resistance to magnetisation direction away from the easy axis) are attractive for ultra high density magnetic recording applications as they allow smaller, thermally stable media grains [66]. Conventional methods used in the determination of anisotropy constants are by torque curve analysis [67][68] and by analysing the magnetisation curve along the hard axis [69].

To minimise the magnetocrystalline energy, domains will form so that their magnetisations point along easy crystallographic directions [70]. Like exchange energy the magnetocrystalline energy prefers large domains with few boundaries [71].

3.3.5 Stress anisotropy

In addition to magnetocrystalline anisotropy there is another effect known as stress anisotropy that arises upon the magnetisation of a magnetic material [63]. When a ferromagnetic material is magnetised it experiences a strain that can be measured as a function of applied field and undergoes a change in length known as magnetostriction [72]. Materials that elongate along the direction of magnetisation are said to have a positive magnetostriction. Materials that contract on magnetisation are said to have a negative magnetostriction. Although length changes are only very small they are sufficient to influence domain structure. Going back to Fig. 3.2(c), the horizontal and vertical domains cannot elongate at the same time and so instead an elastic strain term is introduced to the total energy. The elastic energy (or magnetostrictive energy) is proportional to the volume of the domains of closure, and so can be lowered by reducing the size of the closure domains. However, smaller do-

mains introduces additional domain walls, with corresponding increase in exchange and magnetostatic energy [70].

3.3.6 Domain walls

The interfaces between adjacent domains, in which the magnetisation has different directions are called domain walls [73]. Within the wall, the magnetisation must change direction from that in one domain to that of the other domain. The domain walls have a width that is determined by a balance between the competing energy contributions. The exchange energy acts to keep moments parallel and can be kept small if spin rotation takes place slowly, this favours wide walls. However, the magnetocrystalline anisotropy is optimised if the moments are aligned as closely as possible to the easy axis. This favours narrow walls with sharp transitions between the domains [57].

In a material's initial demagnetised state the domains are arranged so that the magnetisation averages to zero. When a magnetic field is applied to a domain structure, the magnetic field tends to align the magnetisation parallel to the field [71]. There are two ways it can do this, 'domain wall motion' and 'domain rotation' [51]. The domain wall can move ('domain wall motion'), this increases the volume of the domain whose potential energy is lower and decreases the volume of the other, thereby reducing the magnetic potential energy of the crystal. Eventually the applied field is sufficient to eliminate all domain walls, leaving a single domain, with its magnetisation pointing along the easy axis oriented closely to the external magnetic field [57]. To further increase magnetisation, the net magnetic moment of each atom rotates causing the magnetisation direction of the domains to change ('domain rotation'). Magnetisation orientations are determined mainly by the anisotropy, which resists the rotation of the magnetisation, and so domain rotation occurs only if the field is large enough to act against the force of crystal anisotropy. Both these processes can occur in practice [51] [74].

Initially domain wall motion is reversible, i.e. if the field is removed, they return to their original positions [75]. In larger fields the domain wall motion becomes irreversible - the walls do not return to their original positions when the field is removed.

The main reason of that is that when the domain walls move on the application of a magnetic field it encounters crystal imperfections (dislocations, grain boundaries, voids, lattice distortions, impurities etc), which have an associated magnetostatic energy [57]. The applied magnetic field provides the energy required for the wall to move over the energy barriers associated with the imperfection. When the field is removed, these imperfections may prevent the domain walls from returning to their original configuration. It is the demagnetising field that drives the growth of reverse magnetic domains, and it is not strong enough to overcome the energy barriers encountered when the domain walls intersect crystal imperfections. Some magnetisation remains even when the field is completely removed. It then becomes necessary to apply a rather strong field in the opposite direction to restore the demagnetised state.

Magnetisation reversal is one of the most important processes associated with thin film magnetic storage media [76]. In the magnetic recording process, magnetisation reversals form local magnetisation transition patterns in the magnetic medium as the means of recording data and so it is important for the reversal mechanism to be studied to understand the recording process [77][78][79].

3.3.7 Shape anisotropy and inter-particle interactions

Shape anisotropy occurs in polycrystalline materials with no preferred orientation of its grains (a grain can be considered as the single crystalline building block of a thin film [80]). In these cases the shape of the grains can affect the direction of magnetisation. For a long needle shaped grain the demagnetisation field is less along the long axis than it is along the short axis [51]. This leads to an easy axis of magnetisation along the long axis. A sphere, on the other hand, has no shape anisotropy.

Shape anisotropy in small particles can lead to a reduction in the coercive field of the material as the packing density is increased [57]. This is a result of interparticle interactions. Consider Fig. 3.5, initially both particles A and B are magnetised in the up direction. Particle A exerts a field on its neighbour B, this field acts in the down direction. If subsequently an external field is reversed and applied in the down direction, the field acting on particle B (from particle A) assists the applied

external field, and so B reverses its magnetisation at a lower applied field than it otherwise would have done if no field from particle A was acting on it. Overall the sample has a lower coercivity than a collection of isolated particles. As the packing density increases the interactions increase and the coercivity decreases [57].

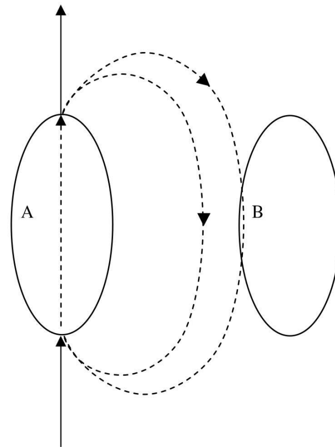

Figure 3.5: Interparticle interactions.

3.3.8 Hysteresis loops

A great deal of information can be learned about the magnetic properties of a material by studying its hysteresis loop. A hysteresis loop shows the relationship between the magnetisation, M (or induced magnetic flux density, B) and the magnetic field, H [51]. Fig. 3.6 shows a schematic of a generic hysteresis loop.

A ferromagnetic material, in an unmagnetised state would start at the origin and follow the dashed curve up to a as the field is increased in the positive direction. At point a almost all the magnetic domains are aligned and an additional increase in the magnetic field will produce very little increase in magnetisation. The material has reached the point of saturation, the value of magnetisation at point a is called the *saturation magnetisation*. When the field is reduced to zero after saturation, the magnetisation decreases from a to b, which indicates the level of residual magnetism in the material. It is known as the *remanence* or retentivity where some of the magnetisation remains in the material (i.e. some of the magnetic domains remain aligned but others have lost their alignment). At the coercivity point c, the magnetisation point is reduced to zero. This is the point at which the reversed magnetic

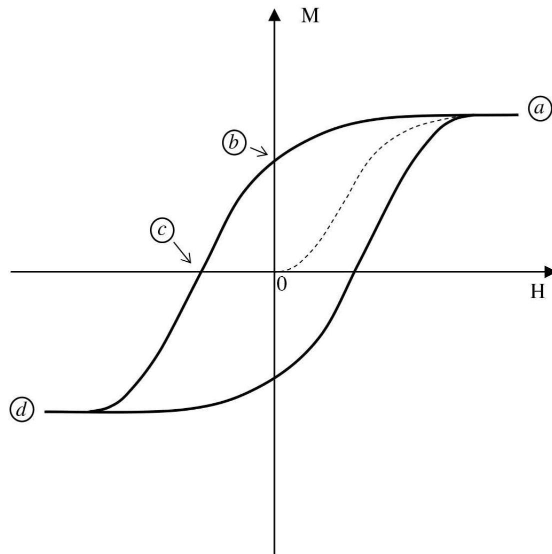

Figure 3.6: Typical M–H hysteresis loop.

force has flipped enough of the domains so that the net magnetisation within the material is zero. The force required to remove the residual magnetisation from the material is called the *coercivity* or coercive force of the material. When the reversed magnetic force is increased further, saturation is achieved in the reverse direction (point d). To complete the loop magnetic field is increased in the positive direction.

Chapter 4

Magnetic data storage

Over the last decades, tremendous developments have occurred in the magnetic storage industry. Of the magnetic storage technologies, magnetic hard disk recording is the most widely used. In this chapter, the focus is on the hard disk drive technology and the processes of writing, storing and retrieving data on magnetic hard disks. A potential future material for magnetic storage media – the $L1_0$ FePt is also discussed, including the challenges facing its fabrication.

4.1 The basic hard disk drive

Fig. 4.1 shows a schematic of a hard disk drive (HDD) with the major components identified. The disk, where information is stored magnetically, is attached to a spindle motor that will spin the disk. Read and write heads are attached to an electronically controlled arm that moves radially (in a straight line from the centre of the drive to the outer edge and back again).

There are 3 main components that make up a HDD, these are the write head, the read head and the storage medium. Since this work investigates the potential use of FePt as high anisotropy media and also increasing the sensitivity of read head devices, these components shall be discussed in more detail than the write head.

4.1.1 The recording process

In magnetic hard disks the recording (or *write*) processs is achieved by electromagnetic induction. Older ferrite and metal-in-gap (MIG) heads consist of wire coils

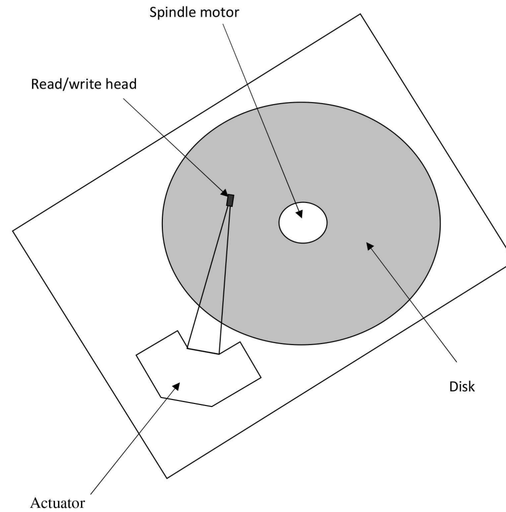

Figure 4.1: Schematic of the basic hard disk drive.

wound around a C-shaped iron magnetic core [81]. When a current flows through the coil a magnetic field is generated in the gap between the poles and a fringing field extends out of the gap and intercepts the recording medium, changing its magnetic state. Drive channel electronics receive data in binary form from the computer and converts them into a current in the write head coil. The current reverses at the transitions (representing a '1' bit) and is constant at each '0' bit. Fig. 4.2 shows this principle. The magnetic material in the write head should have a large permeability so that large magnetic field can be generated, and a low coercivity, so that its direction can be easily reversed; permalloy is an example of such material [82].

Thin film heads are currently used in HDDs. They work using the same principles as the ferrite and MIG heads in that the magnetic field of the inductive write element rotates the magnetisation within the grains of a bit towards the field direction such that on average, the remanent magnetisation inside a bit cell points in either N-S or S-N directions [11]. These heads, however, are manufactured in a very different way. They are made via a photolithographic process and sputtering, creating very precise head structures with very specific head gaps capable of being used on higher density drives and has eliminated the large cumbersome ferrite head designs.

In Fig. 4.2, data is shown to be recorded in horizontal magnetisation patterns.

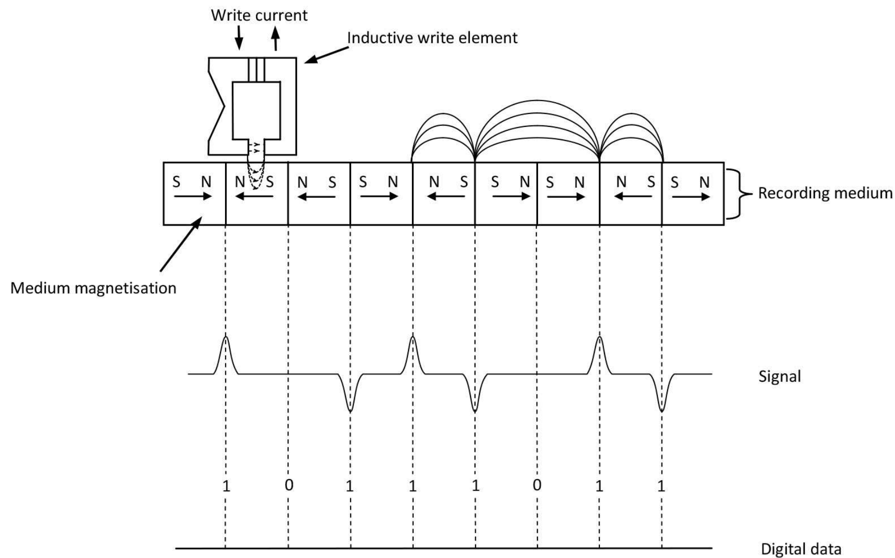

Figure 4.2: Longitudinal recording principle.

This conventional way of recording is known as longitudinal recording. Longitudinal recording media does have its limits and in order to achieve higher areal density recording further grain size reduction was required. Smaller grains are more susceptible to thermal switching - the reversal of magnetisation without an external field. This is phenomenon is known as the superparamagnetic effect and was considered as a serious threat to the areal density growth of longitudinal recording [83]. *Perpendicular* recording has allowed further growth of areal density by improving the write efficiency [84] and has been used in hard disk drives since 2006 [85].

The Perpendicular recording architecture is shown in Fig. 4.3. In longitudinal recording the field that is used to write the data is the fringing field that extends from the poles (refer back to Fig. 4.2); this field is weaker than the field available at the gap by about 50 % [11]. This was realised and so perpendicular media was introduced. In this technology the gap field is essentially used to write the data. This is achieved by using a soft underlayer (SUL), Cr or CrV are often the materials of choice for this layer [86]. The SUL is highly permeable and so when the write head is energized, flux is concentrated beneath the narrow pole tip and an intense magnetic field is generated between the pole tip and SUL. Higher fields allow higher coercivity media to be used and smaller grain sizes can be tolerated before the thermal stability (superparamagnetic) limit is reached.

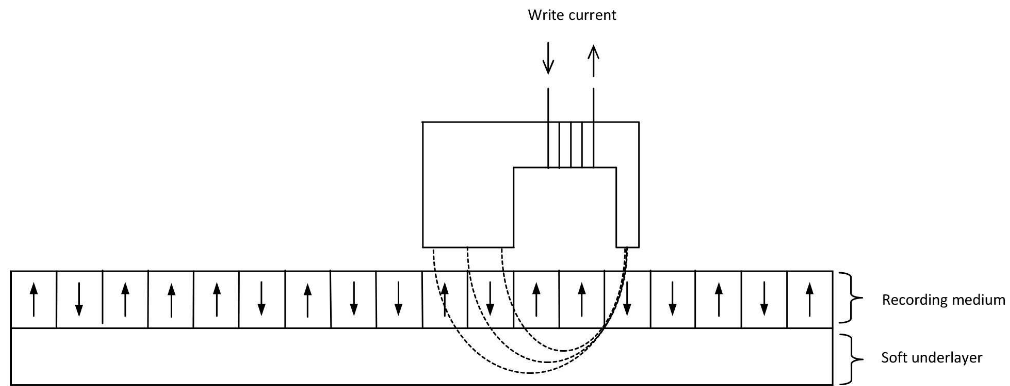

Figure 4.3: Perpendicular recording using the stronger "gap fields" for writing.

4.2 Data read out

In the read-back process, the stored information is retrieved by scanning a read head over the recording medium. The read head intercepts magnetic flux from the magnetisation patterns on the recording medium and converts it into electrical signals which are then detected and decoded [87].

Older heads used the inductive method (induced current in the coil from the magnetic flux) to read back the information. Since data bits are tightly packed together the stored fields are very small and very weak. Increasing areal density means even smaller and weaker fields. So as to read weakening fields read heads must become increasingly sensitive to accurately distinguish between the different magnetisation states. Read heads today use the principle of magneto-resistance to intercept the magnetic flux from the media. Magneto-resistance is the concept that certain materials exhibit a change in resistance upon applying a magnetic field [88]. Magneto-resistance will be introduced with a more detailed description of the giant magneto-resistance (GMR) effect as a device based on this structure is used in this PhD project.

4.2.1 Magneto-resistive Effect

The effect by which the electrical resistance of a magnetic material could be changed in the presence of a magnetic field is known as the *magneto-resistive* (MR) effect [89]. The magneto-resistive ratio is defined as the ratio of the change in resistance when the field is applied to the resistance at zero field, and is expressed as a percentage, that is:

$$MR\ ratio = (\frac{R_0 - R}{R_0}) \times 100\% = (\frac{\Delta R}{R}) \times 100\%. \quad (4.1)$$

R_0 is the resistance in the absence of a magnetic field and R is the resistance in the presence of a magnetic field. It is this MR effect that is employed in MR read heads. As the head passes over the surface of a disk, the magnetic material changes in resistance as the magnetic fields change corresponding to the stored patterns on the disk.

Although the total signal change or magneto-resistance (MR) ratio was typically two percent for earlier heads comprising of $Ni_{80}Fe_20$ alloy [90], its field sensitivity was still much greater than that obtained through coil windings. These earlier heads are termed anisotropic magneto-resistive (AMR) heads. AMR based read heads replaced inductive readers in the early 1990s. Not long later higher MR ratios were observed in a certain materials and structures, this was termed the giant magneto-resistive (GMR) effect and due to its improved signal compared to AMR materials, GMR films resulted in enhanced device performance.

4.2.2 Giant Magneto-resistive Effect

Albert Fert and Peter Grünberg were awarded The Nobel Prize in Physics in 2007 for the discovery of the giant magneto-resistive (GMR) Effect [91]. It was observed that for a multilayer structure comprising magnetic Fe separated by non-magnetic Cr, when subjected to magnetic fields, showed very large changes in resistance (up to 50 % at low temperatures) [91]. This effect is known as the GMR effect. This effect was subsequently found to occur in a number of other magnetic/non-magnetic multilayer thin film systems. The alternate ferromagnetic layers separated by a metallic layer of specific thickness couple anti parallel to each other [92]. Under the influence of an external magnetic field the relative orientation of the magnetisation of the layers switches and the electrical resistance decreases to a minimum when the magnetisation directions of the layers are parallel. A GMR read head operates on the same basic principles as AMR heads but the larger percentage change of resistance makes them more sensitive and superior. GMR heads rapidly replaced AMR read head sensors during 1995 and 1996 [93].

4.2.3 Giant magneto-resistance in multilayers

The GMR effect can be seen in simple multilayer structures consisting of a spacer layer of non-magnetic material, for example copper, sandwiched between two ferromagnetic materials, for example permalloy (Figs. 4.4(a) and 4.4(b)) [81].

In ferromagnetic transition metals the outer conduction electrons are the $3d$ [73]. The conduction electrons are divided into two classes: those whose spin is parallel to the local magnetisation and those whose spin is antiparallel. When an electric field is applied, these conduction electrons accelerate until they encounter a scattering centre [94]. It is the spin-dependent scattering in ferromagnetic materials at the interfaces between the ferromagnetic and non-magnetic layers that forms the basis of the physical mechanism of the GMR effect. Consider Fig. 4.4(a) where the conduction electrons have the same spin orientation as they move through both layers they have relatively long mean free paths, resulting in little scattering and low resistance. Where the magnetic moments are anti-parallel, as in Fig 4.4(b), the conducting electrons that carry the majority of the current in both layers do not have the same spin orientation as they move through both layers. This results in strong scattering at the interface, a short mean free path and high resistance [82].

Typically, in multilayer structures, fields exceeding 200 to 300 Oe are required to rotate the magnetisation [95] to the ferromagnetic configuration and so were not attractive to use in head devices. Systems have been developed where *uncoupled* magnetic thin films can be switched from the antiparallel to the parallel configuration. These are known as *spin valve structures* and are used in magnetic recording.

4.2.4 Basic principles of the reading process using GMR spin valves

A simple spin-valve structure consists of four thin film layers sandwiched together (see Fig. 4.5) [9]:

A *free layer*, usually made of NiFe passes over the media and over the data that will be read. It is free to rotate in response to the magnetic patterns on the disk [96]. A *spacer* made from non-magnetic material (typically Cu) is positioned between the

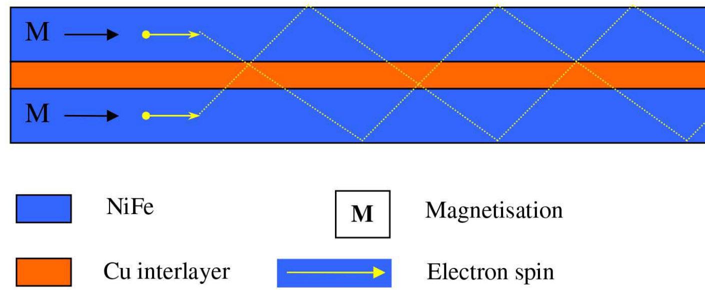

(a) Low resistance. Negligible scattering at interface

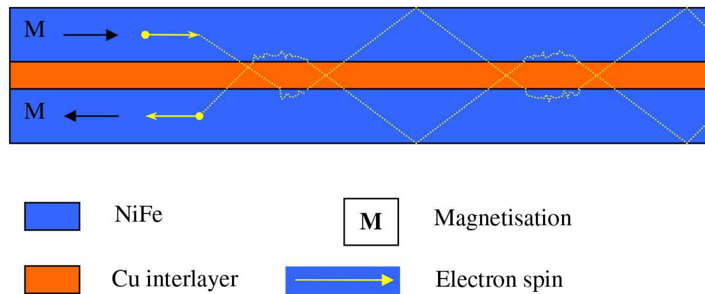

(b) High resistance. Strong scattering at interface

Figure 4.4: NiFe/Cu/NiFe GMR structure.

free and pinned layers to separate them magnetically [97]. The thickness of the spacer is large enough to ensure that the coupling between the two magnetic layers is neglibible [98]. A *pinned layer*, usually Co is held, or 'pinned,' in a fixed magnetic orientation by a virtue of its adjacency to the *anti-ferromagnetic layer*. The anti-ferromagnetic material, for example PtMn, fixes the pinned layer's magnetic orientation, by exchange coupling [99]. Exchange coupling is an important property and is discussed separately.

When the read head passes over one polarity of magnetisation in the disk (e.g. '0'), electron spins in the free layer turn to be aligned with those of the pinned layer, this creates a lower resistance in the entire head structure. When the head passes over a field of the opposite polarity (e.g. '1'), the electron spins in the free layer turn so that they are not aligned with those of the pinned layer. This causes an increase in resistance of the overall structure. It is changes to the spin characteristics of electrons in the free layer that cause the resistance changes. The principle for lowering the

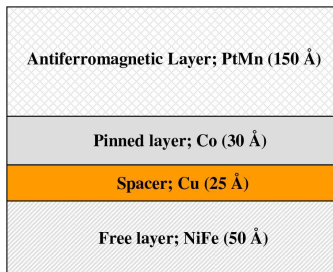

Figure 4.5: Simple GMR spin valve.

resistance is the same as in the GMR multilayer, i.e spin dependent scattering gives a low resistance state when the magnetic layers are ferromagnetically aligned, whilst a high resistance state is obtained in the anti-ferromagnetic configuration. The resistance of the spin valve is continuously monitored with the aid of a measuring current.

4.3 Exchange coupling

Exchange coupling (or exchange bias) is one of a number of phenomena observed at the interface between an anti-ferromagnet and a ferromagnet [51]. When ferromagnetic/anti-ferromagnetic heterostructures are cooled through the N*é*el temperature (T_n) of the anti-ferromagnet (with the Curie temperature, T_c, of the ferromagnet larger than T_n) in the presence of an applied magnetic field, an anisotropy is induced in the ferromagnetic layer. In a simple model when a magnetic field, H, is applied to an ferromagnet/anti-ferromagnet heterostructure in a temperature range $T_n < T < T_c$ exchange interaction occurs causing the ferromagnetic spins to line up along the applied field direction while the anti-ferromagnetic moments predominantly remain in a random state above the ordering temperature (see Fig. 4.6(a)). While if the temperature is lowered to below the N*é*el temperature ($T < T_n$), the top 'row' of the anti-ferromagnet moments align parallel to the moments in the ferromagnet in order to minimize the exchange energy of the system. Once this has occurred the remaining spins in the anti-ferromagnet follow suit and align in order to produce a zero net magnetisation for the anti-ferromagnetic material (see Fig. 4.6(b)). If a magnetic field opposite to the direction of the cooling field is applied, the spins in the ferromagnet attempt to rotate, however, for sufficiently large anti-ferromagnetic anisotropy the anti-ferromagnet spin structure remains unchanged. The pinned spins in the anti-ferromagnet and the spins in the ferromagnet try to maintain the parallel

alignment (to minimise energy). This can be thought of as an additional internal field preventing the ferromagnet spins from rotating freely. A larger magnetic field must be applied in the direction opposite to the cooling field direction in order to completely switch the ferromagnet when it is in contact with an anti-ferromagnet. When a field parallel to the original cooling field is applied to complete the magnetic hysteresis loop, the spins in the ferromagnet will begin to rotate at a smaller field because of the same internal field from the anti-ferromagnet. This combination of interactions across the interface results in an exchange biased system that gives rise to a shift in the magnetic hysteresis loop (see Fig. 4.6(c)).

Anti-ferromagnetic exchange coupling in GMR devices was exploited in hard disk drives until 2005 [93] when another type of spin valve entered the market. These are magnetic tunnel junction (MTJ) devices with even higher sensitivities than GMR devices. A brief description of MTJ is given below for completeness as they have been an important step to bringing the hard disk drive to the stage it is at present. Although GMR devices have been taken over by TMR devices in hard disks, they are still used and investigated for other applications such as biological sensors. Due to their relative ease of fabrication, GMR devices are used in this project to investigate improving read head technology by using the magneto-electric effect that is observed in multi-ferroic materials (see Chapter 5 for background information on multi-ferroic materials and the magneto-electric effect).

4.4 Magnetic Tunnel Junctions

The magnetic tunnel read sensor has attracted much interest since the mid-1990s [100][101]. It is similar to a GMR multilayer except the non-magnetic metallic layer is replaced by an insulator. A magnetic tunnel junction (MTJ) is a ferromagnetic/insulator/ferromagnetic sandwich [102][103]. The insulator acts as the tunnel barrier [104]. Electrons can tunnel through this barrier with their spin directions preserved. The signals from these sensors (the Δ R/R value) are much larger than for GMR structures due to the high resistance of the tunnel barrier [105].

Fig. 4.7 depicts a simple MTJ structure showing the spin tunneling of electrons through the sandwich structure. When the magnetisations (M) of the ferromagnetic

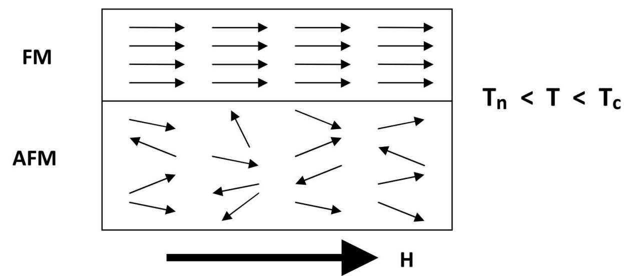

(a) aligned ferromagnetic spins and random anti-ferromagnetic spins

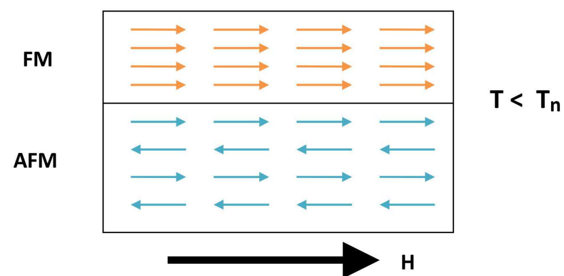

(b) aligned spins in both ferromagnet and anti-ferromagnet

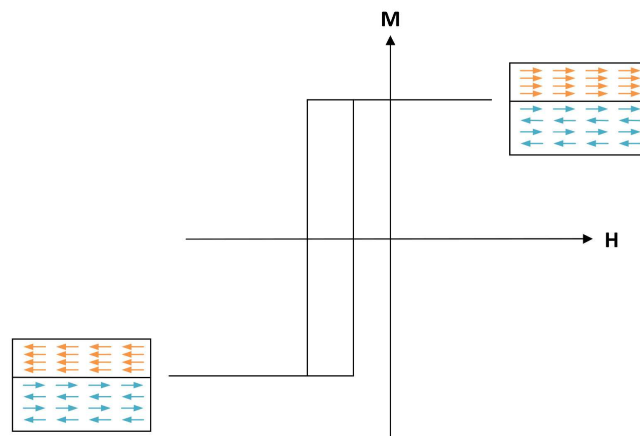

(c) shift in hysteresis loop as a result of exchange bias

Figure 4.6: Exchange coupling in ferromagnetic/anti-ferromagnetic heterostructures.

(FM) layers are parallel, the majority band electrons from FM 1 tunnel through to the majority band of FM 2 and the minority band electrons from FM 1 tunnel through to the minority band of FM 2, as shown in Fig. 4.7(a). When the magnetisations are parallel, it allows the best matching of densities of spin states either side of the barrier, resulting in high conductance and low resistance [106].

When the magnetisations of the ferromagnetic (FM) layers are anti-parallel, the majority band electrons from FM 1 tunnel through to the minority band of FM 2 and the minority band electrons from FM 1 tunnel through to the majority band of FM 2, as shown in Fig. 4.7(b). Where the magnetisations are anti-parallel there is a reduced number of states available when the electrons tunnel from FM 1 to FM 2. This increases the tunnel resistance, leading to low conductance. A change from parallel to anti-parallel configurations, therefore, causes a change in the conductance [106].

The tunneling magneto-resistance (TMR) is similar to that of GMR, and is defined as the ratio of difference between the two states to the resistance in the low state [107]. Conduction is perpendicular to the magnetisation of the layers and so TMR depends on the tunnel-barrier thickness. The structure is also characterized by the resistance-area (RA) product [108]. An ideal device would show high TMR and low RA product [109].

The signal from these devices is much larger than those produced by GMR devices which makes them attractive for use in read heads and other magnetic sensor applications. Many hard disk drives today contain MTJ read heads [110]. TMR values of 500 % have been reported [111].

4.5 Data storage media

The storage medium comprises a thin magnetic layer, where the data is stored, deposited onto a substrate. The most common disk substrate material is an Al-Mg alloy [112][113]. A 10 μm thick nickel phosphide layer is plated onto the substrate to allow easy polishing [11]. The use of glass substrates is common for mobile applications where shock resistance is important.

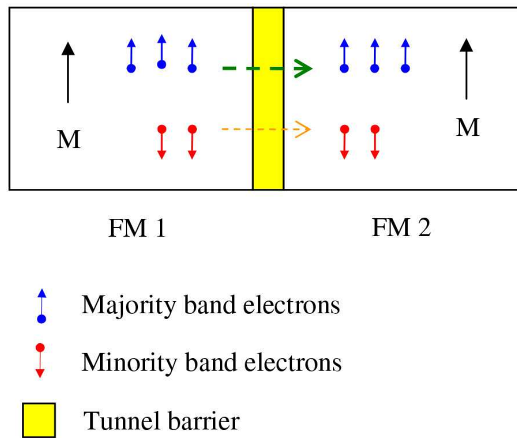

(a) Parallel magnetisation

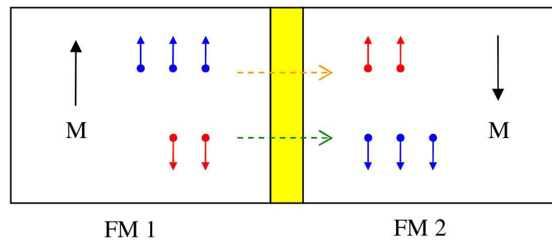

(b) Anti-parallel magnetisation

Figure 4.7: Basic TMR structure and electron spin tunneling.

Particulate magnetic media were used in the first few generations of HDDs [114]. Particulate media consisted of small, needle-like magnetic particles , for example $\gamma - Fe_2O_3$ or CrO_2, dispersed in polymeric binders. Each particle contained a single domain that magnetised preferentially with its moment aligned along the long axis (due to shape anisotropy). Each recorded bit was made up of many of these particles storing binary data [115].

Iron oxide particles were widely used due to its chemical stability; it is a pollution free material and can be manufactured at a low cost. $\gamma - Fe_2O_3$ single domain particles were used in the RAMAC and other tape and disk coatings until the mid 1970s. $\gamma - Fe_2O_3$ particles have a coercivity of around 300 Oe [115] so could only be used for low recording density applications. Cobalt modified $\gamma - Fe_2O_3$ ($Co - Fe_2O_3$) and other particles such as chromium dioxide, composite of $Fe_3O_4 - Fe_2O_3$, metal-

lic iron and barium ferrite were used to obtain higher coercivities for higher density recordings from the mid 1970s onwards [114].

Particulate media were not ideal [115]. Their magnetic constituent occupied typically only 40 % of the coating volume in tapes and flexible disks and only 20 % in HDDs [86]. The saturation magnetisation could not be high as the magnetisation was diluted by the binder. It was difficult to produce a homogenous distribution of particles without voids, which resulted in less uniform orientation and lower coercivity. Areal density requirements were increasing at such high rates that the coercivity of the particulate media could not be tailored easily to meet the requirements. For these reasons particulate media were phased out by metallic thin film media. Thin film media could be prepared by electroplating, autocatalytic plating, evaporation and sputtering [115].

As well as providing smoother surfaces, thin film growth processes produced nanometer sized grains with far better packing efficiencies and higher coercivities than particulate media which allowed for higher storage densities [115]. Thin film HDD media consist of approximately 10 to 50 nm thick polycrystalline magnetic alloys such as CoPtCr or CoCrTa [116]. Typical grain diameters are about 8 to 10 nm and there are 100 to 500 weakly coupled grains per bit cell [117][118]. The primary magnetic component is Co, while Pt or Ta is used to increase the coercivity by increasing the anisotropy. Cr is known to segregate to the grain boundaries, so reducing the inter-particle exchange coupling between grains leading to reduced transition noise in Co-alloys having high Cr concentrations [119].

In spite of their desirable hysteresis properties, there are problems associated with using small particles or grains that are densely packed together for the magnetic media in storage devices [120]. The first is the effect of inter-particle interactions (Section 3.3.7) and the second is *superparamagnetism*, whereby excitation by thermal energy overcomes the magnetic anisotropy energy and spontaneous reversal of the magnetic moments of the recording occurs (without any external field), this is further addressed in Section 4.5.2.

4.5.1 Important magnetic properties of magnetic recording media

Since the recorded information is stored as patterns of magnetisation, the magnetic material must have high remanence, M_r [116]. This in turn calls for high saturation magnetisation, M_s. The recorded pattern of opposed magnetic dipoles is subject to demagnetisation and hence the coercivity H_c must also be high enough to allow permanent stable storage.

In general a large squareness ratio (SQR) is desired for a recording medium (i.e. a large square hysteresis loop) [121]. The SQR is given by the ratio of (M_r/M_s). A square loop means that there are two distinct stable magnetisation states, and that the magnetisation takes place at a well defined magnetic field strength. The magnetisation reversals must be sharply defined. This calls for a narrow distribution of switching fields, this is the switching field distribution (SFD) and is defined by the dM/dH curve and $\Delta H/H_c$ where ΔH is the full width at half maximum [115](see Fig. 4.8).

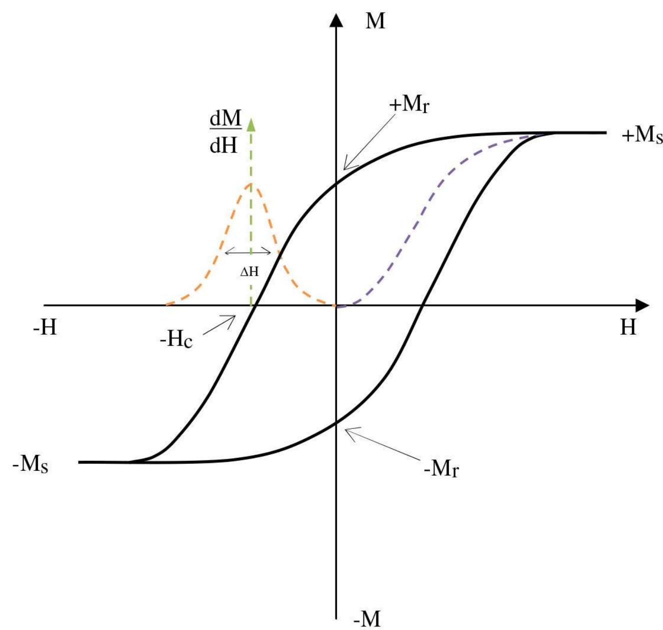

Figure 4.8: Magnetic hysteresis loop indicating certain properties important for media materials.

The loop shown in Fig. 4.8 represents a realistic curve. Fig. 4.9 shows the hysteresis loops in the magnetic easy and magnetic hard directions of a sample

with uniaxial magnetic anisotropy in an ideal scenario. For the FePt studies in this project it is hoped that a large square loop in the perpendicular magnetisation direction can be achieved.

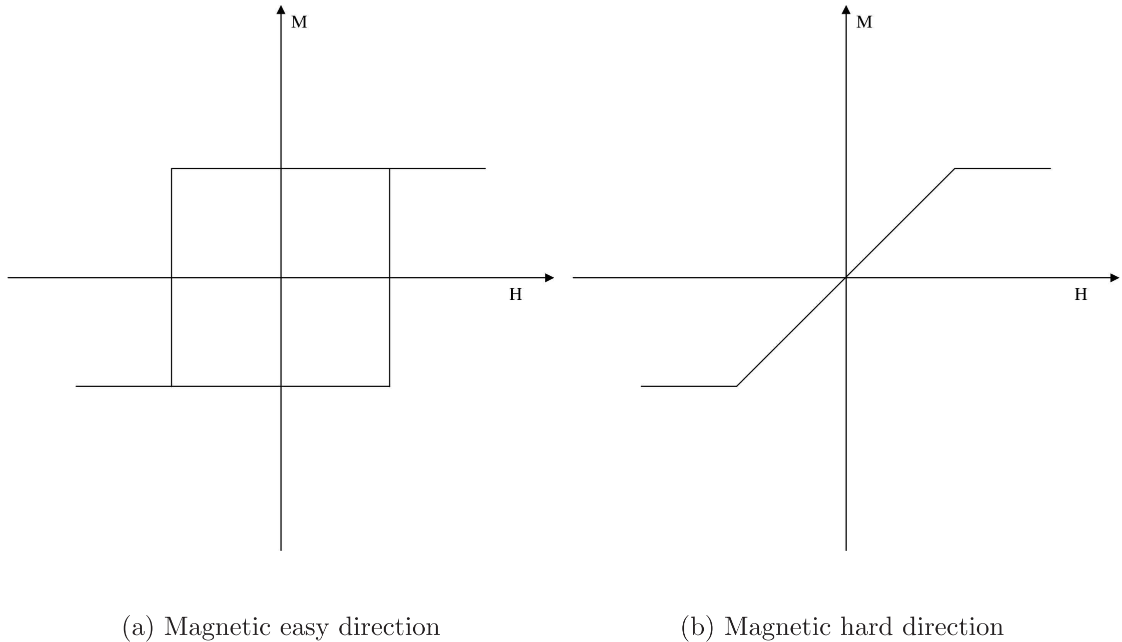

(a) Magnetic easy direction

(b) Magnetic hard direction

Figure 4.9: Ideal hysteresis loops of a magnetic uniaxial sample.

4.5.2 Recording media challenges

Thermal stability is an important obstacle for increasing areal bit density of current magnetic recording beyond 1 Tbit/in^2. The writability of the medium and signal to noise ratio (SNR) are also heavily researched topics because a trade-off between these three obstacles (i.e. thermal stability, writability and SNR) is necessary [84].

Thermal stability

The anisotropy constant, K_u, is related to the magnetisation energy barrier for reversal by the equation $\Delta \mathrm{E} = K_u \mathrm{V}$, where V is the magnetic switching volume (or bit cell volume), see Fig. 4.10.

To maintain thermal stability, the energy barrier ΔE (or stored magnetic energy, $K_u V$) must be larger than the thermal fluctuation energy $k_B T$ by a minimal stability

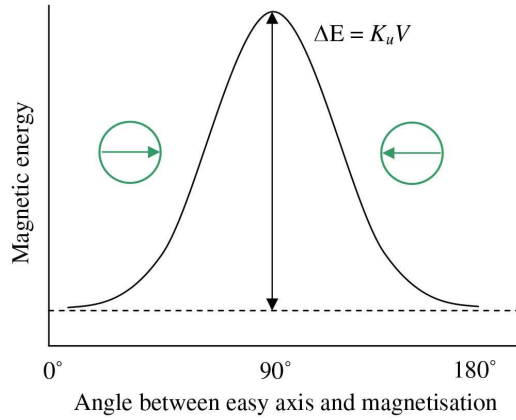

Figure 4.10: Energy barrier for magnetisation reversal.

ratio, i.e. ΔE>50 to 70 $k_B T$ [3] where k_B is the Boltzmann's constant and T is the absolute temperature. However, the reduction of the grain volume leads to the reduction of $K_u V$ (ΔE). The energy required per unit volume to rotate the magnetic moments away from the easy direction (the **anisotropy energy**) must therefore increase in order to maintain thermal stability [122] [123]. Currently used Co- based alloys have a relatively low anisotropy energy, whereas the $L1_0$ phase of FePt with its very high K_u is an ideal candidate.

Signal to noise

The signal to noise ratio (SNR) of the magnetic read-out signal is approximately given by the expression 4.2 [124]:

$$SNR = log_{10}(N). \tag{4.2}$$

That is, the SNR is proportional to the number of grains per bit, N. When bit sizes become smaller and smaller, the volume of the individual media grains should decrease to maintain a near constant number of grains per bit in order to satisfy the SNR requirements. However smaller grains are thermally unstable and interparticle interaction effects also increase [125]. The magnetic exchange coupling between grains contributes to noise. If the intergrain magnetostatic and exchange interaction can be reduced, the media noise could be reduced significantly [126].

Writability

Switching of magnetisation occurs at $H_{sw} = 2K_u/M_s$ [116][124]. The absolute easy axis switching field H_{sw} is uniquely determined by the uniaxial anisotropy constant K_u and the saturation magnetisation M_s [127]. Increasing K_u increases H_{sw}. The ratio K_u/M_s cannot exceed the write field capability of the head.

Thus, the writability of the recording medium is limited by the magnetic writing field generated by the write head. Materials with high K_u require high switching fields. At present, very high K_u media would not be writable using conventional inductive write heads. Assist strategies such as heat assisted magnetic recording (HAMR) [128], microwave assisted magnetic recording (MAMR) [129], tilted media [125] and exchange coupled composites [130] will be required for high K_u media.

4.6 High K_u materials

$L1_0$ FePt belongs to the tetragonal $L1_0$ family of ferromagnets. Other members of this family include CoPt, FePd [131] and MnAl alloy systems [3][132]. The tetragonal $L1_0$ ferromagnets all exhibit high uniaxial magnetocrystalline anisotropies, K_u, of about 10^7 to 10^8 $ergs/cm^3$ [133]. $L1_0$ CoPt and FePt, due to their high uniaxial magnetocrystalline anisotropy (4.9×10^7 $ergs/cm^3$ and 6.7×10^7 $ergs/cm^3$) and chemical stability have been widely investigated in recent years in view of their potential application for ultra high density recording media. Table 4.1 compares the magnetic properties of $L1_0$ CoPt and FePt with some other ferromagnetic materials [3] and shows that the FePt system has K_u of about 15 times larger than in hcp Co and over 30 times larger than in advanced CoPtCr media alloy. The high K_u associated with the $L1_0$ phase allows for a minimum thermally stable grain size of 2 to 3 nm [134] [135].

The crystal structure of $L1_0$ phase CoPt and FePt is a chemically ordered phase and at the equiatomic composition comprises of alternating atomic planes of Co or Fe and Pt along the unit cell c-axis. In the CoPt system, the as deposited films are generally not chemically ordered and exhibit soft ferromagnetic properties. The desired $L1_0$ ordered phase can be obtained by annealing at moderately high

Material	K_u (10^7 erg/cm^3)	M_s (emu/cm^3)	H_{SW} (kOe)
Co - alloys			
CoPtCr	0.20	298	13.7
Co	0.45	1400	6.4
Co_3Pt	2.0	1100	36
$L1_0$ phases			
FePd	1.8	1100	33
FePt	6.6 - 10	1140	116
CoPt	4.9	800	123
MnAl	1.7	560	69
Rare earth transition metals			
$Fe_{14}Nd_2B$	4.6	1270	73
$SmCo_5$	11-12	910	240-400

Table 4.1: Magnetic properties of $L1_0$ and other ferromagnetic alloys, (from [3]).

temperatures (over 500 °C) [136]. However, high annealing temperatures leads to considerable particle coalescence. There have been a number of investigations to reduce the ordering temperature for example by the use of underlayers [137].

A number of processing routes have been used to fabricate $L1_0$ CoPt, these include sputter deposition with subsequent annealing [138], sputtering at elevated temperatures [139] [140], ion irradiation of disordered films [141], annealing of Co/Pt multilayers [142], depositing onto single crystal structures, molecular beam epitaxy [143] and by chemical synthesis [144] [145]. More recently Newman et al. [146] have demonstrated the fabrication of $L1_0$ CoPt by co-sputtering Pt, Co and silicon nitride followed by rapid thermal annealing. This route embeds the magnetic particles into a silicon nitride matrix and has been shown to be a promising route for fabricating $L1_0$ CoPt . A similar idea is presented in this thesis but using FePt since $L1_0$ FePt exhibits a higher magnetocrystalline anisotropy which makes it a better candidate for high density recording media. However, it is expected that FePt will be significantly

more challenging to fabricate since Fe is more susceptible to oxidation than Co.

4.7 Crystal structures

Before continuing on to discuss the structure and phases of $L1_0$ FePt it is useful here to review the basics of crystallography.

Crystalline solids have a highly regular arrangement of atoms, in a repeating 3-D pattern (called a lattice) [147]. The manner in which the atoms are arranged in a crystal is known as its crystal structure. The simplest, smallest repeating unit in a crystal from which the overall structure can be constructed is known as the **unit cell**; it is the building block of the crystal. The pattern of **points** made by the comers of the unit cells when they are packed together is called the space lattice [148].

The shape and size of a unit cell can be defined by six lattice constants [149]. Three of these are its axial lengths (lengths of the edges of the unit cell along its major axes) which are usually denoted $a,\ b\ and\ c$. The other three constants are its inter - axial angles, which are usually denoted $\alpha,\ \beta\ and\ \gamma$, see Fig. 4.11. In some crystal structures the edge lengths are equal ($a = b = c$), so only lattice constant a is used to describe its dimension. Knowledge of crystal structure and lattice constant values are used to calculate distances between neighbouring atoms in a crystal, as well as determining some of the crystal's physical and electrical properties [150].

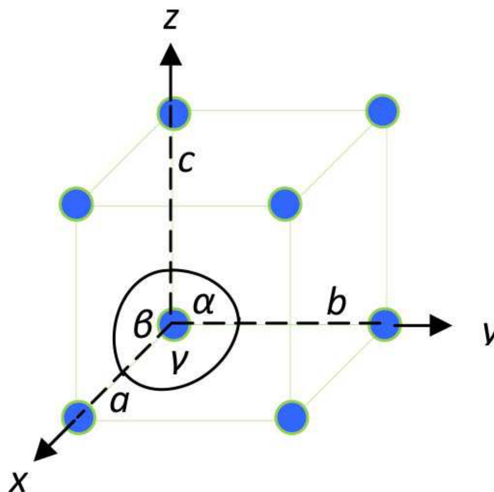

Figure 4.11: The edge lengths ($a,\ b,\ c$) and axial angles ($\alpha,\ \beta,\ \gamma$) of a unit cell.

There are seven crystal classes and these are shown in Table. 4.2.

Category	Description	Edge lengths	Internal angles
Cubic	Three equal axes at right angles	$(a = b = c)$	$(\alpha = \beta = \gamma = 90°)$
Tetragonal	Three axes at right angles, two equal	$(a = b \neq c)$	$(\alpha = \beta = \gamma = 90°)$
Monoclinic	Three unequal axes, one pair not at right angles	$(a \neq b \neq c)$	$(\alpha = \gamma = 90° \neq \beta)$
Orthorhombic	Three unequal axes at right angles	$(a \neq b \neq c)$	$(\alpha = \beta = \gamma = 90°)$
Rhombohedral	Three equal axes, equally inclined	$(a = b = c)$	$(\alpha = \beta = \gamma \neq 90°)$
Hexagonal	Two equal axes at 120°, third axes at right angles	$(a = b \neq c)$	$(\alpha = \beta = 90°, \gamma = 120°)$
Triclinic	Three unequal axes, unequally inclined and none at right angles	$(a \neq b \neq c)$	$(\alpha \neq \beta \neq \gamma \neq 90°)$

Table 4.2: The seven unit cell categories.

The two lattice structures of FePt that are of particular interest this thesis are the **cubic** and **tetragonal** structures, and so discussion on the other structures shall be omitted, however detailed information on the other structures can be found in books on crystallography such as those by Hammond [151] and Tilley [147].

Within the cubic category there are three lattice arrangements, shown in Fig. 4.12. These are known as the simple cubic (or primitive) where the atoms are found only at the corners of the unit cell, body centred cubic (bcc) where atoms are found at the corners and in the centre of the unit cell, and face-centered cubic (fcc) where the atoms are found at the corners of the unit cell and on 2 (or more) faces. The tetragonal class consists of lattice arrangements similar to those in the cubic category, shown in Fig. 4.13, with the difference that the c edge length is longer. These are known as the simple (or primitive tetragonal), body centered tetragonal (bct) and face centered tetragonal (fct).

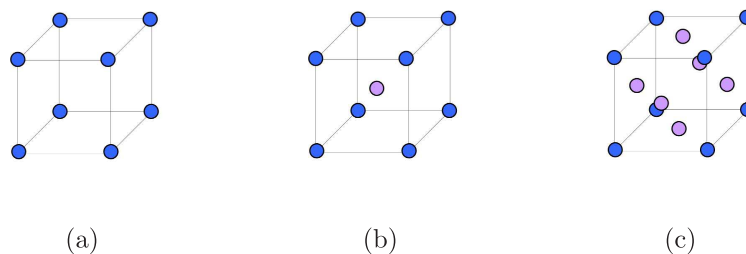

Figure 4.12: The cubic crystal class, (a) primitive, (b) bcc and (c) fcc.

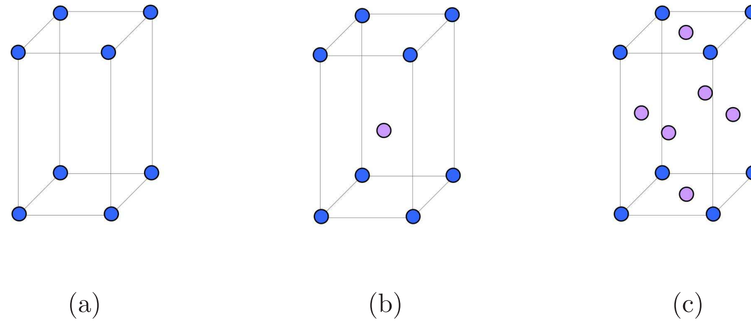

(a) (b) (c)

Figure 4.13: The tetragonal crystal class, (a) primitive, (b) fcc and (c) fct.

4.7.1 Miller System

The Miller system is a labelling system that uses combinations of integers or indices to define crystallographic directions and planes [151]. The Miller indices , *(h,k,l)* are a set of numbers which quantify the intercepts and thus may be used to uniquely identify the directions and planes [152]. The letters *h, k* and *l* refer to the principle axes *x, y* and *z.* For directions, the index is the axis coordinate of the end point of the vector, converted to nearest whole numbers. For planes, the index is the reciprocal of the value of the intersection of the plane with a particular axis, converted to whole numbers. The basics are summarised below by considering a simple cubic system.

Miller indices : Directions

A crystallographic direction is basically a vector between two points in the crystal. Consider the example in Fig. 4.14 where a crystallographic direction has been drawn in the unit cell and is shown by a dotted blue arrow. The projection of the vector onto the three axes in terms of the unit cell dimensions is as follows: x = *1,* y =*1* and z = *0.5.* To arrive at the Miller index the vector is expressed as a set of whole numbers and enclosed in square brackets. For the example shown, the numbers are multiplied by two to remove the 0.5 and the Miller index shown is [221]. Directions are indicated by square brackets, i.e. [hkl]. Families of square brackets are indicated by angle brackets, i.e. ⟨hkl⟩. An example of a family of directions is ⟨100⟩= [100], [010], [001], [-100], [0-10] and [00-1], corresponding to directions defined by the vectors *x, y* and *z* in both positive and negative directions [153].

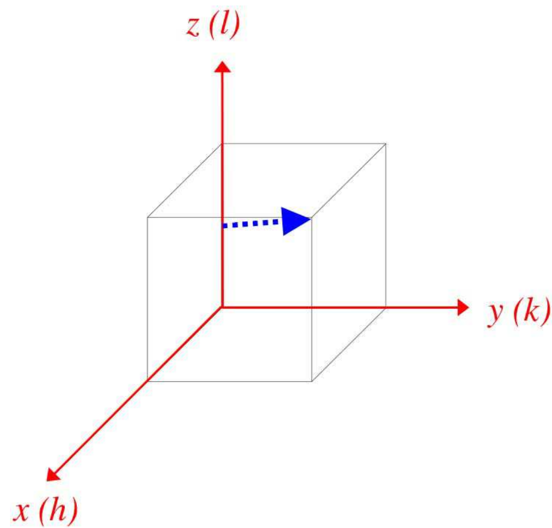

Figure 4.14: Miller indices ($h,\ k,\ l$) and example crystallographic direction, represented by the blue arrow.

Miller indices : Planes

The orientation of a surface or a crystal plane may be defined by considering how the plane intersects the main crystallographic axes of the solid. Assignment of Miller indices of crystal plane involves identifying the intercepts on the $x,\ y$ and z axes. For the cubic system shown in Fig. 4.15 with unit dimensions of $a \times a \times a$, the green plane, or surface, displays the intercepts a, ∞, ∞. If the plane is parallel to an axis, it is said to cut at ∞. Once identified, these coordinates are converted to fractional coordinates by dividing by the respective cell dimension, for example, a point *(x, y, z)* in a unit cell of dimensions $a \times b \times c$ has fractional coordinates of $(x/a, y/b, z/c)$. Therefore, in the case of the green surface, the fractional intercepts are $a/a,\ \infty/a,\ \infty/a$ (i.e 1,∞, ∞). The Miller indices are the reciprocals of the fractional coordinates. The reciprocals of 1 and ∞ are 1 and 0 respectively, thus yielding (100) for the green surface. Planes are indicated by rounded brackets, (hkl) and families of planes are indicated by curly brackets, i.e. {hkl}. An example of a plane family is as follows: {100} = (100), (010), (001), (-100), (0-10), and (00-1). These are all six faces of a cube.

4.8 $L1_0$ FePt structure and phases

Equiatomic FePt has two main crystal structures. These are face centred cubic (fcc) and face centred tetragonal (fct), shown in Fig. 4.16.

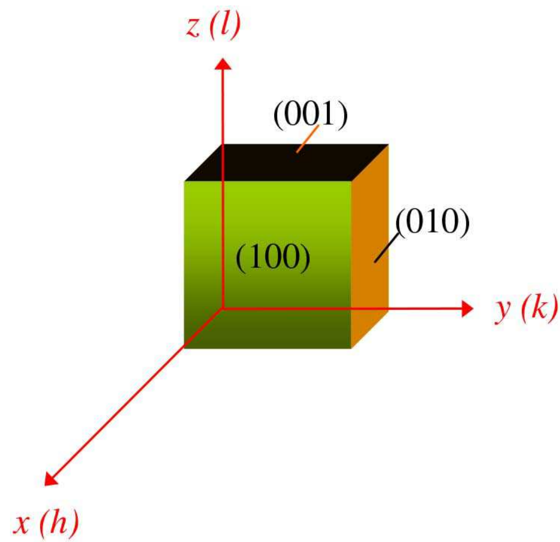

Figure 4.15: Miller indices (h, k, l) and three equivalent planes are shown for a cubic unit cell.

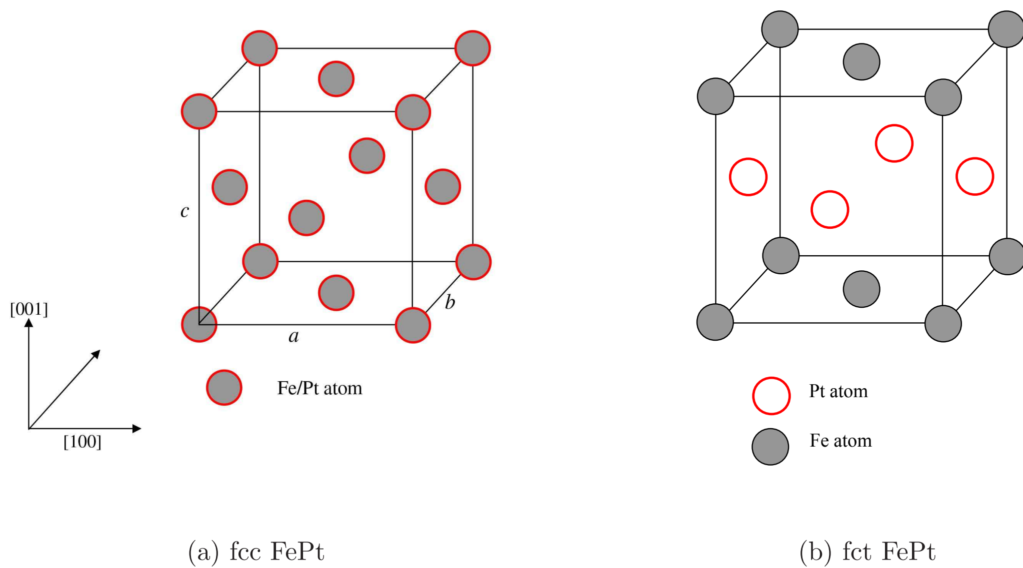

(a) fcc FePt

(b) fct FePt

Figure 4.16: Two main crystal structures of equiatomic FePt.

In fcc FePt the probability of each face and corner site being occupied by either Fe or Pt is the same; i.e. Fe and Pt atoms are randomly arranged. The lattice constants $a = b = c$ and all angles are 90°. As deposited FePt usually takes the fcc phase which is a disordered structure with soft magnetic properties [154] [155].

In the fct phase, otherwise known as the $L1_0$ structure, the Fe and Pt are atom-

ically ordered, comprising of alternating atomic planes of Fe and Pt along the unit cell “c-axis” which is the easy axis. The lattice constants $a = b \neq c$ and all angles are 90°. An important crystallographic feature of the $L1_0$ structure is its c/a ratio. The lattice constant, a, of $L1_0$ FePt is slightly larger than lattice constant, c. In $L1_0$ FePt $a = 3.85$ Å and $c = 3.71$ Å giving c/a of 0.96 [156].

It is the fct $L1_0$ chemically ordered phase that has attracted considerable attention as a candidate for next generation data storage media, due to the strong magnetocrystalline anisotropy along specific crystallographic directions, large M_s and high corrosion resistance. The high magnetic anisotropy is thought to be attributed to the strong coupling between the 3d electrons in Fe and the 5d electrons in Pt [65].

4.9 Challenges for FePt

Before FePt can be used as magnetic media, several key problems must be overcome:

1. Controlling the easy axis orientation in the out-of-plane direction with the easy axis distribution of less than 5 degrees [135][157][158].
2. Reduction of ordering temperature [159][160].
3. Reduction of grain size while ensuring a narrow particle size distribution and magnetically decreasing the exchange interaction between neighbouring grains (as this increases as the grain size diminishes) [161][162].

The additional problem of the ease at which Fe reacts with oxygen makes FePt a sensitive material to produce and special measures may be required during its fabrication, particularly during any heat treatment.

4.9.1 Controlling the easy axis

An important aspect regarding magnetic anisotropy in $L1_0$ systems is that it strongly develops along the c-axis, which corresponds to the stacking direction of alternate pure planes of both elements. A consequence of obtaining structures with this c-axis perpendicular to the plane is the appearance of perpendicular magnetic anisotropy

[158].

In general, FePt films deposited directly onto amorphous substrates tend to possess a (111) texture since the close packing plane of the $L1_0$ FePt structure is the (111) plane and surface energy is minimised. This leads to the tilting of the [001] axis about 36° away from the film's plane (Fig. 4.17) [163]. For perpendicular magnetic recording applications the orientation of FePt should have the c axis (or [001] axis) perpendicular to the film plane [157] (refer to Fig. 4.16(b)).

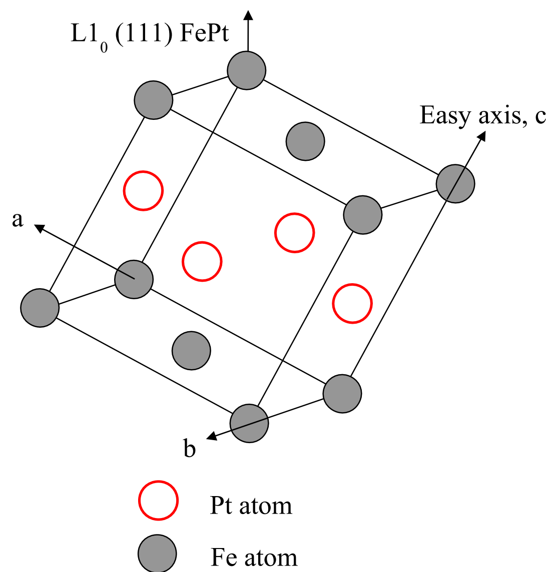

Figure 4.17: Tilting of the [100] axis for fct FePt.

The growth of thin films is affected by thermodynamic and kinetic factors [6][164]. The crystal structure, and hence preferred orientation, are closely related to surface free energy, interface energy and strain energy; all of which contribute to the total energy of the system [165].

Surface energy

Surface energy is the work stored in a system that can be used to create a surface [52]. All surfaces are energetically unfavourable [166]. Surface energy can be minimised by:

1. By reducing the amount of surface area exposed
2. By predominantly exposing surface planes which have a low surface free energy

3. By altering the local surface atomic geometry in a way which reduces the surface free energy

Systems already possessing a high surface energy (as a result of the preparation method) will not always readily interconvert to a lower energy state at low temperatures due to the kinetic barriers associated with the restructuring. In FePt, to minimize the surface energy, the film develops the (111) texture, since (111) is the closest-packed plane [167].

Interface energy

The excess reversible work required to generate a unit area of an interface is known as the interfacial free energy [168]. For the initial growth of a thin film , it is the energy contribution that exists at the substrate – film interface. Interfacial energies are minimized when the contact angle of growing atoms is at minimum to the substrate [169]. In the case of a single crystal substrate, the film – substrate interface energy also depends on the orientation of the grain lattice with respect to the substrate lattice [170][171]. Since the interface free energy is the contribution to the free energy of a system due to the presence of an interface separating two coexisting phases at equilibrium, interfacial energies exist between grains and by introducing materials into grain boundaries of for example, FePt films, the interfacial energy can be reduced [172].

Strain energy

The transformation of FePt from the fcc disordered phase to the fct ordered phase involves the expansion of the a lattice parameter and the contraction of the c lattice parameter [173]. This distortion is unfavorable as it generates a high strain energy which then becomes an activation barrier for ordering [174].

Since it is the process and energetics of thin film formation that leads to the atomic arrangement of a crystal structure, its orientation is affected by many preparation factors [174]. Therefore, by controlling the preparation processes of a material, the total free energy and orientations of growing films may be tuned. Much attention has been paid to seek appropriate substrates, seed and buffer layers for reducing the total energy of FePt film growth and so to promote the growth of FePt

with the (001) texture [175][176]. For example, MgO underlayers or MgO substrates have been used widely to decrease the lattice misfit between film and substrate [177] [178] [179]. Unfortunately, single crystalline MgO substrates are of high cost, therefore not acceptable for commercial applications [180].

The addition of Cr [122], CrRu [181], combined Ta/MgO [182] and RuAl [183] underlayers have also been used to to promote the perpendicular orientation. FePt films with perpendicular magnetic anisotropy have also been achieved from alternating $[Fe/Pt]_n$ multilayer films [184], [185]. However, multilayers result in higher cost and post annealing may result in undesirable diffusions between the FePt magnetic layers and underlayers [186].

4.9.2 Reduction of ordering temperature

Generally, using magnetron sputtering methods at low substrate temperatures produces FePt films with a disordered face centred cubic (fcc) structure. Annealing temperatures of over 500 °C are necessary to transform FePt films from the disordered fcc phase to the face centred tetragonal (fct) ordered structure. Above 650 °C is usually required for nano composite/granular films [161]. Sun et al. [187] reported that 4 nm diameter nanoparticles were produced by a chemical synthesised procedure without sputtering, but annealing at 580 °C during the assembly stage of synthesis was still required to get high K_u .

High processing heat treatment of the as deposited soft fcc structure leads to both grain size and exchange coupling increases, which are unfavourable for obtaining high recording density and SNR [188]. As a result much effort has focussed on decreasing the ordering temperature of FePt films.

Through the addition of additional materials to FePt, such as nitrogen [189], Cu [134], [190] , TiN [180], Ag [191], CrRu [192] and Al [193] the ordering temperature has been reduced to as low as 350 °C [192]. Underlayers have also been introduced to transform the kinetics of the transformation or to improve the lattice mismatch between the film and the substrate. Underlayers such as Bi [159], MgO [160], Ag [194], Cr [195] and Cu [190] have shown good promise. The $L1_0$ texture was shown

to appear at 300 °C with use of the Cr underlayer. Multilayering of Fe and Pt [184], [185], deposition onto heated substrates [196], ion irradiation [197] and the addition of top layers such as MgO [198] and Ag [199] have all been used in efforts to reduce the ordering temperature.

Lattice strain can also influence phase transformation and so attempts to reduce the ordering temperature by means of controlling lattice strain has also been investigated [135].

Although some of the above methods have produced (001) textured FePt with high coercivities in the temperature range 300 °C to 400 °C (either by depositing in this temperature range or by post deposition annealing) , only partial transformation from the fcc phase took place. The coexistence of fcc FePt and $L1_0$ FePt particles are not favored for high density recording applications [192].

4.9.3 Reduction of grain size

The addition of non-magnetic materials into the FePt magnetic films to form granular films is an efficient method for controlling grain size. Materials such as W [200], Au [201], SiO_2 [202], B_2O_3 [203] and Cr [204] have shown promising applications in controlling FePt grain sizes and magnetic coupling in the composite films. Xu et al. [205] found that when embedding FePt particles in a C matrix increasing the concentration of C decreased the grain size and intergrain interaction . The growth conditions and post annealing methods can also contribute to the reduction of grain sizes, for example Suzuki et al. [206] showed that grain size decreased significantly with increasing the heating rate of rapid thermal annealing. This was confirmed by Eppler et al. [207].

Chapter 5

Multi-ferroism

An introduction to the topic of multi-ferroic (MF)materials is given in this chapter, followed by a description of the ideas in using MF devices for data storage applications. Multi-ferroic materials possess multiple functional properties. They usually exhibit at least two of the three primary ferroic orders: ferromagnetism, ferroelectricity and feroelasticity [208][209]. The ferromagnets have a spontaneous magnetisation (M) that is switchable using an applied magnetic field (H). Ferromagnetic materials have already been discussed in Chapter 3 so only a description of the other two ferroic orders is provided.

5.1 Ferroelectricity

Ferroelectric materials have a spontaneous electric polarization (P) that is switchable by applying an electric field (E) [210]. They possess permananent non-zero dipole moments and are classed as 'polar' [62].

The electric dipole moment

An electric dipole moment consists of two equal and opposite charges, q and $-q$, separated by a distance, l. The moment of the dipole, μ, is a vector of magnitude that points from the negative charge to the positive charge [211]:

$$\mu = ql. \tag{5.1}$$

The dipole moment in ferroelectric materials arises from the existence of an imbalance in the distribution of electric charge [52]. For example, the structure shown in Fig. 5.1(a) is said to be *non-polar*. Its constituent ions have a centrosymmetric arrangement and so there is no net dipole moment. In Fig. 5.1(b), however, the central negative ion (negative ions are known as *cations*) is displaced relative to the corner positive ions (positive ions are known as *anions*). This displacement causes an imbalance of electric charge [73], leading to a net dipole moment and so the structure is said to be *polar*. The *polarization*, P, of a sample is the electric dipole moment density, i.e. the total dipole moment per unit volume [52].

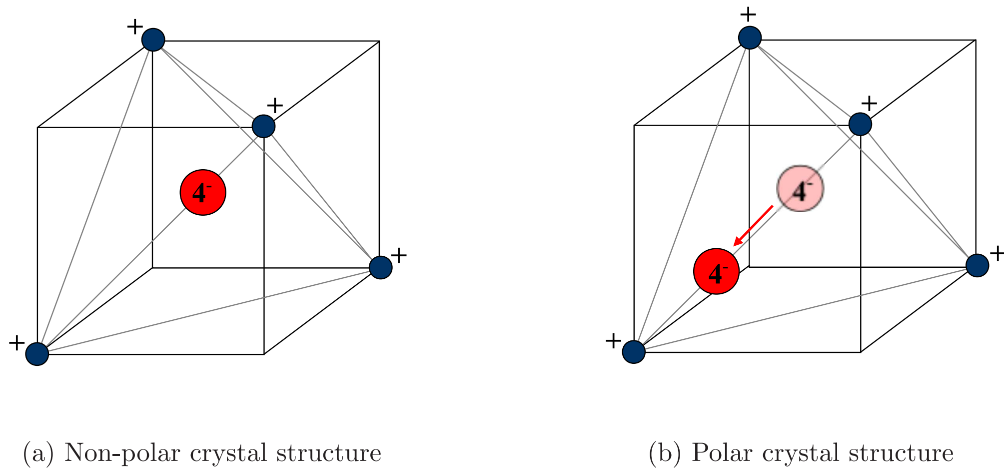

(a) Non-polar crystal structure

(b) Polar crystal structure

Figure 5.1: (a) A non-polar crystal structure displaying a centre of symmetry. (b) Cation displacement resulting in polarization; the red arrow shows movement of the cation possessing a charge of 4^-.

.

In an electric field, E, any dipole moments within a polarized material which lie parallel to the electric field are lowered in energy, while moments that lie perpendicular to the field are higher in energy and moments that lie anti-parallel are even higher in energy. This induces a driving force to minimise the energy, such that all dipole moments align with the electric field [73][212]. For a material to be ferroelectric it must be insulating; otherwise an applied electric field will cause current to flow rather than re-orient its polarization.

Ferroelectric materials possess properties which are analogous to ferromagnets,

for example the presence of ‘ferroelectric domains’ (regions of oppositely oriented polarization within the sample)[213][214][215]. They also show a hysteretic response to an applied electric field (Fig. 5.2). Typical ferroelectric P-E hysteresis loops are similar to M-H hysteresis loops in ferromagnets. Due to the properities of domains and hysteretic behavious, ferrolectrics also find their way into data storage applications, e.g. ferroelectric random access memories (FRAM) [216][217][218].

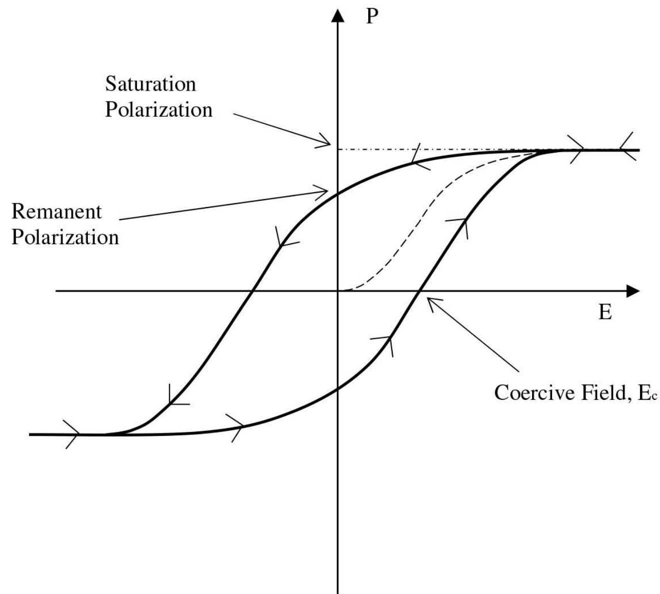

Figure 5.2: Characteristic P-E hysteresis loop for a ferroelectric material.

5.2 Ferroelasticity

A ferroelastic material is defined as a material that has a spontaneous deformation that is switchable with an applied mechanical stress [57]. Below a transition temperature, T_c, a ferroelastic material has ferroelastic orientation states that are separated by domain walls. These states can be re-orientated to one of the other crystallographically equivalent states under the influence of an externally applied stress [219] as one orientation state may be favoured over the other(s). The switching process, called a ferroelastic phase transition, is a displacive structural phase transition that gives rise to an observable shape change in the material. Above T_c, the material is ‘paraelastic’ and no domains exist [220][221].

Fig. 5.3 illustrates ferroelastic behaviour for the well known 'shape memory alloys.' Shape memory alloys are a class of ferroelastic materials that are able to change their crystallographic structure via stress or temperature induced phase transformations [222][223]. The crystallographic structural changes can be observed as deformations, and are recoverable once the stress has been removed or the original temperature restored. Fig. 5.3 depicts a crystallographically ordered phase (known as 'austenite,' represented by A) and a crystallographically less ordered phase (known as 'marstenite,' represented by M). When stress, σ, is applied to the austenite phase, a shear-like strain is produced and transformation to the marstenite phase occurs. The figure shows the stress applied in two opposing directions ($+\sigma$ and $-\sigma$) producing two distorted marstenite phases (+M and -M). When the stress is removed, the martensite reverts to austenite and correspondingly returns to its original geometry exhibiting zero strain [224].

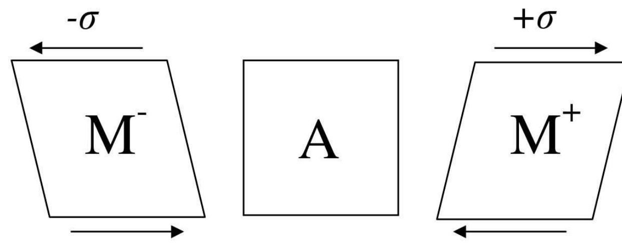

Figure 5.3: Stress induced strain on austenite (A), resulting in two phases of marstenite (+M and -M).

Temperature changes may also cause this type of crystallographic deformation. Cooling a shape memory alloy below a critical temperature (which depends on the specific alloy) causes an austenite phase to transform into the marstenite phase which is reversible if the original temperature is restored [225][226].

A measure of the crystal distortion is the "spontaneous strain", analogous to the spontaneous magnetisation and polarization associated with ferromagnetic and ferroelectric transitions, respectively [227]. Since the work contained in this thesis is concerned with stress induced strain, their definitions are given below.

Stress and strain

Stress, σ, in its simplest term is a force, F, divided by the area, A, across which it is applied (applies only for uniform cross section) [211].

$$\sigma = \frac{F}{A}. \tag{5.2}$$

Strain, ϵ, is simply a ratio of a change in dimension, Δl, to the original dimension, l, [211]:

$$\epsilon = \frac{\Delta l}{l}. \tag{5.3}$$

Whilst ferroelasticity can occur independently of other ferroic orderings, it also often accompanies ferroelectricity. The coupling between strain and polarization in ferroelectrics leads to a mechanical deformation that is coupled to the ferroelectric polarization. This coupling manifests itself in the widely used "piezoelectric response" of ferroelectrics [228][229]. Ferroelectric ferroelastics are therefore a well established group of multi-ferroics used in sensor and actuator applications [230][231][232][233].

5.3 The piezoelectric effect

Piezoelectricity is a property exhibited by certain classes of materials. When mechanical pressure is applied to these materials, a strain is produced that results in a change in the dipole moments, that is, they become electrically polarized. This in turn produces a voltage that is proportional to the pressure applied [234]. This conversion of mechanical energy to electrical energy is known as the *direct piezoelectric effect* [235][236]. Conversely, when an electric field is applied to a piezoelectric material, the crystalline structure changes shape, producing dimensional changes. This is known as the *inverse or converse piezoelectric effect* [236]. When the electric field is removed, the dipoles remain locked in alignment, giving the material a remanent polarization and permanent deformation as well as making it permanently polarized (hysteresis behaviour). All ferroelectric materials are piezoelectric but not all piezoelectric materials are ferroelectric [73]. Quartz is a well known example of

a material that is piezoelectric but not ferroelectric.

The piezo-response of a material can be described by the constants known as the "piezoelectric charge coefficient" or the "piezoelectric voltage coefficient" [237][238].

Piezoelectric charge constant

The piezoelectric charge coefficient, d, is the ratio of electric charge generated per unit area to an applied force. The units of d are m/V or C/N.

$$d = \frac{strain\ developed}{applied\ field\,(V/m)} = \frac{charge\ density\,(C/m^2)}{applied\ stress\,(N/m^2)} \tag{5.4}$$

Piezoelectric voltage constant

The piezoelectric voltage coefficient, g, is the ratio of the electric field produced to the mechanical stress applied. The units of g are m^2/C or Vm/N.

$$g = \frac{strain\ developed}{applied\ charge\ density\,(C/m^2)} = \frac{field\ developed\,(V/m)}{applied\ mechanical\ stress\,(N/m^2)} \tag{5.5}$$

Usually the charge and voltage coefficients contain two subscripts, i and j e.g. d_{ij} and g_{ij}, where i represents the direction of applied electric field and j the direction of induced displacement. The symmetry axes of a piezoelectric crystal is shown in Fig. 5.4. The direction of polarization is conveniently taken as axis 3, with axes 1 and 2 perpendicular to this. The terms 4, 5 and 6 apply to shear strains associated with the 1, 2 and 3 directions. For example for the charge coefficient d_{33}, the first subscript indicates that the electrodes are perpendicular to axis 3 and the second subscript indicates that the piezoelectric induced strain or the applied stress is in direction 3. For the voltage coefficient g_{15}, the first subscript indicates that the electrodes are perpendicular to axis 1 and that the applied stress, or piezoelectrically induced strain is in shear around axis 2.

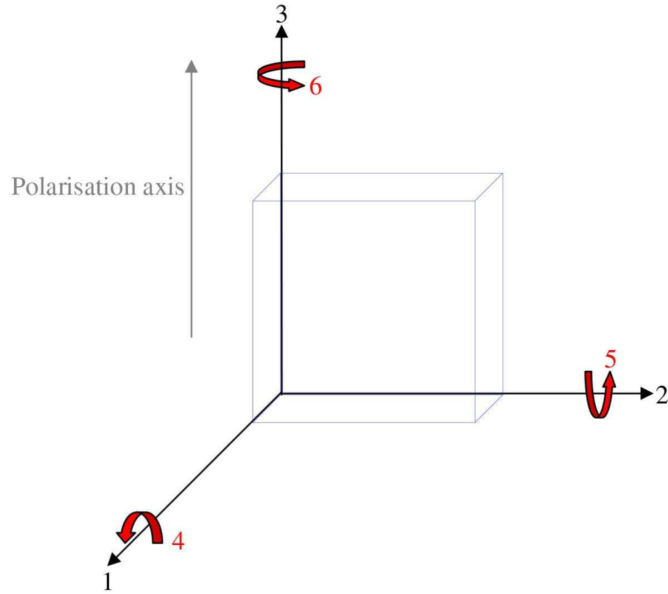

Figure 5.4: Defined symmetry axes for a piezoelectric crystal.

5.4 Lead zirconate titanate

Lead zirconate titanate (PZT) ceramics, with the general formula $Pb(Zr_{1-x}Ti_x)O_3$ are widely used as sensors and actuators due to their excellent dielectric, ferroelectric and piezoelectric properties [239][240]. PZT is used for the the work described in Chapter 8 and so some background to this material is provided in this section.

PZT belongs to the structural family of perovskites, having the crystal structure of the form ABX_3, where A is a large cation, B a smaller cation and X an anion [241][242][243]. PZT is non-polar (also known as paraelectric) above its Curie temperature of 766 K [244], and has the cubic perovskite structure (Fig. 5.5 (a)). The cubic perovskite structure is characterized by a small cation B (Ti^{4+} and Zr^{4+} occupying the B site at random) at the centre of an octahedron of oxygen anions, with large cations A *(Pb)*, at the unit cell corners. Above its Curie temperature it possess no spontaneous dipole, so behaves like a simple dielectric (where an applied electric field induces an electric polarization, which returns to zero when the field is removed). Below the Curie temperature the structure undergoes a phase transition to form a ferroelectric tetragonal (spontaneous polarization along the $\langle 100 \rangle$ direction), or rhomohedral phase (spontaneous polarization along the $\langle 111 \rangle$ direction). These directions and their equivalent variants are shown in Figs.5.5 (b) and (c).

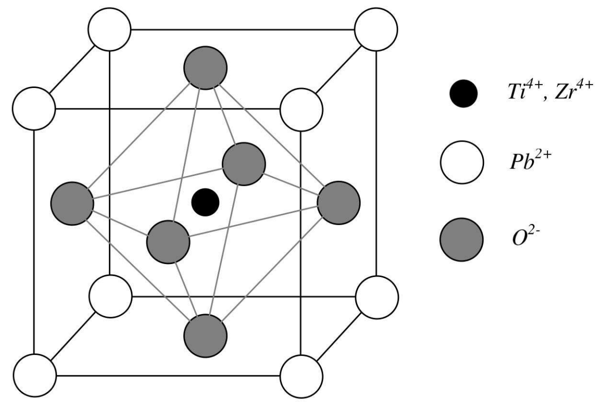

(a)

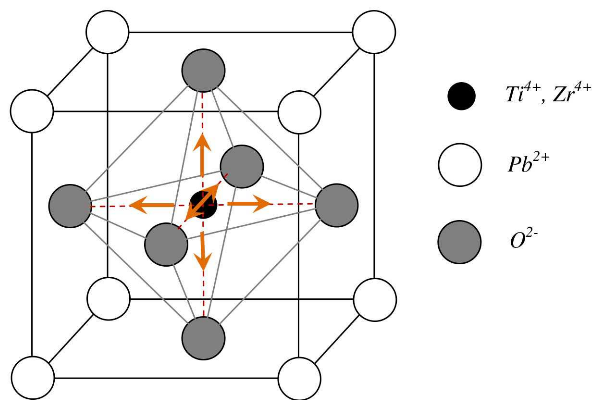

(b)

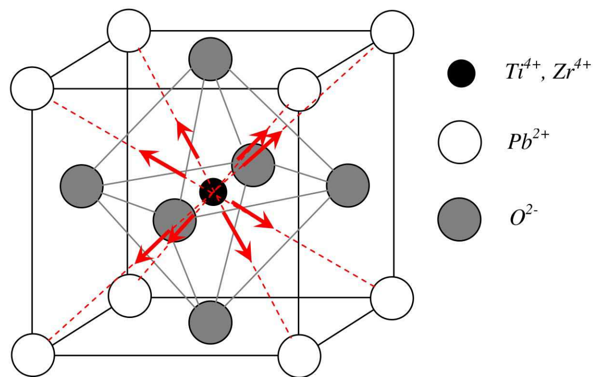

(c)

Figure 5.5: (a) The cubic perovskite structure, (b) arrows to show the six equivalent $\langle 100 \rangle$ directions that results in the tetragonal crystalline phase, (c) arrows to show the eight equivalent $\langle 111 \rangle$ directions that results in the rhombohedral crystalline phase.

The spontaneous polarization of the ferroelectric phase is derived largely from the electric dipole moment created by the movement of the Ti ion from the centre of the O_6 octahedra. Every unit cell over a large domain acquires an electric dipole moment that persists even in the absence of an electric field.

Thin film PZT itself is a candidate for non-volatile memories due to its excellent ferroelectric properties, such as high remanent polarization and low coercive field. However, reliable polarization cycling of the data and data retention needs to be improved before it can be widely used [245].

5.5 Combining ferromagnetism and ferroelectricity

Being able to control magnetization, M, with electric fields, E, and vice versa, is a particularly attractive field for microelectronic devices. The coupling between the ferromagnetic (FM) and ferroelectric (FE) orders produces an effect known as the **magneto-electric (ME) effect** [246][247]. The 'direct' effect (ME_H) is the magnetic field control of electric polarization $\Delta P = \alpha_H \Delta H$ where α is the ME coefficient. The 'converse' effect (ME_E) is the electric control of magnetisation ($\Delta M = \alpha_E \Delta E$) [248][249]. An interesting potential application that could result from strong coupling between the magnetic and ferroelectric orderings is data storage devices [250][251][252]. If re-orientation of the magnetisation were to also cause re-orienration of the electric polarization, it would then be possible to write or detect recording data bits with either electric or magnetic fields [253].

Despite their similarities (e.g. behaviour in external field, anomalies at a critical temperature, domain structures), the origins of ferromagnetism and ferroelecticity in solids are very different. Magnetism is related to ordering of electron spins in incomplete shells [254], ferroelectricity results from the relative shifts of negative and positive ions [62].

The coexistence of these two orders in a single material (single phase) is rare. This is because magnetism requires transition metal ions with *partially filled d shells*,

as the spins of electrons occupying completely filled shells add to zero and do not participate in magnetic ordering [51]. The exchange interaction between uncompensated spins of different ions gives rise to long range magnetic ordering. Most ferroelectrics are transition metal oxides, in which the transition metal ions have *empty d shells* [255][256]. These positively charged ions like to form 'bonds' with one or several of the neighbouring negative oxygen atoms (electrons from the filled oxygen shell are effectively shared into the empty d shell of the transition metal ion). This collective shift of cations and anions inside a periodic crystal induces bulk electric polarization [212][244].

Therefore, for ferroelectricity and magnetism to co-exist in a single phase, the atoms that move off-centre to form the electric dipole moment should be different from those that carry the magnetic moment [257]. Single phase multi-ferroics exhibiting ferromagnetic and ferroelectric properties belong mainly to two groups - the hexagonal manganites and the Bi-based perovskites, e.g. $TbMnO_3$ and $BiMnO_3$ [257].

The development of single phase MF materials for device applications has not yet been successful mainly due to one important reason. Most of them have low Néel or Curie temperatures, which are below room temperature, and so exhibit the ME effect only at low temperatures [258].

Attractive alternatives are hybrid or composite systems where a ferromagnetic (FM) and ferroelectric (FE) compound are artificially assembled, making use of the magnetostrictive and piezoelectric properties that these materials possess to generate the required coupling. All pure substances, including ferromagnetic materials exhibit *magnetostriction* [51]. Magnetostriction is the changing of a material's physical dimensions in response to changing its magnetisation (in other words, a magnetostrictive material will change shape when it is subjected to a magnetic field)[259]. Ferroelectric materials display piezoelectric properties and include the lead titanates, lead zirconates, lead zirconate titanates (PZT), barium titanates, barium tantalate and lead magnesium niobates.

In such composites, the ME arises from the product of the magnetostrictive ef-

fect (magnetic/mechanical effect) in the magnetic phase and the piezoelectric effect (mechanical/electrical effect) in the ferroelectric phase [260]. An applied magnetic field thus induces an electric field, and an applied electric field induces a change in magnetic permeability in the composite [261].

In the case of the direct effect, ME_H , when a magnetic field is applied to the composite the magnetostrictive material is strained and changes its shape. The strain induces a stress on the piezoelectric which generates the electric field [261][262]. In the converse effect, ME_E, when an electric field is applied to the piezoelectric material strain is produced in it, which is transferred as stress to the magnetostrictive material. This causes the change in magnetic permeability of the material [263].

The ME response is described by the fundamental ME parameter known as the ME susceptibility (α_{me}), given as:

$$\alpha_{me} = \frac{\Delta P}{\Delta H} \tag{5.6}$$

in units of (s/m), where P is the polarization and ΔH is the applied magnetic field [264].

The composite approach allows for flexibility in tailoring the ME response through the choice, ratio and microstructure of the constituents. Room temperature ME coupling co-efficients have been achieved that exceed the low temperature values found in single phase compounds by three to five orders of magnitude [265]. As an example, laminate composites consisting of magnetostrictive $Tb_{1-x}\ Dy_xFe_2$ (or Terfenol-D) and piezoelectric $PbZr_{1-x}Ti_xO_3$ (PZT) offers a high α_{me} in the 10^{-8} s/m region [247] compared to α_{me} of 2 to 3×10^{-12} s/m offered by the single phase Cr_2O_3 crystals [266]. Composite magneto-electric multi-ferroics could find uses in attenuators, filters, field probes and data recording devices based on electric control of magnetisation and vice versa. Other applications include electric current sensors and magnetic field sensors [267].

Though much work on MF composites has been concentrated on bulk materials,

the focus has now turned to thin film nanocomposites, which would provide more degrees of freedom, such as lattice strain or interlayer interaction to modify ME behaviour [268][269].

5.6 Magneto-electric coupling mechanisms

There are three main coupling mechanisms between the ferroic order parameters that are widely explored: interface charge mediated coupling , exchange bias mediated coupling and strain mediated coupling [270][271]. Each one is outlined below with the latter mechanism (strain mediated coupling) more directly related to the work described here.

5.6.1 Interface charge mediated coupling

Interface charge mediated coupling is a carrier-mediated mechanism and occurs at the interface between a dielectric insulator and a magnetic metal. As an example, for a structure FM ∥ non polar dielectric ∥ FM (Fig 5.6); if an external electric field is applied free carriers accumulate at the capacitor plates. Negative charges accumulate at one end of the dielectric, and positive charges at the other end. Spin up electrons of the FM accumulate at the positive side of the dielectric whilst there becomes a depletion of spin up electrons from the negative side of the dielectric. In metallic systems, the materials' intrinsic magnetic properties are primarily determined by unpaired electrons in the d-orbital with energies close to the Fermi energy [254][73]. Theses properties will be affected by changing the electron density at the Fermi energy under an applied field. A change in magnetisation in the metal at the interface will be induced by the field [270].

5.6.2 Exchange bias mediated coupling

Exchange bias mediated coupling is displayed in multi-ferroic materials that couple antiferromagnetic and ferroelectric behaviour [272]. $YMnO_3$ and $HoMnO_3$ are examples of such materials [272][273]. A good example to describe exchange bias mediated coupling is $BiFeO_3$ (BFO). BFO is a very rare room temperature multiferroic material with a high ferroelectric Curie temperature (1143 K)[274] and a

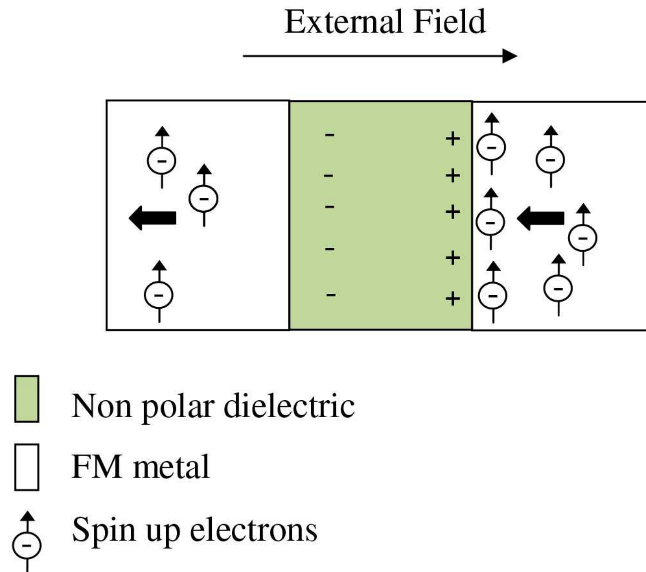

Figure 5.6: Carrier mediated mechanism.

high antiferromagnetic Néel temperature (673 K) [275]. Two successive coupling interactions are exploited. The first is the coupling interaction that exists within the BFO between the ferroelectric (FE) and antiferromagnetic (AF) orders in which antiferromagnetic domains can be switched by switching the ferroelectric polarization [276]. Chu et al. [277] and Lebeugle et al. [274] both showed that with an electric field the antiferromagnetic domain structure of BFO can be changed. The second coupling interaction is the well known exchange coupling between a ferromagnet (FM) and the AF at the interface. So, for a structure comprising a ferromagnet on top of BFO; if the AF domain structure of BFO is altered by an electric field, this in turn alters the magnetisation of the FM [277]. Being able to control the AF domain structure is considered an interesting alternative to conventional current driven magnetic switching of spin valves [278].

5.6.3 Strain mediated coupling

In FM/FE hybrids an electric field can induce elastic strain in the ferroelectric material via the inverse piezoelectric effect or via ferroelectric domain reconfiguration. This strain is mechanically transferred to the FM layer next to the FE. In the FM film, inverse magnetostriction modifies the magnetic anisotropy, thus enabling electromechanical magnetization control [279][280][281]. FM complex oxides and common FM materials have been used to realise such FM/FE hybrid structures in order to investgate this coupling interaction. Example oxides and FM materials are

$La_{1-x}Sr_xMnO_3$ [282][283], $SrRuO_3$ [284], $CoFe_2O_4$ [285][286], Fe [287], CoFe [288] and Ni [289][290].

Chapter 6

Characterisation techniques

The characterisation of thin film properties such as structural and magnetic properties is important not only to understand the underlying physics of the material or structure, but also to guide in the search for ideal growth conditions. In this chapter the instrumentation used to characterise the samples prepared in Chapters 7 and 8 is reviewed.

6.1 Vibrating sample magnetometry

The characteristics of magnetic materials are best described in terms of their hysteresis loop. A common method for measuring hysteresis loops is by Vibrating sample magnetometer (VSM).

The working principle of VSM is based upon Faraday's law of induction which tells us if the magnetic flux through a coil is changed, a voltage will be produced in the coil (induced e.m.f) [291]. In addition, how fast the flux is changing is important, a quick change induces more e.m.f than a gradual change. So by measuring this voltage, information about the changing magnetic flux is obtained. A schematic of a typical VSM is shown in Fig. 6.1.

A sample, typically a circular disc, is mounted onto one end of a non-magnetic rod and placed in a uniform magnetic field, which magnetises the sample. The other end of the sample rod is mounted in an electromechanical transducer. The transducer is driven by a power amplifier which itself is driven by an oscillator at a fixed frequency. The sample is mechanically vibrated in a vertical direction at a fixed

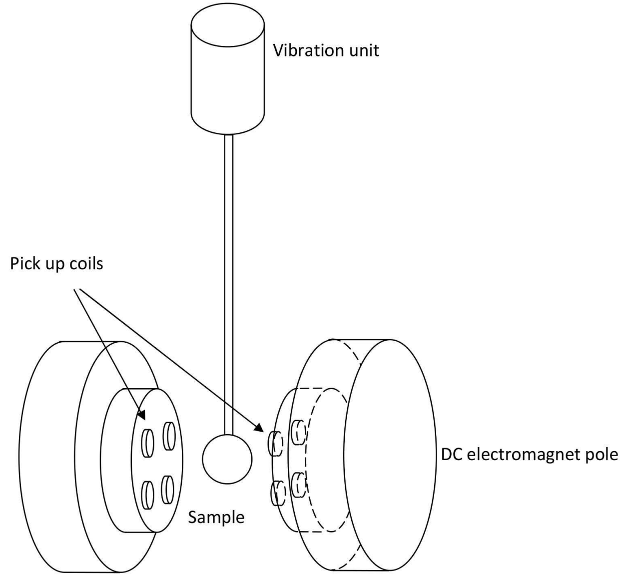

Figure 6.1: Schematic of a vibrating sample magnetometer.

frequency [292]. The magnetic stray field from the sample (which is proportional to the sample's magnetic moment) changes as a function of time so altering the magnetic flux through the coils. The changing magnetic flux induces an alternating voltage signal in the stationary sensing coils that is proportional to the magnetic moment of the sample [291]. The vibrating sample induced signal in the pick-up coil system is fed to a differential amplifier. The output of the differential amplifier is subsequently fed into a tuned amplifier and an internal lock-in amplifier that receives a reference signal supplied by the oscillator. The output of this lock-in amplifier is a DC signal proportional to the magnetic moment of the sample being studied [293].

6.1.1 Theory of VSM

According to Faraday the induced voltage, ϵ, in a single winding of a sensing coil is given by equation 6.1:

$$\epsilon = -\frac{\Delta\phi}{\Delta t} \tag{6.1}$$

where $\Delta\phi$ is the change in flux that is responsible for the induced voltage in a certain time interval, Δt [71]. The negative sign comes from the fact that the e.m.f induced in the coil acts to oppose any change in the magnetic flux (Lenz's law) [294].

The response of a material to an applied magnetic field is called its magnetic induction, **B**. The magnetic induction, **B**, is the same as the density of flux *inside* the medium [57] so *within* a loop of flat surface area A with N number of coils, **B** inside the coils can be written as:

$$\mathbf{B} = \frac{\phi}{AN}. \tag{6.2}$$

Faraday's law can be re-written as:

$$\epsilon = -NA\left(\frac{\Delta\mathbf{B}}{\Delta t}\right). \tag{6.3}$$

When a sample is placed in a uniform field, **H**, it will be magnetized and have the magnetization **M**. The magnetic flux density **B** near the (ferromagnetic) sample is now:

$$\mathbf{B} = \mu_0\left(\mathbf{H} + \mathbf{M}\right) \tag{6.4}$$

where μ_0 is the permeability of free space, **M** the magnetization of the medium, and **H** the applied field. So if **H** is constant:

$$\frac{\Delta\mathbf{B}}{\Delta t} = \frac{\Delta\mathbf{M}}{\Delta t}. \tag{6.5}$$

Magnetisation is defined as the magnetic moment, **m**, per unit volume, v:

$$\mathbf{M} = \frac{\mathbf{m}}{v}\,\frac{(emu)}{(cm^3)}. \tag{6.6}$$

As the sample is vibrated, the change in **B** induces a voltage which is proportional to **m**.

Vibrating sample magnetometry has been used extensively in the characterisation of samples produced during the work of this thesis (see Chapter 7). A MicroSense Model 10 Vector VSM with a maximum applied field of 20 kOe has been

used for measuring the magnetic properties of samples along both in-plane and out of plane directions. The EasyVSM software was used for the measurements. Using this VSM the vector coil noise can be as low as 5 micro-emu without any signal averaging and 0.5 micro-emu when the signal is averaged 100 times [295]. Calibration of the vibrating sample magnetometer is done by measuring the signal of a pure Ni standard of known the saturation magnetic moment placed in the saddle point. At the saddle point, the sample is located symmetrically with respect to the detection coils [293].

6.2 Magneto-optical Kerr effect magnetometry

A Magneto-optical Kerr Effect (MOKE) magnetometer is used extensively to characterise magnetic materials, especially magnetic thin films, by providing information in the form of a hysteresis loop. The principles of the MOKE magnetometer are based on the magneto-optic (MO) effects characterised by the Kerr effect. The magneto-optic effects observed are proportional to the magnetisation, M, of a sample. It is an important technique used to study surface magnetism since it is highly sensitive to the magnetisation within the skin depth region, which is typically 10 to 20 nm for most metals [296].

6.2.1 Magneto-optic effect

The magneto-optic effect concerns the interaction of light (electromagnetic radiation) with birefringent materials, including magnetic materials. Birefringence is defined as the difference between the refractive indices in two planes [297][298]. That is; the speed of a propagating light wave transversing a material is not the same in all directions (optical anisotropy) but is dependent upon the direction and polarization of the light waves transversing the material, resulting in different refractive indices. In magnetic materials the optical anisotropy is due to the magnetisation within surface domains, which can be altered by external forces such as magnetic fields.

There are two important and related magneto-optic phenomena. These are the Kerr effect and the Faraday effect.

6.2.2 Magneto-optic Kerr effect

The Kerr effect is concerned with the interaction of plane polarised light with a material subjected to a magnetic field. This interaction can produce several effects, including the rotation of the polarised light, introduction of ellipticity in the reflected beam and a change in the intensity of the reflected beam [299].

The Kerr effect is similar to the Faraday effect with the difference in that the Faraday effect corresponds to the plane of polarised light being rotated as it is transmitted through a material subjected to a magnetic field, whereas the Kerr effect is associated with a reflection geometry. It is convention to refer to effects in reflection as Kerr effects and in transmission as Faraday effects.

The MO effect has become a powerful method used for studying the magnetic properties of ultra thin and multilayer films. For example, the MO effect can be used to observe magnetic domains by use of an MO microscope [300][301]. Another important use for the MO effect is the determination of normalised magnetisation loops of magnetic thin films by use of a MOKE magnetometer.

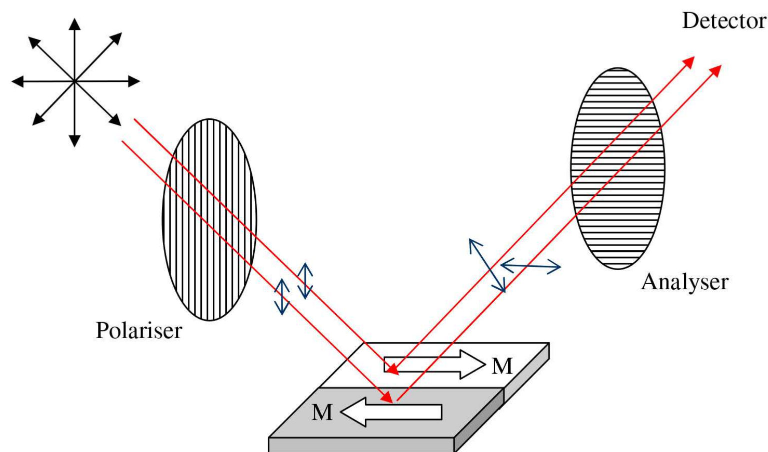

Figure 6.2: Principle of the magneto-optic Kerr effect.

To observe the Kerr effect, radiation from a light source passes through a polarizer (Fig. 6.2). The resulting plane polarized light beam is rotated on *reflection* from the surface of the magnetic material. Different orientations of magnetic domain moments give rise to different rotations of the polarization plane. If for example, for a material containing two domains with antiparallel magnetisations, the light

incident on one domain is rotated in the opposite direction from that incident on the other domain. So, if an analyser is oriented such that the light reflected from the first domain is allowed to fully emerge, then the plane of polarized light reflected from the other domain is not aligned with the analyser, and transmission is reduced [57]. In magneto-optical microscopy the change in the polarisation state of the reflected light can be detected by means of an analyser in an optical relection polarisation microscope [302]. The rotation of the plane-polarised light is converted into a domain contrast that can be enhanced by digital image processing.

MOKE magnetometers provide data that can be presented in the form of a normalised hysteresis loop. For a magnetic thin film, the film is placed in a uniform magnetic field and the magnetic field is swept. A laser beam is reflected off the surface of the film into a photodector via an analyser. The polarisation of the relected beam will be altered depending on the strength of the magnetisation of the film. Since the modification of the light polarisation state of a magnetic material is proportional to the sample magnetisation [303], a hysteresis loop can be constructed based on the intensity of the polarised light reflected and the strength of the magnetisation [304]. Therefore, MOKE is used to measure the hysteresis loops of thin magnetic films by studying the light intensity as a function of applied magnetic field.

6.2.3 Operating geometries

There are three main operating geometries for the MOKE: longitudinal, transverse and polar, as shown in Fig. 6.3. The three orientations are defined in terms of the direction of the magnetisation vector, $\mathbf{M}$, with respect to the surface of the material and the plane of incidence of an incident optical beam. The longitudinal and transverse modes are used to study samples exhibiting in-plane anisotropy, whereas polar mode is used to study samples exhibiting out of plane anisotropy.

In the longitudinal orientation the magnetic field is parallel to both the plane of incidence and the sample surface. In the transverse case the magnetic field is normal to the plane of incidence and parallel to the sample surface. In the polar geometry the magnetic field is applied parallel to the plane of incidence and normal to the sample surface (see Fig. 6.3).

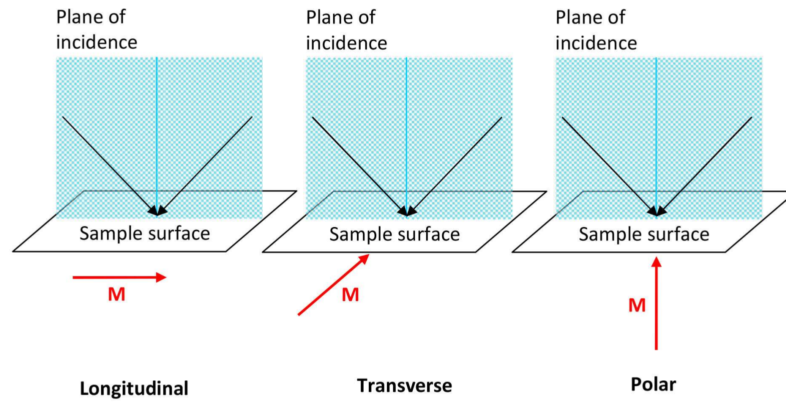

Figure 6.3: Longitudinal, transverse and polar MOKE geometries.

A MOKE instrument, designed and built by M. Vopson at National Physical Laboratory (NPL), has been used in this thesis to study the magnetic properties of ferromagnetic thin films as part of the multi-ferroic investigations (see Chapter 8). A schematic drawing of the set up is shown in Fig. 6.4.

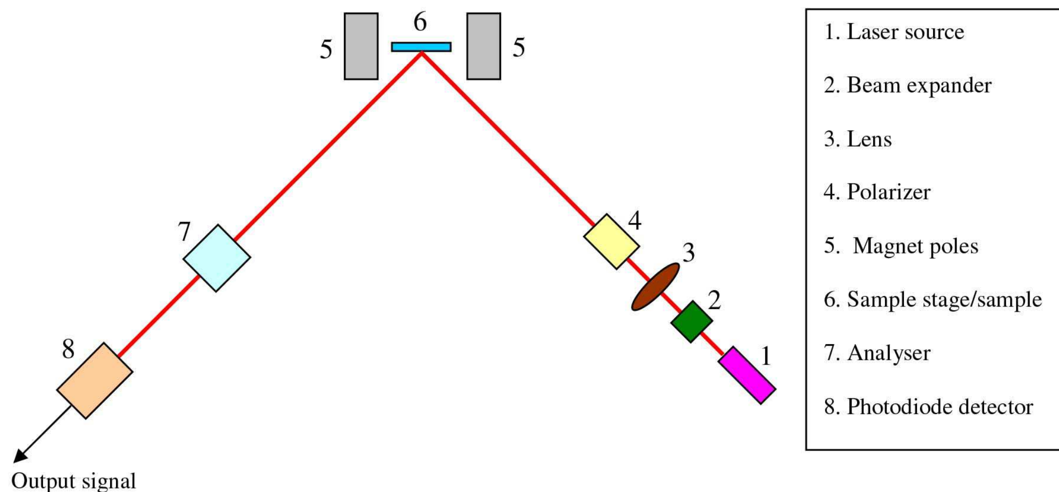

Figure 6.4: Schematic of MOKE measurement setup.

The laser source is a red HeNe laser of wavelength 632.8 nm (Melles Griot). The focused laser beam passes through a Glan-Thompson polarizer (Melles Griot) with an extinction ratio of 5 x 10-5 which produces a high degree of polarization. The beam is reflects off the sample and then transmits through an analyser. Detection technique is longitudinal MOKE via lock-in detection. The continuous wave laser beam is modulated by a beam chopper at around 1 kHz frequency and the reflected

signal is measured via lock-in detection using a SR830 Stanford Instruments Lock-in amplifier.

A standard electromagnet powered by a bi-polar power 1000W Kepkoo supply generates magnetic fields calibrated by a Hall probe sensor (Magnet Physik). The magnetic field control, intensity measurements and subsequent data collection were co-ordinated with a computer installed with data acquisition boards (DAQ) and LabVIEW software (National Instruments). The magnetic power supply and lock-in amplifier were controlled with the computer via a General Purpose Interface Bus card.

6.3 X-ray diffractometry

Diffraction is the interference that appears between electromagnetic waves as a result of an object in their path [305]. Diffraction occurs when the dimensions of the diffracting object are similar to the wavelength of the radiation wave.

X-Ray Diffractometry (XRD) is a powerful tool for studying the crystal structures of materials [306]. It is a fast, non-destructive technique and sample preparation is simple. X-rays are used to interact with a crystalline solid to generate a diffraction pattern (varying patterns of intensity are produced). Each crystalline solid has a unique x-ray diffraction pattern. X-rays are of similar wavelengths to the size of atoms, therefore it is used to explore within crystals. A lot of information can be gained, for example, the crystal size, internal elastic strains, the preferred orientations of crystallites (texture) and the degree of crystallinity, and the average spacings between layers or rows of atoms, which can lead to the determination of the crystal structure of unknown materials and phases. The wavelength is fixed and the variation of intensity with direction is measured, i.e the scattering of monochromatic radiation is measured.

6.3.1 Theory

The atoms in a crystal are arranged in an ordered periodic pattern. It is the electrons in the atoms that interact with the incident x-rays and scatter (diffract) them.

When the rays emerge they can interfere with one another in either a constructive or destructive manner.

Constructive interference occurs when the waves are in phase with one another, that is, their crests and troughs occur in exactly the same position [305]. Another way of saying this is they are out of phase by an integer number of wavelengths, $n\lambda$, where n = 1, 2, 3 etc. Their amplitudes will add together to produce a resultant wave of higher amplitude leading to well defined diffracted x-ray beams leaving the sample.

Destructive interference occurs when waves are out of phase with one another by a non-integer number of wavelengths leading to the reduction of the amplitude of waves, in the extreme case the resultant wave will have no amplitude and be completely destroyed [305].

W. L. Bragg [307] showed that when an x-ray beam hits a crystal, every diffracted beam that can be produced by an appropriate orientation of the crystal can be regarded geometrically as if it were a reflection from sets of parallel planes passing through lattice points [148]. This is pictured in Fig. 6.5.

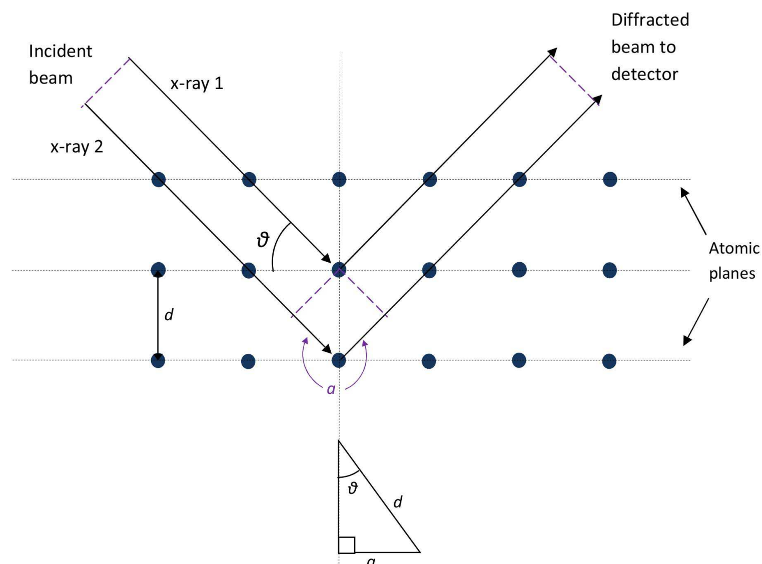

Figure 6.5: Diffraction of x-rays by planes of atoms. The blue circles represent atoms.

The figure shows an x-ray beam of angle θ incident on a plane of atoms, separated by the interplanar spacing (the spacing between atomic planes), d. The reflection of the x-rays waves by the adjacent planes gives the interference effects. The angles of incidence and reflection are equal. X-ray 1 will reflect off the upper plane, while x-ray 2 will reflect off the plane below. However, x-ray 2 travels deeper into the structure than x-ray 1. The extra distance x-ray 2 travels is denoted a. As it's reflected beam also travels further by a distance of a, the total further distance travelled by x-ray 2 is $2a$. If this distance $2a$ is equal to an integral number of wavelengths ($n\lambda$), then x-rays 1 and 2 will be in phase on their exit from the crystal and constructive interference will occur. A reflected beam of maximum intensity will result.

If the distance $2a$ is not an integral number of wavelengths, then destructive interference will occur and the waves will not be as strong as when they entered the crystal. A reflected beam with lower intensity will be observed. Thus, the condition for constructive interference is: $n\lambda = 2a$. From trigonometry the distance $2a$ can be deduced in terms of the d-spacing between atomic planes to be $a = dsin(\theta)$ or $2a = 2dsin(\theta)$. Bragg expressed this condition in an equation:

$$n\lambda = 2dsin(\theta) \tag{6.7}$$

which is known as **Bragg's Law** [308].

If the wavelength of the x-rays is known and the angle of the diffracted x-rays can be measured, the spacing between the atomic planes can be calculated using Bragg's Law. This spacing, d, is known as the d-spacing; $d = n\lambda/2sin(\theta)$. This diffraction will only occur if the rays interfere constructively when they emerge, and this will only occur at the appropriate values of n and at certain angles known as Bragg angles θ [148]. The 2θ values where diffractions are possible are determined by the unit cell dimensions. Exposing different atomic planes of the sample to the x-rays and obtaining the d-spacing values it is possible to deduce information on the crystal structure and size of the unit cell.

6.3.2 Diffraction measurements

An x-ray diffractometer examines the reflection of x-rays from crystals at various angles. A common diffractometer arrangement is shown in Fig. 6.6 and is known as the Bragg Brentano geometry [151]. The sample is stationary in the horizontal position, the x-ray tube and the detector both move simultaneously over the angular range, θ. The theorem of a circle is used to focus the x-rays [309].

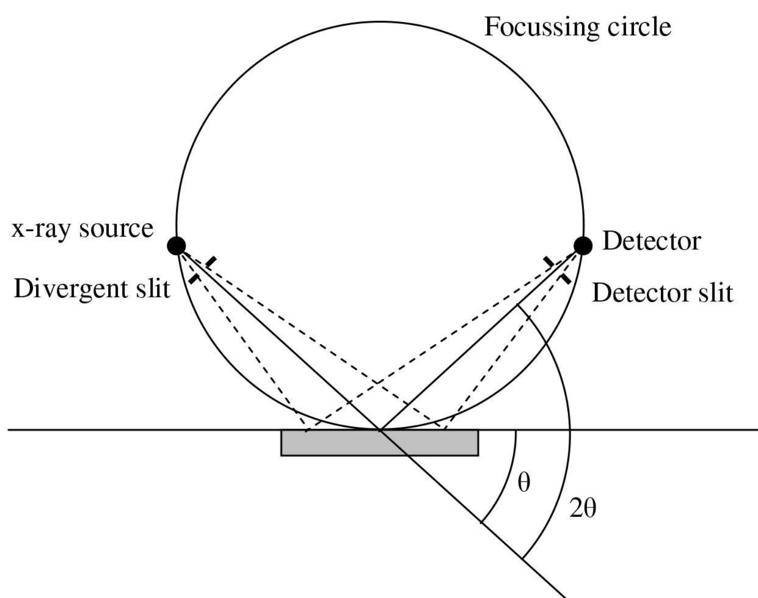

Figure 6.6: Bragg Brentano focusing geometry of the diffractometer.

Bragg found that very strong reflections occurred at certain angles (Bragg angles) [148]. According to Bragg's Law these reflections depend on the spacing of the planes of atoms inside the crystal. By changing the angle of the incident x-rays, the reflections at different angles from the different planes of the crystal are measured and so the angles where diffraction occurs can be found. Each of these angles will correspond to a different spacing between atomic planes (d-spacing) and so the arrangement of atoms can be worked out [310]. The angle of diffraction, 2θ (angle between the incident beam and the detector angle), is plotted against the detector response. The detector response is the x-ray intensity in counts/second. A series of peaks (diffraction peaks) can be produced from this plot (the diffraction pattern), which correspond to the d-spacing and so the d-spacing obtained from the plot can be calculated using the Bragg equation.

The diffraction pattern can also be used for phase identification by searching

and matching the pattern (peak positions and intensities) to a library database of known diffraction patterns of structures such as the Powder Diffraction File (PDF) which is maintained by the International Center for Diffraction Data (ICDD) [151].

The key features of a diffraction pattern are the number of peaks, the positions of the peaks and the intensities of the peaks [311]. The number of peaks is related to the symmetry of the unit cell, with fewer peaks signifying higher symmetry [150]. The d-spacing between diffracting planes of atoms determines the peak positions. The intensities of the peaks are determined by the distribution of electrons in the unit cell [312]. The highest electron densities are found around atoms, therefore, the intensities are related to the kind of atoms (lighter atoms scatter x-rays weakly, whilst heavy atoms scatter x-rays more strongly) and the location of the atoms in the unit cell. Planes going through areas with high electron density will reflect strongly, planes going through areas with low electron density will give weak intensities.

6.3.3 Crystallite size

The width of a diffraction peak can give information on the crystallite size. By using the Scherrer equation (Equation 6.8), the crystallite size can be estimated for a stress free film after instrumental factors have been deconvoluted from the peak,

$$\beta = \frac{k\lambda}{t cos\left(\theta\right)} \tag{6.8}$$

where β is the width of the x-ray beam at half the maximum intensity (FWHM), k is the crystallite shape correction factor (0.9 is usually used when the shape is unknown), λ is the x-ray wavelength, θ the Bragg angle and t is the mean size of the crystallite.

In this work a Bruker D8 Advance x-ray diffractometer (with DIFFRAC.SUITE software) is used to study the phases of FePt and FePtN and to estimate the crystallite size.

6.4 Atomic force microscopy

Atomic force microscopy (AFM) belongs to a family surface imaging techniques known collectively as Scanning probe microscopy (SPM). It is a technique that allows us to “view” the microscopic features of a surface. SPM techniques rely on a very sharp probe interacting with a sample surface measuring a local physical property to construct an image of the surface [313].

The first of the SPM techniques was developed by Binnig et al. [314] in 1981; this was the scanning tunnelling microscope (STM). The principle of the STM is based on electron tunnelling between two electrodes of which one is a sharp metal probe tip and the other a conducting sample. When the electrodes are very close to each other, i.e. a few atomic radii, electrons can tunnel through the potential energy barrier. The resulting electric current passing between the electrodes can be measured [315]. Electrically biasing the tip electrode relative to the sample allows more electrons to flow in one direction than in the other, so a net current flow is established. Height changes in the sample can be sensed with atomic-scale resolution. The major drawback for STM is the requirement for the sample to be conducting or semiconducting.

Four years after the introduction of the STM, Binnig et al. [316] proposed the AFM , which allows scanning of non-conducting samples. Instead of measuring the tunnelling current, AFM measures the forces between a fine probe tip and a sample. The forces that exist between the probe and the sample are predominantly Van der Waals forces (VdW), which can either be attractive or repulsive (probe-sample distance dependent) [317].

6.4.1 Optical lever detection

The interacting forces between the probe and sample can cause the cantilever on which the AFM tip is ‘mounted’ to be deflected. The deflection is most often detected by the optical cantilever scheme, as shown in Fig. 6.7. A laser beam is bounced off the back of the cantilever and reflected onto a position sensitive four section photodiode detector. Any deflection of the cantilever causes the laser to change position on the photodiode array, changing the voltage output of the photo-

diode. The voltage measured on the photodiode in the vertical direction is defined as the difference voltage between the top and bottom photodiode output, (A+B)-(C+D)/SUM, where SUM is the total signal output, i.e. A+B+C+D [318]. The voltage measured on the photodiode in the lateral direction is defined as the difference voltage between the left and right photodiode output, (A+C)-(B+D)/SUM. These normalised difference values are used as a measure of the degree of vertical and lateral deflections of the AFM probe and can be used to construct an image. The difference signal is very sensitive to cantilever deflection, and therefore to the tip-sample interaction [319].

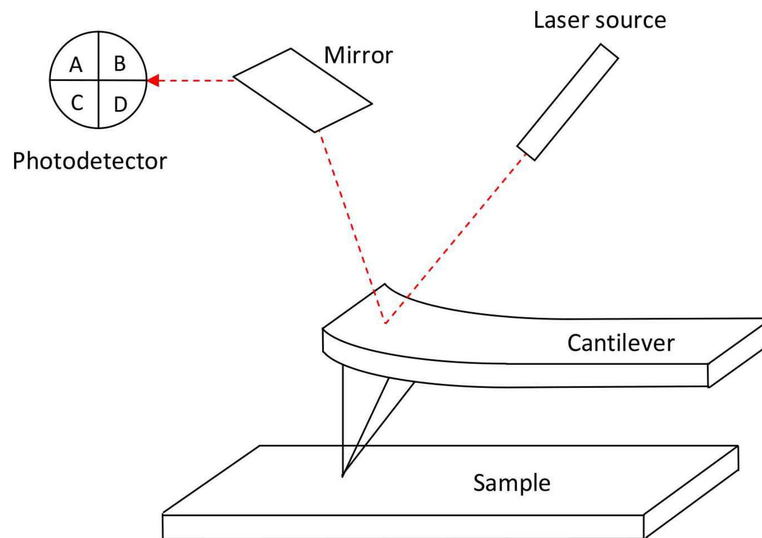

Figure 6.7: Concept of AFM and optical lever detection.

6.4.2 AFM modes

Different modes exist in AFM. They can be divided into those modes which measure the static deflection of the cantilever, and those that measure the dynamic oscillation of the cantilever. There are three primary modes: contact, non-contact and tapping.

Contact mode

In contact mode the probe makes a soft physical contact with the sample. At this close contact the probe experiences repulsive VdW forces. This force, F, and the affect it has on the cantilever's motion (deflection), x, can be described using Hooke's law where k is the spring constant ($F = -kx$). As the probe tip scans, variations

in the sample (height for example) cause deflections of the cantilever.

The deflected signal is monitored by the optical lever and a piezo-scanner adjusts its z-height via a feedback loop to maintain a constant cantilever deflection (and hence keeping the force between the probe-sample constant) [320]. A z-piezo-scanner moves to maintain this constant deflection and the amount of movement by the scanner is taken to be the sample topography [319].

Very high resolution surface images are obtainable using contact mode. Lateral resolution of <1 nm and height resolution of <1 Å can be obtained [321][322] (for comparison, the resolution of SEM is 5 nm and TEM is 0.1 nm [320]). It is the quickest of all the modes since the deflection of the cantilever leads directly to the topography of the sample. However, soft samples are easily damaged.

Non-contact mode

The probe does not make contact with the sample surface but is oscillated (usually with an additional piezoelectric element) at its resonant frequency above the sample (tens to hundreds of angstroms above). During scanning the forces acting between the sample and the tip are now attractive VdW. These forces cause changes in the cantilever resonant frequency, resulting in a change in the amplitude and phase of the oscillation. The oscillation is monitored by the optical lever and the piezo-scanner adjusts the z-height via the feedback loop to maintain the probe at a fixed distance from the sample, just as in contact mode [320]. The change in amplitude or in phase can be detected and used in the feedback circuit to maintain the tip at a fixed distance from the sample surface. The very low force exerted on the sample means soft and fragile samples can be scanned and the lifetime of the probe is extended compared to contact mode. The resolution in non-contact mode can reach atomic dimension [323][324]. However, measurements can be more difficult than using contact mode as most surfaces of samples in air are covered with a contamination layer, such as water. The surface tension of the contamination layer can pull the tip downwards and trap the tip which can interfere with the oscillations [325].

Tapping mode

Tapping mode overcomes the major drawbacks of contact and non-contact modes. It eliminates the frictional forces caused by contact mode and the adhesive meniscus forces from surface contammination layers in non-contact mode [319]. In tapping mode, the probe is oscillated with a large amplitude, typically in the range 1 to 100 nm and the feedback is usually based on the amplitude signal. During a scan the tip of the probe strikes the surface on each oscillation cycle then detaches from the surface; it "taps" the surface. In this mode the forces experienced by the probe are both attractive and repulsive. When the probe contacts the surface, the cantilever oscillation is reduced due to the energy lost caused by the tip contacting the surface. In a similar way to deflection in contact mode, the amplitude signal may be used as to illustrate surface features of a sample. In addition to height and amplitude data, the phase-shift may also be saved as an image.

In this thesis, the Veeco INNOVA scanning probe microscope has been used, in tapping mode, for studying the surface morphology of FePt and FePtN thin films (Chapter 7). The NanoScope analysis software (Veeco Instruments Inc.) was used for data analysis.

6.5 Magneto-resistivity measurements

The four point probe method is a standard technique used for making resistance measurements. The standard four point probe geometry involves four in-line probes of equal spacing contacting the surface of a sample (Fig. 6.8). A constant current, I, is made to flow between the two outer probes and the voltage created, V, is measured between the two inner probes. The average resistance, R, can then be calculated using Ohm's Law ($R = V/I$).

In Chapter 7 a four point probe has been used to determine the specific resistivity of the FePt and FePtN films. A Keithley current source is used to supply current through the outer two probes; a voltmeter measures the voltage across the inner two probes. Throughout this work, each resistivity calculation was determined from the voltage resulting from several different applied currents. A plot of voltage against

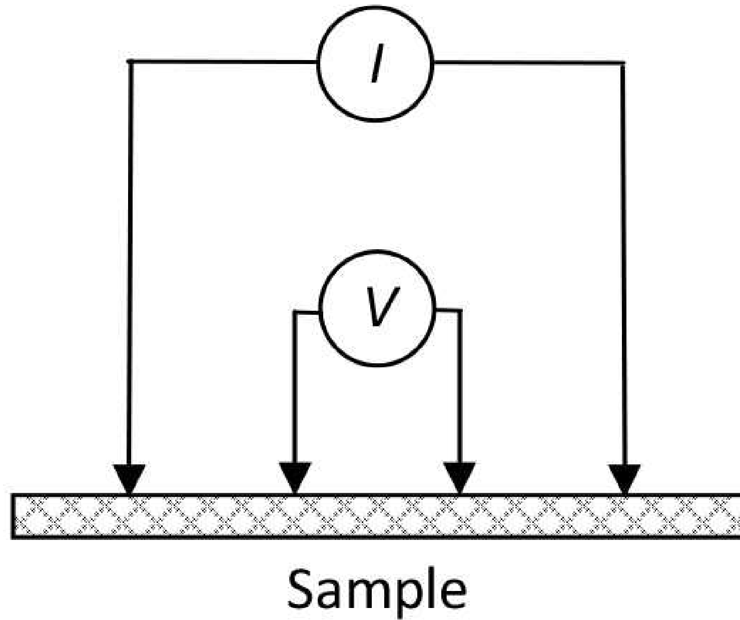

Figure 6.8: Four point probe setup.

current then yields a straight line with $gradient = sheet\ resistance/k$ where k is a geometric factor, equal to 4.53 assuming that the thickness of the thin film is significantly less than the probe tip spacing [326][327].

In Chapter 8 a four point probe method was also used for magneto-resistivity measurements. By centering the sample in between the poles of an electromagnet, the resistance with an applied magnetic field can be measured, and the magneto-resistance ratio can be calculated as follows:

$$GMR = \frac{R_0 - R}{R_0} = \frac{\Delta R}{R_0} \tag{6.9}$$

where R_0 is the resistance in the absence of a magnetic field and R is the resistance in the presence of a magnetic field (and so ΔR represents the difference in resistance when the magnetisations of the neighbouring magnetic layers are aligned in the antiparallel and parallel states).

The measurement set-up was constructed by M. Vopson (NPL) and is shown in Fig. 6.9. A four point probe measurement technique was used, with the current applied to the outer two probes and voltage measured from the inner two probes. The four point probe measurements were made using a constant current source (Kei-

theley 6221 AC/DC current source) and a digital lock in amplifier (SR830 Stanford Instruments). An AC current of 1 mA with a frequency of 777 Hz was employed. The change in resistance, ΔR, for the sample be presented as $\Delta R = \Delta V / I$ where ΔV is the potential change which is measured by a lock in amplifier and I is the current flowing through the sample. The current source was AC already and a reference signal from the current source was itself used to feed the reference to the lock-in for voltage measurements. The magnetic field was co-ordinated with a computer installed with data acquisition boards (DAQ) and LabVIEW software (National Instruments).

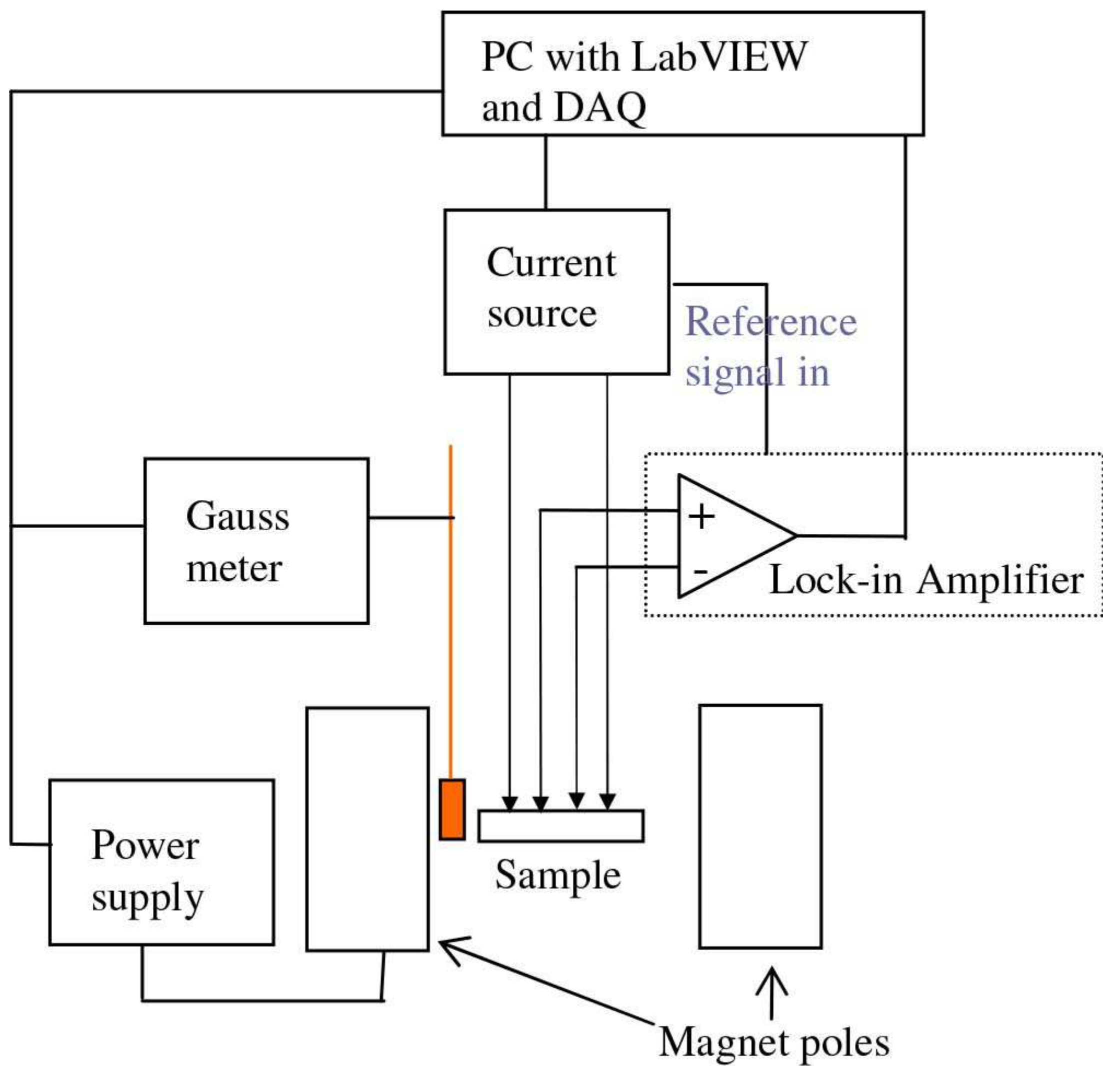

Figure 6.9: GMR measurement setup at NPL.

Chapter 7

Fabrication and characterisation of annealed FePt thin films

The HiTUS technique has been used to prepare FePt and FePtN thin films. Details of the fabrication, processing and measured properties of these films are presented and discussed in this chapter.

7.1 Introduction

The requirement for high areal density for magnetic recording is continually growing. However, there is a limit to which the areal density can be achieved by conventional Co alloy media used in current commercial perpendicular media due to thermal instabilities [328][83]. It is believed that conventional Co based perpendicular media can only support areal densities up to 1 Tb/in^2 [118]. The scaling law of recording density versus grain size requires that for recording density to further increase, grain sizes must decrease. As the grain size of current commercial perpendicular media using CoCrPt alloy approaches 8 to 10 nm [329], the magnetic direction of each grain is at risk of flipping itself due to thermal fluctuation, therefore rendering the recording data unstable. This magnetic moment instability is known as "superparamagnetism" [330].

In order to keep magnetic grains thermally stable, materials with larger magnetic anisotropy (K_u) are needed. (001) textured $L1_0$ FePt is a promising material for overcoming the thermal stability issue. Its high anisotropy of about 10^7 to 10^8

erg/cm^2 [331], high coercivity, excellent chemical stability and good corrosion resistance renders it an attractive material. The advantages of FePt over conventional CoCrPt alloy media can only be realised if FePt media with FePt columnar grains of less than 5 nm, which are (001) oriented, magnetically isolated, and have high enough anisotropy energy and high coercivity can be reliably produced. If this were achieved, areal density higher than 1 Tb/in^2 would be possible [332].

The processing routes for FePt synthesis include DC and RF magnetron sputtering [196], [123], [333], molecular beam epitaxy [333], chemical synthesis [334], gas condensation methods [335] and mechanical ball milling [336].

As a relatively new sputtering method, HiTUS has not yet been used by Plasma Quest Ltd to study magnetic materials for hard disk drive applications. Since this system has proved to enhance properties or lower annealing temperatures in other materials which usually required post-deposition annealing at high temperatures, for example the transparent conducting oxide ITO and photoluminescent ZnS:Mn [48], it is interesting to see how this system would perform on sputtering FePt. Also, by taking advantage of the ease at which reactive sputtering can be used on this system, the inclusion of nitrogen into FePt thin films to produce FePtN is also investigated; since this inclusion has been shown to improve the hard magnetic properties of FePt [189] and may provide an alternative route for the production of $L1_0$ FePt layers.

7.2 Sputtering with nitrogen

Wang et al. [189] found that introducing an appropriate amount of nitrogen to the argon during sputtering enhances the magnetic properties of $L1_0$ FePt films. In their studies the coercivities of FePtN films are always larger than those of FePt . After annealing at 600 °C for 10 mins the coercivity of $(Fe_{56}Pt_{44})_{100-x}N_x$ film is 1027 kA/m ($\approx$ 12.9 kOe) compared to 682 kA/m ($\approx$ 8.6 kOe) for $Fe_{56}Pt_{44}$. The remanence of the FePtN is also higher than that of FePt: 1.24 T compared to 0.87 T. Soft magnetic phases of iron nitride are thought to be contributing factors. On the release of nitrogen atoms from the film during annealing, vacancies and defects are left behind. This is thought to promote the transformation of FePt to the ordered phase. Reddy et al. [337] supported the findings of Wang et al. [189]. Reddy

et al. prepared FePt by ion beam sputtering. Two sets of films were produced. One set produced using argon only as the sputtering gas, and the other set using a mixture of nitrogen and argon as the sputtering gas. It was shown by XRD and Mossbauer spectroscopy that FePt films prepared with nitrogen gas in addition to argon gas transformed into the orderd fct phase from the fcc structure at a faster rate compared to the film prepared only in an argon atmosphere.

A similar study was carried out by You et al. [338]. By sputtering in a mixture of argon and nitrogen, they achieved an in-plane coercivity of 1303 kA/m ($\approx$ 16.4 kOe), which was about 20 % higher than in a film prepared in a pure argon atmosphere. This was found true only for Fe- rich compositions. The coercivities for $Fe_{50}Pt_{50}$ and $Fe_{44}Pt_{56}$ deteriorated by incorporating nitrogen. One suggestion is that this is due to the formation of antiferromagnetic $L1_2$ $FePt_3$ which would decrease the volume fraction of $L1_0$ ordered phases, causing the deterioration of magnetic properties. For the films rich in Fe, nitrogen can enhance the degree of order and preferential in-plane alignment of the c-axis, enhancing the in-plane coercivity.

The presence of nitrogen in FePt films is believed to improve the magnetic properties of the system in two ways. Firstly, the presence of soft magnetic phases of iron nitride, Fe_4N for example, which segregates at the grain boundaries of the FePt introducing an intergrain coupling mechanism between the soft magnetic nitride and the hard magnetic phase leading to a higher remanence (and coercivity) [189]. Secondly, at high temperature annealing, the escape of nitrogen yields vacancies and defects. This is thought to play a role in increasing the diffusion rate of the Fe and Pt atoms, resulting in the faster transformation of the disordered fcc FePt to the ordered fct $L1_0$ phase [337].

Actual diffusion measurements have been carried out by Phatak et al. [339] on ion-beam sputtered thin films using pure nitrogen as the sputtering gas. The volume diffusion of Fe was shown to be significantly higher in FePtN than in FePt, transforming the FePt in FePtN samples into the fct phase at a faster rate. This is probably attributed to the voids and defects produced by the out-diffusion of nitrogen. It was also shown in this study that nitrogen can hinder grain growth by

gathering in the grain boundary regions. At an annealing temperature of 673 K the crystallite size after $L1_0$ transformation was only 12 nm in FePtN compared with 27 nm in FePt films.

As mentioned in Section 4.6 a previous report by Newman et al. [146] described the development of a fabrication process for the production of homogenised, near mono-disperse, nano-particulate recording media. This two stage process involved initially co-sputtering platinum, cobalt and silicon nitride in an argon/nitrogen plasma. The group suggest that the cobalt reacts with the nitrogen in the plasma and deposits as cobalt nitride (CoN). The platinum deposits as a metallic dispersion throughout the homogeneous mix of CoN and silicon nitride. Following this creation of a precursor, rapid thermal processing of the precursor leads to the dissociation of CoN, releasing the nitrogen and promoting the reaction of Co with platinum forming CoPt nanoparticles embedded in a silicon nitride host. At temperatures of around 600 °C the transformation of the precursor into $L1_0$ CoPt was complete. CoPt media produced by this process demonstrated the ability to support ultra high density recording in the longitudinal and perpendicular modes. Newman et al. believe that by replacing Co with Fe in the production process, higher anisotropies could be achieved [146][189].

7.2.1 Silicon nitride

Nitrogen has also been used in FePt studies 'indirectly' in the form of silicon nitride (SiN). This insulating material has been incorporated as an additional material into FePt films during fabrication to create composite granular thin films [126][340]. The structure of such granular thin films consist of nanoscale ferromagnetic particles which are embedded in an insulator matrix. Silicon nitride has many useful properties such as oxidation resistance, corrosion resistance and wear resistance [341].

The magnetic properties of granular thin films are different to that of continuous metal thin films due to the magnetic particles of a granular film being isolated. Furthermore, the growth of magnetic particles can be constricted by a nonmagnetic matrix during heat treatment [342].

A heated substrate or post-thermal annealing is usually required for obtaining the ordered $L1_0$ structure of FePt. One of the side effects of annealing at relatively high processing temperature (550 °C) is the grain growth. It has been shown that grain growth can be suppressed during heat treatment by isolating magnetic grains in a nonmagnetic matrix [343] [344]. These granular films usually consist of nanoscale ferromagnetic particles which are embedded in an insulator matrix , for example SiO_2 [202], Al_2O_3 [162], B_2O_3 [345], Si_3N_4 [126], and are expected to become suitable for high density magnetic recording media due to their low noise characteristics. Furthermore, with these nano composite structures, the exchange coupling effect can be minimised to decrease the transition noise because the magnetic FePt nanoparticles are isolated.

Fang et al. [346] found that by the addition of SiN into Fe/Pt multilayers (DC and RF magnetron co-sputtering of Fe, Pt and SiN_x targets) and annealing at 700 °C for 30 mins, FePt particles can be isolated and particle size be reduced. They achieved a uniform particle distribution granular structure with an average particle size of about 5 nm. They achieved a large out of plane coercivity of 21.2 kOe and squareness of 0.75. In plane coercivity and squareness were 6.5 kOe and 0.45 respectively.

Composite films of $(Fe_{50}Pt_{50})_{100-x}(Si_3N_4)_x$ were sputtered onto silicon substrates by Kuo et al. [126] using $Fe_{50}Pt_{50}$ and Si_3N_4 targets. They demonstrated by Auger Electron Spectroscopy (AES) that the Fe and Pt diffused deeply into the Si substrate producing iron and platinum silicides at over 600 °C. The volume fraction of Si_3N_4 was found to affect the magnetic properties. At 0 vol.% of Si_3N_4, the M_s was about 750 emu/cm^3, but at 50 vol.% this value was halved to about 375 emu/cm^3. Si_3N_4 is therefore understood to be a non-magnetic phase that dilutes the magnetization of the film. Though the in-plane coercivity H_c was not found to be affected by the volume fraction, the perpendicular coercivity was. With volume fractions of 0 to 20 vol.%, H_c (perpendicular) increased from 60 to 420 Oe but then decreased again at higher volume fractions. The perpendicular values were always higher than the in plane. This may be due to the induced out of plane magnetic anisotropy by the internal stress. The variation of the coercivity with Si_3N_4 volume fraction could be explained as due to the internal stress of the interface between

Si_3N_4 and FePt phases which varies with Si_3N_4 volume fraction. When the annealing temperature was increased it was noticed that the higher the Si_3N_4 content the slower the growth and the smaller the grain size at a particular temperature. This can be attributed to the the grain growth of the magnetic phase being limited by the surrounding Si_3N_4 matrix. At 750 °C, the average grain size of pure FePt film measured by TEM images was 90 nm compared to 70 nm in the $(FePt)_{70}-(Si_3N_4)_{30}$ film. Maximum in-plane coercivity of the FePt-Si_3N_4 film was 11 kOe, a point which occurs at 30 vol.% of Si_3N_4 with the film being annealed at 750 °C for 30 mins - the average particle size of this film was about 40 nm.

The same group went on to further investigate reducing the grain size of such a FePt-SiN system by the addition of Cr to produce a nanocomposite of FePtCr-SiN [347][348]. Due to the Cr diffusion into the FePt grains and Cr being antiferromagnetic, the increase in Cr (and SiN) dilutes the magnetisation and coercivity - suggesting magnetic particle interactions are reduced. A granular $[(FePt)_{90}Cr_{10}]_{85}-[SiN]_{15}$ film with an in plane coercivity value of 3.7 kOe and magnetic particle size of about 9.5 nm was obtained after annealing at 600 °C for 30 mins. Individual $Fe_{50}Pt_{50}$, Cr and Si_3N_4 sputtering targets were used.

Ma et al. [349] used a different approach for producing the SiN matrix, by co-sputtering separate Fe, Pt and Si targets under an argon and nitrogen gas mixture gas . They found that increasing SiN content contributes towards decreasing particle size when samples are annealed and that the SiN matrix can restrain the grain size growth of FePt particles. They suggest that a disproportionate amount of Si or N doping can cause lattice distortions which damages coercivity. With the correct proportions of Si and N content, the FePtSiN films exhibit a small lattice distortion and high coercivity, up to 13.6 kOe in plane and 11.2 kOe out of plane when annealed at 700 °C for 1 hr and an average grain size of 15.1 nm was measured.

7.3 Project Introduction

Thin film materials deposited by HiTUS show significantly higher levels of densification that conventionally sputtered equivalents, with correspondingly improved physical properties. Essentially, the films are nearly 'void free' and process gas inclu-

sion is usually undetectable. The remotely generated high density plasma appears to be a key factor in producing these higher density films [35], essentially appearing to interact with the substrate and provide an additional source of energy to the thin film growth that replicates the effects of 'atomic peening' or substrate heating (though without increasing the bulk substrate temperature). Taking these strengths of HiTUS into account and the challenges facing the production of $L1_0$ FePt discussed in Chapter 3, the HiTUS technique is used to fabricate FePt to determine whether this technique can offer improvements to FePt thin film growth (for example, by reducing the ordering temperature of FePt). Previous work by various groups indicate that nitrogen inclusion into FePt films can enhance its magnetic properties. Also, the fabrication of $L1_0$ CoPt via CoN by Newman et al. [146] gives added confidence that the use of nitrogen could promote $L1_0$ ordering in FePt thin films. The deposition of FePt onto silicon substrates, with and without nitrogen inclusion is investigated. Silicon substrates are readily available and have a high tolerance to heat treatment [350].

7.4 Experimental

Using the HiTUS system and a form of co-sputtering, FePt samples of 25 nm thickness were sputtered directly onto naturally oxidised silicon wafers at ambient temperature. The particular HiTUS system allocated to this project was not equipped to carry out co-sputtering in the usual fashion, i.e. by the individual deposition control of more than one target at a time each with its own power supply. An alternative method for sputtering both iron and platinum at the same time was used and described as follows. An iron target with a diameter of 100 mm $\times$ 6 mm thick was obtained (Kurt J. Lesker) - this target size is standard for the sputter machine used. Also, a platinum disc (99.99 % purity) of 70 mm diameter was obtained (Pi-Kem Ltd). Due to financial reasons the platinum disc ordered was only 1 mm thick and so it was required to be bonded to a copper disc of 70 mm diameter $\times$ 2 mm thick (ready bonded by Pi-Kem Ltd). A 60 mm hole was machined out of the centre the iron target and used to clamp over the iron target. According to sputter yield data [28], both iron and platinum should sputter at similar rates and so the amount of iron machined out from the target was so to obtain similar unit areas of iron and

platinum exposed to the plasma. For target bonding to the target holder conductive elastomer (obtained from Kurt J. Lesker) was used.

The base pressure of the sputter chamber was 1.0 x 10^{-6} mbar. The sputtering pressure remained at 2.2 x 10^{-3} mbar after introducing high purity argon gas (99.995 %). The RF power source was fixed at 1.10 kW and target voltage at 620 V. These chosen parameters were as a result of some preliminary experiments (table of results shown in appendix A), which consisted of depositing 25 nm of FePt using four different RF and voltage combinations and subsequently measuring the hysteresis loops of the samples by VSM. The perpendicular coercivity of the sample that was deposited using 1.10 RF power and 600 V was the highest. One interesting feature of $L1_0$ FePt is its high perpendicular coercivity. This power and voltage combination gave the highest perpendicular coercivity, similar in plane and out of plane magnetisations and squareness values.

FePt samples samples of 25 nm thickness were sputtered directly onto naturally oxidised silicon wafers. Although seed layers and capping layers can be beneficial, they can also react with the main film structure [351][183], therefore for these initial studies, the structure here has been kept as simple as possible, without seed or capping layers. The deposition rate of FePt was 2.63 $\mathring{A}/s$. The deposition rates were arrived at by timing the deposition of a thick layer of FePt and measuring a step height of the film using a profilometer. This was repeated a further two times depositing two other thicknesses to check that the rate was the same in all three cases. One of the FePt samples used to work out the deposition rate (thickness 170 nm) was sent to the University of Surrey for composition analysis using Energy Dispersive X-Ray analysis. The resulting composition was analysed to have the Fe:Pt ratio of 42.43 : 57.57.

For the FePtN samples, 10 sccm of nitrogen was introduced before deposition. The sputtering pressure remained at 2.2 x 10^{-3} mbar after the flow of nitrogen and argon had stabilised. The RF power source was fixed at 1.10 kW and target voltage at 620 V. The deposition rate of FePtN was 2.69 $\mathring{A}/s$.

Following deposition, the samples were annealed in a sealed quartz tube in an argon/hydrogen mixed gas (95 % argon gas and 5 % hydrogen gas). Argon was

used as the carrier gas due to its inertness. After sealing the quartz tube, argon was allowed to flow for 30 minutes to remove any air before hydrogen was introduced. Hydrogen was used to remove oxygen and to prevent oxidation of the films, a zirconium ghetter was also used. The flow of the gases was controlled by a automatic gas flow controllers. The samples were annealed at various temperatures between 300 °C and 800 °C for 60 mins, in accordance with literature reported by groups that have annealed in a similar way [352] [176]. The samples remained in the furnace with the gases flowing until fully cooled to room temperature.

7.5 Results

This section presents the characterisation results of HiTUS prepared FePt and FePtN thin films. The characterisation techniques used have been described in Chapter 6. Magnetic properties were studied with VSM at room temperature with maximum applied field of 20 kOe. Anisotropy constants, which can be obtained by analysis of magnetisation curves, can give an indication of the level of ordering [69]. Due to time constraints on magnetic measurements, the anisotropy constants were not measured but instead the different phases of the films were characterised by XRD, with $Cu-K\alpha$ radiation of wavelength 1.54060 Å to gain an indication of the level of ordering. The crystallite size was also determined by XRD using the EVA program and Scherrer equation. Electrical properties were measured by a standard 4-point probe set-up. Finally, AFM was used to measure the surface roughness of the films.

7.5.1 Magnetic properties

The in plane ($\|$) and perpendicular ($\perp$) magnetic hysteresis loops of FePt and FePtN samples grown on silicon and post-annealed between temperatures of 300 and 800 °C are shown in Figs. 7.1 to 7.4. Both as-deposited films are characteristic of soft materials (low coercivity).

From the hysteresis loops, the following information has been extracted: coercivity (H_c), saturation magnetisation (M_s) and remanence (M_r) for both $\|$ and $\perp$. These are plotted as a function of annealing temperature in Figs. 7.5, 7.6 and 7.7

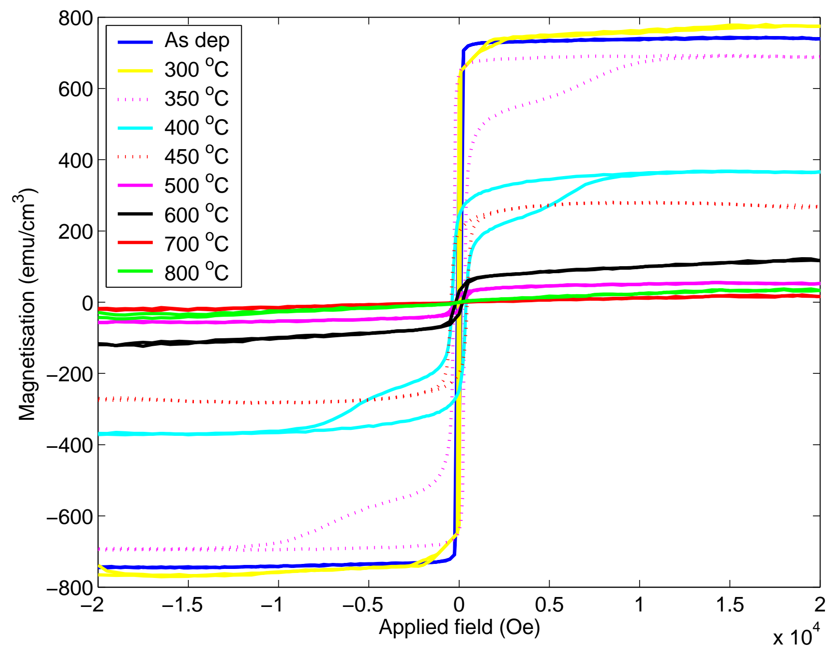

Figure 7.1: In plane VSM magnetic hysteresis loops for FePt at various temperatures.

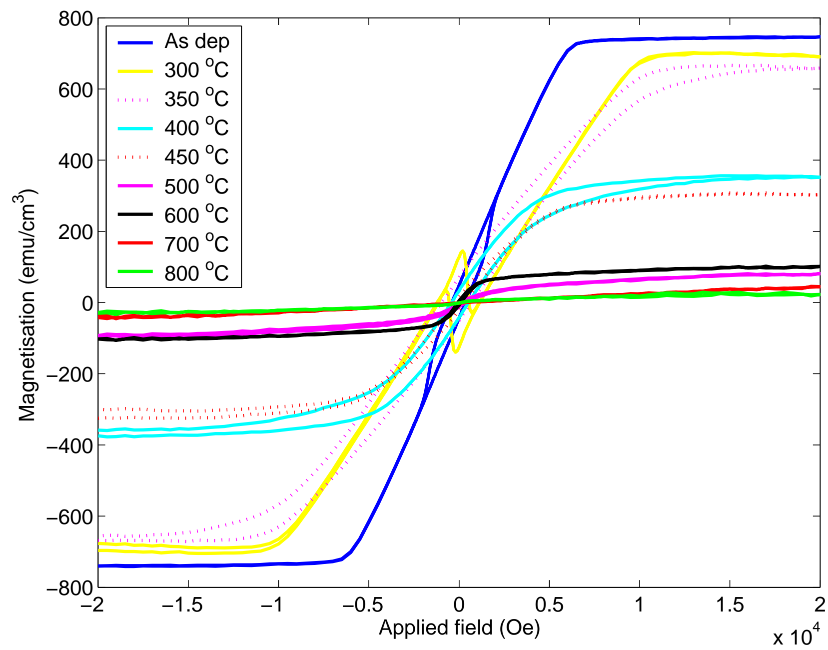

Figure 7.2: Perpendicular VSM magnetic hysteresis loops for FePt at various temperatures.

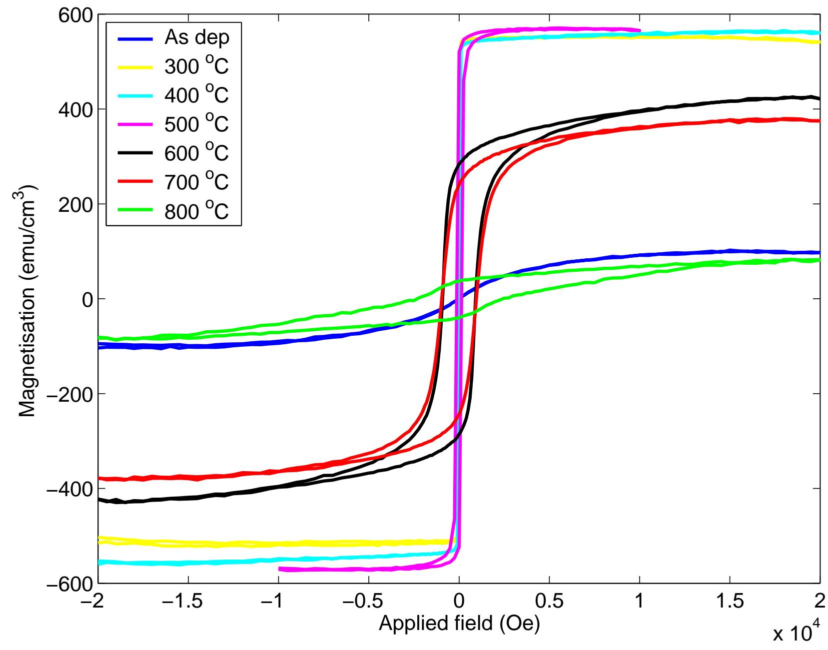

Figure 7.3: In plane VSM magnetic hysteresis loops for FePtN at various temperatures.

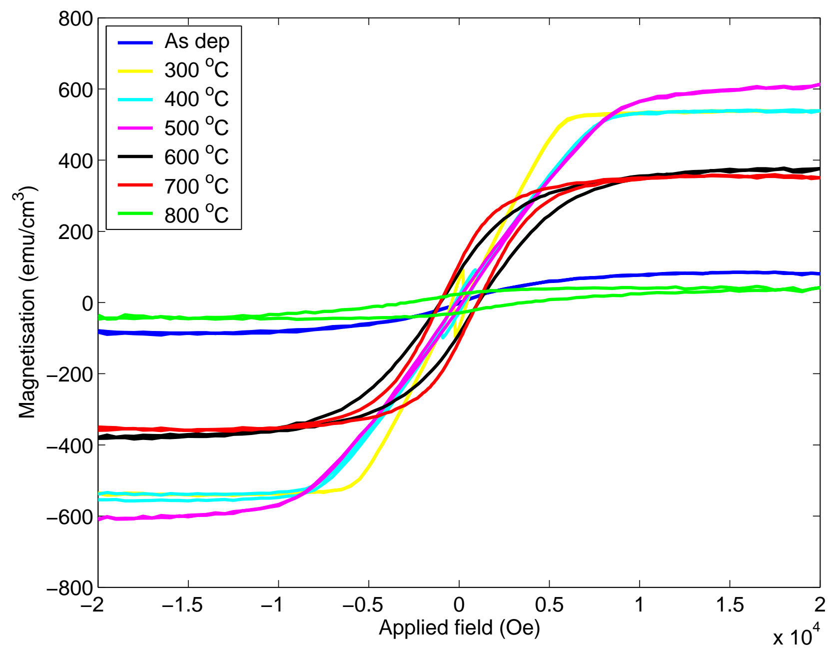

Figure 7.4: Perpendicular VSM magnetic hysteresis loops for FePtN at various temperatures.

respectively.

Coercivity

It can be seen from Fig. 7.5 (a) that the in-plane coercivity, $H_{c\parallel}$, of FePt increases from 95 Oe to a maximum of 450 Oe after annealing at 450 °C. Increasing the temperature further results in a decrease of coercivity. The initial increase and subsequent decrease in coercivity is also observed in the perpendicular measurements, $H_{c\perp}$, 7.5 (b), with an initial $H_{c\perp}$ of 380 Oe rising to a maximum of 825 Oe at 350 °C before decreasing at higher temperatures.

In literature, coercivity values of FePt samples that have been prepared without any form of substrate heating are low. Ma et al. [349] produced FePt films with less than 20 Oe coercivity. Similar low coercivity values were found by others [338] [189]. Post annealing of FePt films or film preparation at elevated temperatures improves the coercivities of the films. Xing et al. [353] co-evaporated FePt films; without annealing the coercivity was 80 Oe but after annealing at 750 °C the coercivity increased to 8 kOe. Yu et al. [157] sputtered FePt films using DC magnetron and a growth temp 375 °C and observed coercivities of 276 Oe (in plane) and 452 Oe (out of plane). Martins et al. [177] deposited FePt films at room temperature and achieved coercivities of 140 Oe (in plane) and 70 Oe (out of plane); when the films were deposited at 600 °C the coercivities were much higher - 8.7 kOe (in plane) and 8.2 kOe (out of plane). Recent publications have shown that films with a high (001) orientation achieved by depositing at temperatures above 350 °C or post deposition annealing can display out of plane coercivity values in the range of 3.8 kOe to 24 kOe [354][343][118].

Both the in-plane and out-of-plane coercivities for the nitrided samples have zero coercivity, as deposited. This indicates successful inclusion of the nitrogen into the film. $H_{c\parallel}$ steadily increases with temperature, but from 500 to 600 °C there is a large increase from 130 to 900 Oe. Another major increase is apparent from 700 to 800 °C with a maximum $H_{c\parallel}$ of 2430 Oe at 800 °C. Interestingly, $H_{c\perp}$ increases to 420 Oe at 300 °C from zero (as deposited) but then decreases and increases again. Again major increases are observed between 500 and 600 °C and 700 to 800 °C

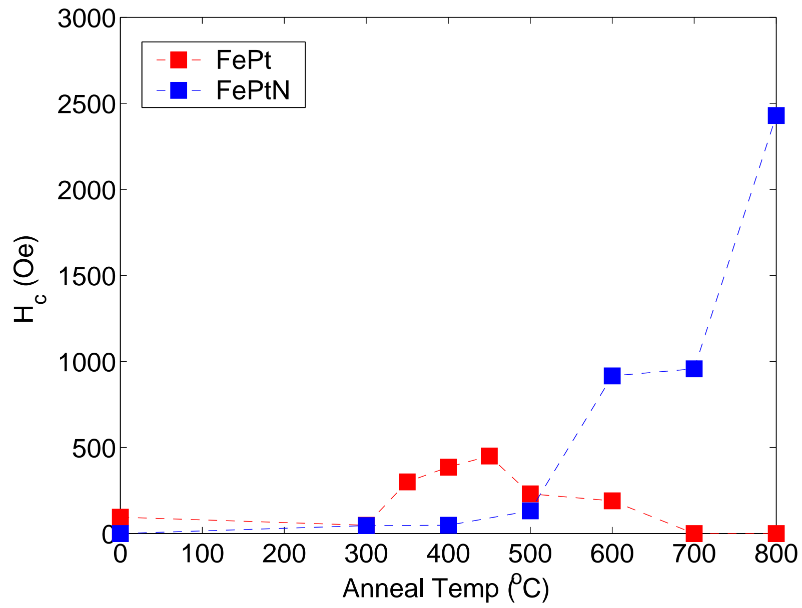

(a) In plane coercivity of FePt and FePtN

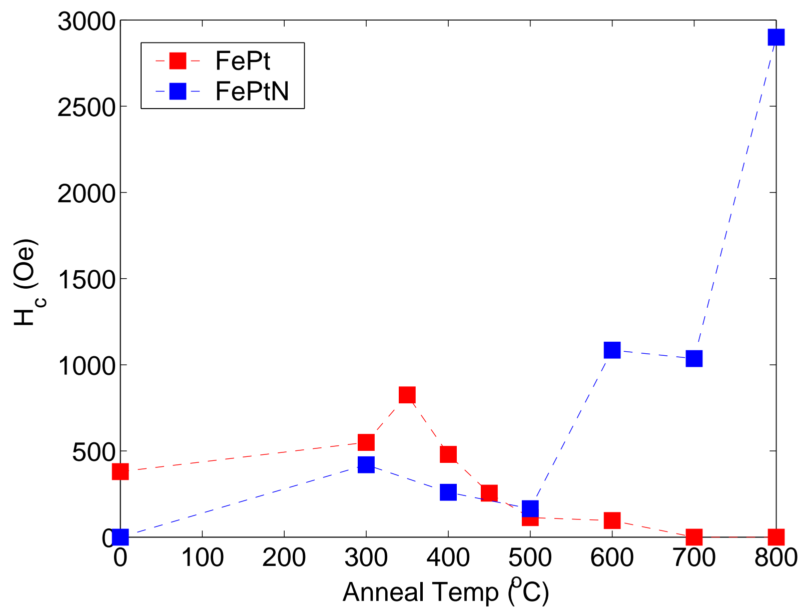

(b) Perpendicular coercivity of FePt and FePtN

Figure 7.5: Coercivity of 250 Å of FePt and FePtN on Si.

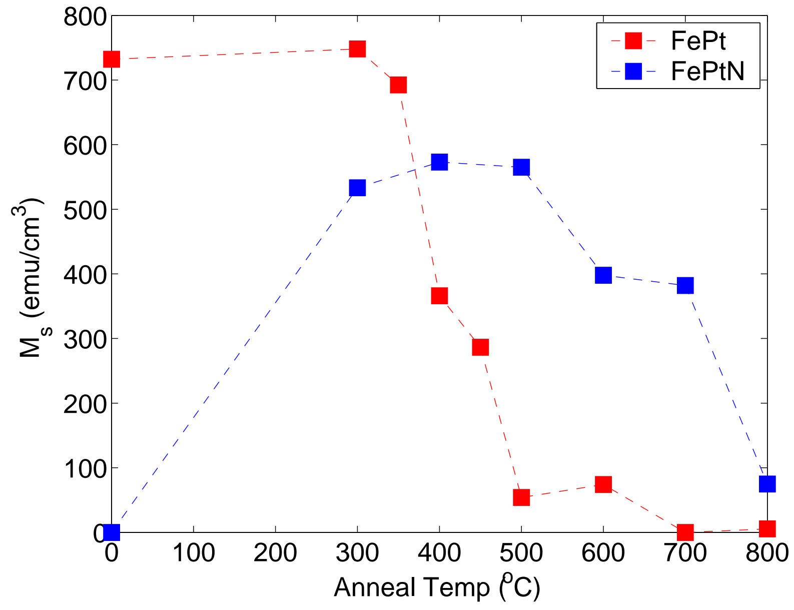

(a) In plane saturation magnetisation of FePt and FePtN

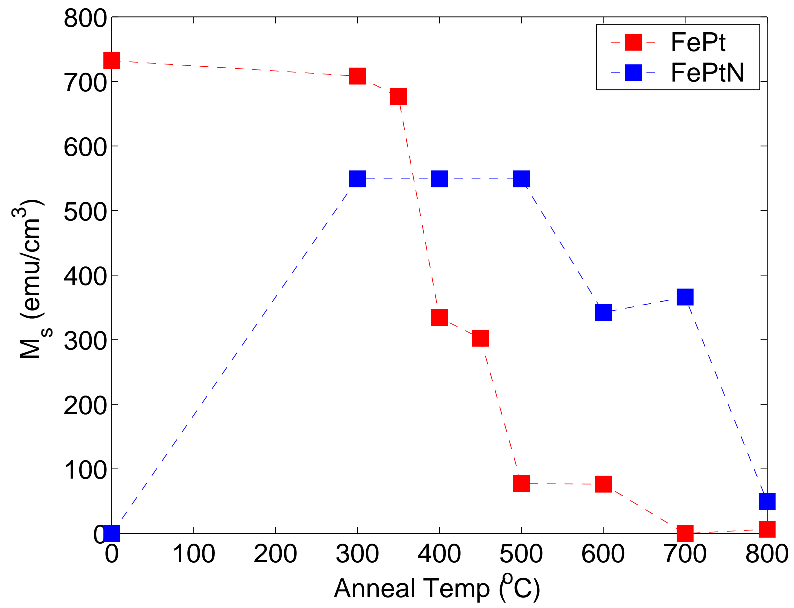

(b) Perpendicular saturation magnetisation of FePt and FePtN

Figure 7.6: Saturation magnetisation of 250 Å of FePt and FePtN on Si.

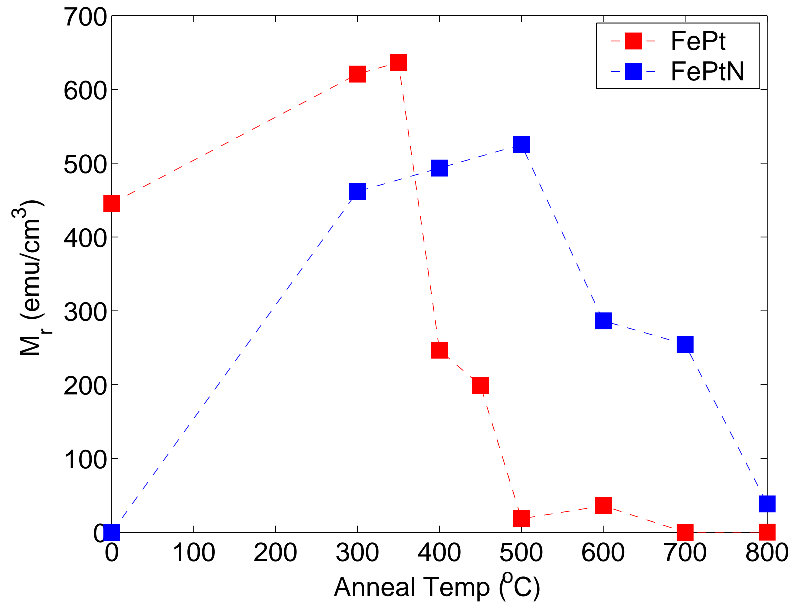

(a) In plane remanence of FePt and FePtN

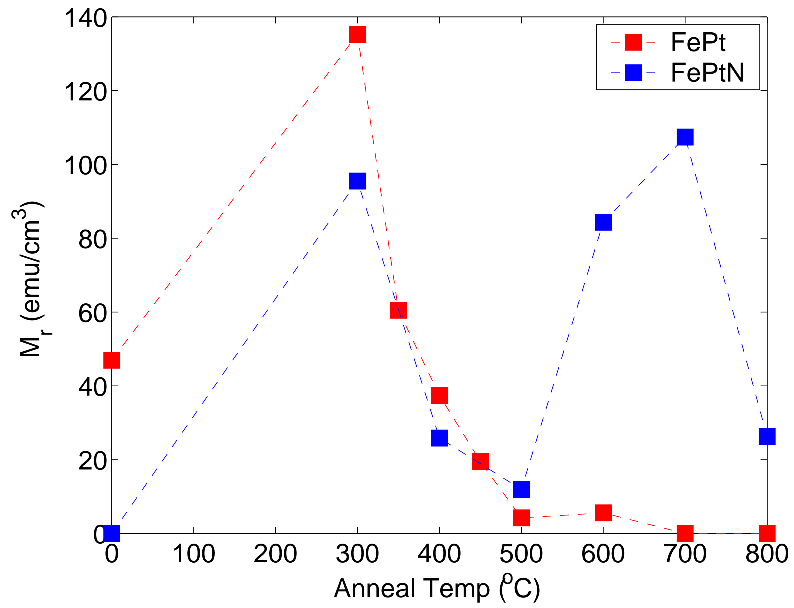

(b) Perpendicular remanence of FePt and FePtN

Figure 7.7: Remanence of 250 Å of FePt and FePtN on Si.

with a maximum $H_{c\perp}$ of 2900 Oe at 800 °C. Phatak et al. [339] showed that for as deposited films of FePtN, no hysteresis loops were obtained but after annealing at 673 K, a hysteresis loop showing a coercivity of 8 kOe was obtained. You et al. [338] co-sputtered FePt with 11 % nitrogen and after annealing at 700 °C for 30 mins, achieved a coercivity of 16.4 kOe. Wang et al. [189] included 13 % nitrogen during sputtering of FePt and after annealing at 600 °C for an hour obtained a coercivity of 14.5 kOe.

Below about 500 °C FePt films have a higher coercivity (both $H_{c\|}$ and $H_{c\perp}$) than those containing nitrogen. Above annealing temperatures of 500 °C the coercivity of FePt diminishes but the coercivity (both $H_{c\|}$ and $H_{c\perp}$) of FePtN rises. This suggests that nitrogen addition does influence the magnetic properties of FePt films.

Magnetisation

For the FePt films in both $\|$ and $\perp$ directions the saturation magnetisation begins at about 730 emu/cm^3 (0.917 T) and a general decrease is observed as temperature is increased (see Fig. 7.6). For the FePtN films in both $\|$ and $\perp$ directions the initial magnetisation is zero, as expected due to the nitrogen incorporation. Once the nitrogen begins to leave the film on annealing M_s initially increases to over 500 emu/cm^3, but then begins to decrease as the film is further annealed. In-plane M_s values are similar to those out-of-plane for both FePt and FePtN.

Different methods of film preparation techniques yield films with different properties such as coercivities and magnetisation. Deviations from expected values of magnetisation could also be due to factors such as inaccurate measurement of film volume, which could be improved in the film preparation stage by using a quartz crystal film thickness monitor. The content of the elements can also affect coercivity and magnetisation as shown in a study by Mahalingam et al. [355]. For a general comparison to literature, Yuan et al. [356] deposited FePt onto MgO substrates at room temperature by DC magnetron sputtering, both in plane and out of plane magnetisation values are about 700 emu/cm^3. Ma et al. [349] deposited FePt films by DC magnetron sputtering with no substrate heating, both in plane and out of plane magnetisations are between 700 - 800 emu/cm^3. Xing et al. [353]

co-evaporated FePt films and obtained a magnetisation of 1160 emu/cm^3. Noh et al. [357] sputtered FePt as nano patterns and after post annealing at 400 °C, an in plane magnetisations of around 1100 emu/cm^3 were obtained. Li et al. [358] deposited Fe/Pt multilayers by sputtering and carried out post deposition annealing. Different Fe:Pt ratios gave different values of magnetisation. for $Fe_{48}Pt_{52}$, annealing at 300 °C, gave an in plane magnetisation of around 750 emu/cm^3 but annealing at the same temperature for a slightly different composition, $Fe_{52}Pt_{48}$ gave an in plane magnetisation of around 630 emu/cm^3.

Remanence

The remanence figures (Figs. 7.7) show that at low annealing temperatures in-plane remanence, $M_{r\parallel}$, for FePt and FePtN improves until about 350 °C for FePt and about 500 °C for FePtN, after which $M_{r\parallel}$ decreases.

In the out-of-plane cases, FePt again, shows an initial improvement with annealing until 300 °C where $M_{r\perp}$ reduces from 135 emu/cm^3 to 60 emu/cm^3. However, something interesting happens in FePtN. After an initial increase to 96 emu/cm^3 (300 °C) $M_{r\perp}$ decreases to 12 emu/cm^3 (500 °C), increases again to 107 emu/cm^3 (700 °C) then decreases again to 26 emu/cm^3 (800 °C). It is also very evident that the perpendicular $M_{r\perp}$ values are slightly lower than the in-plane $M_{r\parallel}$ values.

To try to understand the magnetic measurements, XRD measurements were carried out and the results are presented in the following section.

7.5.2 X-Ray diffractometry

FePt samples

The x-ray diffraction results for FePt samples deposited on Si substrates and annealed at different temperatures are shown in Fig. 7.8. The peaks in as-deposited films match those of $FePt_3$ (as they did in fact also for the as-deposited FePtN films - see Fig. 7.11). The transformation from the disordered fcc structure (with low anisotropy) to the fct $L1_0$ structure (with high magnetic anisotropy) involves breaking of the cubic symmetry due to the stacking of alternate planes of Fe and Pt along the [001] direction [359]. Therefore, the emergence of (001) and (002) peaks

on an XRD pattern can indicate a phase transformation into the $L1_0$ phase.

The main $FePt_3$ (111) occurs at 40.3°, indicated by a dashed line in the figure. As the films are annealed through to 350 °C, this peak is shifted slightly and becomes matched to FePt (111). This indicates a small loss in Pt during annealing.

A loss in Pt could improve the Fe:Pt ratio to a more equiatomic structure which is known to exhibit better magnetic properties than other ratios [360]. This could be responsible for the initial increase of both $H_{c\|}$ and $H_{c\perp}$. What were clearly the main peaks (for FePt $2\theta = 40.6°$ and 47.2°; for $FePt_3$ $2\theta = 40.3°$ and 46.9°) gradually become smaller as annealing temperatures increase and eventually disappear after 400 °C. The highest coercivities at 400 °C and 450 °C could be due to the presence of some ordered FePt (002) phases as shown on the diffraction pattern; the (002) position is at 47.2° and is indicated by a dashed line in the figure. At the same time of the disappearance of the main 'starting' peaks, new peaks appear. These are matched to those of iron silicide, FeSi, and platinum silicide, PtSi. From literature on iron and platinum silicide studies, strong peaks at around 22.5° and 30° can indicate the presence of these silicides [361][362][363][364]. In the figure, the FeSi and PtSi labels are in blue text, with "M" representing a mixture of iron and platinum silicides. Other new peaks match Fe, $Fe_{0.75}Pt_{0.25}$ and $Fe_{0.5}Pt_{0.5}$. At 400 °C at about 45° a new set of peaks begin to take form and become clearly 'separated' by 800 °C. One of these peaks is well matched to Fe (45.1°) and the other to $Fe_{0.75}Pt_{0.25}$ (43.1°). However, a strong peak at 45.3° could still represent the presence of FePt. This indicates that as the FePt film is annealed the Pt is continually being removed from the as deposited structures. Some Pt does remain bonded to the FePt as the $Fe_{0.75}Pt_{0.25}$ and $Fe_{0.5}Pt_{0.5}$ matches show, but a significant amount of Pt appears to have reacted with the silicon substrates forming platinum silicides. Silicide formation in annealed FePt nanoparticles have been studied by Thomson et al. [365].

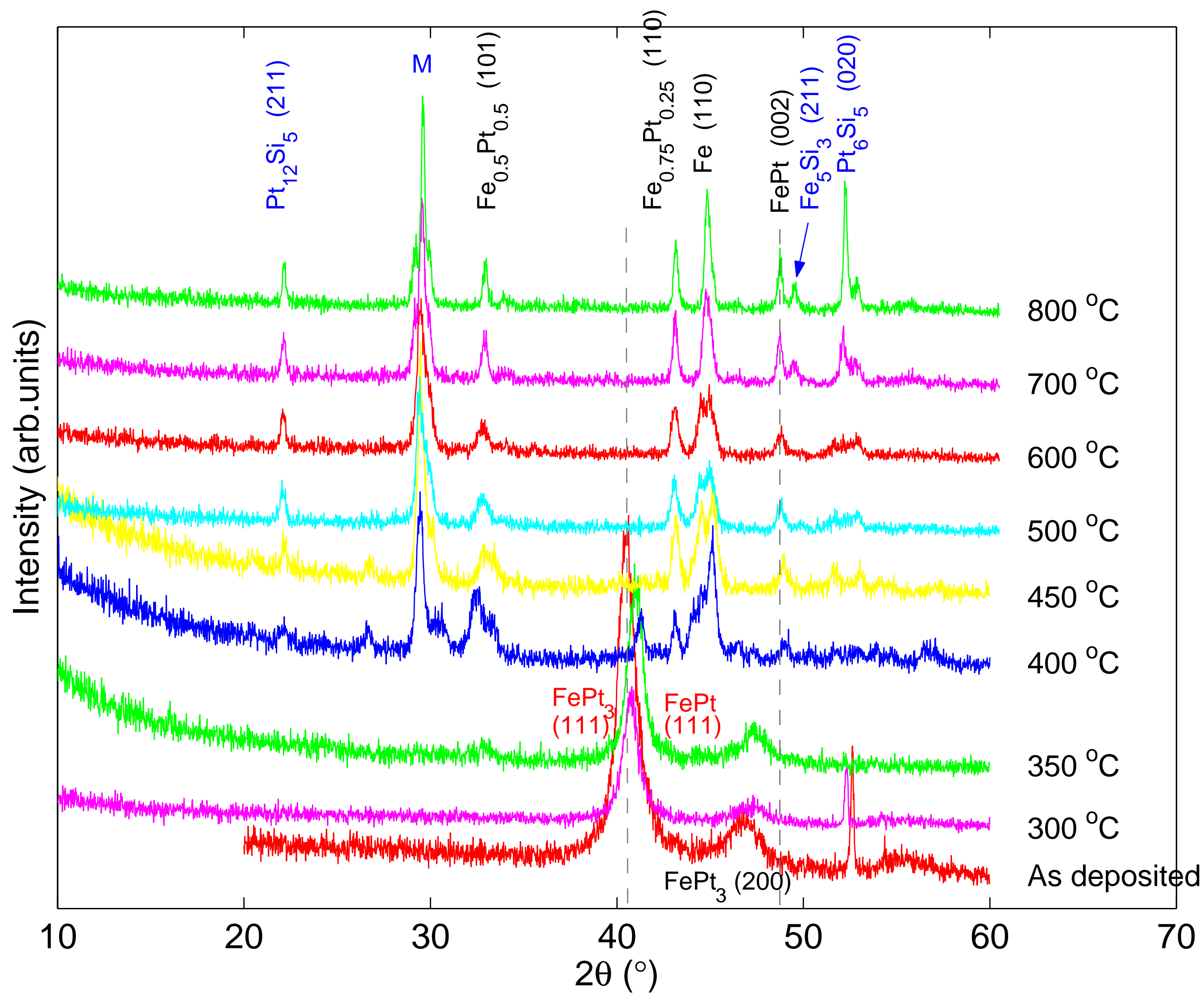

Figure 7.8: X-ray diffraction patterns of FePt for different anneal temperatures (deposited onto Silicon).

The increased formation of the silicides results in the decrease of $H_{c\|}$ and $H_{c\perp}$ of the FePt film. The detrimental role that silicide formation can play in affecting the magnetic properties of FePt films was also 'evidenced' by depositing FePt films onto glass substrates and annealing in the temperature range from 300 °C to 600 °C. In this case no silicide formation is observed, as shown for example in the x-ray diffraction results of Fig. 7.9, and the decrease in coercivity observed for FePt films on Si substrates and annealed above 300 °C does not occur (see for example Fig. 7.10).

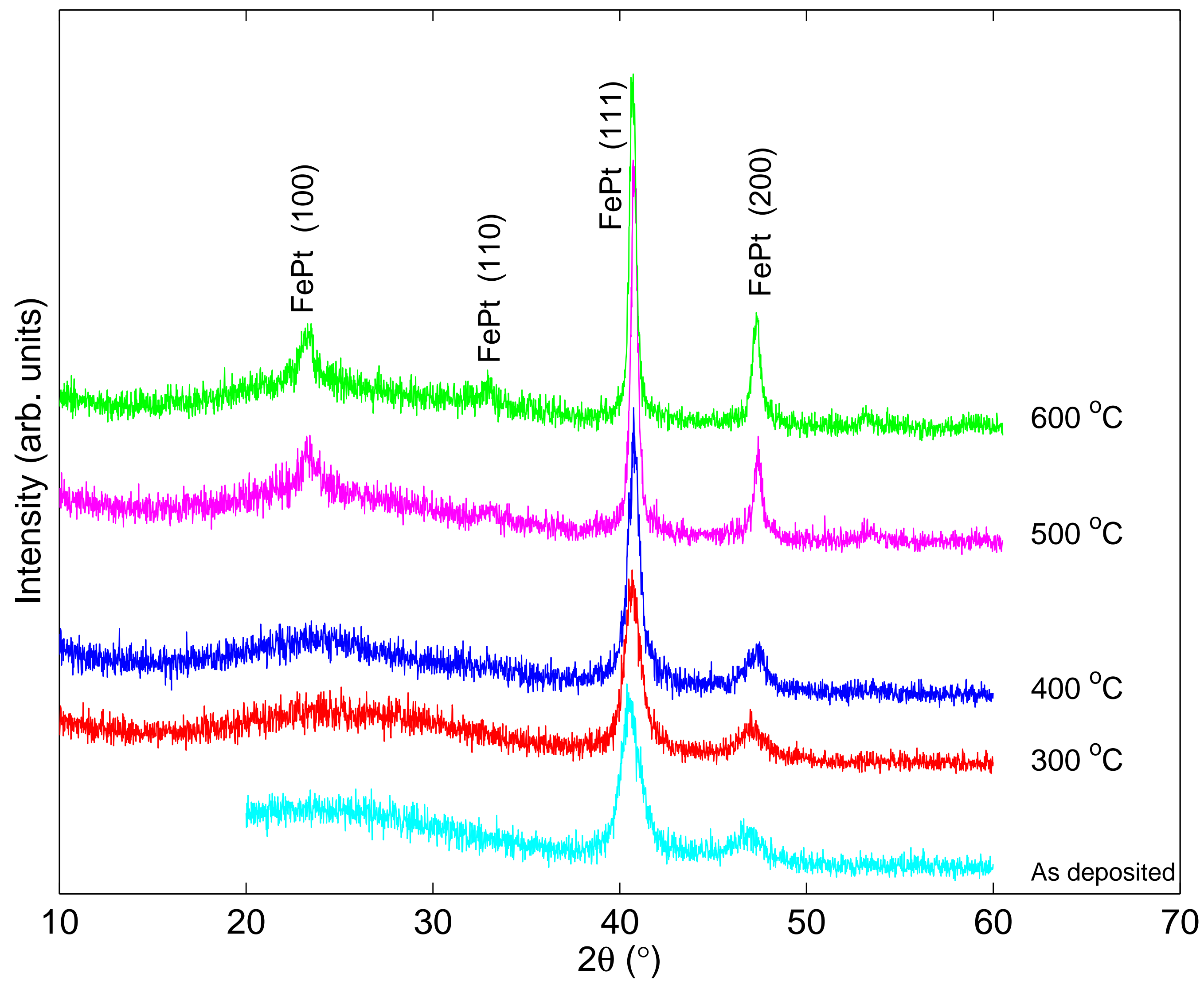

Figure 7.9: X-ray diffraction patterns of FePt for different anneal temperatures (deposited onto glass).

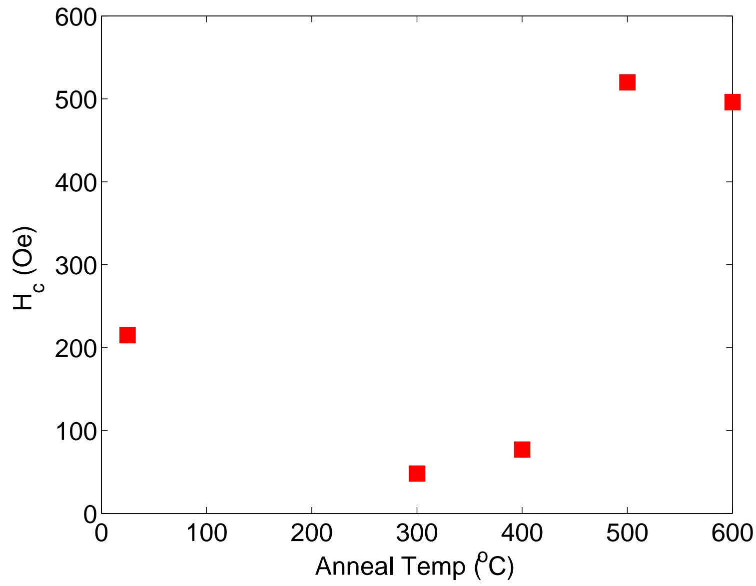

(a) In plane coercivity of FePt

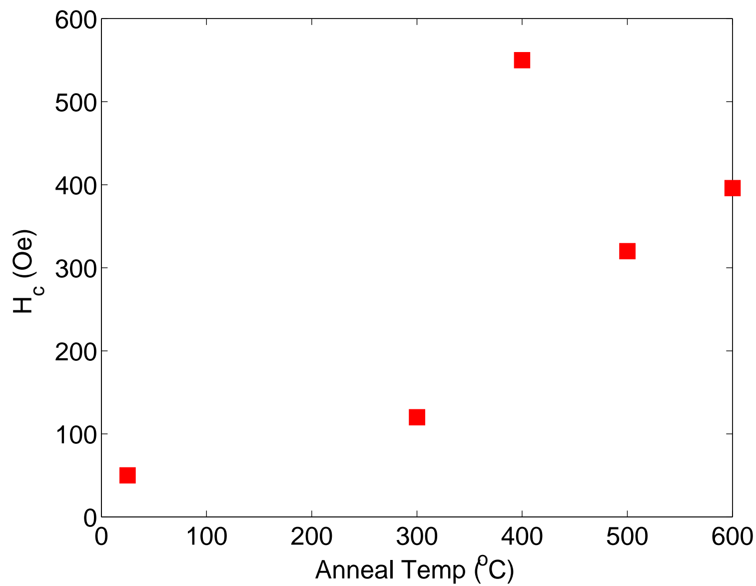

(b) Perpendicular coercivity of FePt

Figure 7.10: coercivity of 250 Å of FePt on glass.

For the samples grown on glass, the evolution of FePt (100) and (200) XRD peaks after 400 °C (Fig. 7.9) show that ordering is taking place, though not in the correct c-axis direction, and so not acquiring the desired magnetic properties. In fcc FePt, the six planes (or faces) of the cubic structure are related by the symmetry elements and are entirely equivalent (please refer back to Section 4.7). So, for

example, the (001), (100) and (010) planes are equivalent. When fcc FePt rearranges into its tetragonal $L1_0$ structure, the (001), (100) and (010) planes are no longer symmetrically equivalent as the Fe and Pt take alternate planes along the [001] direction (c-axis direction). That is to say, (001) and (100) planes are no longer equivalent. Magnetic measurements for these samples showed a maximum $H_{c\|}$ of 520 Oe at 500 °C and $H_{c\perp}$ of 550 Oe at 400 °C. The samples on glass substrates could not be annealed beyond 600 °C due to melting of the glass above this temperature. Although by incorporating silicides such as PtSi [366] [367] and Cu_3Si [367] it has been shown to reduce the ordering temperature, this benefit from silicide formation has not been observed in this study.

FePtN samples

The x-ray diffraction results for the nitrided (FePtN) samples are shown in Fig. 7.11. Where in the FePt samples the disappearance of the main $FePt_3$ (111)/FePt (111) is accompanied by the emergence of new peaks after 350 °C, this does not occur in FePtN. At 800 °C many new peaks do appear but the FePt (111) peak remains at about 40°.

The FePt(001) peak is shown to emerge at 500 °C and is clearly visible at 600 °C. The (001) peak occurs at 23.9° and in the figure is indicated by a dashed line at that angle. This shows improved ordering of the film and it is between 500-600 °C that there was a marked increase in $H_{c\|}$ and $H_{c\perp}$. At 700 °C these (100) and (110) peaks become larger, an indication that there are more crystals of this orientation. When 800 °C is reached, many more new peaks appear. As well as peak matches to iron and platinum silicides, FePt(001) and (002) are also present - these phases would have contributed to the second marked increase in coercivities. The (002) peak, occurring at 48.7° is also indicated by a dashed line. In the figure, the silicide peaks are highlighted in blue text, with "M" representing a mixture of iron and platinum silicides. This XRD data suggests that the FePtN has partially transformed into the FePt fct phase but with undesirable silicide formation, having detrimental effects on M_s, M_r and hindering H_c.

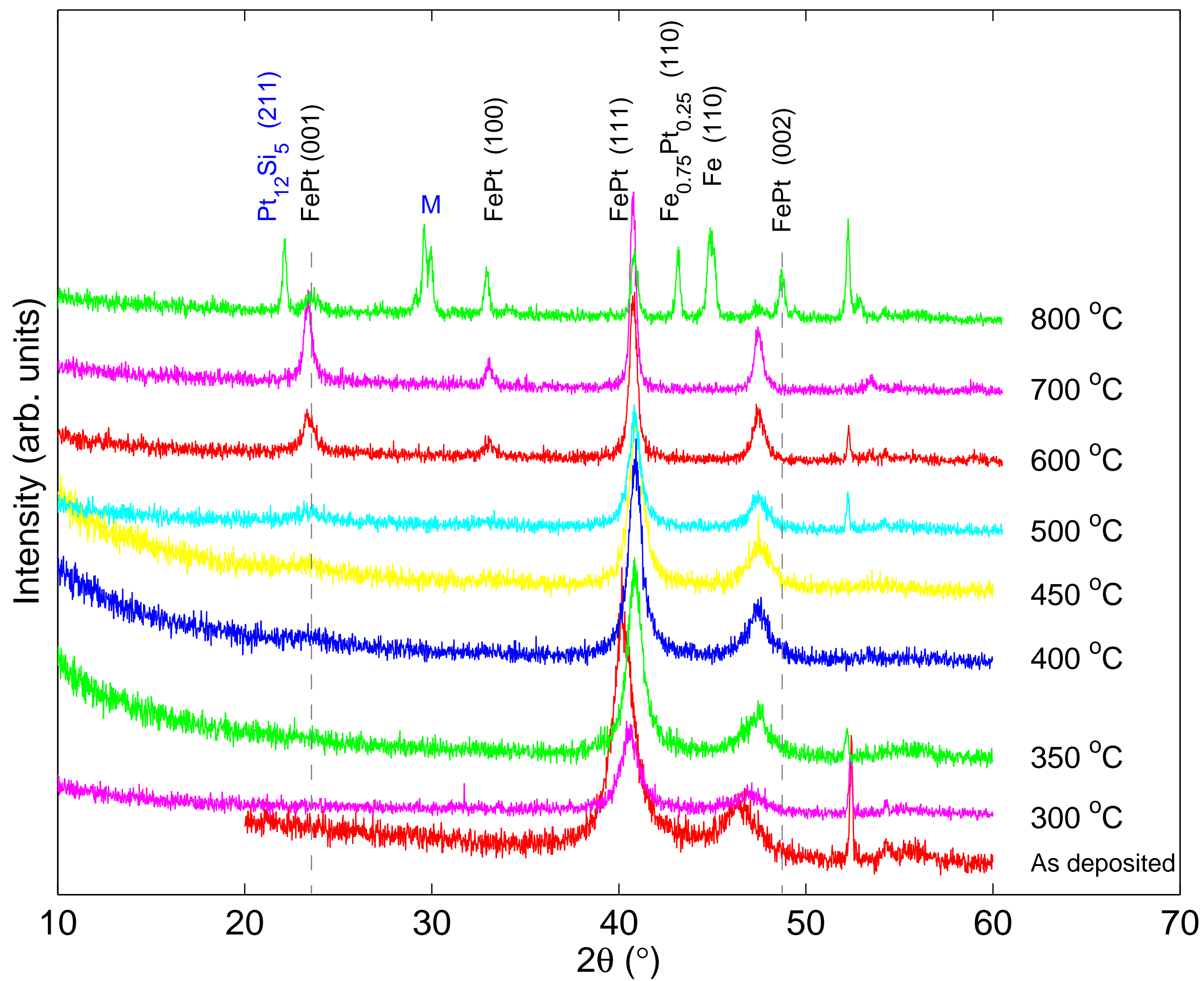

Figure 7.11: X-ray diffraction patterns of FePtN for different anneal temperatures (deposited onto Silicon).

However, it is important to note that the formation of silicides occur at a much lower temperature when nitrogen is not incoropated into the depositing films. In FePt, the silicides form so soon that the film does not have a chance to become ordered. In FePtN, the presence of nitrogen appears to hinder silicide formation [368]. This could be due to reaction of the nitrogen with the Si substrate, preferentially forming silicon nitride over platinum silicide. This can be understood by considering the thermodynamics of the reactants involved.

The thermodynamic data for the likely reactions involving Fe, Pt, N_2 and silicon substrates are shown in Table 7.1. Chemical reactions often involve a change in enthalpy (defined as the heat produced or absorbed during a reaction at constant pressure and the symbol for the change is ΔH). The standard enthalpy of formation is the enthalpy change when 1 mole of a pure substance is formed from its elements (where the reactants and products are in their standard states) [62]. Chemical reactions that have a negative ΔH are said to be exothermic and reactions that have a positive ΔH are endothermic. A negative enthalpy means heat energy is released. If the substance releases heat energy, then the product has a lower value of stored heat energy. Such a change is energetically favourable [211]. The table shows the standard enthalpy of formation values for the various possible materials. The formation of silicides from FePt have been well studied [366], [365]. The enthalpy of formation ,$\Delta_f H^\ominus$,for Si_3N_4 is much more negative than for the formation of the other products. This means that the formation of Si_3N_4 has a lower energy content than the formation of the other products, indicating that Si would preferentially combine with nitrogen rather than with either Fe or Pt.

During deposited, it is thought that nitrogen predominantly bonds to Fe [189]. Platinum-Metal elements (Pt, Ir, Os, Ru, Rh, Pd) do not readily form stable compounds with nitrogen [374]. The initial increase of coercivities can be associated to an initial removal of some of the nitrogen and formation of FePt. As the films are annealed various forms of iron nitride may evolve. Some phases of iron nitride are non-magnetic (e.g. FeN), yet some are soft magnetic materials with high saturation magnetization (Fe_4N and $Fe_{16}N_2$) [375][376]. It is therefore feasible that the decrease in coercivities after 300 °C is due to the formation of non-magnetic iron nitride phases. It is therefore also possible that the increase in coercivities after 500

Material	Enthalpy $(\Delta H_f^{\ominus})(KJmol^{-1})$	Reference
FePt	-27.2	[369]
FeSi	-99.8	[370]
Fe_2N	-3.8	[371]
Fe_4N	-10.9	[371]
PtSi	-59.6	[372]
Pt_2Si	-63.3	[372]
Si_3N_4	-828	[373]

Table 7.1: Enthalpy of formation values.

°C is due to a magnetic phase of iron nitride being formed [377][378]. It is difficult to to match up iron nitride peaks using XRD since their peak positions are similar to those of FePt.

7.5.3 Electrical properties

The electrical properties of FePt and FePtN films will change with annealing temperature, due to changes induced in the film composition and structure. Thus, electrical measurements, for example resistivity, can give a useful (although indirect) indication of the changes that occur with annealing.

Electrical resistivity measurements were carried out using the four point probe technique described in Chapter 6, using applied in plane currents of 0.005 A, 0.01 A, 0.015 A and 0.02 A. For each sample each one of these currents was applied and their respective voltages measured. The gradient for each sample was worked out by plotting voltage (V) against current (I), from which the sheet resistance (R_s), can be calculated (please refer back to Section 6.5). By using the following [327],

$$R_s = 4.53 \times (\frac{V}{I}) \tag{7.1}$$

$$\rho = R_s \times t \tag{7.2}$$

where t is the thickness of a thin film and the resistivity, ρ, can be calculated. An example plot is shown in Fig. 7.12.

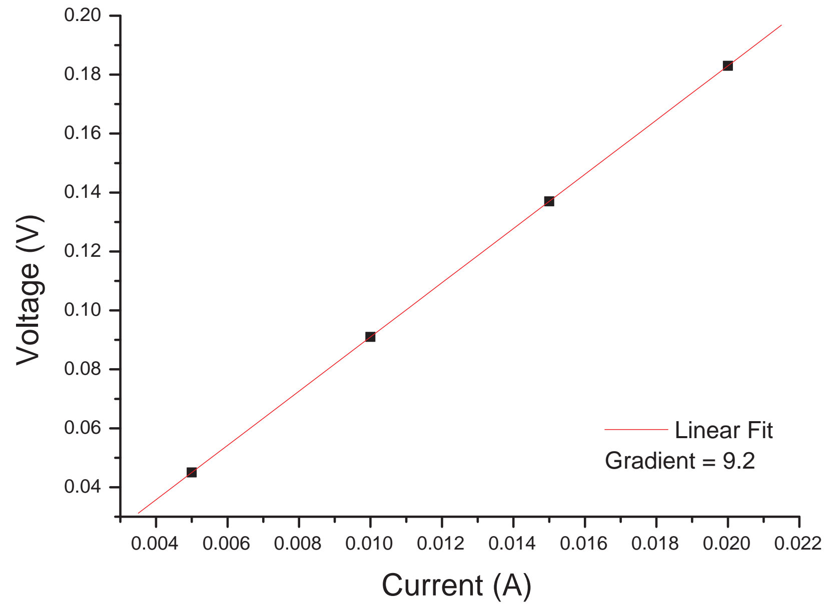

Figure 7.12: Example graph showing measured voltages at various applied currents.

For this example where the gradient is 9.2,

$$R_s = 4.53 \times 9.2 = 41.676\,\Omega/sq \tag{7.3}$$

$$\rho = R_s \times 25 \times 10^{-7} = 104\,\mu\,\Omega\,cm. \tag{7.4}$$

Please note that the line of fit does not pass through zero due to an offset in the voltmeter. A similar plot was created for the FePt and FePtN samples and the resistivity values are shown in Fig. 7.13. A linear plot of voltage against current implies that heating effects are minimal since one would expect the effects to be greater at higher currents and so not show linear behaviour. The resistivity values for samples annealed at 800 °C were too high to be measured.

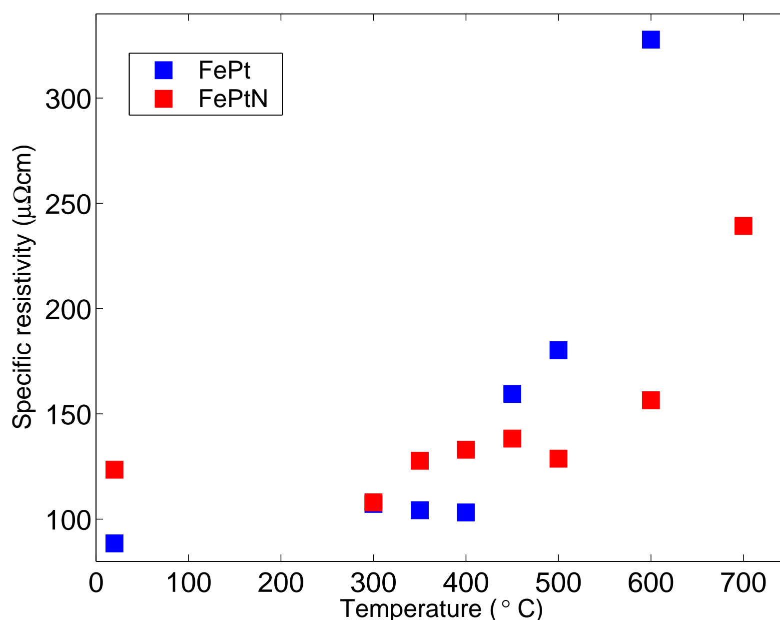

Figure 7.13: Specific resitivity data for 250 Å FePt and FePtN deposited onto Si.

Before any thermal treatment resistivity for FePtN is higher than that of FePt. This is expected as when elemental Fe is nitrided its resistivity increases from about 10 $\mu\Omega cm$ to over 150 $\mu\Omega cm$. Table 7.2 shows the room temperature resistivity values for some likely products that could be formed within the FePt and FePtN films.

Material	Resistivity ($\mu\Omega$ cm)	Reference
Fe	9.87	[371]
Pt	10.7	[371]
FeN	165 - 200	[379]
PtSi	28 - 35	[380]
$FeSi_2$	10^3 - 10^6	[380]
Si_3N_4	20^{20}	[381]
Fe_3O_4	6.07×10^3	[382]
SiO_2	10^{20} - 10^{22}	[383]

Table 7.2: Room temperature resistivities of likely compounds.

The resistivites of FePt remain lower than the resistivities of FePtN on increasing temperature until 400 °C where the values of resistivity for FePt become higher

than those for FePtN. At 400 °C the resistivity of FePt begins to rise sharply. The resistivity of FePtN also shows a sharp increase but not until after 500 °C - the presence of nitrogen appears to 'delay' the increase in resistivity. These temperatures correspond well to the appearance of the "new peaks" on the XRD patterns (i.e the $Pt_{12}Si_5/Fe_5Si_3$) peaks for FePt and FePt(100)/(110) peaks for FePtN), illustrating that new structures and phases can have a significant effect on film resistivity.

According to literature $FeSi_2$ has a much greater resistivity value (10^3 - 10^6 $\mu\Omega cm$) [384][380] than PtSi (28 - 35 $\mu\Omega cm$) [385][386][380]. The initial formation of PtSi in the FePt films could be responsible for maintaining a relatively low resistivity in FePt films until after 400 °C when the increased formation of iron silicides could increase the resistivity greatly. The production of Si_3N_4 could be responsible for the increased resistivity in the FePtN films at 600 °C and 700 °C.

7.5.4 Surface morphology

For real applications it is ideal to have surfaces that are as smooth as possible. How rough a surface is can give an indication of particle or crystal sizes. The surface roughness was therefore investigated using AFM. AFM measurements were performed on an Innova microscope (Veeco Corp.) with a Nanodrive controller (Veeco Corp.). The instrument was operated in tapping mode using a phosphorous doped silicon tapping mode tip. The AFM topographic images (scan size of 1 × 1 μm^2 and scan rate of 0.5 Hz) were analysed for surface roughness using the Veeco Nanoscope software.

Before any annealing, FePt and FePtN films are relatively smooth with measured rms roughness of 0.0511 nm and 0.0555 nm respectively. As shown in Fig. 7.14 the roughness increases significantly as the films are annealed.

After 600 °C, FePtN films have a greater roughness than FePt. By 800 °C, the rms of FePtN is over three times greater than that of FePt. Although FePt films are smoother than FePtN films, their magnetic properties are not as good when annealed above 400 °C or so.

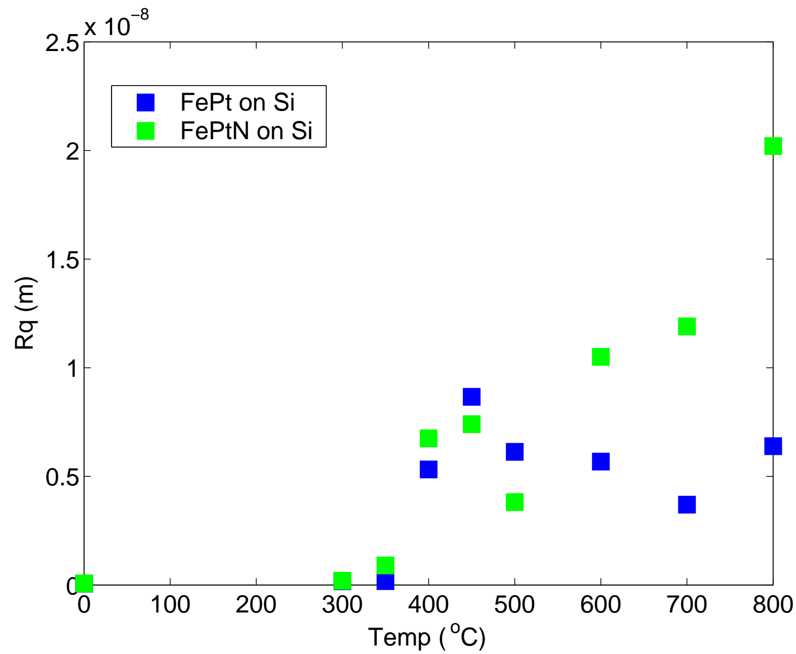

Figure 7.14: RMS roughness of FePt and FePtN on Si measured using AFM.

7.5.5 Crystallite size

The crystallite size has been investigated by XRD using the EVA program and Scherrer equation (Fig. 7.15), from the (111) peak of FePt and from the large silicide peak at about 30°.

As shown in Fig. 7.15 the crystallite size of as-deposited FePt and FePtN films is around 10 nm, consistant with those noted by other groups [387] [349], but annealing does increase the crystallite size drastically. For FePt at 400 °C, crystallites of over 130 nm are observed. Crystallites of PtSi are also increasingly forming in size after 400 °C. At higher annealing temperatures, the crystallite sizes of FePtN remains lower than FePt but still does increase to over 50 nm.

7.5.6 High coercivity FePt

The above results have shown that the formation of silicides has had detrimental effects on FePt and FePtN films. A study by Li et al. [366] has shown that by depositing FePt onto HF-cleaned Si substrates, a reaction occurs between the FePt film and the substrate creating a PtSi layer at the interface. After annealing for

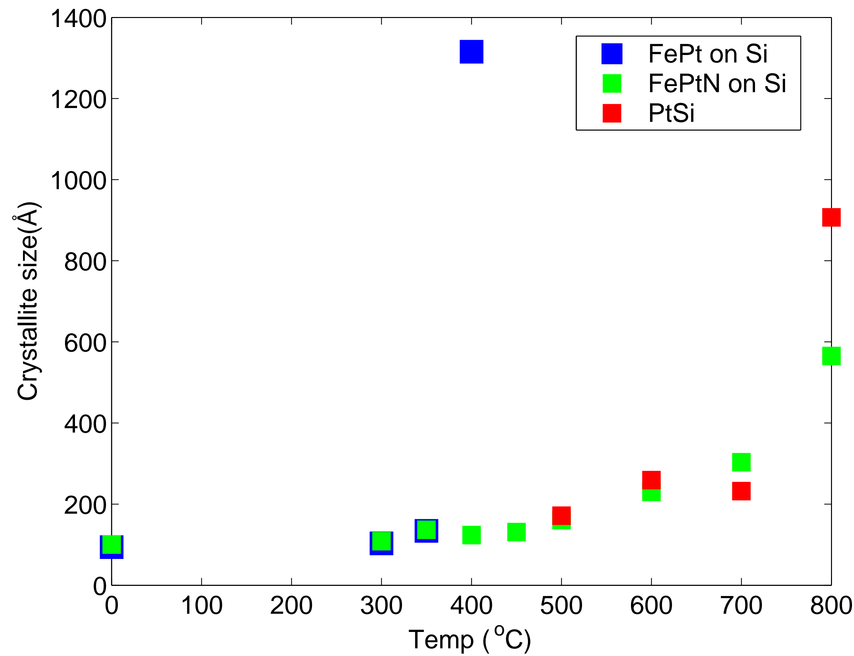

Figure 7.15: Crystallite size of FePt and FePtN on Si measured using XRD.

two hours at 350 °C a coercivity of 6.4 kOe was obtained. This coercivity value was similar to that of FePt films deposited on Si/SiO_2 substrates (where no interface reaction occurred) annealed at 600 °C. It was concluded that a PtSi layer at the film - substrate interface can accelerate $L1_0$ ordering and as a result lower the $L1_0$ transformation temperature to 350 °C.

It is at a similar temperature to Li et al. that an FePt film deposited using HiTUS showed high in plane and perpendicular coercivities. The FePt film (25 nm) was deposited directly onto naturally oxidised Si (unknown oxide thickness) and annealed at 400 °C as described in Section 7.4. This sample is referred to as 'Sample A.' The (‖) and (⊥) hysteresis loops, measured by VSM, for Sample A are shown in Fig. 7.16. 'Sample B' refers to the previously fabricated FePt film onto a Si substrate, also annealed under the same conditions at 400 °C. The hysteresis loops for Sample B are also shown in Fig. 7.16 for comparison. Since the maximum magnetic field strength for VSM measurements was 20 kOe, it is possible that the samples were not fully saturated in the perpendicular measurements. The coercivity, magnetisation and remanence values for Samples A and B have been extracted from the hysteresis loops and are tabulated in Table 7.3. The values for the as deposited FePt sample are also shown in the table for comparison.

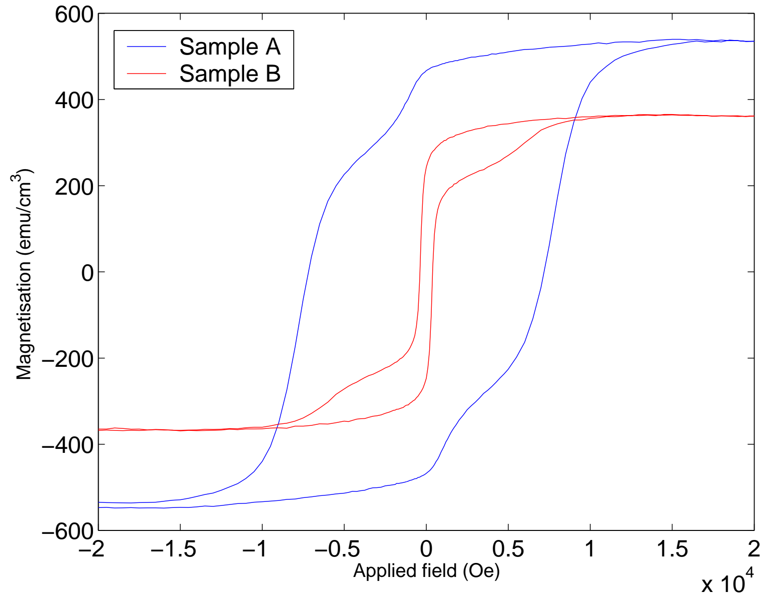

(a) In plane measurements

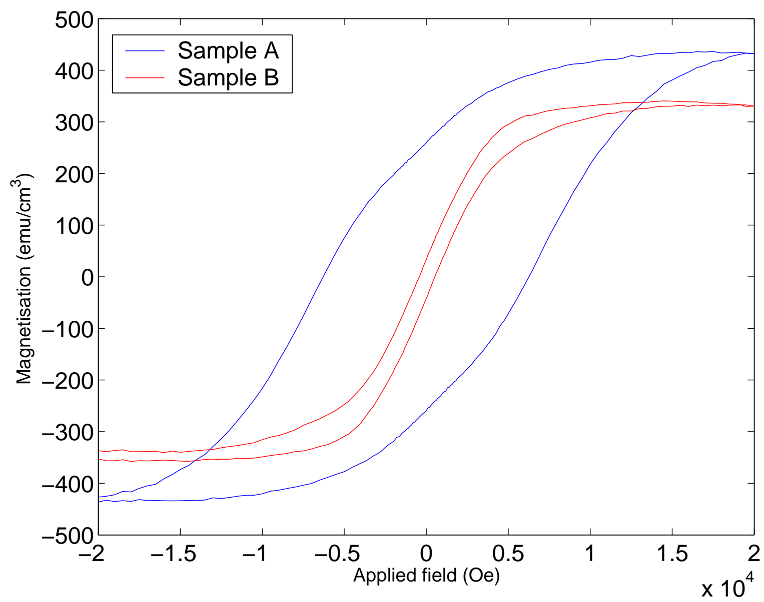

(b) Perpendicular measurements

Figure 7.16: Hysteresis loops, produced using VSM, for 250 Å of FePt deposited onto naturally oxidised Si.

The coercivities of as deposited FePt are 95 Oe (‖) and 380 Oe (⊥). After annealing at 400 °C Sample A shows a much larger increase in coercivity than Sample B. The in-plane coercivity of Sample A, $H_{c\|}$, is 7180 Oe and perpendicular coercivity , $H_{c\perp}$, is 6300 Oe. (Sample B) showed smaller increases to 380 Oe ($H_{c\|}$) and 480 Oe ($H_{c\perp}$). Table 7.3 also shows that the measured crystallite size of Sample A is significantly lower than that of Sample B. With no annealing the crystallite size of the as deposited sample is 93.9 Å. After annealing, Sample A displays a crystallite size of 222.2 Å whereas the crystallite size of Sample B is 1315.5 Å. The surface roughness of Sample B is over twice as rough as that of Sample A. Coercivity can be affected by grain size as shown by work carried out by researchers such as Herzer [388][389]and Pfeifer [390]. They showed that the maximum coercivity for a given material occurs within its single domain range. For larger grain sizes, coercivity decreases as the grain subdivides into domains. For smaller grain sizes, again coercivity decreases, but this decrease is due to the randomizing effects of thermal energy.

The in plane remanence for Sample A increased slightly from 446 emu/cm^3, for the as deposited sample, to 467 emu/cm^3 but had decreased to 243 emu/cm^3 in Sample B. For both Samples A and B, the perpendicular remanence increased from 47 emu/cm^3, for the as deposited sample, to 289 emu/cm^3 in Sample A and to 71 emu/cm^3 in Sample B. Magnetic remanence is associated with the interactions between neighboring magnetic spins and is determined by the competition between exchange energy and anisotropy energy at room temperature [391]. Annealing has been known to cause an increase in remanence and enhance intergrain exchange coupling [391][392].

In both samples, both the in plane and perpendicular saturation magnetisation values had reduced from 732 emu/cm^3 obtained from the as deposited sample; although the values for Sample B reduced by a greater extent than Sample A. According to Toney et al. [393] the disordered FePt phase has a higher moment than the chemically ordered phase. The presence of non-magnetic materials can also dilute the saturation magnetisation [348], that is, the presence of grains with a low M_s can reduce the M_s of the entire film [355]. In this thesis the non-magnetic materials are thought to be iron and platinum silicides.

The XRD patterns for samples A and B, shown in Fig. 7.17, are distinctly different. For Sample A the desirable FePt (001) and (002) peaks are clearly visible at 23.9° and 49.0°; the FePt (111) peak is also still present. This provides some evidence that $L1_0$ ordering has occurred. In the case of Sample B, the large silicide and Fe peaks discussed earlier are dominant. This suggests that the level of silicides is much higher in Sample B than in Sample A. This agrees with the measured magnetic properties. The lower resistivity value of Sample A also suggests that less silicide is in the sample, which is also shown by a less dominant peak in the XRD pattern at about 30° (Fig. 7.17).

Property	As deposited FePt	Sample A	Sample B
$H_{c\parallel}$ (Oe)	95	7180	380
$H_{c\perp}$ (Oe)	380	6300	480
$M_{s\parallel}$ (emu/cm^3)	732	535	362
$M_{s\perp}$ (emu/cm^3)	732	432	333
$M_{r\parallel}$ (emu/cm^3)	446	467	243
$M_{r\perp}$ (emu/cm^3)	47	289	71
Surface roughness (rms, μm)	0.0000641	0.00248	0.00532
Crystallite size (Å)	93.9	222.2	1315.5
Resistivity ($\mu\Omega$cm)	88.5	79	103

Table 7.3: Properties of both samples A and B annealed at 400 °C. The properties of un-annealed FePt are also shown.

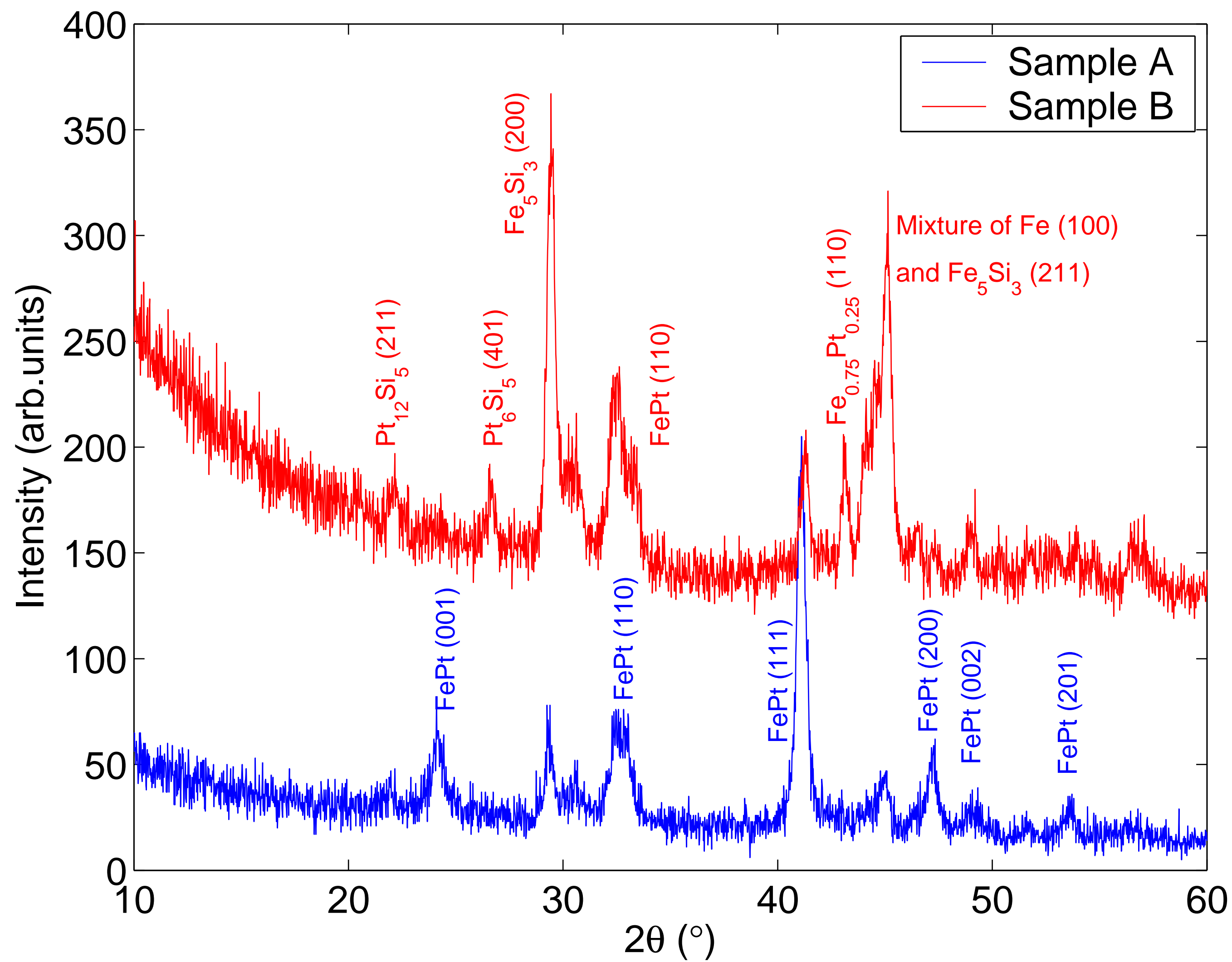

Figure 7.17: X-ray diffraction pattern of 250 Å FePt deposited onto naturally oxidised Si.

At present, the differences between Samples A and B are unknown. One possibility is that the Fe:Pt ratios are different in the two samples. The magnetic properties of FePt are very sensitive to preparation conditions and post annealing treatments [394]. In the study by Li et al. [366] at 350 °C a coercivity of 6.4 kOe was obtained, by increasing the temperature slightly to 360 °C the coercivity increased to 8.9 kOe, implying that FePt films are sensitive to slight variations in temperatures. Further work will be required to determine reasons behind the transformation of sample A from the fcc disordered phase to the fct ordered phase and also the relatively small grain growth. Further studies using the HiTUS system to better understand the influence of processing conditions on FePt thin film properties would help tune the properties. This is an interesting result and worth further investigations but unfortunately it is not possible to continue on this project due to time constraints.

7.6 Summary and conclusions

The ever increasing demand for higher storage densities has fuelled the research into high anisotropy materials for recording media, for enabling stable grain sizes below 10 nm and so increasing storage densities beyond $1Tb/in^2$. Face centred tetragonal (fct) FePt ($L1_0$) is a strong candidate for achieving this goal as it is recognised for its high anisotropy constant. Reducing the ordering temperature of FePt from its as deposited face centred cubic (fcc) phase to the fct phase, obtaining the correct (001) orientation and producing small grains which do not interact with one another remain to be key challenges for this material.

The aim for this project was to sputter FePt using the HiTUS system and investigate if the addition of nitrogen could contribute to the improvement of magnetic properties.

Thin films of FePt have been deposited directly onto naturally oxidised silicon substrates at ambient temperature. The magnetic properties obtained for the as deposited samples have $H_{c\parallel}$ of 95 Oe, $H_{c\perp}$ of 380 Oe, and $M_{s\parallel}$ and $M_{s\perp}$ are both 730 emu/cm^3. For the FePt films, annealing causes an increases in $H_{c\parallel}$ until 450 °C and $H_{c\perp}$ until 350 °C before both $H_{c\parallel}$ and $H_{c\perp}$ decrease. $M_{s\parallel}$ and $M_{s\perp}$ remain almost constant until 300 °C before decreasing drastically. $M_{s\parallel}$ and $M_{s\perp}$ for the as-

deposited samples are about 730 emu/cm^3 but by 400 ° this has more than halved. Initial annealing improves M_r in $\|$ and $\perp$ directions but after 300 °C M_r decreases substantially. $M_{r\perp}$ is always much lower than $M_{r\|}$ even for the as-deposited films.

The degradation of magnetic properties for annealing temperatures of 300 °C and above in the FePt films is attributed to the formation of silicides. Though some studies have shown that silicides can be beneficial to the fcc to fct transformation this has not been the case for the films in this study.

The addition of nitrogen to FePt films appear to suppress the formation of silicides until a much higher temperature of 800 °C. This is likely to be due to the reaction of the silicon with nitrogen forming silicon nitride, this reaction would be promoted by increasing annealing temperatures until around 800 °C when the nitrogen is suspected to have been removed from the sample. It is around this temperature that nitrogen has been reported to be released from iron nitride films [395].

The $\|$ and $\perp$ coercivities for FePtN increases with annealing temperature with the highest coercivity of 2900 Oe at 800 °C. However, at this temperature M_s and M_r values drop considerably, it is at this point that the silicide peaks are observed in the XRD patterns. It is believed that with increasing annealing temperatures different phases of iron nitride form within the film. The increases in $H_{c\|}$ and $H_{c\perp}$ between 500 - 600 °C could be due in part to a magnetic phase of FeN, but more importantly to the ordering of FePt as shown by the appearance of FePt (100) and (200) peaks in the XRD pattern. Also between 500 - 600 °C $M_{s\|}$ decreases from 565 emu/cm^3 to 398 emu/cm^3, $M_{s\perp}$ decreases from 549 emu/cm^3 to 342 emu/cm^3 and $M_{r\|}$ decreases from 525 emu/cm^3 to 287 emu/cm^3. Although there is a degradation in M_s and M_r in FePtN films, for temperatures up to 700 °C the decreases are not as severe as in the FePt films. Therefore, it can be said that nitrogen inclusion can offer some protection against falling M_s and M_r during thermal treatment. Crystallite size analysis of FePt and FePtN at different annealing temperatures indicate that nitrogen can inhibit the growth of grains. As expected, crystallite size and surface roughness all increase with increasing annealing temperatures.

It can be concluded that below 700 °C the addition of nitrogen to FePt can

reduce silicide formation for FePt thin films deposited onto silicon substrates and aid the stabilisation of magnetic properties. It is difficult to confirm if nitrogen enhances magnetic properties of FePt due to the early formation of silicides in FePt films.

FePt has been produced, with $\parallel$ and $\perp$ coercivities of 7180 Oe and 6300 Oe respectively annealed at 400 °C. This temperature is relatively low compared to temperatures reported by other groups, especially since no third material has been added, no underlayer nor expensive substrates used. The XRD diffraction pattern shows a clear (001) peak indicating the formation of $L1_0$ FePt. This suggests that HiTUS has the potential to reduce the FePt fcc to fct ordering temperature.

The type of substrate, underlayers, composition variation, annealing and growth conditions are amongst key factors for careful consideration when producing FePt thin films. With the easy control of deposition parameters of the HiTUS system there remains many more opportunities for developing $L1_0$ FePt. Reactive sputtering with nitrogen can not only offer protection against silicon pollution but contribute to granular media with better properties such as oxidation resistance, corrosion resistance and wear resistance.

Chapter 8

Multi-ferroics for future data read sensors

In the previous section the HiTUS technique has been used to deposit FePt for high K_u media applications. How the inclusion of nitrogen into FePt affects the magnetic properties was also studied. The research into high K_u media for future data storage is extensive. Such media would in turn require stronger write head fields to switch the magnetisation of the recorded bits. One promising approach to assist the writing on high K_u media is 'heat assisted magnetic recording' (HAMR) [396]. Recently, it has also been demonstrated that the magnetic anisotropy of materials can be modified electrically [397] [270] [398] [251]. The way by which magnetisation can be controlled by electric field paves the way towards purely electric-field controlled devices. These devices would cause less Joule heating than magnetic devices that are switched with a current (MRAM, for example [399]) and improvements in miniturization and power consumption should be expected. A voltage controlled write head has even been proposed [253]. The phenomenon by which magnetisation can be controlled by electric fields (and vice versa) is known as the *magneto-electric (ME) effect* and arises in a special class of materials known as "multiferoics" [269][400][246].

This relatively new class of materials is not only being investigated to provide alternative method for writing data, but also for the read-out of data. Potentially the combination of the two functions could lead to an electric field controlled novel read/write head design as proposed by several research groups [401] [402] [135]. In this section the possibility of using the magneto-electric effect in the design of future

read heads will be explored.

8.1 ME for data storage read out applications

Modern magnetic read heads are based on magneto-resistive (MR) effects such as GMR and TMR [108][403]. These effects rely on changing the internal resistance of a sensor stack structure on interacting with the stray field from the recorded bits of a magnetic recording medium. A constant DC current passes through the sensor stack and the change in the stack resistance is translated into a read signal as a voltage amplitude change $\Delta V = I \times \Delta R$ [404][405][406]. With increasing recording densities, the read sensor must become smaller and more sensitive to the ever decreasing bit size [407]. Magneto-resistive read sensors contain extra structures and layers to ensure reliable biasing and shielding [408][409][410]. These impose limitations on higher recording densities. Active research is underway to improve current magneto-resistive sensor technologies [411] [412][413]. Multi-ferroic magneto-electric materials have attracted great interest for this purpose [401][402].

In 2005, Binek and Doudin [414] theoretically proposed device architectures combining a GMR or TMR device with a magneto-electric film, where the electric field is used as an alternative means for controlling the magnetic configuration of spintronic devices. By taking advantage of the insulating anti-ferromagnetic nature of some ME materials such as Cr_2O_3, they proposed to use the anti-ferromagnetic ordering to provide control of the magnetic configuration of spintronic devices through strong exchange coupling to adjacent ferromagnetic films. For the TMR case they suggest to use an anti-ferromagnetic ME thin film as a dielectric tunnel barrier between two ferromagnetic metallic layers (FM1 and FM2) of which one is hard or pinned, and the other is soft. On applying a voltage, the electric field can cause a net magnetisation to occur in the anti-ferromagnetic ME layer. Changing the voltage polarity across the FM1 || ME || FM2 device changes the direction of the net magnetisation of the ME layer which in turn would affect the magnetisation of the soft magnetic layer (this takes advantage of the exchange field between the magnetised ME layer and the two adjacent ferromagnetic films). For devices based on GMR; they proposed that the ME thin film can be used as a tunable pinning layer to which the bottom of the GMR device is pinned. A voltage difference controls the ME layer

magnetisation, tuning the exchange coupling with the bottom pinned layer. Controlling the voltage of the ME layer will therefore allow switching of the bottom layer.

A similar theoretical idea was proposed by Chen et al. [135]. Two types of spintronic devices based on the ME effect were proposed - 'magneto-electric random access memory' (MERAM) and 'magneto-electric XOR cell' (MEXOR). In both cases a magneto-electric anti-ferromagnet (ME-AF) layer is used for data storage. The bottom layer (which is a soft ferromagnet) comprising of a GMR or TMR structure is pinned to the ME-AF layer to read the data. The soft ferromagnetic layer is exchanged coupled to the magneto-electric anti-ferromagnetic, and so the magnetic moment of the soft ferromagnetic (FM) layer is controlled by the spin structure of the magneto-electric anti-ferromagnet. The spin structures of the AF define the spin orientations of the FM, therefore subsequent resistance measurements of the GMR/TMR stack will read the data.

Vopsaroiu et al. [401] have theoretically described a magnetic recording head technology that works via the stress mediated ME effect . An AF || FM || FE || FM structure is used making use of the AF || FM interface. The AF biases the magnetisation that provides a DC magnetic bias field (the exchange coupling effect) [415] which induces a magnetostrictive stress on the FM layers. As the head moves along the magnetic recording track, the stray field from the recoded bit provides an AC media field. The read head essentially plays the role of transforming the magnetic field signals to the output voltage waveform. The sensor's AC response voltage oscillates following the pattern of the recorded bits. Using FM Terfenol-D as the FM and Pb(Zr,Ti)O_3 as the FE, they estimate that such a sensor could be capable of reading a 1 $Tbit/in^2$ recording medium. Whereas an MR read head requires a constant DC test current passing through it, this theorectical ME read head does not because data is directly read back as an induced ME voltage output. This shows a clear benefit regarding Joule thermal heating issues that occur in the high resistance tunnelling MR sensors [416][417][418] and also reduces the power consumption [419].

Zhang et al. [402] demonstrated this idea experimentally by producing a prototype ME read head using ME heterostructures of magnetic oxides ($NiFe_2O_4$, $CoFe_2O_4$) and the FE oxide, $BaTiO_3$, grown on $SrTiO_3$ single crystal substrates.

They showed that the ME structures sensed the fields generated by a signal generator (which model media fields from the bits in the recording medium) and that a ME output voltage waveform was produced. The response signal, however, was too low for recording medium applications.

Continued efforts into understanding the ME coupling and theoretical approaches to the use of ME heterostructures in future read head technologies has prompted us to consider a read structure design which is relatively simple to manufacture.

8.2 The GMR effect on ferroelectric PZT

8.2.1 Introduction

Following the theoretical predictions by Vopsaroiu et al. [401] a collaboration is arranged with Vopsaroiu and colleagues to investigate the possibility of using the ME effect for future read heads experimentally. The overall aim is to produce a FM/FE hybrid structure (Fig. 8.1) and investigate the change in properties of the FM layer by electrically activating the FE layer. A GMR structure was chosen to act as the FM component. GMR structures, as mentioned in Section 4.4 are considered to have played a major contribution to advancing read heads and are, relatively, simple structures. A well known FE material, lead zirconium titanate (PZT) was chosen to be the substrate material for producing the GMR structure onto. PZT is known for its excellent ferroelectric and piezoelectric properties such as low coercive fields and large piezoelectric coefficients, allowing a high piezoresponse at low operating switching voltages [420][421][422][423]. Upon the application of a voltage to the ferroelectric substrate, a strain is induced in it via the piezoelectric effect, which is transferred to the GMR multilayer. Any changes the voltage may cause to the stack may be observed by changes in magneto-resistance measurements (four point probe method).

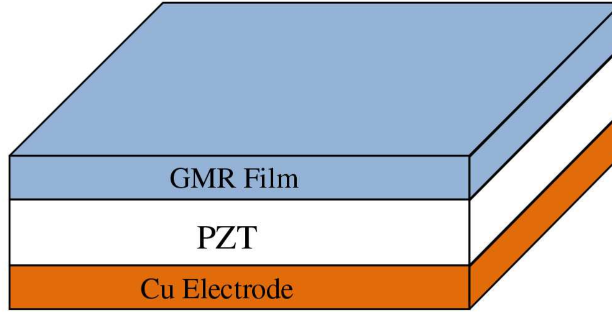

Figure 8.1: Proposed GMR/PZT hybrid.

8.2.2 Co/Cu GMR multilayers

The GMR effect is observed in certain multilayers (ML) consisting of alternating ferromagnetic/non-ferromagnetic films (please refer back to Chapter 4). The GMR ratio refers to the drop in the resistance of coupled magnetic/non-magnetic layers when a sufficiently high magnetic field is applied to the sample. It is calculated from:

$$GMR\ ratio = (\frac{R_0 - R}{R_0}) \times 100\% = (\frac{\Delta R}{R}) \times 100\% \tag{8.1}$$

where R_0 is the measured resistance in the absence of a magnetic field and R is the resistance in the presence of a magnetic field.

The Co/Cu system is one of the earliest ML systems to have been studied and has been used to provide understanding for the GMR phenomenon [424][425][426][427]. Fig. 8.2 shows a basic Co/Cu multilayer system formed onto a substrate; a buffer layer is often used to create an improved surface for the multilayer to grow on. Co is one of the few elements with ferromagnetic behaviour at room temperature [428] and Cu is a very good conducting non-magnetic material. Co/Cu MLs exhibit a strong anti-ferromagnetic exchange coupling [429] and high giant magneto-resistance GMR effects of up to 65% at room temperature [430].

In Co/Cu multilayer systems the magnitude of the giant magneto-resistance effect oscillates as a function of copper thickness [431][432]. This oscillation in magneto-resistance is related to an oscillation in the interlayer coupling between the

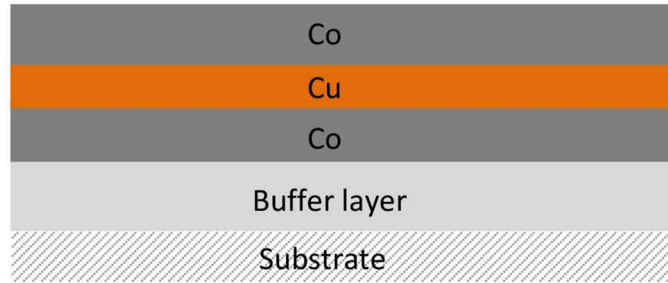

Figure 8.2: An illustration of a Co/Cu multilayer system.

anti-ferromagnetic and ferromagnetic layers as the thickness of the Cu spacer is varied. An example of this is shown in Fig. 8.3. The peaks occur when the alignment of the magnetic layers are anti-parallel and, at the low magneto-resistance values, the alignment of the magnetic layers are parallel. In polycrystalline Co/Cu multilayers the oscillation period is about 10 Å, so anti-ferromagnetic coupling (corresponding to high magneto-resistance, $\Delta R/R$) occurring at about 10 Å, 20 Å and 30 Å (known as the first oscillation peak, second oscillation peak, 3rd oscillation peak). Usually the first oscillation peak displays the highest GMR ratio and is the most narrow. The heights of the peaks progressively become smaller and the peaks broaden as the Cu thickness increase, therefore usually only the first 3 oscillation peaks are observed. Similar oscillations in magneto-resistance and interlayer coupling are present in other GMR multilayer structures such as polycrystalline Fe/Cr, Co/Cr and Co/Ru multilayers [433], and Fe/Cu [434]. The coupling via the non-magnetic metal is long range and of the Ruderman-Kittel-Kasuya-Yosida (RKKY) type [435]. RKKY interactions describe the long range coupling of magnetic moments via the interaction with conduction electrons of non-magnetic layers [436][437][438][439].

In general, experimental techniques for growing Co/Cu ML structures have concentrated mostly on RF or DC magnetron sputtering [440], [441], [442]. These structures have also been reported to have been grown by MBE [443], electrodeposition [444], pulsed laser [445], ion beam deposition [446] and e-beam evaporation techniques [447].

To date there are no reports on Co/Cu GMR structures prepared by the HiTUS technology. One important feature of the HiTUS technique is its ability to sputter thick ferromagnetic targets, which is a major limitation in conventional magnetron

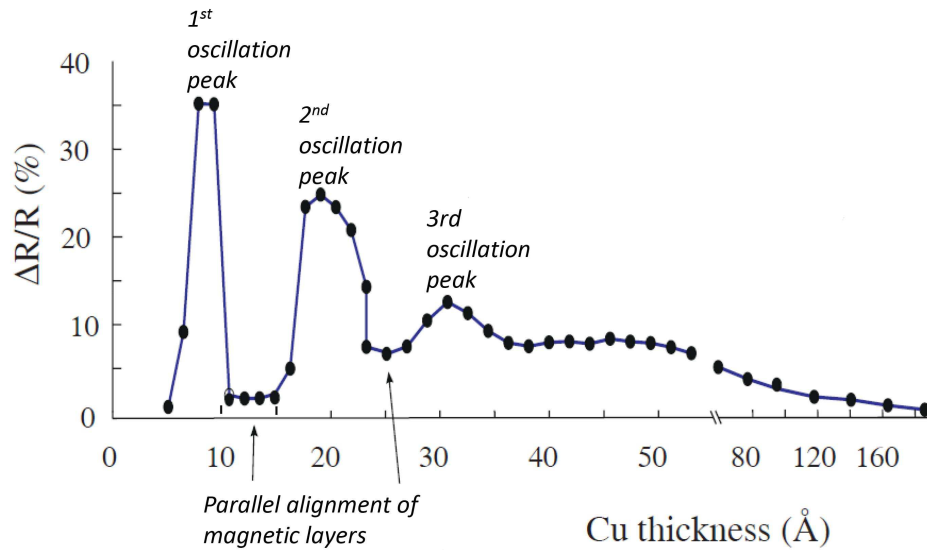

Figure 8.3: Magneto-resistance versus Cu spacer layer thickness for a series of Co/Cu multilayers, adapted from [2].

sputtering systems. By using HiTUS, which has the added advantage of tuning thin film properties via RF power, target voltage and sputter gas pressure, it is expected that HiTUS can produce spin valve GMR structures that are comparable to those produced by conventional sputtering for use in this project on multi-ferroics.

To fabricate GMR multilayers a slow deposition rate would be required to control the thickness of the ultra thin layers of Co and Cu. Due to the independent control of ion energy and ion density with using a HiTUS system, a high ion density can be maintained. Thus, all the benefits associated with sputtering using a high density plasma (such as producing high density films) can be maintained whilst simultaneously maintaining a slow deposition rate; resulting in precise control of film thickness. Preliminary experiments were necessary to assess the capability of HiTUS to produce such thin multi-layer films and to obtain a suitable GMR structure for combining with a PZT substrate.

8.3 Preliminary experiments

8.3.1 Experimental

Alternate layers of Co and Cu were deposited by HiTUS onto commercially available glass slides (Menzel-Glser microscope slides from Thermo Scientific), silicon wafers (IDB Technologies Ltd) and flexible kapton film (50 micron thick polyimide from DuPont Teijin). Prior to deposition the substrates were ultrasonic cleaned in isopropanol. For film thickness control of ultra thin films a low deposition rate is required. This was achieved by using a low RF power of 0.34 kW, a value high enough to strike and maintain a stable plasma, and a voltage of 500 V to the target. Typical operating voltages at Plasma Quest Ltd range between 200 V and 800 V. A mid-value of 500 V was chosen to ensure that the sputtered atoms had enough mobility when arriving at the substrate to form a continuous film. Too high a voltage could lead to disruption of such thin delicate films due to high atom mobility. The base pressure before deposition was 7.0 $\times$ 10^{-7} $mbar$ and the pressure during sputtering was kept at 1.2 $\times$ 10^{-3} $mbar$. HiTUS process pressure influences the surface roughness of thin films. Co and Cu thin films have been produced using different process pressures and their surface roughness was measured. The rms surface roughness for 100 nm Co and Cu deposited at different process pressures are found in Appendix B. These results indicate that for these materials a low sputtering pressure of 1.2 $\times$ 10^{-3} $mbar$ gives smoother films than at higher pressures. The deposition rates for Co and Cu were 0.43 $\AA/s$ and 0.81 $\AA/s$ respectively, under the process conditions mentioned (RF power = 0.34 kW, target voltage = 500 V and process pressure = 1.2 $\times$ 10^{-3} $mbar$). These rates were arrived at by initially depositing a series of thick films of Co and Cu and measuring their thicknesses using a profilometer.

GMR measurements have been carried out at room temperature by a standard four-point probe technique (described in Chapter 6) with a constant current of 4.53 mA applied to the sample. The output voltage was measured to give the resistance of the sample. A magnetic field of 3 kOe was applied in plane of the film. According to Parkin et al. [430] and Shukh et al. [448], 3 kOe should be a high enough field to magnetically saturate Co/Cu multilayers . The magneto-resistance ratio of the

multilayers was determined by the expression (R_0 - R_s)/R_0 where R_0 is the resistance of the sample in the absence of the magnetic field and R_s the resistance in the presence of the magnetic field.

The structure $[Co(8\ \AA)/Cu(t_{Cu})]_{\times 20}$ was used. Since the thickness of the Cu interlayer is mainly responsible for the oscillatory exchange coupling effects [449], initially the thickness of the Cu layer was varied, t_{Cu}. A thickness of 8 Å for the magnetic Co layers was used, chosen in accordance with literature [449][430]. Subsequently the thickness of the Co layer was varied using the optimum t_{Cu} obtained to check if 8 Å is the optimum Co thickness for this work. The number of Co/Cu bilayers influences the GMR ratio [428]. 20 bilayers was chosen by considering the number of bilayers used by other groups [432][448] [450][451][446] and the manual operation of the HiTUS system. A $[Co(18\ \AA)/Cu(48\ \AA)]$ buffer layer and $Co(12\ \AA)$ capping layer was initially used. Subsequently, a GMR multilayer was also deposited onto other buffer layers to seek improvement in GMR values since it is generally known that the type of buffer layer used influences the GMR ratio [440].

8.3.2 Results

Cu thickness variation

Fig. 8.4 shows the magneto-resistance ratio as a function of Cu layer thickness, t_{Cu} for the structure $[Co(8\ \AA)/Cu(t_{Cu})]_{\times 20}$ prepared using the HiTUS technique on three different substrates: silicon, glass and kapton film. A maximum GMR ratio of 16.15 % was obtained for the ML deposited onto silicon at $t_{Cu} = 11$ Å (1st oscillation peak). For the same sample a GMR ratio of 14.55 % was obtained at $t_{Cu} = 20$ Å, corresponding to the second oscillation peak.

For the multilayers deposited on the glass substrate the first and second oscillation peaks are still present, although the first peak is not as pronounced as the ML deposited on silicon. The GMR % is 2.76 % ($t_{Cu} = 10\ \AA$) and at the second oscillation peak is 12.88 % ($t_{Cu} = 21\ \AA$). The first oscillation peak is not observed for the multilayers deposited onto flexible kapton film but the GMR % for the second oscillation peak remains relatively high at 14.39 % for ($t_{Cu} = 22\ \AA$).

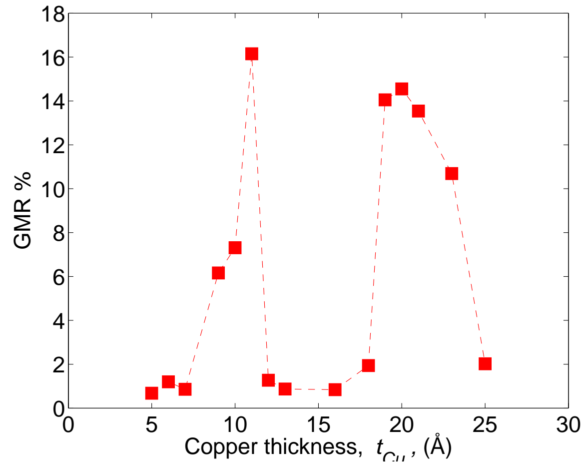

(a) Silicon

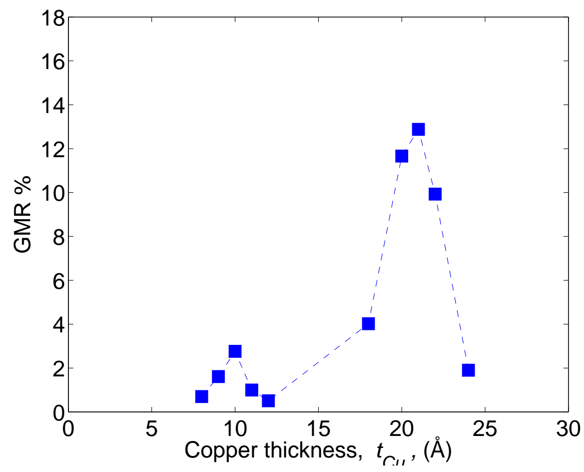

(b) Glass

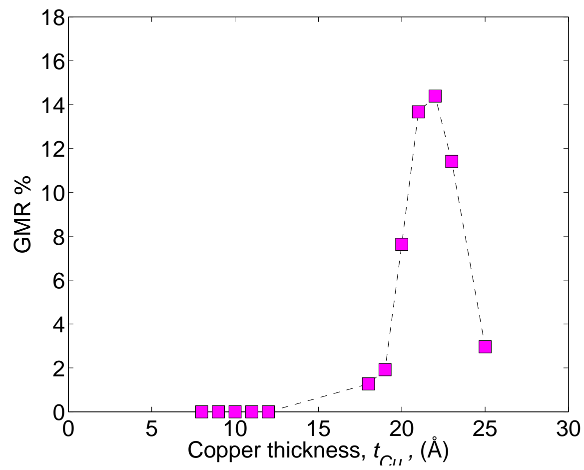

(c) Kapton

Figure 8.4: Measured GMR ratios with varying Cu thickness on (a) silicon, (b) glass and (c) kapton film.

Co/Cu ML structure	Deposition method	GMR at room temperature (%)	Reference
$[Co(10\ \AA)/Cu(20\ \AA)]_{\times 16}$	UHV DC magnetron sputtering	~ 18.5	[452]
$[Co(11\ \AA)/Cu(19\ \AA)]_{\times 20}$	DC magnetron sputtering	25	[448]
$[Co(8\ \AA)/Cu(20\ \AA)]_{\times 30}$	RF magnetron sputtering	~ 25	[449]
$[Co(11\ \AA)/Cu(19\ \AA)]_{\times 25}$	RF magnetron sputtering	~ 19	[453]
$[Co(10\ \AA)/Cu(19\ \AA)]_{\times 16}$	UHV DC magnetron sputtering	~ 25	[432]
$[Co(15\ \AA)/Cu(20\ \AA)]_{\times 30}$	Triode sputtering	~ 19	[425]
$[Co(20\ \AA)/Cu(20\ \AA)]_{\times 10}$	E-beam evaporation	7.2	[447]
$[Co(20\ \AA)/Cu(21\ \AA)]_{\times 11}$	Focused ion beam sputtering	6.7	[446]
$[Co(22\ \AA)/Cu(21\ \AA)]_{\times 30}$	DC magnetron sputtering	24	[454]
$[Co(9\ \AA)/Cu(14\ \AA)]_{\times 62}$	Electro-deposition	~ 16.8	[444]

Table 8.1: Second anti-ferromagnetic coupling GMR values, from literature.

Table 8.1 shows examples of second anti-ferromagnetic coupling GMR values obtained from literature. The multilayers deposited using HiTUS with second oscillation GMR values of 14.55 % (on silicon), 12.88 % (glass) and 14.39 % (kapton) compare well with literature considering that the HiTUS process has not been optimised to produce a better anti-ferromagnetic coupling.

Literature GMR values of over 40 % have been reported for Co/Cu multilayers at the first oscillation peak [430][450][449]. For example, Hall et al. [1996 Hall] achieved room temperature GMR of 61.6 %, Mosca et al. [425] achieved room temperature GMR of about 50 % and Bouziane et al. [441] achieved 42.5 % . For the first oscillation peak, both the Co and Cu layers are extremely thin (10 Å). At this kind of film thickness it is difficult to achieve smooth well defined interfaces without pinholes, which is an important property for large GMR values [449]. Increased interfacial roughness may induce local contacts of neighbouring Co layers, which decrease the magneto-resistance values [455]. Therefore, the GMR of Co/Cu multilayers can be governed by the interfacial roughness [456].

Interfacial roughness may be induced by substrate roughness [457][458]. Interfacial roughness studies have been carried out by various research groups. Interfacial roughness can be generated by using different buffer layers. Wawro et al. [458]

measured the surface roughness of two buffer materials :300 Å of Cu and 300 Å of Co, deposited onto float glass. The surface roughness of the Cu was measured to be 30 Å, and the surface roughness the Co measured to be 10 Å. When Cu was used as a buffer layer the GMR value was 2.62 %. However, when the same multilayer was deposited onto the Co buffer layer the GMR value almost doubled to 5.22 %. El Harfaoui et al. [440] investigated Co/Cu multilayers deposited onto glass and a range of buffer layers. Without a buffer layer the roughness of the glass was 5 Å and gave a GMR of 18 %. 80 Å of Fe deposited onto the glass yielded the smoothest buffer of 1.4 Å giving a GMR of 42.5 %. Ben Youssef et al. [453] produced Co/Cu multilayers with different interface structures by changing the sputtering gas pressure. By examining the roughness at the interface using low angle x-ray diffraction they deduced that GMR was at the maximum when interface roughness had a minimum value.

The surface roughness of Si, glass and kapton substrates used for the Co/Cu multilayers, prepared by HiTUS, were measured by AFM. The rms values for the three different substrate roughness were 7.8 Å, 10.0 Å, and 110 Å respectively. Smooth substrates for ultra thin films is important for obtaining a continuous film. The smoothest substrate is the Si and hence produced the highest quality multilayer. Kapton film was the most rough and hence no first oscillation peak is observed. The surface roughness of 7.8 Å for the silicon substrate is higher than the glass substrate used by El Harfaoui et al. [440] mentioned above (where 18 % GMR was obtained). Substrate roughness may be a contributing factor to the lower GMR value of 16.15 % (multilayer produced on silicon) compared to higher values achieved by other groups.

The crystalline texture and microstructure of thin films and multilayers is very dependent on the method and conditions of their deposition [452]. The second anti-ferromagnetic coupling appears to be less susceptible to substrate roughness than the first. By experience, using the Cu thickness at the second anti-ferromagnetic Cu thickness gives high reproducibility. Therefore t_{Cu} of 21 Å is chosen to be a standard thickness to use in order to create a sensor with maximum GMR ratio.

Co thickness variation

To ensure the thickness of the Co layer used was optimum, its thickness was varied, whilst keeping the thickness of Cu at 21 Å. Multilayers with 10 bilayers of the structure [Co(18 Å)/Cu(48 Å)]/[Co(t Å)/Cu(21 Å)]$_{\times 10}$/Co(12 Å) were deposited onto glass slides, where t is the thickness of the Co layers, [Co(18 Å)/Cu(48 Å)] the buffer layer and 12 Å Co was deposited on top of the ML to help protect the stack from oxidation. Co thicknesses investigated were 7 Å, 8 Å, 9 Å, 10 Å, and 12 Å. GMR measurements have been carried out by the four-point probe technique described in Section 8.3. The results are shown in Table 8.2.

Co thickness (Å)	GMR ratio (%)
7	6.21
8	8.99
9	7.77
10	6.49
12	6.60

Table 8.2: Effect of changing Co thickness on GMR.

By decreasing the Co thickness from 10 Å to 8 Å the GMR increased to nearly 9 % from 6.49 %. The above experimental values indicate that Co thickness does have an effect on the GMR ratio and that 8 Å is a good thickness for use in the fabrication of these multilayer structures.

Effect of buffer layers on GMR ratio

Pure Fe, Cu and Co (66 Å) were deposited onto glass slides and silicon, followed by the structure [Co(8 Å)/Cu(21 Å)]$_{\times 20}$/Co(12 Å). GMR measurements were obtained using the approach described earlier in Section 8.3 and are reported in Table 8.3. The GMR ratio for the combined [Co(18 Å)/Cu(48 Å)] buffer is also shown for comparison.

Although Fe has been reported to give the highest GMR values by other groups [440], [441], a combined Co/Cu buffer layer seems to better suit the films in this

Buffer	GMR ratio (%) on glass	GMR ratio (%) on silicon
None	11.95	14.39
Fe	6.51	11.55
Cu	8.31	12.98
Co	9.95	14.07
Co/Cu	12.88	16.39

Table 8.3: GMR ratio of $[Co(8 Å)/Cu(21 Å)]_{\times 20}/Co(12 Å)$ on different buffers using glass and silicon substrates.

study, probably due to providing the films with more desirable structural properties. This finding is different to other groups because texture of thin films is not only related to the buffer layer used, but also with the type of sputtering method [440].

8.3.3 Observations

A suitable GMR structure has been obtained for use in further studies. The HiTUS system has the ability to deposit ultra thin multilayer films at a slow deposition rate, allowing greater control over the thickness of very thin films. The GMR ratios obtained are comparable with studies by other groups. For example, Bouziane et al. [33] obtained a second oscillation GMR ratio of just below 20 % for a Fe (100 Å)/$[Co (11 Å)/Cu (20 Å)]_{\times 25}$ /Co (12 Å) structure. Honda et al. [449] achieved a second oscillation GMR ratio of about 20 % for a $[Co (8 Å / Cu (20 Å)]_{\times 30}$ structure. Since an increased number of bilayers results in an increased GMR ratio, the result of 16.15 % could be enhanced by increasing the number of bilayers to over 20.

Further support for the ability of the HiTUS system for fabricating ultra thin films is provided by a cross sectional micrograph (Fig. 8.5), taken by a Hitachi HD2300A Scanning Transmission Electron Microscope (STEM) at the University of Surrey. The micrograph shows that although some debris is present, overall a well defined multilayer structure is established.

It is worth stating that the two previously mentioned groups also obtained over 40 % GMR change for the first oscillation peak. This has not been achieved so far in

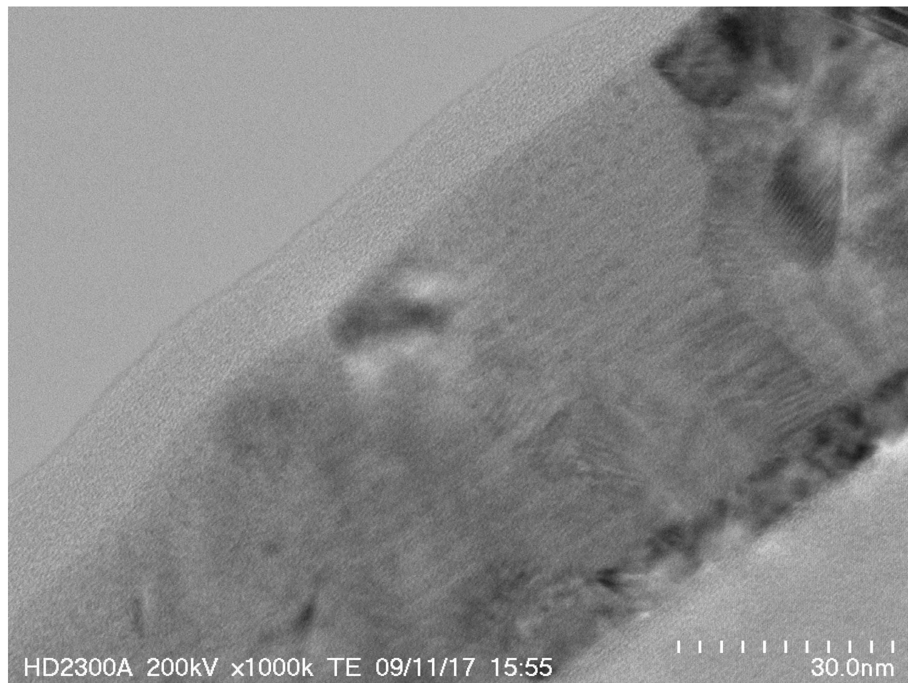

Figure 8.5: STEM image of [Co(18 Å)/Cu(48 Å)]/[Co(8 Å)/Cu(21 Å)]$_{\times 20}$/Co(12 Å) deposited on glass.

this work. The GMR effect is strongly dependent on the growth conditions, temperature, lattice structure, interfacial quality and structural imperfections [459], [454], [460], [452], [451]. With improvements to substrate cleaning and process control, it is believed that a better GMR ratio first oscillation peak is achievable.

The results obtained on flexible kapton film are themselves very interesting. The integration of magneto-electronics such as GMR devices onto lightweight and flexible substrates are attractive for a variety of applications, for example flexible displays, photovoltaic cells and flexible memory devices. Over recent years limited progress has been made in this area due to the small GMR effect achieved. Parkin [95] deposited an exchanged biased sandwich (spin valve structure) onto organic films but only obtained a GMR ratio of about 3 %. Yan et al. [461] used a pulsed laser electrodeposition technique to electrodeposit Co/Cu multilayers onto conducting polymer films and obtained an MR ratio of about 4 % . Uhrmann et al. [462] deposited a spin valve structure onto flexible polyamide substrates by DC magnetron sputtering and reported a GMR effect of 8.6 % and GMR sensors on polyimide substrates prepared by Ozkaya et al. [463] achieved a GMR ratio of only about 2 % . A relatively high GMR ratio of about 35 % comprising of Co/Cu multilayers and

20 bilayers (the same number of bilayers in HiTUS fabricated structures) has been obtained by initially spin coating a 2 μm thick photoresist onto polyester substrates prior to deposition of the multilayer [464]. In this latter study, the thickness of the Co layer was 1 nm and that of the Cu layer was also 1 nm, these thicknesses correspond to the first anti-ferromagnetic coupling maximum. Without the requirement of photoresist, a second anti-ferromagnetic coupling maximum of 14.39 % has been achieved by using HiTUS.

The 14.39 % GMR ratio achieved in this work, on flexible kapton film for the second anti-ferromagnetic coupling peak is encouraging. As mentioned earlier in this section it is believed that the first oscillation coupling peak is achievable with improved film preparation conditions. With this in mind, the HiTUS system is a strong candidate for the deposition of GMR (and other magneto-electronics) onto flexible substrates using simple metallic underlayers, resulting in a simple fabrication process for producing flexible memory devices.

Magnetic sensors are found in computers, aeroplanes, automobiles and factory production lines to name a few [465]. GMR sensors have also been researched for use as chemical and biological sensors [466][88]. For the wide variety of applications of magnetic sensors, the ability to produce flexible devices leads to products that are mobile, mechanically flexible, low cost, low weight and biocompatible [467]. The work regarding GMR on flexible substrates using HiTUS is, therefore, a key finding that is worth further investigations. However, it is not directly relevant to the work on multi-ferroics contained in this thesis, though it has been used to demonstrate that HiTUS can support a range of substrates.

In summary, the HiTUS system has shown to be capable of producing thin film GMR multilayer structures. The GMR value of 16.39 % corresponding to the structure [Co(18 Å)/Cu(48 Å)]/[Co(8 Å)/Cu(21 Å)]$_{\times 20}$/Co(12 Å) relates well to values contained in literature. This structure is highly reproducible and so is chosen for the next phase of work on multi-ferroics, which is described in the next section.

8.4 Combining GMR and PZT

Having obtained a suitable GMR structure, the next phase of work concentrates on studying the magneto-electric properties between the GMR structure and ferro-electric PZT ($PbZrTiO_3$). A GMR multilayer is deposited onto a PZT substrate to investigate its GMR response when the PZT is electrically activated. The ability to produce an electric field induced GMR effect would be an important step towards creating multi-ferroic read heads, as well as electrically tunable spintronic devices [468][469][470].

8.4.1 Experimental

Commercially available PZT ceramic substrates (Fuji ceramics, 10 mm × 5 mm × 150 μm thick, material number C-91) were wet polished, on one side, until optically smooth. Wet polishing was carried out at University of Surrey, using a wet and dry grinder and silicon carbide (SiC) papers of grades 800, 1200, 2500 and 4000. Each polishing stage with SiC lasted 5 minutes and the PZT was cleaned in purified water in an ultrasonic bath between polishing grades. Lastly, 1 μm diamond polish was used and the PZT was placed in purified water in an ultrasonic bath for a final clean. This was important since the magnetic properties are measured by Kerr magnetometry so there must be a substantial intensity of the reflected laser beam coming from the surface. Additionally, a smooth interface between a substrate and film is desirable, especially for ultra thin samples. The PZT has piezo-electric coefficients d_{33} = 640 pm/V, and d_{31} = -330 pm/V (for piezoelectric definitions please see Section 5.3).

The structure [Co(18 Å)/Cu(48 Å)]/[Co(8 Å)/Cu(21 Å)]$_{\times 20}$/Co(12 Å) was deposited onto the polished side of the ceramic substrate at room temperature using a working pressure of 1.2 x10^{-3} mbar, 0.34 kW RF power and 500 V target voltage. The un-polished side of the PZT was coated with 100 nm Cu, using the HiTUS system, to create a good electrical contact to a voltage source.

The magneto-resistance of the multilayers was investigated at room temperature by a four point probe method, described in Section 6.5. An external magnetic field was applied in plane to the sample, perpendicular to the current. Magneto-resistance measurements were taken with various voltages applied across the sample

via electrical contacts to the top surface of the GMR multilayer and the Cu electrode (Fig. 8.6).

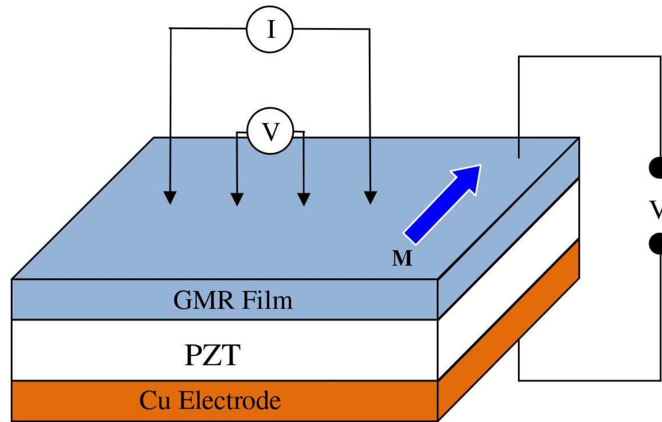

Figure 8.6: Magneto-resistive measurements with applied voltages.

8.4.2 Results

In order to investigate the GMR response of the GMR/PZT structure on the application of an electric field across the ferroelectric PZT, GMR measurements were taken whilst various DC voltages between -350 V and +350 V were applied. Ferroelectric ceramics, including PZT contain grains with multiple domains [471]. The polarisation of each domain has its own orientation. If the polarisation direction of the domains israndomly arranged so that the net polarisation is zero, the material will exhibit no piezoelectric effect. By applying an adequate DC electric field, the ferroelectric domains align to the induced field. When the field is removed, the dipoles remain locked in alignment, giving the material a polar state. This process is known as "poling." Before measurements were carried out on the GMR/PZT structures, the PZT was poled in the plane of the surface to ensure a polar state. Strain measurements conducted by M. Vopson (NPL) confirmed successful poling.

Fig. 8.7 shows the magneto-resistance ratio of the sample with zero voltage applied. The GMR ratio of around 15 % is almost as high as the value obtained by depositing the multilayer onto silicon substrates (16.39 %). Fig. 8.8 shows the results of the experiments on applying various DC voltages. There appears to be no effect on the GMR ratio when DC voltages are applied.

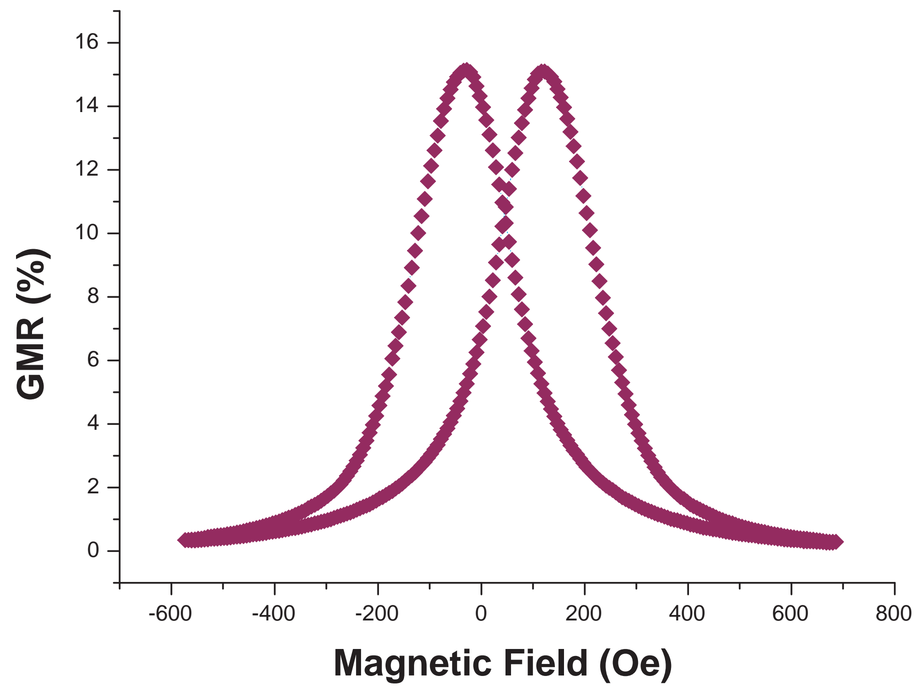

Figure 8.7: Magneto-resistance measurements for hybrid structure PZT/[Co(18 Å)/Cu(48 Å)]/[Co(8 Å)/Cu(21 Å)]$_{\times 20}$/Co(12 Å).

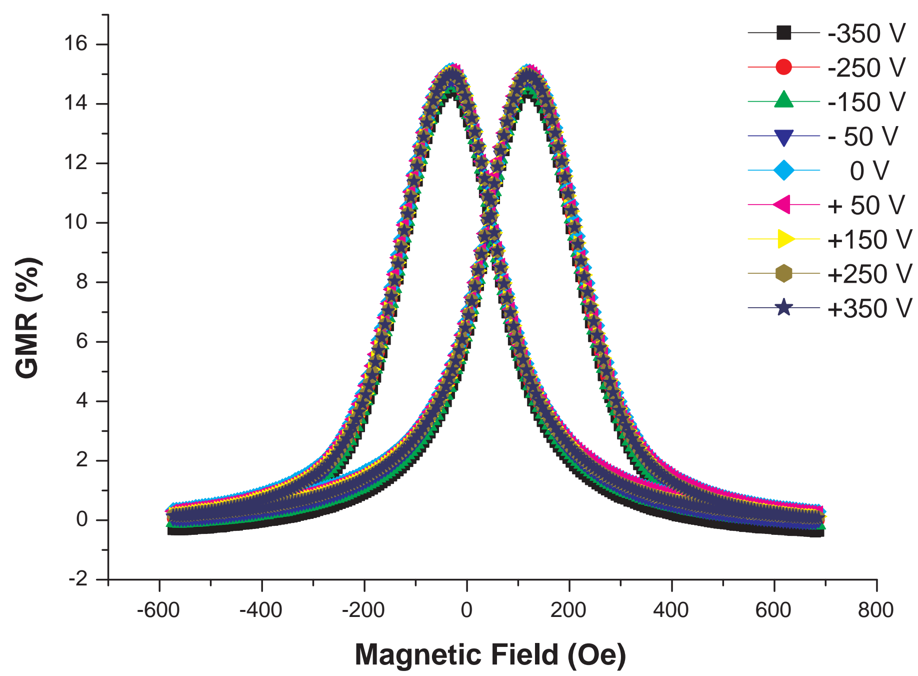

Figure 8.8: Magneto-resistance measurements for different DC applied voltages.

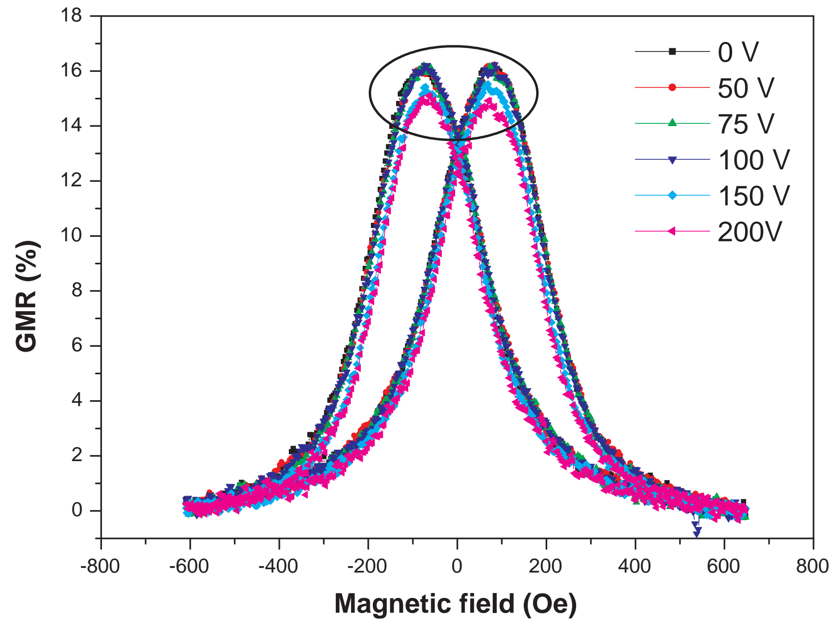

(a)

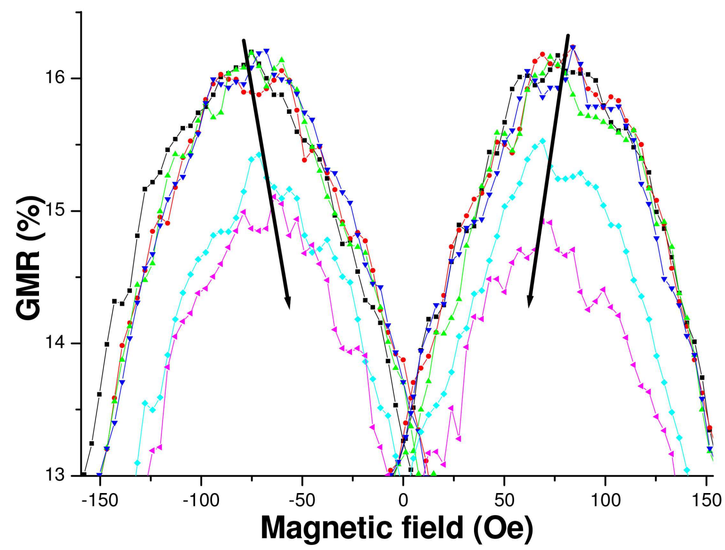

(b)

Figure 8.9: (a) Changes in magneto-resistance with applied AC voltages and (b) a closer view of these changes for the circled area in (a).

However, on the application of an AC voltage across the structure, the magneto-resistance loops reveal a shift in the GMR peak position (i.e. switching field of the GMR stack) to lower fields at larger applied voltages. In addition it appears that the absolute GMR effect is also lowered by the application of the AC voltage on the PZT substrate. This is shown in Fig. 8.9 (a) and (b) shows a closer view of the shift. The GMR ratio is reduced from 16.22 % to 14.88 %. It is predicted that applying AC voltages causes an increase in temperature of the structure, and it is this temperature increase that is responsible for the observed changes, rather than an AC coupling mechanism (please see later work in Section 8.4.3).

Changes in coercive field of soft magnetic films via an applied DC voltages in FM/FE bilayers have been observed by some groups using MOKE measurements [419] [288] [472]. It was therefore expected that if magneto-electric coupling was present in the GMR/PZT films an effect would have been seen using DC voltages. At the maximum voltage applied of 350 V gives an electric field of 23.33 kV/cm (calculated using *electric field = voltage developed/thickness of PZT*), enough to saturate PZT [473][474]. Both Moutis et al. [288] and Boukari et al. [475] studied $Co_{50}Fe_{50}$ on commercial PZT substrates in the final form of interdigitated stripes. Moutis' structure consisted of 17 nm FM, while Boukari deposited 10 nm. In both cases the PZT was poled in the thickness direction, normal to the surface and a DC electric field, E, applied in plane. The piezoelectric charge coefficient, d_{15} (please see Section 5.3 for definition), for their PZT was about 500 pm/V. Moutis et al. showed that applying E in the range of 75 kV/cm (a voltage of 300 V) to the PZT substrate, the applied strain gives an enhancement in H_c of the FM ranging from 50 % to 80 % (applying V in both positive and negative directions caused an increase in H_c). Moutis' work does not fully agree with the work by Boukari. At zero voltage H_c was 16 kA/m, when +200 V (+5 kV/cm) was applied H_c increased to 17.6 kA/m, at -200 V (-5 kV/cm) H_c decreased to 15 kA/m. Resistance measurements also showed a decrease in resistance for increasing voltage in the positive direction but an increase in resistance from zero V to -200 V.

Ma et al. [472] showed that the magnetic characteristics of 30 μm FeBSiC epoxy bonded to a PZT slab could be varied on the application of electric fields larger than the electric coercive field. The PZT slab was poled under a poling field of 40 kV/cm

in the thickness direction and has a d_{33} of 410 pCN^{-1}. During MOKE measurements DC voltages were applied in the thickness direction. They saw significant changes in magnetic anisotropy when an electric field, E, that was higher than the coercive field, E_c, was applied to the PZT. At zero V, a square shaped loop was obtained. Increasing or decreasing DC fields of 20 kV/cm resulted in the loss of squareness and the magnetic field required to saturate the magnetic domains significantly increased. This means that the magnetic layer becomes hard to magnetise and the local magnetisation vector rotates away from in-plane. H_c increased by about 100 % on applying DC fields of around 7 kV/cm then dropped abruptly past the optimum applied electric field.

Zhang et al. [419] reported electric voltage manipulation of the coercive force and saturation magnetisation of NiFe in a NiFe (10 nm)/$BaTiO_3$ structure by applying ± 20 V (DC). The coercive force decreased from 12 Oe at zero bias to about 0.25 Oe at ± 20 V. The saturation magnetisation decreased from 120 emu cm^{-3} at zero bias field to about 40 emu cm^{-3} at ± 20 V.

Where FM/FE hybrids have been shown to display magneto-electric properties, the thickness of the FM films are in the nm or μm regions. As well as those mentioned above other examples include 4μm FeSiB on PZT [476], 70 nm Ni on piezoelectric actuators [289], 10 nm Fe on $BaTiO_3$ [287] and 100 nm Ni on $BaTiO_3$ [290]. Taking this into consideration we questioned whether the 18 Å of Co next to the PZT was thick enough to demonstrate magneto-electric effects.

8.4.3 Additional experimental results

This section presents results of further experimental work and magnetic measurements to confirm that the thickness of the Co underlayer was not likely to be responsible for the sample not displaying any magneto-electric coupling. It was also shown by measurements using a thermocouple that any changes observed using AC fields can be attributed to heating effects.

Magnetic thin films of Co (100 nm) and CoFe (100 nm) were deposited onto

PZT. The magnetisation loops of the samples were taken by a Magneto-Optic Kerr Magnetometer (MOKE), as described in Chapter 6 (see Fig. 8.10). Hysteresis loop measurements were taken in a single sweep, without averaging. The loop sweep duration was 60 seconds. Fig. 8.11 show these measurements taken whilst various applied DC voltages (0 - 200 V) were applied across the PZT substrate.

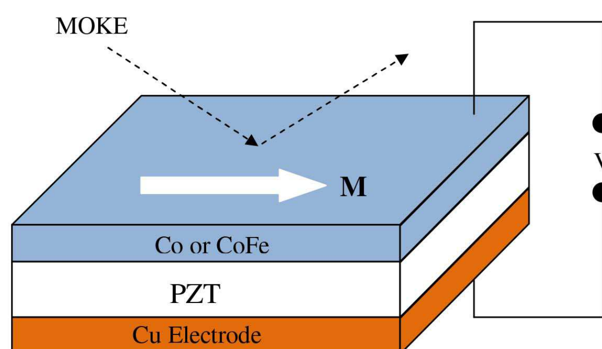

Figure 8.10: MOKE measurements with applied voltages.

Again, there appears to be no effect on the magnetic properties of the magnetic films when the substrate is excited via DC voltages. The laser heating effect from the MOKE instrument has been ruled out by observing fully repeatable hysteresis loops of singly layer ferromagnetic films of various compositions. The DC voltage application on the multi-ferroic composites also had no effect on the coercive field, which also implies that the laser heating effects are negligible.

When AC voltages (at constant frequencies of 117 Hz and 1777 Hz) were applied to the PZT substrate, the magnetic hysteresis loop data reveals a decrease of coercive field as the voltage is increased (Figs. 8.12 to 8.15). Frequencies of 117 Hz and 1777 Hz were chosen as two values that are substantially different from each other and not a multiple of the mains frequency. For the Co/PZT hybrid, the coercivity at zero applied field is 63 Oe; this is reduced to 33 Oe at 117 Hz and 27.5 Oe at 1777 Hz measurement frequency. A similar trend is observed for the CoFe/PZT hybrid. At zero applied field the coercivity of CoFe is 145 Oe but when 200 AC V is applied the coercivity is reduced to 124 Oe at 117 Hz and 121 Oe at 1777 Hz. The coercive values have been extracted from the data presented in Figs. 8.12 to 8.15 and are

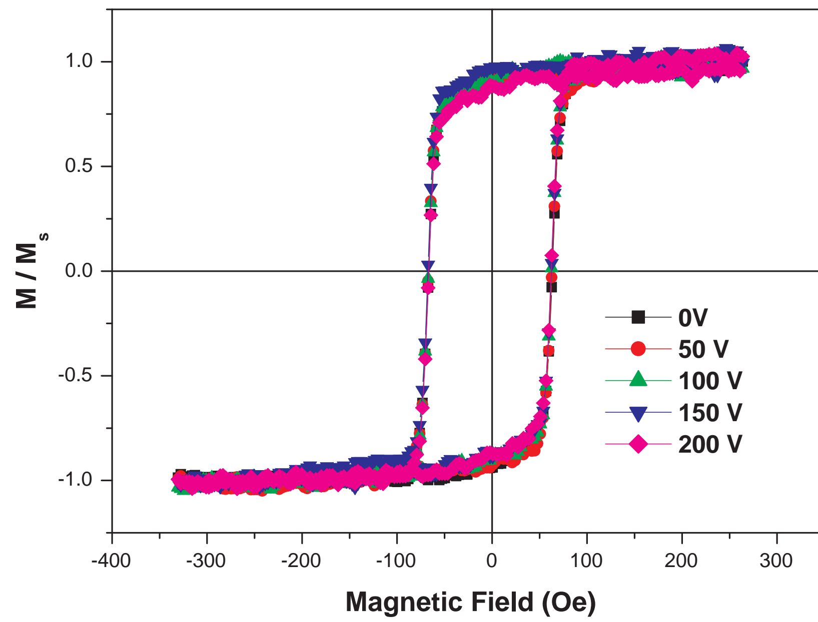

(a)

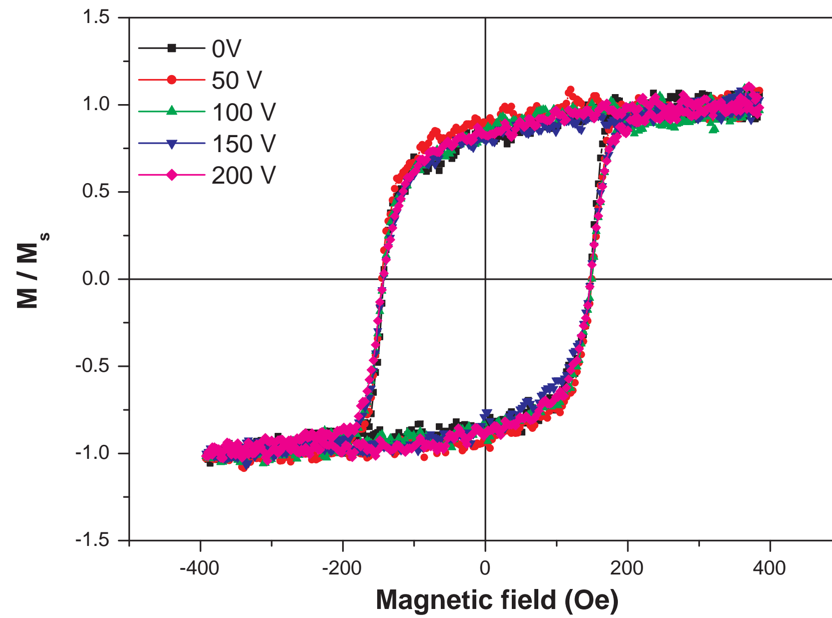

(b)

Figure 8.11: Normalised hysteresis loops for (a) Co and (b) CoFe with different applied DC voltages, measured using MOKE.

shown in Fig. 8.16 as the variation of the coercive field as a function of the AC applied voltage for the two different frequencies. For comparison, the coercive field has been extracted from the DC data, showing the almost constant values.

A small thermocouple was attached to the Co/PZT hybrid to make repeating in situ temperature measurements at the same voltage amplitudes and frequencies. The thermocouple was 0.5 mm^2 and was physically attached to the surface of the sample by using kapton tape. The temperature was read for each voltage amplitude at each frequency directly from the thermocouple controller. Table 8.4 shows a clear increase in temperature of the sample as the voltages are increased, and this heating effect is greater at the higher measurement frequency.

Voltage amplitude (V)	Temperature at 117 Hz (°C)	Temperature at 1777 Hz (°C)
0	21.6	21.6
50	21.9	23.7
100	23.6	38.7
150	57.3	120
200	64.3	120.6

Table 8.4: Temperature of ferromagnet/PZT on applying AC voltages.

Since both the magnetocrystalline and magnetostriction constants are dependent on temperature it is highly likely that this is the source of the coercive field reduction observed. When the coercive fields and the inverse of measured temperature are plotted as a function of the applied voltage at the two different frequencies (Fig. 8.17), it is clear that the two follow a very similar profile.

Since the magnetic coercive field is proportional to the magnetocrystalline (anisotropy) constant, a reduction in the anisotropy constant at higher temperatures would result in a lower coercive field. Although a weak ME coupling may be occurring in the samples, undoubtly the above observed results are dominated by thermal effects [477].

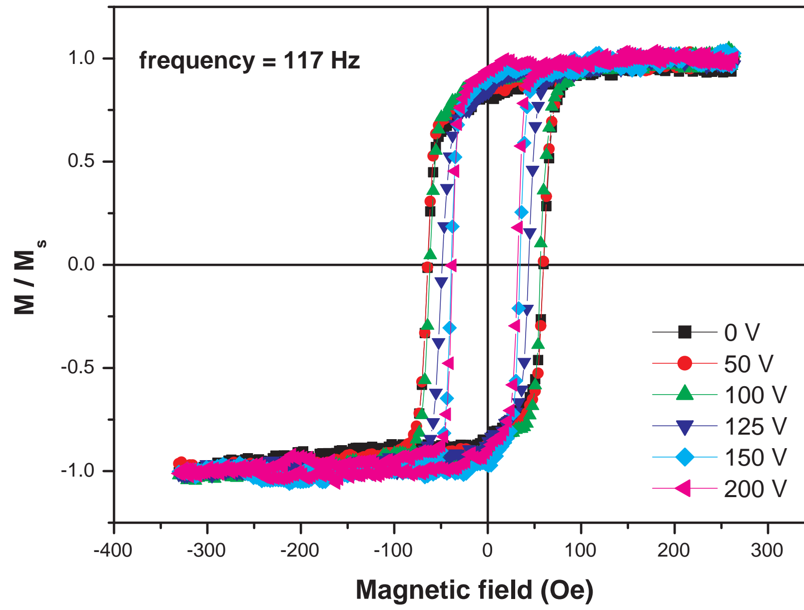

Figure 8.12: MO loops for 100 nm Co film, with applied AC voltages at 117 Hz.

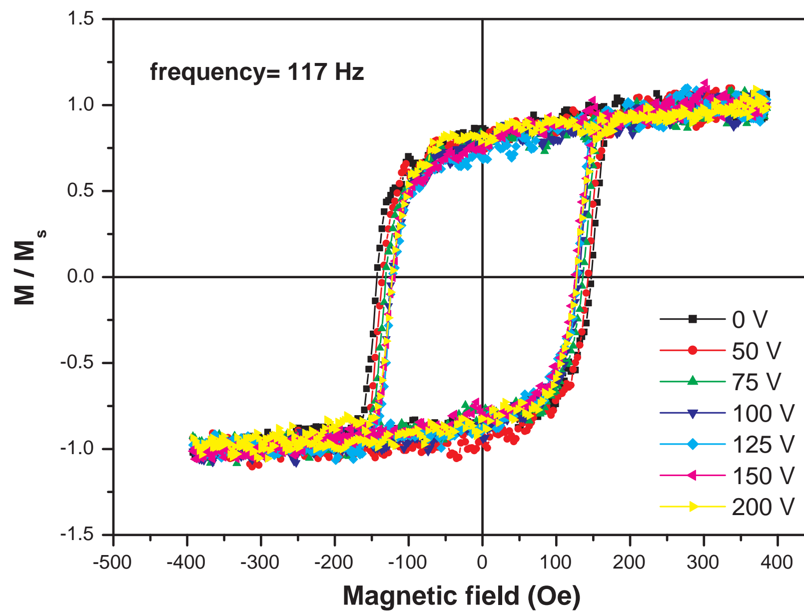

Figure 8.13: MO loops for 100 nm CoFe, with applied AC voltages at 117 Hz.

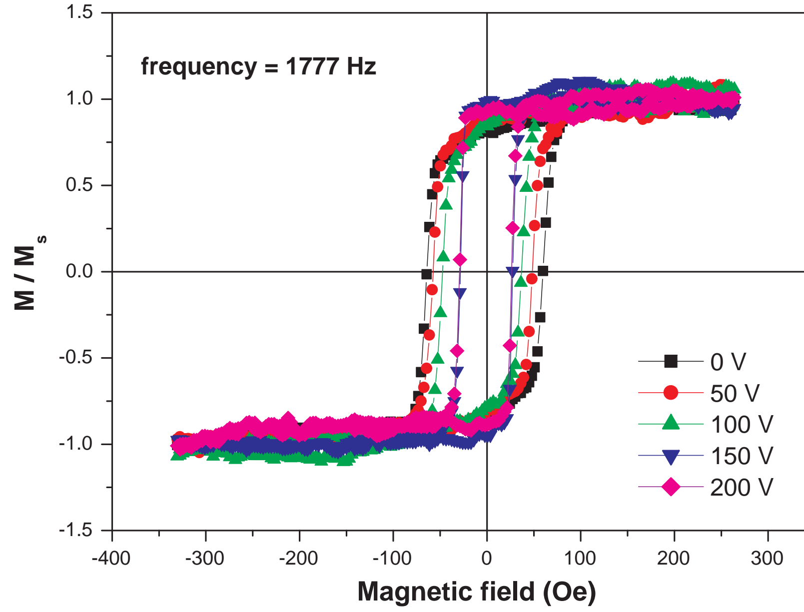

Figure 8.14: MO loops for 100 nm Co, with applied AC voltages at 1777 Hz.

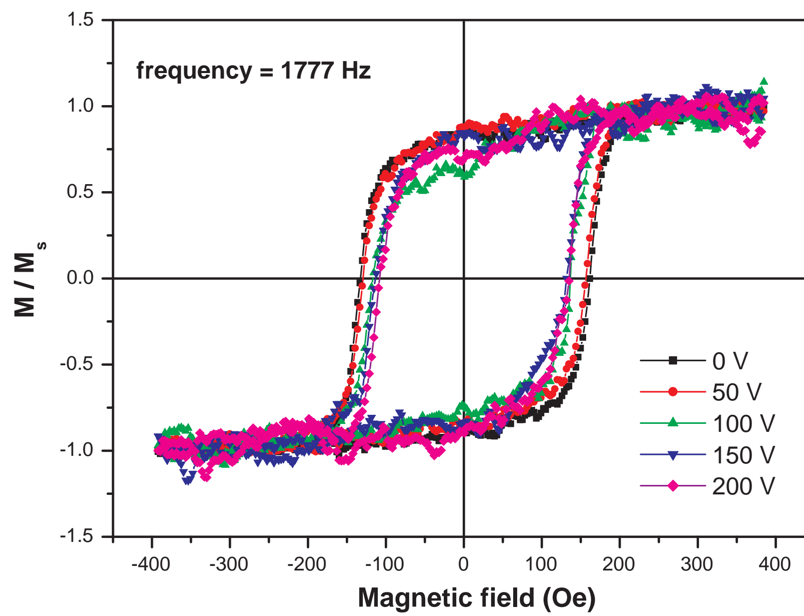

Figure 8.15: MO loops for 100 nm CoFe, with applied AC voltages at 1777 Hz.

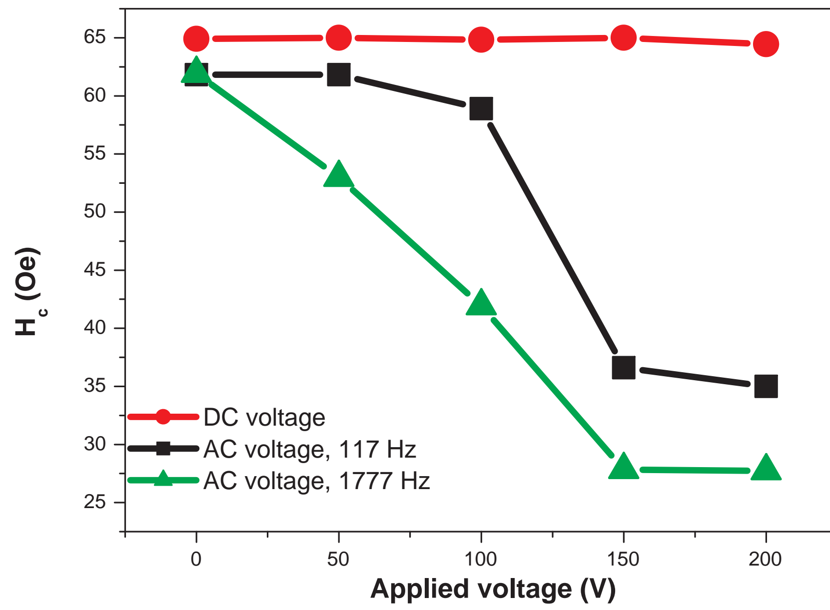

(a)

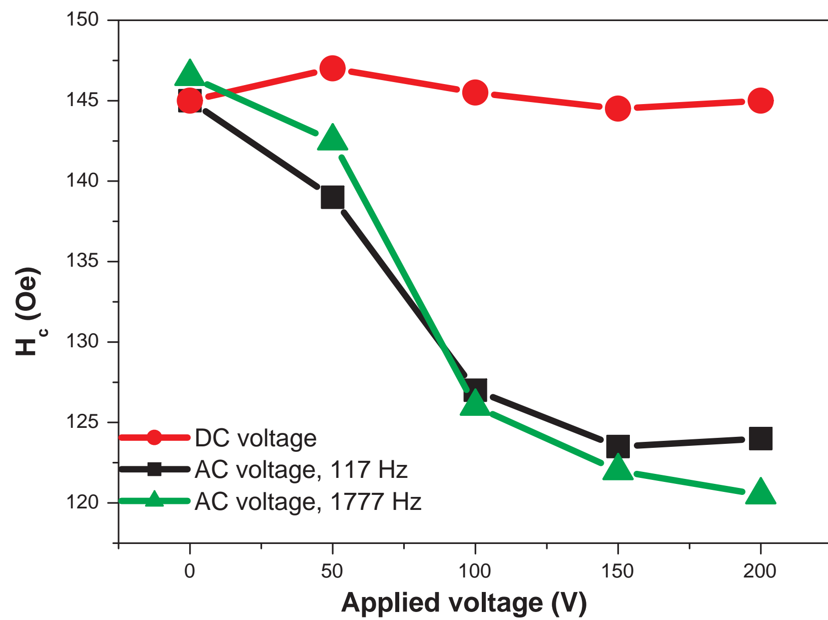

(b)

Figure 8.16: Decrease in coercive field for (a) Co and (b) CoFe on application of AC voltages to PZT.

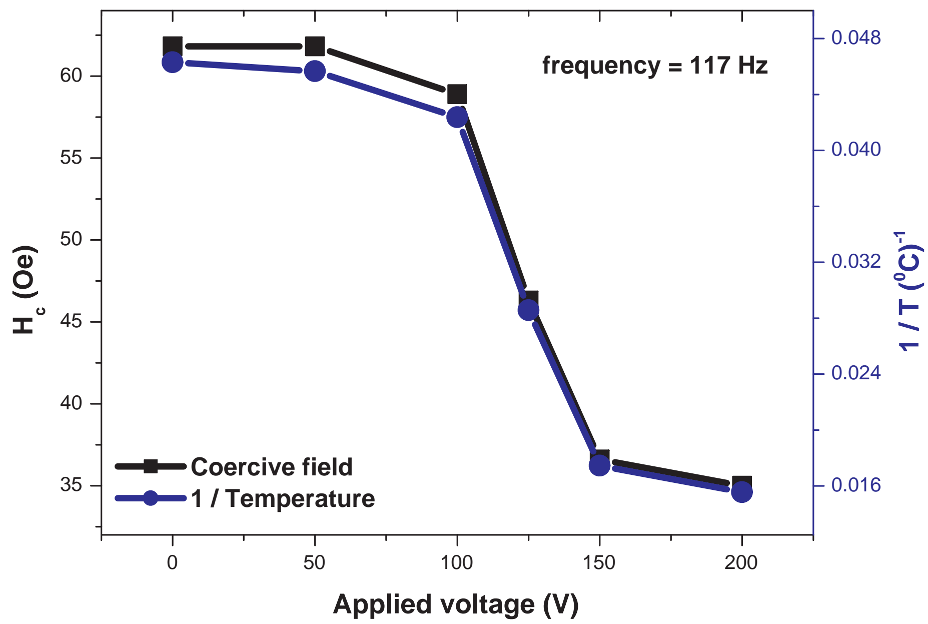

(a)

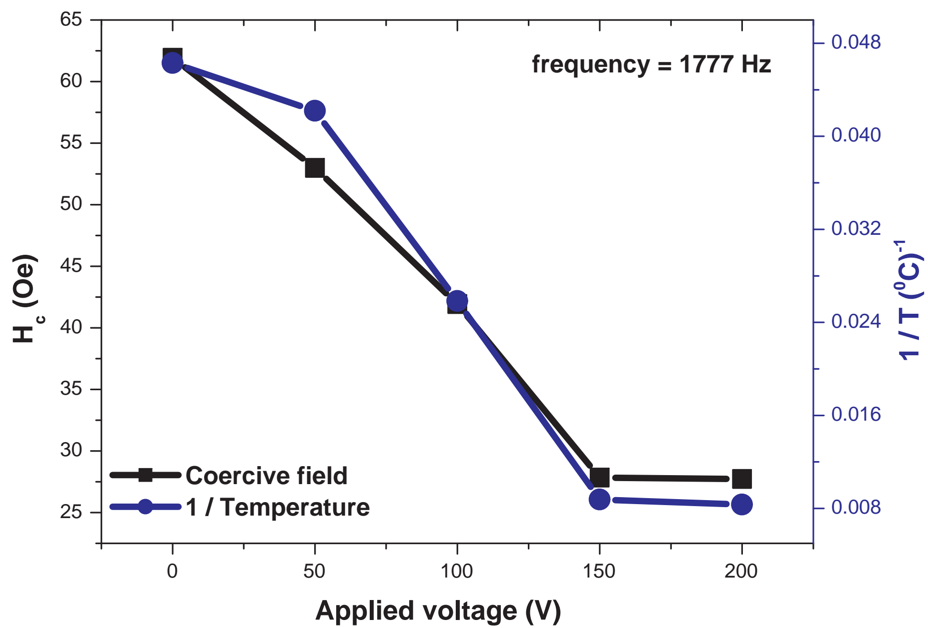

(b)

Figure 8.17: Coercive field and inverse of measured temperature as a function of applied voltage at (a) frequency = 117 Hz and (b) frequency = 1777 Hz.

8.5 Summary and conclusions

Magneto-electric multi-ferroics have attracted considerable interest as they are regarded as playing a large part in future pioneering devices due to their multi-functionalality. The magneto-electric (ME) effect, the effect by which magnetism can be induced by an electric field and vice versa, has been known for decades. One of the first studies which gave evidence of the ME effect was published in the very early 1960's using Cr_2O_3 [478]. The last decade has seen a resurgence of research in this field, driven, in part by the development of thin film growth techniques [479][480][275]. The HiTUS system is one such technique.

In this chapter the relatively new HiTUS system has been used to produce a GMR/FE hybrid in an attempt to address some key issues relating to the design of future read heads in hard disk drives. By producing a sensor which could be manipulated by electric fields would be advantageous in many ways, for example, miniturization of devices, reduction in energy consumption and the range of materials that could be exploited would lead to increased sensitivity of devices.

The HiTUS system has been assessed to be capable of producing ultra thin GMR multilayer structures giving a GMR ratio of 16.15 % for a structure deposited on silicon, which compares well with literature values. These multilayers were also successfully deposited onto glass substrates, kapton film and PZT. Although improvements on the structure could have continued, it was not necessary as this resistance change was adequate to use in the GMR/FE hybrid. The GMR results obtained on flexible kapton films give great encouragement that HiTUS could play a role in developing future flexible electronic applications.

PZT, a well known ferroelectric was used as the substrate to which a GMR multilayer was successfully deposited. A magnetic field was applied in plane to the sample. The magneto-resistance of the multilayers was investigated at room temperature by a four point probe method. Unexpectedly, when DC voltages were applied to the hybrid no change was observed in the measured magneto-resistance curve. However, when AC voltages were applied to the same sample a shift in the magneto-resistance loop was observed, showing a decrease in the coercivity of the

structure, as well as a decrease in GMR ratio. The changes observed on the application of AC voltages was confirmed to be attributed to heating effects, an artifact that cannot be attributed to a multi-ferroic coupling. Whilst these results cannot be generalized or invalidate previous studies, such possible artifacts should be given proper consideration in future studies of magneto-electric multi-ferroics [481].

The GMR/PZT hybrid did not display any evidence of ME coupling. It has been shown by depositing 100nm of magnetostrictive Co and CoFe onto PZT that film thickness is not a primary cause for not obtaining ME coupling in this work. Other underlying features must be addressed if this work continues. There are many complications including the mis-match of lattice constants between the multilayer and PZT leading to misfit dislocations at the interface. In addition, very thin films cannot relax their unit cell dimensions when they are attached to a thicker substrate or layer and any strain induced must stay continuous across the interface. Due to the multi disciplinary character of such hybrid sub-micron architectures, it is not trivial to obtain successfully an effective coupling between FM and PE properties.

Chapter 9

Concluding remarks

High target utilisation sputtering (HiTUS) is a relatively new deposition technique. It has been used in this thesis to deposit thin film magnetic materials with two main objectives, both of which contribute towards the development of current magnetic hard disk drives. The first addresses the threat of superparamagnetism on storage density limits by using high K_u materials as the storage medium. The second delves into the fascinating research area of multi-ferroics; and the possibility of using multi-ferroic materials to improve upon magneto-resistive read sensors for higher density recording media.

$L1_0$ FePt is a top candidate for use as magnetic media due to its high K_u. Using HiTUS, FePt and FePtN have been deposited onto silicon substrates, annealed the films at temperatures between 300 and 800 °C and investigated their magnetic, electrical and structural properties. It has generally been found for the FePt films that the magnetic properties initially improved on annealing but then degraded at about 400 °C without achieving the desired ordering of the as-deposited structure. XRD analysis strongly suggests that this was due to the reaction of the FePt film with the silicon substrate before the transformation from fcc (dis-ordered) phase to fct $L1_0$ (ordered) phase could take place. Although some groups have shown that silicides can improve the transformation kinetics of the disordered FePt phase to the ordered phase, it has not been the case in this work. It has also been shown that the addition of nitrogen to FePt thin films can hold off silicide formation up to temperatures of 700 °C. For the FePt films the coercivity reached a maximum of 450 Oe when annealed at 450 °C, whereas the maximum coercivity of the FePtN

films was measured as 2900 Oe at 800 °C. With reference to thermodynamic data it is predicted that silicon nitride is continually forming as the nitrogen reacts with the silicon substrate and as the temperature is increased, the rate of this reaction is also increased until the nitrogen has been totally removed from the FePt film by either reaction with the substrate or diffusion into the atmosphere in which annealing is taking place (after about 700 °C). The presence of FeN and the formation of its different phases are also considered to influence the properties shown by FePtN. The use of nitrogen can also help reduce the rate at which M_s and M_r decreases during thermal treatment as compared to un-nitrided FePt films. It can therefore be said that below 700 °C the addition of nitrogen during deposition can reduce silicide formation for FePt thin films deposited onto silicon substrates and can aid the stabilisation of magnetic properties.

At the time of writing this thesis XRD data provides evidence of the ordered $L1_0$ phase present in an FePt film that has been annealed at 400 °C. A clear (001) orientation peak is present in the diffraction pattern at 400 °C which according to XRD data, ordering occurred just before silicide formation took over. In plane and out of plane coercivities of 7180 Oe and 6300 Oe were measured. It would be worth returning to this sample for detailed analysis, for example composition analysis, and drawing comparisons to a sample prepared under the same conditions which show very different magnetic properties. This would help us identify key differences between the samples which could lead to further improvements in future films. It would also be interesting to reproduce this sample with and without lower traces of nitrogen (to resist silicon pollution) and investigate annealing temperatures in a narrow range around 400 °C. These are encouraging signs that HiTUS can produce $L1_0$ FePt at temperatures below 400 °C on silicon substrates if silicide formation can be controlled. Some studies performed on glass slides showed ordering of as-deposited films between 400 and 500 °C but not along the c-axis (requirement for $L1_0$ FePt). Particularly for mobile electronics it would be worth conducting more experiments on high temperature glass substrates.

A thermodynamic simulation could be conducted to provide theoretical evidence to support the results obtained on the formation of silicon nitride in FePtN films. A simulated model could also provide insight into the possible results should different

annealing conditions be used, for example the effects of different annealing times or different Ar/H_2 gas ratios. Since it is suggested that not enough nitrogen was present in the FePtN films to fully form a silicon nitride matrix host material a theoretical model could also predict the amounts of nitrogen required to form a silicon nitride matrix by reaction of nitrogen within a film with a silicon substrate. Experimentally, methods of introducing more nitrogen into a film could be performed readily by introducing more nitrogen into the sputtering gas during deposition. The nitrogen content could even be enhanced during thermal annealing by adding nitrogen to the annealing gas environment.

Further studies would enable a better understanding in the behaviour of the films produced. Detailed structural studies, for example cross sectional TEM analysis could clarify the formation of silicide layers. Composition analysis, for example by Energy disperse x-ray diffractometry could provide valuable information about the films, particularly after the initial film deposition stage.

There are ample opportunities that remain to be explored on the fabrication of $L1_0$ FePt using the HiTUS system. The properties of the growing film may be changed at ease by controlling the deposition conditions. For example changing the RF and target voltages can impact the magnetic properties of FePt films (see Table A.1 in Appendix A). Another parameter for future studies, that can affect the growing film, is the process pressure. In some earlier studies it has been observed, by AFM, that by lowering the process pressure in cobalt and copper films, surface roughness can be reduced (see Table B.1 in Appendix B).

FePt films have been deposited at ambient temperatures and post deposition annealing was performed in an encapsulated quartz tube within a tube furnace. Different annealing methods yield different structures. A common annealing method used by other research groups is that of ultra high vacuum annealing, it would be interesting to also use this method and compare results obtained from different annealing methods. In addition, a heated substrate table can be put into the HiTUS system in order to investigate the deposition of FePt at non-ambient temperatures.

To investigate the magneto-electric effect for potential future read sensors, ba-

sic GMR multilayers were initially produced onto silicon, glass, flexible kapton film and PZT substrates. Though interesting results emerged with the samples on kapton this was not investigated further due to it not being an essential part of this program. However, by obtaining GMR ratios on kapton that are similar to results achieved on silicon, it has been shown that HiTUS is a promising deposition tool for future flexible electronic applications.

The GMR multilayer deposited onto PZT was subjected to a range of voltages and the change in magneto-resistive properties has been studied. By way of MOKE measurements the change in magnetic properties of single layers of Co and CoFe on PZT, when subjected to various voltages, have been studied. Unfortunately it was not possible to demonstrate changes in magneto-resistance, nor change the magnetic properties of Co and CoFe by applying DC voltages across the PZT. On the application of AC voltages a decrease in GMR ratio for the GMR/PZT hybrid and a decrease in hysteresis properties of Co and CoFe was observed. These changes by AC voltages were confirmed to be due to heating effects and not a magneto-electric coupling mechanism; this highlighted the requirement for careful measuring techniques when conducting such experiments. Theoretically, a read sensor based on the magneto-electric effect could be possible but experimentally there have been very few successful reports.

Appendix A

Magnetic data for FePt films deposited under different conditions

RF power (kW)	Voltage (V)	$\parallel$ *or* $\perp$	M_s (emu/cm^3)	M_r (x10^{-3} emu)	H_c (Oe)	Magnetic moment (x10^{-3} emu)	SQR
1.10	310	$\parallel$	906	0.860	125	1.14	0.75
1.10	310	$\perp$	949	0.00698	225	1.19	0.01
0.50	310	$\parallel$	683	0.654	22	0.859	0.76
0.50	310	$\perp$	750	0.111	225	0.942	0.12
1.10	620	$\parallel$	731	0.547	95	0.918	0.60
1.10	620	$\perp$	730	0.620	380	0.918	0.68
0.50	620	$\parallel$	936	0.843	125	1.18	0.72
0.50	620	$\perp$	1010	0.110	80	1.27	0.09

Table A.1: Summary of some magnetic information extracted from hysteresis loops on FePt samples deposited under different RF power and target voltages. By changing these two parameters the magnetic properties change, as is particularly evident by the coercivity and squareness (SQR) values.

Appendix B

Surface roughness of Co and Cu films sputtered at different process pressures

Material	Process Pressure (x$10^{-3} mbar$)	rms roughness (nm)
Cu	3.2	0.815
Cu	2.2	0.680
Cu	1.2	0.574
Co	3.2	0.681
Co	2.2	0.574
Co	1.2	0.338

Table B.1: The reduction in film roughness as process pressure is reduced

Appendix C

Journal articles published as a result of the work of this thesis

Journal of Magnetism and Magnetic Materials 331 (2013) 216–219

Contents lists available at SciVerse ScienceDirect

Journal of Magnetism and Magnetic Materials

journal homepage: www.elsevier.com/locate/jmmm

Suppressed silicide formation in FePt thin films by nitrogen addition

Y. Tran, C.D. Wright *

College of Engineering, Mathematics and Physical Sciences, Harrison Building, Streatham Campus, University of Exeter, North Park Road, Exeter EX4 4QF, UK

A R T I C L E I N F O

Article history:
Received 30 August 2012
Available online 1 December 2012

Keywords:
FePt thin film
FePtN thin film
Silicidation
HiTUS

A B S T R A C T

FePt and FePtN thin films have been prepared on silicon substrates by the relatively new deposition technique known as High Target Utilization Sputtering. Films were annealed post-deposition at temperatures up to 800 °C in order to induce the high-anisotropy $L1_0$ phase. The FePt films initially showed an improvement in magnetic properties with annealing temperature, but for annealing above around 400 °C the magnetic properties deteriorated markedly. The magnetic properties of the FePtN films, however, continued to improve with increasing annealing temperature, right up to the maximum temperature applied of 800 °C. Analysis by X-ray diffraction revealed the formation of iron and platinum silicides in FePt films above 400 °C, but that such silicides are absent from the FePtN at all annealing temperatures except 800 °C. This behavior is attributed to the nitrogen in FePtN films reacting preferentially with the silicon in the substrate to form silicon nitride, thus suppressing the formation of platinum and iron silicides. Thus, by introducing nitrogen during the deposition of FePt films on Si substrates the formation of deleterious silicides appears to be suppressed during thermal treatment, thereby offering protection against silicon pollution.

© 2012 Elsevier B.V. All rights reserved.

1. Introduction

FePt thin films have attracted considerable attention for their potential as high density magnetic recording materials. The $L10$ ordered phase of FePt alloy is one of the most promising candidates for perpendicular magnetic recording beyond 1 Tbit/in^2 because of its high magnetocrystalline anisotropy constant K_u of about 10^7 erg/cm^3 [1] which leads to a high thermal stability against superparamagnetic effects [2]. However, as-deposited films fabricated by sputtering are of the disordered A1 phase. To obtain the $L1_0$ phase, post-deposition annealing above 500 °C is usually required (alternatively high deposition temperatures may be used [3]). High temperature processes are not attractive for industrial production, and high temperature treatments also typically lead to both grain size and exchange coupling increases [4] which are unfavorable for obtaining high recording density and high signal-to-noise ratios. It is therefore important to examine ways in which the A1 to $L1_0$ transformation temperature might be reduced, and also ways in which inter-granular coupling might be alleviated.

Some approaches already investigated to reduce the ordering temperature have included the addition of additional materials to FePt (e.g. Cu [5,6], CrRu [7] and Al [8]), the use of underlayers (e.g. Bi [9], MgO [10] and Ag [11]) and the multilayering of Fe and Pt [12,13]. It has also been shown that grain growth can be suppressed during heat treatment by isolating magnetic grains in a nonmagnetic matrix [14,15] such as SiO_2 [16], Al_2O_3 [17], B_2O_3 [18], and Si_3N_4 [19]. In this work we examine the efficacy of a novel thin film sputter deposition technique (the so-called High Target Utilization Sputtering (HiTUS) approach) for the preparation of FePt alloy thin films, in particular when combined with an approach that incorporates nitrogen via the reactive sputtering of FePtN.

The HiTUS sputtering technique was originally developed by Thwaites et al. [20,21] and uses a remotely generated plasma 'injected' into the sputter chamber, rather than relying on a plasma generated directly above the sputter target. By this approach the 'racetrack' target erosion encountered in conventional magnetron sputtering is avoided, so enhancing target life and utilization. In addition, it has been suggested that the remote plasma aids with densification of the growing thin film, avoiding process gas inclusion and poor intergrain boundaries or voids [20,22]. Furthermore, the production of high-anisotropy FePt films by the incorporation of nitrogen via a FePtN starting composition may have beneficial effects; for example Wang et al found that introducing an appropriate amount of nitrogen during sputtering enhances the magnetic properties of $L1_0$ FePt films [23], while Newman et al. [24,25] found that high-anisotropy $L1_0$ CoPt thin films could be successfully produced by thermal annealing of as-deposited CoPtN material. In this paper we show that this method can also be used within the HiTUS system to produce FePt thin films and, importantly, that nitrogen introduced during sputtering appears to suppress the formation of Fe and Pt silicides during post-deposition thermal

* Corresponding author.
E-mail address: David.Wright@exeter.ac.uk (C.D. Wright).

0304-8853/$ - see front matter © 2012 Elsevier B.V. All rights reserved.
http://dx.doi.org/10.1016/j.jmmm.2012.11.045

annealing, and the consequent deleterious effect on magnetic properties that such silicide formation introduces.

2. Experimental

Using the HiTUS system FePt samples of 25 nm thickness were sputtered directly onto naturally oxidized silicon wafers at ambient temperature. The base pressure of the sputter chamber was 1.0×10^{-6} mbar. The sputtering pressure remained at 2.2×10^{-3} mbar after introducing high purity argon gas (99.995%). The RF power source was fixed at 1.10 kW and target voltage at 620 V. The deposition rate of FePt was 2.63 Å s^{-1}. For the FePtN samples, 10 sccm of nitrogen was introduced before deposition. The sputtering pressure remained at 2.2×10^{-3} mbar after the flow of nitrogen and argon had stabilized. The RF power source was fixed at 1.10 kW and target voltage at 620 V. The deposition rate of FePtN was 2.69 Å s^{-1}.

Following deposition, the samples were annealed in a sealed quartz tube in an argon/hydrogen mixed gas. The samples were annealed at various temperatures between 300 °C and 800 °C for 60 min. The different phases of the film were characterized by X-ray diffractometry (XRD) with Cu-Kα radiation of wavelength 1.54060 Å. The magnetic properties were studied with vibrating sample magnetometry (VSM) at room temperature with maximum applied field of 20 kOe.

3. Results and discussion

The X-ray diffraction patterns for the as-deposited FePt samples and those annealed at different temperatures are shown in Fig. 1. The peaks in as-deposited films match those of $FePt_3$ of which the main $FePt_3$ (111) peak occurs at 40.3°. As the films are annealed through to 350 °C, this peak is shifted slightly and becomes matched to FePt (111). This indicates a small loss in Pt during annealing up to this temperature. What were clearly the main peaks (for $FePt_3$ $2\theta=40.3°$ and 46.9°; for FePt $2\theta=40.6°$ and 47.2°) gradually become smaller as annealing temperatures increase and eventually disappear after 400 °C. At 400 °C a new set of peaks begin to take form at about 45° and become clearly 'separated' by 800 °C. One of these peaks is well matched to Fe (45.1°) and the other to $Fe_{0.75}Pt_{0.25}$ (43.1°). However, a strong peak at 45.3° could represent the presence of the iron silicide Fe_5Si_3 (211). This indicates that as the FePt film is annealed the Pt is continually being removed from the as deposited structures. Some Pt does remain bonded to the FePt as the $Fe_{0.75}Pt_{0.25}$ and $Fe_{0.5}Pt_{0.5}$ matches show, but a significant amount of Pt appears to have reacted with the silicon substrate forming platinum silicides. As annealing temperatures are increased to over 350 °C, a mixture of various iron silicides and platinum silicides are produced.

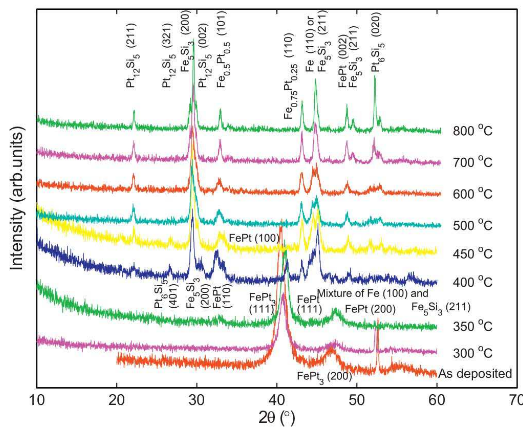

Fig. 1. X-ray diffraction patterns of FePt for different anneal temperatures (deposited onto silicon).

The X-ray diffraction results for the nitrided (FePtN) samples are shown in Fig. 2. Where in the FePt samples the disappearance of the main $FePt_3$ (111)/FePt (111) peaks is accompanied by the emergence of new peaks after 350 °C, this does not occur in FePtN. At 800 °C many new peaks do appear but the FePt (111) peak remains. FePt(100) and (110) peaks are shown to emerge at 500 °C and are clearly visible at 600 °C. This shows improved ordering of the film. When 800 °C is reached, many more new peaks appear. As well as peak matches to iron and platinum silicides, FePt (001) and (002) peaks are also present, which represent the phases for the high anisotropy $L1_0$ structure.

By comparison of Figs. 1 and 2 it can be seen that in FePtN starting films the presence of nitrogen appears to hinder silicide formation. This is most likely due to reaction of the nitrogen with the Si substrate, preferentially forming silicon nitride over platinum silicide. This is supported by considering thermodynamic data for the likely reactions expected for our films (Table 1). The enthalpy of formation for Si_3N_4 is much more negative than for the formation of the other products. This means that the formation of Si_3N_4 has a lower energy than the formation of the other products, indicating that Si would preferentially combine with nitrogen rather than with either Fe or Pt.

Silicide formation can play a detrimental role in the magnetic properties of FePt films. Fig. 3 shows the variation of the in-plane

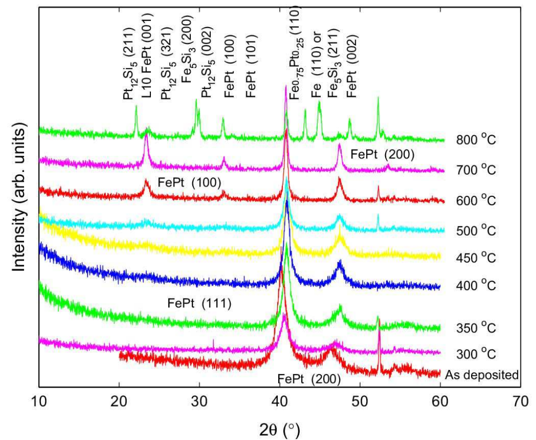

Fig. 2. X-ray diffraction patterns of FePtN for different anneal temperatures (deposited onto silicon).

Table 1
Enthalpy of formation values.

Material	Enthalpy ($\Delta H_f^{\ominus}$) (K J mol^{-1})	Reference
FePt	−27.2	[26]
FeSi	−99.8	[27]
PtSi	−59.6	[28]
Pt_2Si	−63.3	[28]
Si_3N_4	−828	[29]

and perpendicular coercivity values for the FePt and FePtN films as a function of temperature. These values have been extracted from hysteresis loops measured by vibrating sample magnetometry.

It can be seen from Fig. 3 that the in-plane coercivity of FePt increases from 95 Oe to a maximum of 450 Oe after annealing at 450 °C. Increasing the temperature further results in a decrease of coercivity towards zero. The initial increase and subsequent decrease in coercivity is also observed in the perpendicular measurements, with an initial coercivity of 380 Oe rising to a maximum of 825 Oe at 350 °C before decreasing to zero at higher temperatures.

Both the in-plane and out-of-plane coercivities for the as-deposited nitrided samples have zero coercivity. This indicates successful inclusion of the nitrogen into the as-grown films, which are essentially nonmagnetic (not ferromagnetic). The in-plane coercivity steadily increases with temperature, but from 500 to 600 °C there is a large increase from 130 to 900 Oe. Another major increase is apparent from 700 to 800 °C with a maximum in-plane coercivity of 2430 Oe at 800 °C. Interestingly, the out-of-plane coercivity increases to 420 Oe at 300 °C from zero (as deposited) but then decreases and increases again. These observations are likely to be due to the presence of iron nitride phases influencing the magnetic properties. Again major increases are observed between 500 and 600 °C and 700–800 °C with a maximum out-of-plane coercivity of 2900 Oe at 800 °C. Below about 500 °C FePt films have a higher coercivity (both in-plane and out-of-plane) than those containing nitrogen. Above annealing temperatures of 500 °C the coercivity of FePt diminishes but the coercivity (both in-plane and out-of-plane) of FePtN rises. These results suggest that the addition of nitrogen can offer FePt thin films protection against silicide pollution, therefore helping to preserve magnetic properties during thermal treatment and alleviating the requirements for inter-facial barrier layers between Si substrates and the magnetic film.

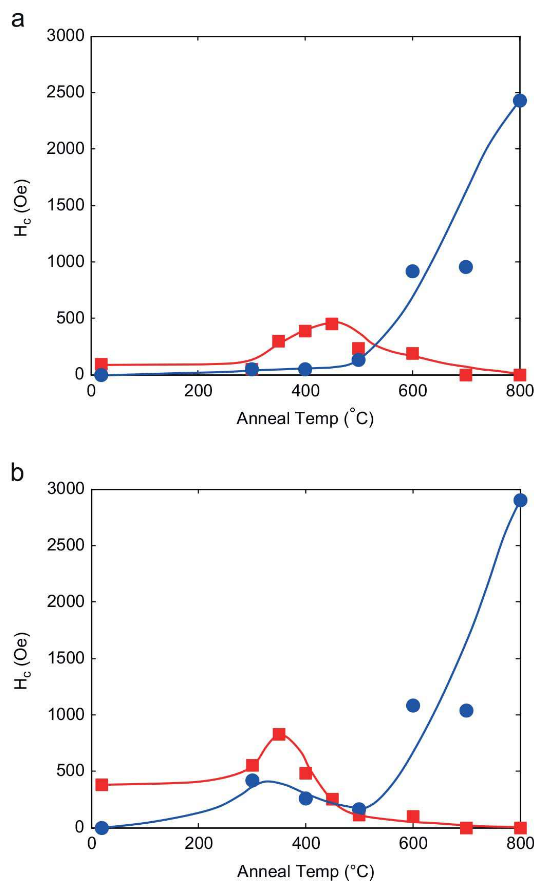

Fig. 3. In-plane (a) and perpendicular (b) coercivities of 25 nm FePt (squares) and FePtN (circles) films deposited on Si (solid lines are guides for the eye only).

4. Conclusion

The High Target Utilization Sputtering (HiTUS) approach has been used to fabricate FePt and FePtN thin films onto silicon substrates. The effect of annealing on the structural phases and magnetic properties of the films were investigated. We show that during thermal annealing there is a degradation in magnetic properties of the FePt films at around 400 °C due to the formation of silicides, since the thermal processing promotes the reaction of the film with the substrate. However, in FePt films produced via a FePtN starting composition silicide formation is suppressed and the sample coercivity continued to rise with annealing temperatures up to the maximum temperature used of 800 °C.

Acknowledgments

We are thankful to Plasma Quest Ltd for providing funding for this work and for access to their facilities. We are also grateful to Prof. Tom Thomson from the University of Manchester for access to his vibrating sample magnetometry equipment, Dr. Mustafa Aziz and Prof. Dave Newman from the University of Exeter for their input and useful discussions.

References

[1] D. Weller, A. Moser, L. Folks, M. Best, W. Lee, M. Toney, M. Schwickert, J.-U. Thiele, M. Doerner, IEEE Transactions on Magnetics 36 (2000) 10–15.
[2] Y. Wang, P. Sharma, A. Makino, Journal of Physics: Condensed Matter 24 (2012) 076004.
[3] B. Wang, K. Barmak, Journal of Applied Physics 111 (2012) 07B718.
[4] T. Thomson, B.D. Terris, M.F. Toney, S. Raoux, J.E.E. Baglin, S.L. Lee, S. Sun, Journal of Applied Physics 95 (2004) 6738–6740.
[5] T. Maeda, T. Kai, A. Kikitsu, T. Nagase, J. Ichi Akiyama, Applied Physics Letters 80 (2002) 2147–2149.
[6] Y.K. Takahashi, M. Ohnuma, K. Hono, Journal of Magnetism and Magnetic Materials 246 (2002) 259–265.
[7] J.S. Chen, B.C. Lim, J.F. Hu, B. Liu, G.M. Chow, G. Ju, Applied Physics Letters 91 (2007) 132506.
[8] F.J. Yang, H. Wang, H.B. Wang, B.Y. Wang, X.L. Wang, H.S. Gu, C.P. Yang, Applied Surface Science 257 (2011) 3216–3219.
[9] C. Feng, B.-H. Li, G. Han, J. Teng, Y. Jiang, Q.-L. Liu, G.-H. Yu, Applied Physics Letters 88 (2006) 232109.
[10] A. Perumal, Y.K. Takahashi, T.O. Seki, K. Hono, Applied Physics Letters 92 (2008) 132508.
[11] Y.-N. Hsu, S. Jeong, D.E. Laughlin, D.N. Lambeth, Journal of Applied Physics 89 (2001) 7068–7070.
[12] C. Luo, D. Sellmyer, IEEE Transactions on Magnetics 31 (1995) 2764–2766.
[13] Y. Endo, N. Kikuchi, O. Kitakami, Y. Shimada, Journal of Applied Physics 89 (2001) 7065–7067.
[14] N. Kaushik, P. Sharma, S. Nagar, K. Rao, H. Kimura, A. Makino, A. Inoue, Materials Science and Engineering: B 171 (2010) 62–68.
[15] H. Zeng, R. Sabirianov, O. Mryasov, M.L. Yan, K. Cho, D.J. Sellmyer, Physical Review B 66 (2002) 184425.
[16] C.P. Luo, S.H. Liou, D.J. Sellmyer, Journal of Applied Physics 87 (2000) 6941–6943.
[17] B. Bian, D.E. Laughlin, K. Sato, Y. Hirotsu, Journal of Applied Physics 87 (2000) 6962–6964.
[18] M.L. Yan, H. Zeng, N. Powers, D.J. Sellmyer, Journal of Applied Physics 91 (2002) 8471–8473.

[19] C.-M. Kuo, P.C. Kuo, Journal of Applied Physics 87 (2000) 419–426.
[20] P.J. Hockley, M.J. Thwaites, G. Dion, in: Society of Vacuum Coaters 48th Annual Technical Conference Proceedings, vol. 505, 2005, pp. 856–7188 .
[21] M. Vopsaroiu, M. Georgieva, P.J. Grundy, G.V. Fernandez, S. Manzoor, M.J. Thwaites, K. O'Grady, Journal of Applied Physics 97 (2005) 10N303.
[22] S. Ladak, L. Fernández-Outón, A. Smith, T. Harrison, H. Patel, T. Kwan, R. Chantrell, K. OGrady, Journal of Magnetism and Magnetic Materials 321 (2009) 996–1000.
[23] H.Y. Wang, W.H. Mao, X.K. Ma, H.Y. Zhang, Y.B. Chen, Y.J. He, E.Y. Jiang, Journal of Applied Physics 95 (2004) 2564–2568.
[24] D.M. Newman, M.L. Wears, M. Jollie, D. Choo, Nanotechnology 18 (2007) 205301.
[25] M.M. Aziz, D.M. Newman, A. Sidwell, M.L. Wears, C.D. Wright, Nanotechnology 21 (2010) 505303.
[26] B. Wang, D.C. Berry, Y. Chiari, K. Barmak, Journal of Applied Physics 110 (2011) 013903.
[27] A. Zaitsev, M. Zemchenko, B. Mogutnov, The Journal of Chemical Thermodynamics 23 (1991) 831–849.
[28] S. Meschel, O. Kleppa, Journal of Alloys and Compounds 280 (1998) 231–239.
[29] P. O'Hare, I. Tomaszkiewicz, C. Beck II, H.-J. Seifert, The Journal of Chemical Thermodynamics 31 (1999) 303–322.

Voltage control of the magnetic coercive field: Multiferroic coupling or artifact?

M. Vopsaroiu,[1,a)] M. G. Cain,[1] P. D. Woolliams,[1] P. M. Weaver,[1] M. Stewart,[1] C. D. Wright,[2] and Y. Tran[2,3]
[1]*National Physical Laboratory, Teddington TW11 0LW, United Kingdom*
[2]*University of Exeter, Harrison Building, Exeter EX4 4QF, United Kingdom*
[3]*Plasma Quest Ltd., Hook RG27 1QT, United Kingdom*

(Received 13 November 2010; accepted 21 January 2011; published online 16 March 2011)

The ability to dynamically tune the coercive field of magnetic thin films is a powerful tool for applications, including in magnetic recording disk technologies. Recently, a number of papers have reported the electrical voltage control of the coercive field of various magnetic thin films in multiferroic composites. Theoretically, this is possible in magneto-electric (ME) multiferroics due to the piezoferroelectric component that can be electrically activated to dynamically modify the properties of the magnetic component of the composite via a direct or strain mediated ME coupling. In this paper we fabricated and examined such structures and we determined that the magnetic coercive field reduction is most likely due to a heating effect. We concluded that this effect is probably an artifact that cannot be attributed to a multiferroic coupling. [doi:10.1063/1.3558982]

INTRODUCTION

Controlling the properties of magnetic thin films is of great importance for technological applications. Traditionally, this is achieved via annealing, thermal treatment, or by controlling the micro-structure of the materials, including the grain size, crystallographic texture or magnetic texture. Although these methods can tune the magnetic properties of a specific sample, the changes are permanent. A new way of dynamically controlling the magnetic properties of materials is to use the strain mediated coupling between magnetically and electrically ordered materials. Such a structure forms a so-called multiferroic composite, which has the ability of modifying the magnetic properties of its magnetic phase via the application of a voltage. Successful measurements of the electric field induced magnetization change[1,2] and the switching of the exchange bias field in ferromagnet (FM)/anti-ferromagnet structures via a voltage have been reported.[3,4] In addition, a few ideas combining spintronics with multiferroic composites in order to create random access storage memory or logic devices have been proposed.[5,6] However, more recently a few papers have reported a remarkable reduction of the magnetic coercive field via an applied voltage in FM/FE type of bi-layer structures, with (FM and FE being ferromagnetic and ferroelectric layer, respectively).[7,8]

Dynamical control of the magnetic coercive field of FM thin films via an applied voltage is a very important scientific and technical issue. Therefore in this work we report the fabrication and testing of FM/FE thin film multiferroic composite structures with the intention of achieving a magnetic coercive field control via an applied voltage.

The FE layer is a 150 μm thick polycrystalline $PbZrTiO_3$ (PZT) film prepared by Fuji Ceramics and commercially available. Prior to the deposition of the FM thin film, the PZT was polished until optically smooth in order to make the samples suitable for magneto-optical testing. The PZT has piezoelectric coefficients $d_{33} = 640$ pm/V, $d_{31} = -330$ pm/V and a coercive voltage of 75 V, which corresponds to a coercive field of ~8 kV/cm. The FM layer is 100 nm Co thin film deposited on top of the PZT via plasma sputtering using a HiTUS system.[9]

One electrode of the PZT is a 100 nm Cu film, while the FM acts as the second electrode. Magnetic properties of the Co film deposited on PZT have been investigated using a longitudinal mode Magneto-Optic Kerr Effect (MOKE) instrument. All measurements were performed at room temperature under identical conditions (i.e., measurement time, magnetic applied field ranges, etc). Each MOKE hysteresis loop has been measured in a 40 s single scan without averaging.

In terms of the electrical activation of the PZT substrate, the MOKE data has been acquired in two modes: a) static mode with the PZT substrate in relaxed state; b) dynamic mode with the PZT substrate excited by the application of an ac/dc voltage ranging from low to saturating voltages.

Upon the application of a voltage to the PZT, a strain is induced in it via the piezoelectric effect. Since the magnetic film is deposited directly on the PZT and assuming a perfect interface between FM and PZT, we deduce that the piezostrains generated by the substrate are fully transferred to the magnetic film. Hence, we expect to inflict modifications of the magnetic state of the FM film when voltages are applied on the ferroelectric PZT substrate. Interestingly, there appears to be no effect on the magnetic properties of the magnetic film when the substrate is excited via a dc voltage. However, when ac voltages are applied to the PZT substrate, magnetic hysteresis loop data reveals a substantial effect of the applied ac voltage on the coercive field of the FM film. Figures 1(a), 1(b), and 1(c) show the magnetic hysteresis

a)Currently known as Melvin M. Vopson. Electronic mail: mv1@npl.co.uk.

Author complimentary copy. Redistribution subject to AIP license or copyright, see http://jap.aip.org/jap/copyright.jsp

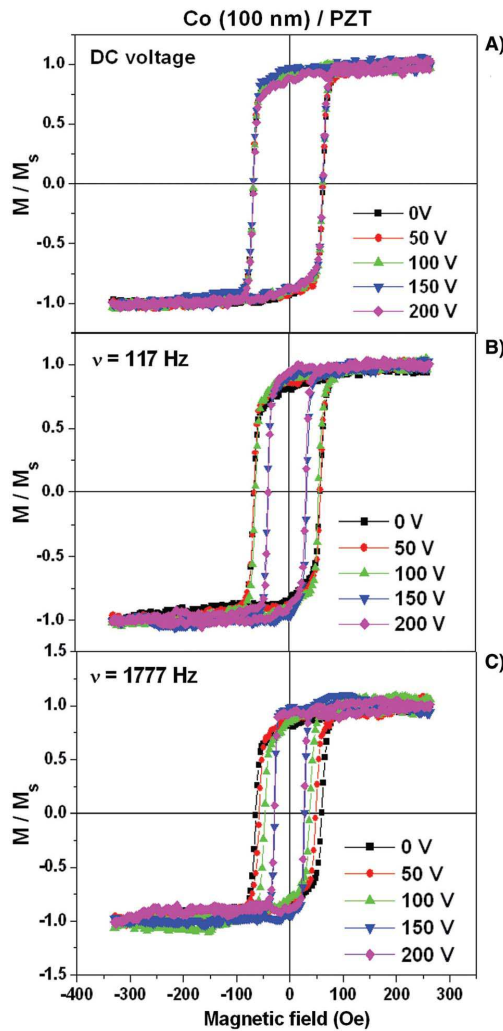

FIG. 1. (Color online) Magnetic hyteresis loops of Co thin film sample measured using MOKE at various dc and ac-applied voltages (0, 50, 100, 150, and 200 V). (a) dc voltages; (b) frequency 117 Hz; (c) frequency 1777 Hz.

loop data acquired at incremental amplitudes of the applied voltage from 0 to 200 V in dc, ac mode at 117 Hz, and 1777 Hz frequency, respectively. The results indicate a consistent decrease of the coercive field of the FM as the applied voltage increases. Figure 2 shows the variation of the coercive field as a function of the applied voltage for the two different frequencies. For comparison, we also plot in Fig. 2 the coercive field extracted from the dc data, showing a constant value of around 63 Oe. At the largest applied voltage, the magnetic coercive field has been reduced from ~63 Oe in relaxed state to 33 Oe at 117 Hz and 27.5 Oe at 1777 Hz measurement frequency. This corresponds to a reduction of the magnetic coercive field of almost 46% and 57%, respectively. The result appears to be in good agreement to previously published data. Assuming this result is attributed to a

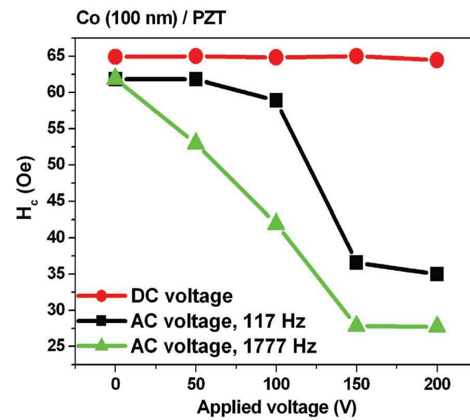

FIG. 2. (Color online) Coercive field vs the applied voltage at dc (0 Hz), 117 Hz and 1777 Hz measurement frequency. Voltage ac amplitudes and dc values used are: 0, 50, 100, 150, and 200V, respectively.

strain mediated magneto-electric (ME) coupling, it is quite remarkable and it would open the possibility of many technical applications. However, by attaching a thermocouple to the sample and repeating the measurements under identical sequence of applied voltage amplitudes and frequencies we have determined a clear thermal heating effect. Table I shows the measured sample temperatures at each corresponding applied voltage amplitude and frequency. Based on this result we suggest that the coercive field reduction is in fact a consequence of the observed thermal effect. Our assumption is further enforced by the results plotted in Figs. 3(a) and 3(b), which show the coercive fields and the inverse of the measured sample's temperature plotted as a function of the applied voltage at the two different frequencies. Thermal variation follows almost identical profile to the coercive field data. This indicates a clear relationship between the coercive field and the temperature. We believe that higher temperatures result in a reduction of the magneto-crystalline anisotropy constant of Co (Ref. 10), which will result in a lower magnetic anisotropy field. Since the magnetic coercive field is directly proportional to the magnetic anisotropy field,[11] then a lower anisotropy field would also result in a lower coercive field, which explains our experimental data. This explanation is also supported by previously reported experimental data regarding the thermal variation of the coercive field of Co and Co alloys (see pages 267 and 568 of Ref. 12). Therefore, the observed effect is

TABLE I. Voltage amplitudes and the corresponding sample's temperature measured at 117 Hz and 1777 Hz, respectively.

Voltage Amplitude (V)	T (°C) at 117 Hz	T (°C) at 1777 Hz
0	21.6	21.6
50	21.9	23.7
100	23.6	38.7
150	57.3	120
200	64.3	120.6

Author complimentary copy. Redistribution subject to AIP license or copyright, see http://jap.aip.org/jap/copyright.jsp

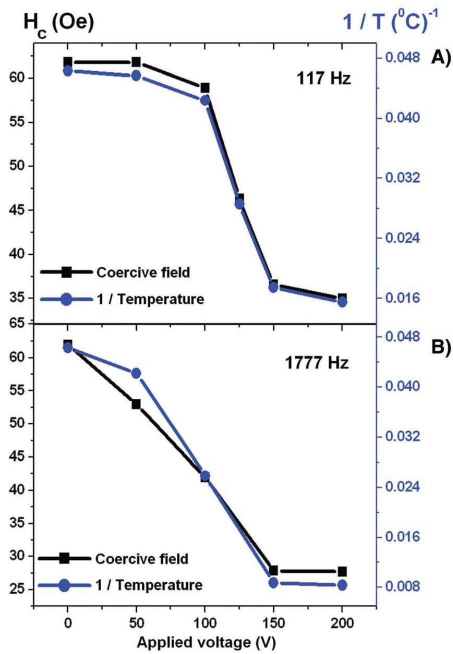

FIG. 3. (Color online) Coercive field and the inverse of the sample's temperature vs the applied voltages (0, 50, 100, 150, and 200 V) at 117 Hz and 1777 Hz measurement frequency.

probably not related to the ME coupling but it is most likely due to the thermal variation of the magneto-crystalline anisotropy constant of Co. Undoubtedly a weak ME coupling could also occur, but in the present study this is dominated by the thermal effects. Although not shown here, we have also observed similar results on CoFe and NiFe thin films. While our results cannot be generalized or invalidate previous studies, such possible artifacts should be given proper consideration in future studies of magneto-electric multiferroics.

[1]C. Thiele, K. Dorr, O. Bilani, J. Rodel, and L. Schultz, Phys. Rev. B **75**, 054408 (2007).
[2]J. Ma, Y. Lin, and C. W. Nan, J. Phys. D: Appl. Phys. **43**, 012001 (2010).
[3]X. He, Y. Wang, N. Wu, A. N. Caruso, E. Vescovo, K. D. Belashchenko, P. A. Dowben, and C. Binek, Nat. Mat. **9**, 579 (2010).
[4]P. Borisov, A. Hochstrat, X. Chen, W. Kleemann, and C. Binek, Phys. Rev. Lett. **94**, 117203 (2005).
[5]X. Chen, A. Hochstrat, P. Borisov, and W. Kleemann, Appl. Phys. Lett. **89**, 202508 (2006).
[6]J. M. Hu, Z. Li, J. Wang, and C. W. Nan, J. Appl. Phys. **107**, 093912 (2010).
[7]Y. Zhang, J. Liu, X. H. Xiao, T. C. Peng, C. Z. Jiang, Y. H. Lin, and C. W. Nan, J. Phys. D: Appl. Phys. **43**, 082002 (2010).
[8]J. Ma, Y. Lin, and C. W. Nan, J. Phys. D: Appl. Phys. **43**, 012001 (2010).
[9]M. Vopsaroiu, M. J. Thwaites, S. Rand, P. J. Grundy, and K. O'Grady, IEEE Trans. Magn. **40**, 2443 (2004).
[10]R. R. Birss, G. J. Keeler, and C. H. Shepherd, J. Phys. F: Metal Phys. **7**(9) 1683 (1977).
[11]O. Kitakami, T. Shimatsu, S. Okamoto, Y. Shimada, and H. Aoi, Jpn. J. Appl. Phys. **43**, L115, (2004).
[12]R. M. Bozorth, *Ferromagnetism* (IEEE Press, 1991) ISBN: 0-7803-1032-2.

Author complimentary copy. Redistribution subject to AIP license or copyright, see http://jap.aip.org/jap/copyright.jsp

Bibliography

[1] S. Wakeham, *et al.*, *physica status solidi (a)* **207**, 1614 (2010).

[2] A. MacKintosh, D. McMorrow, J. Jensen, H. Rønnow, *Magnetism in Metals: A Symposium in Memory of Allan MacKintosh, Copenhagen, 26-29 August 1996 : Invited Review Papers* (Kongelige Danske Videnskabernes Selskab, 1997). S.S.P.Parkin, Magnetotransport in transition metal multilayered structures, http://www.fys.ku.dk/ jjensen/Book/parkin.pdf.

[3] D. Weller, *et al.*, *Magnetics, IEEE Transactions on* **36**, 10 (2000).

[4] J. E. Greene, *Journal of Vacuum Science & Technology A: Vacuum, Surfaces, and Films* **21**, S71 (2003).

[5] K. Seshan, *Handbook of Thin Film Deposition: Principles, Methods, Equipment, and Applications*, Materials Science and Process Technology (Noyes Publ., 2002).

[6] K. Leaver, B. Chapman, *Thin Films* (London : Wykeham : Distributed by Chapman and Hall, 1971).

[7] P. Barna, M. Adamik, *Thin Solid Films* **317**, 27 (1998).

[8] J. Thomas J. Watson (IBM press release, September 14, 1956).

[9] T. M. Coughlin, *Digital Storage in Consumer Electronics: The Essential Guide (Embedded Technology* (Newnes; 1 edition (March 14, 2008), 2008).

[10] S. Matsuo, *et al.*, *Fuji Electric Review* **55** (2009).

[11] D. Weller, M. F. Doerner, *Annual Review of Materials Science* **30**, 611 (2000).

[12] O. Heavens, *Thin film physics* (London : Methuen, 1970).

[13] H. M. Urbassek, *Dynamics*, E. Hasselbrink, B. Lundqvist, eds. (North-Holland, 2008), vol. 3 of *Handbook of Surface Science*, pp. 871 – 913.

[14] *Handbook of Deposition Technologies for Films and Coatings (Third Edition)*, P. M. Martin, ed. (William Andrew Publishing, Boston, 2010), pp. 1 – 31, third edition edn.

[15] C. Kleijn, R. Dorsman, K. Kuijlaars, M. Okkerse, H. van Santen, *Journal of Crystal Growth* **303**, 362 (2007).

[16] I. Brodie, J. Muray, *The physics of microfabrication* (New York; London : Plenum, 1982).

[17] C. Andre, *et al.*, *Journal of Crystal Growth* **298**, 181 (2007).

[18] D. M. Mattox, *Handbook of Physical Vapor Deposition (PVD) Processing (Second Edition)* (William Andrew Publishing, Boston, 2010), pp. 195 – 235, second edition edn.

[19] G. Weissler, R. Carlson, *Methods of Experimental Physics: Vacuum Physics and Technology*, Methods of Experimental Physics Series (Academic Press, 1979).

[20] G. Korotcenkov, *Chemical Sensors: Volume 1 General Approaches*, Sensor Technology (McGraw-Hill Education, 2010).

[21] V. S. Smentkowski, *Progress in Surface Science* **64**, 1 (2000).

[22] A. Tracton, *Coatings Technology Handbook, Third Edition* (Taylor & Francis Group, 2005).

[23] M. Murty, *Surface Science* **500**, 523 (2002).

[24] A. Bogaerts, E. Neyts, R. Gijbels, J. van der Mullen, *Spectrochimica Acta Part B: Atomic Spectroscopy* **57**, 609 (2002).

[25] J. Bittencourt, *Fundamentals of Plasma Physics* (Springer, 2004).

[26] A. Fridman, *Plasma Chemistry* (Cambridge University Press, 2008).

[27] B. Chapman, *Glow discharge processes : sputtering and plasma etching* (Wiley-Blackwell, 1980).

[28] D. L. Smith, *Thin Film Deposition: principles and practice* (McGraw-Hill, Inc., 1995).

[29] L. Holland, *Vacuum deposition of thin films* (London:Chapman and Hall, 1956).

[30] D. Gough, *Spectrochimica Acta Part B: Atomic Spectroscopy* **54**, 2067 (1999).

[31] N. P. Mahalik, *Mems* (McGraw-Hill Education (India) Pvt Limited, 2008).

[32] D. M. Mattox, *Handbook of Physical Vapor Deposition (PVD) Processing (Second Edition)* (William Andrew Publishing, Boston, 2010), pp. 237 – 286, second edition edn.

[33] F. Bloch, *Phys. Rev.* **70**, 460 (1946).

[34] R. J. Allen, *American Journal of Physics* **30**, 867 (1962).

[35] P. J. Hockley, M. J. Thwaites, *Society of Vacuum Coaters, 48th Annual Technical Conference Proceedings* **505**, 856 (2005).

[36] A. J. Flewitt, *et al.*, *Semiconductor Science and Technology* **24**, 085002 (2009).

[37] F. M. Li, *et al.*, *Applied Physics Letters* **98**, 252903 (2011).

[38] R. Chow, *et al.*, *Society of Vacuum Coaters 505/856-7188 31* **49th Annual Technical Conference Proceedings**, 31 (2006).

[39] M. Hasan, A. Haseeb, R. Saidur, H. Masjuki, M. Hamdi, *Optical Materials* **32**, 690 (2010).

[40] M. G. Krishna, S. Kanakaraju, S. Mohan, *Vacuum* **46**, 33 (1995).

[41] D. Kuo, K. Tzeng, *Thin Solid Films* **420 - 421**, 497 (2002).

[42] C. Yang, H. Fan, Y. Xi, J. Chen, Z. Li, *Applied Surface Science* **254**, 2685 (2008).

[43] V. Pervak, F. Krausz, A. Apolonski, *Thin Solid Films* **515**, 7984 (2007).

[44] T. Bright, J. Watjen, Z. Zhang, C. Muratore, A. Voevodin, *Thin Solid Films* **520**, 6793 (2012).

[45] P. Thomsen-Schmidt, *et al.*, *Thin Solid Films* **253**, 28 (1994).

[46] P. Kelly, R. Arnell, *Vacuum* **56**, 159 (2000).

[47] J. Veldeman, H. Jia, M. Burgelman, *Magnetics Conference, 2000. INTERMAG 2000 Digest of Technical Papers. 2000 IEEE International* (2000), p. 130.

[48] S. J. Wakeham, *et al.*, *Semicond. Sci. Technol.* **26**, 045016 (2011).

[49] S. Wakeham, *et al.*, *Thin Solid Films* **518**, 1355 (2009).

[50] M. Vopsaroiu, M. J. Thwaites, G. V. Fernandez, S. Lepadatu, K. O'Grady, *Journal of Optoelectronics and Advanced Materials* **7**, 2713 (2005).

[51] B. D. Cullity, C. D. Graham, *Introduction to Magnetic Materials* (Wiley-IEEE Press; 2 edition, 2008).

[52] P.W.Atkins, *Concepts in Physical Chemistry* (OUP Oxford, 1995).

[53] R. Tilley, *Understanding Solids: The Science of Materials* (Wiley, 2005).

[54] U. Fourier, *Magnetism: Fundamentals* (Springer, 2004).

[55] A. A. Kaufman, R. O. Hansen, R. L. Kleinberg, *Principles of the Magnetic Methods in Geophysics*, R. H. A.A. Kaufman, R. L. Kleinberg, eds. (Elsevier, 2008), vol. 42 of *Methods in Geochemistry and Geophysics*, pp. 207 – 254.

[56] P. A. M. Dirac, *Proceedings of the Royal Society of London. Series A* **112**, 661 (1926).

[57] N. A. Spaldin, *Magnetic Materials: Fundamentals and Applications* (Cambridge University Press; 2 edition, 2010).

[58] H. R. Kirchmayr, *Journal of Physics D: Applied Physics* **29**, 2763 (1996).

[59] M. T. Johnson, P. J. H. Bloemen, F. J. A. den Broeder, J. J. de Vries, *Reports on Progress in Physics* **59**, 1409 (1996).

[60] P. Bruno, *Phys. Rev. B* **39**, 865 (1989).

[61] D. Weller, *et al.*, *Phys. Rev. Lett.* **75**, 3752 (1995).

[62] P. Atkins, *Physical Chemistry* (Macmillan Higher Education, 1997).

[63] D. Jiles, *Introduction to magnetism and magnetic materials* (Chapman and Hall, 1991).

[64] E. du Trémolet de Lacheisserie, D. Gignoux, M. Schlenker, *Magnetism: Materials and Applications*, no. v. 2 (Springer, 2004).

[65] A. B. Shick, O. N. Mryasov, *Phys. Rev. B* **67**, 172407 (2003).

[66] D. Weller, T. McDaniel, *Advanced Magnetic Nanostructures*, D. Sellmyer, R. Skomski, eds. (Springer US, 2006), pp. 295–324.

[67] H. Kanazawa, G. Lauhoff, T. Suzuki, *Journal of Applied Physics* **87**, 6143 (2000).

[68] J.-U. Thiele, L. Folks, M. F. Toney, D. K. Weller, *Journal of Applied Physics* **84**, 5686 (1998).

[69] R. F. C. Farrow, *et al.*, *Journal of Applied Physics* **79**, 5967 (1996).

[70] E. du Trémolet de Lacheisserie, D. Gignoux, M. Schlenker, *Magnetism: Materials and Applications*, no. v. 2 (Springer, 2004).

[71] K. Buschow, F. de Boer, *Physics of Magnetism and Magnetic Materials*, Focus on biotechnology (Springer, 2003).

[72] M. Gibbs, N. A. T. O. S. A. Division, *Modern Trends in Magnetostriction Study and Application* (Kluwer Academic, 2001).

[73] J. Hook, H. Hall, *Solid state physics*, The Manchester physics series (Wiley, 1991).

[74] S. Zhang, *et al.*, *Thin Solid Films* **520**, 5746 (2012).

[75] H. Szambolics, J.-C. Toussaint, A. Marty, I. Miron, L. Buda-Prejbeanu, *Journal of Magnetism and Magnetic Materials* **321**, 1912 (2009).

[76] T. Thomson, K. O'Grady, *Journal of Physics D: Applied Physics* **30**, 1566 (1997).

[77] T. Tanaka, K. Ouchi, S. Iwasaki, *Magnetics in Japan, IEEE Translation Journal on* **2**, 124 (1987).

[78] P. Krone, D. Makarov, M. Albrecht, T. Schrefl, D. Suess, *Journal of Magnetism and Magnetic Materials* **322**, 3771 (2010).

[79] J.-G. Zhu, H. N. Bertram, *Journal of Applied Physics* **69**, 6084 (1991).

[80] A. Berger, *Physica B: Condensed Matter* **407**, 1322 (2012).

[81] J. Mallinson, *Magneto-Resistive Heads: Fundamentals and Applications*, Electromagnetism Series (Academic Press, 1996).

[82] J.-G. J. Zhu, *Materials Today* **6**, 22 (2003).

[83] S. Piramanayagam, K. Srinivasan, *Journal of Magnetism and Magnetic Materials* **321**, 485 (2009).

[84] M. H. Kryder, R. W. Gustafson, *Journal of Magnetism and Magnetic Materials* **287**, 449 (2005).

[85] R. Wood, Y. Hsu, M. Schultz, *Perpendicular Magnetic Recording Technology* (Hitachi Global Storage Technologies, 2007).

[86] S. N. Piramanayagam, *Journal of Applied Physics* **102**, 011301 (2007).

[87] S. Luitjens, W. Folkerts, H. V. Kesteren, J. Ruigrok, *Philips Journal of Research* **51**, 5 (1998).

[88] M. Djamal, Ramli, *Procedia Engineering* **32**, 60 (2012).

[89] A. Hütten, K.-H. Müller, *Sensors and Actuators A: Physical* **59**, 236 (1997).

[90] K.-M. Lenssen, *et al.*, *Sensors and Actuators A: Physical* **60**, 90 (1997).

[91] M. N. Baibich, *et al.*, *Phys. Rev. Lett.* **61**, 2472 (1988).

[92] B. Dieny, *et al.*, *Journal of Applied Physics* **69**, 4774 (1991).

[93] P. P. Freitas, R. Ferreira, S. Cardoso, F. Cardoso, *Journal of Physics: Condensed Matter* **19**, 165221 (2007).

[94] G. W. Fernando, *Metallic Multilayers and their Applications Theory, Experiments, and Applications related to Thin Metallic Multilayers*, G. W. Fernando, ed. (Elsevier, 2008), vol. 4 of *Handbook of Metal Physics*, pp. 1 – 32.

[95] S. S. P. Parkin, *Applied Physics Letters* **69**, 3092 (1996).

[96] P. Freitas, *et al.*, *Sensors and Actuators A: Physical* **81**, 2 (2000).

[97] H. Kanai, K. Norma, J. Hong, *Fujitsu Scientific and Technical Journal* **37**, 174 (2001).

[98] H. Zabel, *Superlattices and Microstructures* **46**, 541 (2009).

[99] E. Tsymbal, D. Pettifor, *Solid State Physics - Advances in Research and Applications*, H. Ehrenreich, F. Spaepen, eds. (Academic Press, 2001), vol. 56, pp. 113 – 237.

[100] E. Y. Tsymbal, O. N. Mryasov, P. R. LeClair, *Journal of Physics: Condensed Matter* **15**, R109 (2003).

[101] D. Edwards, R. Erickson, J. Mathon, R. Muniz, M. Villeret, *Materials Science and Engineering: B* **31**, 25 (1995).

[102] C. Kaiser, S. van Dijken, S.-H. Yang, H. Yang, S. S. P. Parkin, *Phys. Rev. Lett.* **94**, 247203 (2005).

[103] S. Yuasa, D. D. Djayaprawira, *Journal of Physics D: Applied Physics* **40**, R337 (2007).

[104] M. Julliere, *Physics Letters A* **54**, 225 (1975).

[105] S. Parkin, *et al.*, *Proceedings of the IEEE* **91**, 661 (2003).

[106] J.-G. J. Zhu, C. Park, *Materials Today* **9**, 36 (2006).

[107] J. S. Moodera, G. Mathon, *Journal of Magnetism and Magnetic Materials* **200**, 248 (1999).

[108] K. Z. Gao, O. Heinonen, Y. Chen, *Journal of Magnetism and Magnetic Materials* **321**, 495 (2009).

[109] J. J. Åkerman, *et al.*, *Journal of Magnetism and Magnetic Materials* **240**, 86 (2002).

[110] R. Wood, *Journal of Magnetism and Magnetic Materials* **321**, 555 (2009).

[111] S. Yuasa, *Journal of the Physical Society of Japan* **77**, 031001 (2008).

[112] G. Totten, *The Handbook of Lubrication And Tribology: Application and Maintenance*, Handbook of Lubrication and Tribology (CRC PressINC, 2006).

[113] C.-C. Wang, S.-C. Lin, H. Hochen, *International Journal of Machine Tools and Manufacture* **42**, 979 (2002).

[114] J. Mallinson, *The foundations of magnetic recording* (Academic Press, 1987).

[115] G. Bate, *Journal of Magnetism and Magnetic Materials* **100**, 413 (1991).

[116] P. J. Grundy, *Journal of Physics D: Applied Physics* **31**, 2975 (1998).

[117] S. J. Lister, *et al.*, *Applied Physics Letters* **97**, 112503 (2010).

[118] S. D. Granz, M. H. Kryder, *Journal of Magnetism and Magnetic Materials* **324**, 287 (2012).

[119] W. Grogger, *et al.*, *Applied Physics Letters* **80**, 1165 (2002).

[120] O. Fruchart, A. Thiaville, *Comptes Rendus Physique* **6**, 921 (2005).

[121] N. Honda, K. Ouchi, *Journal of Magnetism and Magnetic Materials* **235**, 289 (2001).

[122] T. Suzuki, H. Muraoka, Y. Nakamura, K. Ouchi, *Magnetics, IEEE Transactions on* **39**, 691 (2003).

[123] A. Asthana, Y. Takahashi, Y. Matsui, K. Hono, *Journal of Magnetism and Magnetic Materials* **320**, 250 (2008).

[124] J. Judy, *Journal of Magnetism and Magnetic Materials* **287**, 16 (2005).

[125] K.-Z. Gao, H. Bertram, *Magnetics, IEEE Transactions on* **38**, 3675 (2002).

[126] C.-M. Kuo, P. C. Kuo, *Journal of Applied Physics* **87**, 419 (2000).

[127] H. Bretislav, B. J.A.C., *Ultra thin magnetic structures IV* (2005).

[128] M. Seigler, *et al.*, *Magnetics, IEEE Transactions on* **44**, 119 (2008).

[129] J.-G. Zhu, X. Zhu, Y. Tang, *Magnetics, IEEE Transactions on* **44**, 125 (2008).

[130] R. Victora, X. Shen, *Magnetics, IEEE Transactions on* **41**, 537 (2005).

[131] D. E. Laughlin, K. Srinivasan, M. Tanase, L. Wang, *Scripta Materialia* **53**, 383 (2005).

[132] Z. Yan, *et al.*, *Scripta Materialia* **53**, 463 (2005).

[133] N. Luong, *et al.*, *Journal of Magnetism and Magnetic Materials* **290 - 291, Part 1**, 559 (2005).

[134] T. Maeda, T. Kai, A. Kikitsu, T. Nagase, J. ichi Akiyama, *Applied Physics Letters* **80**, 2147 (2002).

[135] J. Chen, B. Lim, Y. Ding, G. Chow, *Journal of Magnetism and Magnetic Materials* **303**, 309 (2006). The 6th International Symposium on Physics of Magnetic Materials.

[136] A.-C. Sun, F.-T. Yuan, J.-H. Hsu, H. Lee, *Scripta Materialia* **61**, 713 (2009).

[137] F.-T. Yuan, A.-C. Sun, J.-H. Hsu, *Scripta Materialia* **62**, 762 (2010).

[138] J. Aboaf, S. Herd, E. Klokholm, *Magnetics, IEEE Transactions on* **19**, 1514 (1983).

[139] J.-P. Hu, P. Lin, *Magnetics, IEEE Transactions on* **32**, 4096 (1996).

[140] M. Li, Z.-H. Jiang, Z.-Q. Zou, D.-F. Shen, *Journal of Magnetism and Magnetic Materials* **176**, 331 (1997).

[141] M. Abes, *et al.*, *Materials Science and Engineering: C* **23**, 229 (2003).

[142] A. Markou, *et al.*, *Journal of Applied Physics* **110**, 083903 (2011).

[143] W. Grange, C. Ulhaq-Bouillet, M. Maret, J. Thibault, *Acta Materialia* **49**, 1439 (2001).

[144] A. Demortiere, C. Petit, *Journal of Applied Physics* **109**, 084344 (2011).

[145] H. Khurshid, Y. Huang, M. Bonder, G. Hadjipanayis, *Journal of Magnetism and Magnetic Materials* **321**, 277 (2009).

[146] D. M. Newman, M. L. Wears, M. Jollie, D. Choo, *Nanotechnology* **18**, 205301 (2007).

[147] R. Tilley, *Crystals and Crystal Structures* (Wiley, 2006).

[148] P. W. Clegg, *Crystal Structure Determination (Oxford Chemistry Primers)* (Oxford University Press, USA, 1998).

[149] R. J. D. Tilley, *Crystallography and Crystal Structures* (John Wiley & Sons Ltd, 2005), pp. 115–147.

[150] M. De Graef, M. McHenry, *Structure of Materials: An Introduction to Crystallography, Diffraction and Symmetry* (Cambridge University Press, 2007).

[151] C. Hammond, *The basics of crystallography and diffraction*, IUCr texts on crystallography (Oxford University Press, 2009).

[152] V. Rangarajan, G. Rangarajan, *Materials Science* (Tata McGraw-Hill, 2004).

[153] C. Kachhava, *Solid State Physics, Solid State Device And Electronics.* (New Age International, 2003).

[154] T. J. Klemmer, *et al.*, *Applied Physics Letters* **81**, 2220 (2002).

[155] K. Torres, G. Thompson, *Ultramicroscopy* **109**, 606 (2009).

[156] A. Cebollada, R. Farrow, M. Toney, *Magnetic Nanostructures: Structure and Magnetic Properties of Chemically Ordered Magnetic Binary Alloys in Thin Film Form* (American Scientific Publishers, 2002).

[157] Y. S. Yu, *et al.*, *Journal of Applied Physics* **108**, 073906 (2010).

[158] A.-C. Sun, J.-H. Hsu, P. Kuo, H. Huang, *Thin Solid Films* **516**, 1155 (2008).

[159] C. Feng, *et al.*, *Applied Physics Letters* **88**, 232109 (2006).

[160] A. Perumal, Y. K. Takahashi, T. O. Seki, K. Hono, *Applied Physics Letters* **92**, 132508 (2008).

[161] W. B. Mi, E. Y. Jiang, H. L. Bai, H. Liu, *Journal of Applied Physics* **99**, 034315 (2006).

[162] B. Bian, D. E. Laughlin, K. Sato, Y. Hirotsu, *Journal of Applied Physics* **87**, 6962 (2000).

[163] Y. Li, *et al.*, *Journal of Magnetism and Magnetic Materials* **322**, 3789 (2010).

[164] J. A. Venables, G. D. T. Spiller, M. Hanbucken, *Reports on Progress in Physics* **47**, 399 (1984).

[165] J. S. Chen, B. C. Lim, J. P. Wang, *Applied Physics Letters* **81**, 1848 (2002).

[166] J. A. Venables, *Introduction to Surface and Thin Film Processes* (Cambridge University Press, 2000).

[167] H. Zeng, M. L. Yan, N. Powers, D. J. Sellmyer, *Applied Physics Letters* **80**, 2350 (2002).

[168] P. Pirzadeh, E. N. Beaudoin, P. G. Kusalik, *Crystal Growth & Design* **12**, 124 (2012).

[169] A. Rusanov, *Surface Science Reports* **58**, 111 (2005).

[170] C. V. Thompson, R. Carel, *Journal of the Mechanics and Physics of Solids* **44**, 657 (1996).

[171] R. Carel, C. Thompson, H. Frost, *Acta Materialia* **44**, 2479 (1996).

[172] Y.-C. Wu, L.-W. Wang, C.-H. Lai, *Applied Physics Letters* **91**, 072502 (2007).

[173] P. Rasmussen, X. Rui, J. E. Shield, *Applied Physics Letters* **86**, 191915 (2005).

[174] J.-S. Kim, Y.-M. Koo, B.-J. Lee, S.-R. Lee, *Journal of Applied Physics* **99**, 053906 (2006).

[175] B. Lim, J. Chen, J. Wang, *Surface and Coatings Technology* **198**, 296 (2005).

[176] A. Breitling, D. Goll, *Journal of Magnetism and Magnetic Materials* **320**, 1449 (2008).

[177] A. Martins, M. C. A. Fantini, A. D. Santos, *Journal of Magnetism and Magnetic Materials* **265**, 13 (2003).

[178] Z. L. Zhao, *et al.*, *Metallurgical and Materials Transactions A* **38**, 811 (2007).

[179] S. Chen, *et al.*, *Materials and Design* **31**, 1742 (2010). Design of Nanomaterials and Nanostructures.

[180] G. R. Trichy, D. Chakraborti, J. Narayan, J. T. Prater, *Applied Physics Letters* **92**, 102504 (2008).

[181] S. Chen, *et al.*, *Journal of Magnetism and Magnetic Materials* **310**, e921 (2007). Proceedings of the 17th International Conference on Magnetism: The International Conference on Magnetism.

[182] C. S. Kim, *et al.*, *Magnetics, IEEE Transactions on* **46**, 2282 (2010).

[183] E. Yang, S. Ratanaphan, D. Laughlin, J.-G. Zhu, *Magnetics, IEEE Transactions on* **47**, 81 (2011).

[184] C. Luo, D. Sellmyer, *Magnetics, IEEE Transactions on* **31**, 2764 (1995).

[185] Y. Endo, N. Kikuchi, O. Kitakami, Y. Shimada, *Journal of Applied Physics* **89**, 7065 (2001).

[186] T. Sun, *et al.*, *Thin Solid Films* **520**, 774 (2011).

[187] S. Sun, E. Fullerton, D. Weller, C. Murray, *Magnetics, IEEE Transactions on* **37**, 1239 (2001).

[188] T. Klemmer, Y. Peng, X. Wu, G. Ju, *Magnetics, IEEE Transactions on* **45**, 845 (2009).

[189] H. Y. Wang, *et al.*, *Journal of Applied Physics* **95**, 2564 (2004).

[190] Y. K. Takahashi, M. Ohnuma, K. Hono, *Journal of Magnetism and Magnetic Materials* **246**, 259 (2002).

[191] K. Kang, Z. G. Zhang, C. Papusoi, T. Suzuki, *Applied Physics Letters* **82**, 3284 (2003).

[192] J. S. Chen, *et al.*, *Applied Physics Letters* **91**, 132506 (2007).

[193] F. Yang, *et al.*, *Applied Surface Science* **In Press, Corrected Proof**, (2010).

[194] Y.-N. Hsu, S. Jeong, D. E. Laughlin, D. N. Lambeth, *Journal of Applied Physics* **89**, 7068 (2001).

[195] A. C. Sun, F. T. Yuan, J.-H. Hsu, *Journal of Physics: Conference Series* **200**, 102009 (2010).

[196] T. Shimatsu, *et al.*, *Journal of Applied Physics* **109**, 07B726 (2011).

[197] C.-H. Yang, C.-H. Lai, C. Chiang, *Magnetics, IEEE Transactions on* **40**, 2519 (2004).

[198] L. Qiu, *et al.*, *Magnetics, IEEE Transactions on* **43**, 2157 (2007).

[199] Z. L. Zhao, *et al.*, *Journal of Applied Physics* **97**, 10H502 (2005).

[200] C.-M. Kuo, P. Kuo, W.-C. Hsu, C.-T. Li, A.-C. Sun, *Journal of Magnetism and Magnetic Materials* **209**, 100 (2000).

[201] C. L. Platt, *et al.*, *Journal of Applied Physics* **92**, 6104 (2002).

[202] C. P. Luo, S. H. Liou, D. J. Sellmyer, *Journal of Applied Physics* **87**, 6941 (2000).

[203] C. P. Luo, S. H. Liou, L. Gao, Y. Liu, D. J. Sellmyer, *Applied Physics Letters* **77**, 2225 (2000).

[204] P. C. Kuo, Y. D. Yao, C. M. Kuo, H. C. Wu, *Journal of Applied Physics* **87**, 6146 (2000).

[205] X.-H. Xu, H.-S. Wu, X.-L. Li, F. Wang, J.-F. Duan, *Physica B: Condensed Matter* **348**, 436 (2004).

[206] T. Suzuki, F. Sequeda, H. Do, T. C. Huang, G. Gorman, *Journal of Applied Physics* **67**, 4435 (1990).

[207] W. R. Eppler, B. K. Cheong, D. E. Laughlin, M. H. Kryder, *Journal of Applied Physics* **75**, 7093 (1994).

[208] D. Khomskii, *Journal of Magnetism and Magnetic Materials* **306**, 1 (2006).

[209] S.-W. Cheong, M. Mostovoy, *Nature Materials* **6**, 13 (2007).

[210] N. Kirova, S. Brazovskii, *Physica B: Condensed Matter* **404**, 382 (2009).

[211] J. H. Noggle, *Physical Chemistry* (Little, Brown and Co, Boston, 1985).

[212] C. H. Ahn, K. M. Rabe, J.-M. Triscone, *Science* **303**, 488 (2004).

[213] S. Brazovskii, N. Kirova, *Synthetic Metals* **159**, 2205 (2009).

[214] Z. Zhang, D. Fang, A. Soh, *Mechanics of Materials* **38**, 25 (2006).

[215] C. Byun, J. W. Jang, B.-W. Lee, *Materials Letters* **34**, 308 (1998).

[216] Y.-J. Seo, J.-S. Park, W.-S. Lee, *Microelectronic Engineering* **83**, 2238 (2006). Materials for Advanced Metallization (MAM 2006).

[217] Y. Li, S. Zhang, W. Fei, T. Sritharan, C. Xu, *Thin Solid Films* **515**, 8371 (2007).

[218] G. Jha, A. Roy, A. Dhar, I. Manna, S. Ray, *Physica B: Condensed Matter* **400**, 33 (2007).

[219] A. S. Bhalla, G. Raina, S. K. Sharma, *Materials Letters* **35**, 28 (1998).

[220] W. Känzig, *Phys. Rev. Lett.* **7**, 304 (1961).

[221] C. Ru, R. Batra, *International Journal of Solids and Structures* **32**, 3289 (1995).

[222] C. Wayman, *Progress in Materials Science* **36**, 203 (1992).

[223] Y. Bellouard, *Materials Science and Engineering: A* **481 - 482**, 582 (2008).

[224] F. Auricchio, E. Sacco, *International Journal of Non-Linear Mechanics* **32**, 1101 (1997).

[225] Y. Huo, X. Zu, A. Li, Z. Wang, L. Wang, *Acta Materialia* **52**, 2683 (2004).

[226] M. Langelaar, F. van Keulen, *Computers & amp; Structures* **86**, 955 (2008).

[227] E. K. Salje, *Annual Review of Materials Research* **42**, 265 (2012).

[228] R. Ahluwalia, T. Lookman, A. Saxena, W. Cao, *Applied Physics Letters* **84**, 3450 (2004).

[229] H. Guo, A. A. Bokov, Z.-G. Ye, *Phys. Rev. B* **81**, 024114 (2010).

[230] D. Damjanovic, M. Demartin, H. Shulman, M. Testorf, N. Setter, *Sensors and Actuators A: Physical* **53**, 353 (1996). ¡ce:title¿Proceedings of The 8th International Conference on Solid-State Sensors and Actuators¡/ce:title¿.

[231] A. Endriss, M. Hammer, M. Hoffmann, A. Kolleck, G. Schneider, *Journal of the European Ceramic Society* **19**, 1229 (1999).

[232] J. Guyonnet, H. Bea, P. Paruch, *Journal of Applied Physics* **108**, 042002 (2010).

[233] V. Nagarajan, *et al.*, *Nat Mater* **2**, 43 (2003).

[234] D. Damjanovic, *Reports on Progress in Physics* **61**, 1267 (1998).

[235] J. Minase, T.-F. Lu, B. Cazzolato, S. Grainger, *Precision Engineering* **34**, 692 (2010).

[236] S. Sriram, M. Bhaskaran, K. Short, G. Matthews, A. Holland, *Micron* **40**, 109 (2009).

[237] J.-M. Liu, *et al.*, *Materials Chemistry and Physics* **75**, 12 (2002).

[238] M. Es-Souni, M. Kuhnke, A. Piorra, C.-H. Solterbeck, *Journal of the European Ceramic Society* **25**, 2499 (2005).

[239] M. Soares, A. Senos, P. Mantas, *Journal of the European Ceramic Society* **19**, 1865 (1999).

[240] Y.-C. Hsu, C.-C. Wu, C.-C. Lee, G. Cao, I. Shen, *Sensors and Actuators A: Physical* **116**, 369 (2004).

[241] R. J. Tilley, *Endeavour* **14**, 124 (1990).

[242] K. Bhattacharya, G. Ravichandran, *Acta Materialia* **51**, 5941 (2003).

[243] C. Li, K. C. K. Soh, P. Wu, *Journal of Alloys and Compounds* **372**, 40 (2004).

[244] R. E. Cohen, *Nature* **358**, 136 (1992).

[245] N. Setter, *et al.*, *Journal of Applied Physics* **100**, 051606 (2006).

[246] G. Lawes, G. Srinivasan, *Journal of Physics D: Applied Physics* **44**, 243001 (2011).

[247] W. Eerenstein, M. Wiora, J. L. Prieto, J. F. Scott, N. D. Mathur, *Nat Mater* **6**, 348 (2007).

[248] J. Zhai, Z. Xing, S. Dong, J. Li, D. Viehland, *Journal of the American Ceramic Society* **91**, 351 (2008).

[249] C.-W. Nan, M. Bichurin, S. Dong, D. Viehland, G. Srinivasan, *Journal of Applied Physics* **103** (2008).

[250] Z. Surowiak, D. Bochenek, *Archives of acoustics* **33**, 243 (2008).

[251] J.-M. Hu, C. W. Nan, *Phys. Rev. B* **80**, 224416 (2009).

[252] N. Tiercelin, Y. Dusch, V. Preobrazhensky, P. Pernod, *Journal of Applied Physics* **109**, 07D726 (2011).

[253] W. Kleemann, *Physics* **2**, 105 (2009).

[254] D. Shriver, P. Atkins, *Inorganic Chemistry* (W. H. Freeman, 2006).

[255] B. B. Van Aken, T. T. Palstra, A. Filippetti, N. A. Spaldin, *Nature Materials* **3**, 164 (2004).

[256] C. Ederer, N. A. Spaldin, *Nature Materials* **3**, 849 (2004).

[257] R. Ramesh, N. A. Spaldin, *Nature Materials* **6**, 21 (2007).

[258] J. Ryu, A. V. Carazo, K. Uchino, H.-E. Kim, *Japanese Journal of Applied Physics, Part 1: Regular Papers and Short Notes and Review Papers* **40**, 4948 (2001).

[259] N. Ekreem, A. Olabi, T. Prescott, A. Rafferty, M. Hashmi, *Journal of Materials Processing Technology* **191**, 96 (2007).

[260] M. Fiebig, *Journal of Physics D: Applied Physics* **38**, R123 (2005).

[261] Y. Fetisov, A. Bush, K. Kamentsev, A. Ostashchenko, G. Srinivasan, *Sensors Journal, IEEE* **6**, 935 (2006).

[262] S. Dong, J.-F. Li, D. Viehland, *Applied Physics Letters* **83**, 2265 (2003).

[263] T.-K. Chung, G. P. Carman, K. P. Mohanchandra, *Applied Physics Letters* **92**, 112509 (2008).

[264] S. Stein, M. Wuttig, D. Viehland, E. Quandt, *Journal of Applied Physics* **97**, 1 (2005).

[265] N. A. Spaldin, M. Fiebig, *Science* **309**, 391 (2005).

[266] V. J. Folen, G. T. Rado, E. W. Stalder, *Phys. Rev. Lett.* **6**, 607 (1961).

[267] D. Niarchos, *Sensors and Actuators, A: Physical* **109**, 166 (2003).

[268] L. Martin, *et al.*, *Journal of Physics Condensed Matter* **20**, 434220 (2008).

[269] C. Ederer, N. A. Spaldin, *Current Opinion in Solid State and Materials Science* **9**, 128 (2005).

[270] J. M. Rondinelli, M. Stengel, N. A. Spaldin, *Nat Nano* **3**, 46 (2008).

[271] H. J. A. Molegraaf, *et al.*, *Advanced Materials* **21**, 3470 (2009).

[272] V. Laukhin, *et al.*, *Phys. Rev. Lett.* **97**, 227201 (2006).

[273] T. Lottermoser, *et al.*, *Nature* **430**, 541 (2004).

[274] D. Lebeugle, A. Mougin, M. Viret, D. Colson, L. Ranno, *Phys. Rev. Lett.* **103**, 257601 (2009).

[275] L. Martin, Y.-H. Chu, R. Ramesh, *Materials Science and Engineering: R: Reports* **68**, 89 (2010).

[276] T. Zhao, *et al.*, *Nat Mater* **5**, 823 (2006).

[277] Y.-H. Chu, *et al.*, *Nat Mater* **7**, 478 (2008).

[278] P. Borisov, A. Hochstrat, X. Chen, W. Kleemann, C. Binek, *Phys. Rev. Lett.* **94**, 117203 (2005).

[279] K. Dörr, C. Thiele, *physica status solidi (b)* **243**, 21 (2006).

[280] D. Dale, A. Fleet, J. D. Brock, Y. Suzuki, *Applied Physics Letters* **82**, 3725 (2003).

[281] M. I. Bichurin, *et al.*, *Phys. Rev. B* **68**, 132408 (2003).

[282] C. A. F. Vaz, *et al.*, *Phys. Rev. Lett.* **104**, 127202 (2010).

[283] C. Thiele, K. Dörr, O. Bilani, J. Rödel, L. Schultz, *Phys. Rev. B* **75**, 054408 (2007).

[284] M. K. Lee, T. K. Nath, C. B. Eom, M. C. Smoak, F. Tsui, *Applied Physics Letters* **77**, 3547 (2000).

[285] F. Zavaliche, *et al.*, *Nano Letters* **5**, 1793 (2005).

[286] J. J. Yang, *et al.*, *Applied Physics Letters* **94**, 212504 (2009).

[287] S. Sahoo, *et al.*, *Phys. Rev. B* **76**, 092108 (2007).

[288] N. Moutis, D. Suarez-Sandoval, D. Niarchos, *Journal of Magnetism and Magnetic Materials* **320**, 1050 (2008).

[289] M. Weiler, *et al.*, *New Journal of Physics* **11**, 013021 (2009).

[290] S. Geprags, A. Brandlmaier, M. Opel, R. Gross, S. T. B. Goennenwein, *Applied Physics Letters* **96**, 142509 (2010).

[291] H. Nalwa, *Handbook of Thin Films, Five-Volume Set*, no. v. 5 (Academic Press, 2001).

[292] R. Indeck, M. Muller, *Encyclopedia of Materials: Science and Technology (Second Edition)*, E. in Chief: K. H. Jrgen Buschow, *et al.*, eds. (Elsevier, Oxford, 2002), pp. 1 – 14, second edition edn.

[293] S. Foner, *Review of Scientific Instruments* **30**, 548 (1959).

[294] W. Saslow, *Electricity, Magnetism, and Light* (Academic Press, 2002).

[295] http://www.microsense.net/products-vsm-model-10.htm.

[296] J. A. C. Bland, M. J. Padgett, R. J. Butcher, N. Bett, *Journal of Physics E: Scientific Instruments* **22**, 308 (1989).

[297] P. Maadeswaran, S. Thirumalairajan, J. Chandrasekaran, *Optik - International Journal for Light and Electron Optics* **121**, 773 (2010).

[298] J. Senkevich, S. Desu, V. Simkovic, *Polymer* **41**, 2379 (2000).

[299] P. N. Argyres, *Phys. Rev.* **97**, 334 (1955).

[300] M. Kaneko, K. Aso, *Magnetics in Japan, IEEE Translation Journal on* **5**, 225 (1990).

[301] J. Teixeira, *et al.*, *Materials Science and Engineering: B* **126**, 180 (2006).

[302] A. Zvezdin, A. Zvezdin, V. Kotov, *Modern Magnetooptics and Magnetooptical Materials*, Studies in Condensed Matter Physics (Inst. of Physics Publ., 1997).

[303] J. Bansmann, *et al.*, *Surface Science Reports* **56**, 189 (2005).

[304] Y. Zhu, *Modern Techniques for Characterizing Magnetic Materials* (Springer, 2005).

[305] H. Ohanian, *Physics* (Norton, 1989).

[306] D. Brabazon, A. Raffer, *Emerging Nanotechnologies for Manufacturing*, W. Ahmed, M. J. Jackson, eds. (William Andrew Publishing, Boston, 2010), pp. 59 – 91.

[307] D. Phillips, *Biographical Memoirs of Fellows of the Royal Society* **25**, pp. 74 (1979).

[308] J. A. D. Regato, *International Journal of Radiation Oncology*Biology*Physics* **7**, 83 (1981).

[309] A. West, *Solid State Chemistry and Its Applications* (Wiley, 1991).

[310] M. Birkholz, *Thin Film Analysis by X-Ray Scattering* (Wiley, 2006).

[311] P. A. Schroeder, C. Fleisher, G. B. Stracher, *Coal and Peat Fires: A Global Perspective*, G. B. Stracher, A. Prakash, E. V. Sokol, eds. (Elsevier, Amsterdam, 2011), pp. 155 – 171.

[312] O. Engler, V. Randle, *Introduction to Texture Analysis: Macrotexture, Microtexture, and Orientation Mapping* (CRC PressINC, 2010).

[313] H. G. Hansma, L. Pietrasanta, *Current Opinion in Chemical Biology* **2**, 579 (1998).

[314] G. Binnig, H. Rohrer, C. Gerber, E. Weibel, *Applied Physics Letters* **40**, 178 (1982).

[315] J. Tersoff, D. R. Hamann, *Phys. Rev. B* **31**, 805 (1985).

[316] G. Binnig, C. F. Quate, C. Gerber, *Phys. Rev. Lett.* **56**, 930 (1986).

[317] W. de Souza, G. M. Rocha, *Trends in Parasitology* **27**, 160 (2011).

[318] P. Samori, *STM and AFM Studies on (Bio)molecular Systems: Unravelling the Nanoworld*, Topics in Current Chemistry (Springer, 2008).

[319] W. Bowen, N. Hilal, *Atomic Force Microscopy in Process Engineering: An Introduction to AFM for Improved Processes and Products*, Butterworth Heinemann (Elsevier Science, 2009).

[320] P. Eaton, P. West, *Atomic Force Microscopy* (OUP Oxford, 2010).

[321] *Handbook of Analytical Methods for Materials* (Materials Evaluation and Engineering, Inc, 2001).

[322] C. Mőller, M. Allen, V. Elings, A. Engel, D. J. Műller, *Biophysical Journal* **77**, 1150 (1999).

[323] W. R. Bowen, N. Hilal, R. W. Lovitt, P. M. Williams, *Journal of Membrane Science* **110**, 229 (1996).

[324] J. V. Lauritsen, M. Reichling, *Journal of Physics: Condensed Matter* **22**, 263001 (2010).

[325] Q. Zhong, D. Inniss, K. Kjoller, V. Elings, *Surface Science Letters* **290**, L688 (1993).

[326] F. M. Smits, *Bell System Technical Journal* **34**, 711 (1958).

[327] D. Schroder, *Semiconductor Material and Device Characterization* (Wiley, 2006).

[328] G. W. Qin, *et al.*, *International Materials Reviews* **54**, 157 (2009).

[329] Z. Tiejun, *Storage Unlimited, a quarterly publication of Data Storage Institute* pp. 3 – 4 (2011).

[330] K. Buschow, *Handbook of Magnetic Materials*, Handbook of Magnetic Materials Series (Elsevier Science, 2009).

[331] T. Klemmer, D. Hoydick, H. Okumura, B. Zhang, W. A. Soffa, *Scripta Metallurgica et Materialia* **33**, 1793 (1995).

[332] J. S. Chen, C. Y. Tan, G. M. Chow, *Nanotechnology* **18**, 435604 (2007).

[333] R. F. C. Farrow, *et al.*, *Journal of Applied Physics* **84**, 934 (1998).

[334] H. Zeng, S. Sun, R. L. Sandstrom, C. B. Murray, *Journal of Magnetism and Magnetic Materials* **266**, 227 (2003).

[335] S. Stappert, B. Rellinghaus, M. Acet, E. F. Wassermann, *Journal of Crystal Growth* **252**, 440 (2003).

[336] J. Lyubina, O. Gutfleisch, R. Skomski, K.-H. Mller, L. Schultz, *Scripta Materialia* **53**, 469 (2005).

[337] V. R. Reddy, S. Puranik, A. Gupta, W. Leitenberger, *Vacuum* **81**, 1077 (2007).

[338] C. Y. You, Y. K. Takahashi, K. Hono, *Journal of Applied Physics* **98**, 013902 (2005).

[339] V. Phatak, *et al.*, *Acta Materialia* **58**, 979 (2010).

[340] K. Dong, *et al.*, *Journal of Magnetism and Magnetic Materials* **324**, 2637 (2012).

[341] E. Hierra, J. Salazar, *Silicon Nitride: Synthesis, Properties and Applications*, Chemical Engineering Methods and Technology: Materials Science and Technologies (Nova Science Pub Incorporated, 2012).

[342] A. Sun, J.-H. Hsu, P. Kuo, H. Huang, *Journal of Magnetism and Magnetic Materials* **320**, 3071 (2008).

[343] N. Kaushik, *et al.*, *Materials Science and Engineering: B* **171**, 62 (2010).

[344] Y. Li, T. Feng, Z. Chen, *Applied Surface Science* **257**, 3666 (2011).

[345] M. L. Yan, H. Zeng, N. Powers, D. J. Sellmyer, *Journal of Applied Physics* **91**, 8471 (2002).

[346] Y. Fang, P. Kuo, A. Sun, S. Hsu, S. Chen, *Thin Solid Films* **517**, 5181 (2009).

[347] P. C. Kuo, S. C. Chen, Y. D. Yao, A. C. Sun, C. C. Chiang, *Journal of Applied Physics* **91**, 8638 (2002).

[348] S. Chen, P. Kuo, A. Sun, C. Lie, C. Chiang, *Magnetics, IEEE Transactions on* **39**, 584 (2003).

[349] L. Ma, *et al.*, *Magnetics, IEEE Transactions on* **47**, 3505 (2011).

[350] W. S. Yoo, T. Fukada, I. Yokoyama, K. Kang, N. Takahashi, *Jpn. J. Appl. Phys.* **41**, 4442 (2002).

[351] T. Tahmasebi, *et al.*, *physica status solidi (RRL) Rapid Research Letters* **5**, 426 (2011).

[352] R. A. Ristau, K. Barmak, L. H. Lewis, K. R. Coffey, J. K. Howard, *Journal of Applied Physics* **86**, 4527 (1999).

[353] Y. T. Xing, *et al.*, *physica status solidi (c)* **1**, 3702 (2004).

[354] S. Chen, *et al.*, *Magnetics, IEEE Transactions on* **47**, 524 (2011).

[355] T. Mahalingam, J. P. Chu, J. H. Chen, S. F. Wang, K. Inoue, *Journal of Physics: Condensed Matter* **15**, 2561 (2003).

[356] F.-T. Yuan, *et al.*, *Journal of Applied Physics* **109**, 07B743 (2011).

[357] J.-S. Noh, H. Kim, D. W. Chun, W. Y. Jeong, W. Lee, *Current Applied Physics* **11**, S33 (2011).

[358] Y. Li, T. Feng, Q. Chen, A. Huang, Z. Chen, *Materials Letters* **65**, 2589 (2011).

[359] O. Gutfleisch, J. Lyubina, K.-H. Mller, L. Schultz, *Advanced Engineering Materials* **7**, 208 (2005).

[360] X.-H. Xu, H.-S. Wu, F. Wang, X.-L. Li, *Thin Solid Films* **472**, 222 (2005).

[361] E. J. Faber, R. A. M. Wolters, J. Schmitz, *Applied Physics Letters* **98**, 082102 (2011).

[362] C. Gras, E. Gaffet, F. Bernard, J. Niepce, *Materials Science and Engineering: A* **264**, 94 (1999).

[363] Z. Yan, W. Wang, J. Li, Y. Wang, *Solid State Communications* **69**, 595 (1989).

[364] J. Shi, D. Kojima, M. Hashimoto, *Journal of Applied Physics* **88**, 1679 (2000).

[365] T. Thomson, *et al.*, *Journal of Applied Physics* **95**, 6738 (2004).

[366] X. Li, *et al.*, *Scripta Materialia* **57**, 77 (2007).

[367] C.-H. Lai, C. C. Chiang, C. H. Yang, *Journal of Applied Physics* **97**, 10H310 (2005).

[368] Y. Tran, C. Wright, *Journal of Magnetism and Magnetic Materials* **331**, 216 (2013).

[369] B. Wang, D. C. Berry, Y. Chiari, K. Barmak, *Journal of Applied Physics* **110**, 013903 (2011).

[370] A. Zaitsev, M. Zemchenko, B. Mogutnov, *The Journal of Chemical Thermodynamics* **23**, 831 (1991).

[371] I. Barin, *Thermochemical properties of inorganic substances* (Berlin ; New York : Springer-Verlag, 1973).

[372] S. Meschel, O. Kleppa, *Journal of Alloys and Compounds* **280**, 231 (1998).

[373] P. O'Hare, I. Tomaszkiewicz, C. Beck, II, H.-J. Seifert, *The Journal of Chemical Thermodynamics* **31**, 303 (1999).

[374] D. Åberg, B. Sadigh, J. Crowhurst, A. F. Goncharov, *Phys. Rev. Lett.* **100**, 095501 (2008).

[375] C. Navio, J. Alvarez, M. J. Capitan, F. Yndurain, R. Miranda, *Phys. Rev. B* **78**, 155417 (2008).

[376] M. Gupta, *et al.*, *Journal of Applied Physics* **110**, 123518 (2011).

[377] L. Wang, *et al.*, *Journal of Alloys and Compounds* **443**, 43 (2007).

[378] W. Zhong, *et al.*, *Thin Solid Films* **478**, 61 (2005).

[379] H. Naganuma, R. Nakatani, Y. Endo, Y. Kawamura, M. Yamamoto, *Science and Technology of Advanced Materials* **5**, 101 (2004). 21st Century COE Program, Osaka University.

[380] S. P. Muraka, *Annual Review of Materials Science* **13**, 117 (1983).

[381] R. Doering, Y. Nishi, *Handbook of Semiconductor Manufacturing Technology* (Taylor and Francis Inc, 2007).

[382] Y. Mei, Z.-J. Zhou, H. L. Luo, *Journal of Applied Physics* **61**, 4388 (1987).

[383] J. F. Shackelford, W. Alexander, *The CRC Materials Science and Engineering Handbook* (Taylor and Francis Inc, 2000).

[384] Z. Liu, M. Watanabe, M. Hanabusa, *Thin Solid Films* **381**, 262 (2001).

[385] J. Vobeck, D. Kolesnikov, *Microelectronics Journal* **37**, 236 (2006).

[386] S. P. Murarka, *Intermetallics* **3**, 173 (1995).

[387] N. Zotov, R. Hiergeist, A. Savan, A. Ludwig, *Thin Solid Films* **518**, 4977 (2010).

[388] G. Herzer, *IEEE Transactions on Magnetics* **26**, 1397 (1990).

[389] G. Herzer, H. Warlimont, *Nanostructured Materials* **1**, 263 (1992).

[390] F. Pfeifer, C. Radeloff, *Journal of Magnetism and Magnetic Materials* **19**, 190 (1980).

[391] S. li He, *et al.*, *Journal of Magnetism and Magnetic Materials* **312**, 1 (2007).

[392] D. Suess, M. Dahlgren, T. Schrefl, R. Grossinger, J. Fidler, *Journal of Applied Physics* **87**, 6573 (2000).

[393] M. F. Toney, W.-Y. Lee, J. A. Hedstrom, A. Kellock, *Journal of Applied Physics* **93**, 9902 (2003).

[394] C.-M. Kuo, P. C. Kuo, H.-C. Wu, *Journal of Applied Physics* **85**, 2264 (1999).

[395] H. Chatbi, M. Vergnat, J. F. Bobo, L. Hennet, *Solid State Communications* **102**, 677 (1997).

[396] A. Kaewpukdee, N. Chirdchoo, P. Kovintavewat, *Procedia Engineering* **32**, 315 (2012).

[397] M. Weisheit, *et al.*, *Science* **315**, 349 (2007).

[398] I. Stolichnov, *et al.*, *Nat Mater* **7**, 464 (2008).

[399] J. kerman, *Science* **308**, pp. 508 (2005).

[400] W. Prellier, M. Singh, P. Murugavel, *Journal of Physics Condensed Matter* **17**, R803 (2005).

[401] M. Vopsaroiu, J. Blackburn, A. Muniz-Piniella, M. G. Cain, *Journal of Applied Physics* **103** (2008).

[402] Y. Zhang, *et al.*, *Applied Physics Letters* **92**, 152510 (2008).

[403] J. R. Childress, R. E. F. Jr., *Comptes Rendus Physique* **6**, 997 (2005).

[404] S. Kasatkin, *et al.*, *Sensors and Actuators A: Physical* **85**, 221 (2000).

[405] U. Dibbern, *Sensors and Actuators* **4**, 221 (1983).

[406] D. Mapps, *Sensors and Actuators A: Physical* **59**, 9 (1997).

[407] Y. Zheng, G. Han, B. Liu, *Journal of Magnetism and Magnetic Materials* **320**, 2850 (2008).

[408] K. Tagami, *Journal of Magnetism and Magnetic Materials* **324**, 355 (2012).

[409] A. Deac, *et al.*, *Journal of Magnetism and Magnetic Materials* **290 - 291, Part 1**, 42 (2005).

[410] D. Litvinov, S. Khizroev, *Journal of Magnetism and Magnetic Materials* **264**, 275 (2003).

[411] X. Peng, *et al.*, *Journal of Magnetism and Magnetic Materials* **321**, 1889 (2009).

[412] K. Nikolaev, *et al.*, *Journal of Applied Physics* **103**, 07F533 (2008).

[413] K. Nagasaka, *Journal of Magnetism and Magnetic Materials* **321**, 508 (2009).

[414] C. Binek, B. Doudin, *Journal of Physics Condensed Matter* **17**, L39 (2005). Ferromagnetic films;Nanoparticles;Spin transfer;Tunnel magnetoresistance (TMR);.

[415] E. Fulcomer, S. H. Charap, *Journal of Applied Physics* **43**, 4184 (1972).

[416] W. Oepts, H. J. Verhagen, R. Coehoorn, W. J. M. de Jonge, *Journal of Applied Physics* **86**, 3863 (1999).

[417] D. Rao, *et al.*, *Journal of Applied Physics* **89**, 7362 (2001).

[418] B. Oliver, G. Tuttle, Q. He, X. Tang, J. Nowak, *Journal of Applied Physics* **95**, 1315 (2004).

[419] Y. Zhang, *et al.*, *Journal of Physics D: Applied Physics* **43**, 082002 (2010).

[420] J. F. Scott, C. A. P. D. Araujo, *Science* **246**, pp. 1400 (1989).

[421] I. Kanno, H. Kotera, K. Wasa, *Sensors and Actuators A: Physical* **107**, 68 (2003).

[422] M. Deshpande, L. Saggere, *Sensors and Actuators A: Physical* **135**, 690 (2007).

[423] S. Xiong, H. Kawada, H. Yamanaka, T. Matsushima, *Thin Solid Films* **516**, 5309 (2008).

[424] B. Elsafi, F. Trigui, Z. Fakhfakh, *Computational Materials Science* **50**, 800 (2010).

[425] D. Mosca, *et al.*, *Journal of Magnetism and Magnetic Materials* **94**, L1 (1991).

[426] S. K. Ghosh, P. Chowdhury, A. Dogra, *Journal of Magnetism and Magnetic Materials* **327**, 121 (2013).

[427] I. Bakonyi, L. Pter, *Progress in Materials Science* **55**, 107 (2010).

[428] S. Sakrani, Y. Wahab, Y. Lau, *Journal of Alloys and Compounds* **434-435**, 598 (2007).

[429] S. S. P. Parkin, *Phys. Rev. Lett.* **67**, 3598 (1991).

[430] S. S. P. Parkin, Z. G. Li, D. J. Smith, *Applied Physics Letters* **58**, 2710 (1991).

[431] R. Coehoorn, *Phys. Rev. B* **44**, 9331 (1991).

[432] S. S. P. Parkin, R. Bhadra, K. P. Roche, *Phys. Rev. Lett.* **66**, 2152 (1991).

[433] S. S. P. Parkin, N. More, K. P. Roche, *Phys. Rev. Lett.* **64**, 2304 (1990).

[434] W. R. Bennett, W. Schwarzacher, W. F. Egelhoff, *Phys. Rev. Lett.* **65**, 3169 (1990).

[435] D. M. Deaven, D. S. Rokhsar, M. Johnson, *Phys. Rev. B* **44**, 5977 (1991).

[436] M. A. Ruderman, C. Kittel, *Phys. Rev.* **96**, 99 (1954).

[437] K. Yosida, *Phys. Rev.* **106**, 893 (1957).

[438] G. M. Genkin, M. V. Sapozhnikov, *Applied Physics Letters* **64**, 794 (1994).

[439] P. Grünberg, *Sensors and Actuators A: Physical* **91**, 153 (2001).

[440] M. E. Harfaoui, *et al.*, *Journal of Magnetism and Magnetic Materials* **198199**, 107 (1999).

[441] K. Bouziane, A. A. Rawas, M. Maaza, M. Mamor, *Journal of Alloys and Compounds* **414**, 42 (2006).

[442] A. Paul, *et al.*, *Journal of Physics: Condensed Matter* **15**, 2471 (2003).

[443] J. Egelhoff, W.F., M. Kief, *Magnetics, IEEE Transactions on* **28**, 2742 (1992).

[444] A. Yamada, T. Houga, Y. Ueda, *Journal of Magnetism and Magnetic Materials* **239**, 272 (2002).

[445] Y. Huai, *et al.*, *Journal of Magnetism and Magnetic Materials* **136**, 204 (1994).

[446] S. Nagamachi, M. Ueda, H. Sakakima, M. Satomi, J. Ishikawa, *Journal of Applied Physics* **80**, 4217 (1996).

[447] S. Ma, *et al.*, *Journal of Magnetism and Magnetic Materials* **209**, 131 (2000).

[448] A. M. Shukh, D. H. Shin, H. Hoffmann, *Journal of Applied Physics* **76**, 6507 (1994).

[449] S. Honda, S. Ohmoto, R. Imada, M. Nawate, *Journal of Magnetism and Magnetic Materials* **126**, 419 (1993).

[450] K. Bouziane, *et al.*, *Journal of Magnetism and Magnetic Materials* **165**, 284 (1997).

[451] K. Kok, J. Leake, *Thin Solid Films* **275**, 210 (1996).

[452] P. Grundy, *Journal of Alloys and Compounds* **326**, 226 (2001).

[453] J. B. Youssef, *et al.*, *Journal of Magnetism and Magnetic Materials* **165**, 288 (1997).

[454] M. Hecker, *et al.*, *Journal of Physics D: Applied Physics* **36**, 564 (2003).

[455] E. Rozenberg, D. Mogilaynski, J. Pelleg, G. Gorodetsky, R. Somekh, *Thin Solid Films* **342**, 11 (1999).

[456] T. N. Todorov, E. Y. Tsymbal, D. G. Pettifor, *Phys. Rev. B* **54**, R12685 (1996).

[457] B. Li, H. Shen, Y. Saitoh, T. Fujimoto, I. Kojima, *Thin Solid Films* **315**, 104 (1998).

[458] A. Wawro, L. Baczewski, R. Kalinowski, M. Aleszkiewicz, J. Rauluszkiewicz, *Thin Solid Films* **306**, 326 (1997).

[459] J. W. F. Egelhoff, *et al.*, *Journal of Applied Physics* **82**, 6142 (1997).

[460] A. Paul, *Journal of Magnetism and Magnetic Materials* **240**, 497 (2002).

[461] F. Yan, G. Xue, F. Wan, *J. Mater. Chem.* **12**, 2606 (2002).

[462] T. Uhrmann, *et al.*, *Journal of Magnetism and Magnetic Materials* **307**, 209 (2006).

[463] B. Ozkaya, S. R. Saranu, S. Mohanan, U. Herr, *Physica Status Solidi (A) Applications and Materials* **205**, 1876 (2008).

[464] Y.-F. Chen, *et al.*, *Advanced Materials* **20**, 3224 (2008).

[465] J. Lenz, S. Edelstein, *Sensors Journal, IEEE* **6**, 631 (2006).

[466] S. Oh, M. Jadhav, J. Lim, V. Reddy, C. Kim, *Biosensors and Bioelectronics* **41**, 758 (2013).

[467] S. Patil, V. Chu, J. Conde, *Sensors and Actuators A: Physical* **144**, 201 (2008).

[468] M. Liu, *et al.*, *Applied Physics Letters* **98**, 222509 (2011).

[469] J. Allibe, *et al.*, *Nano Letters* **12**, 1141 (2012).

[470] N. H. Duc, V. N. Thuc, *Journal of the Korean Physical Society* **52**, 1487 (2008).

[471] T. Kamel, F. Kools, G. de With, *Journal of the European Ceramic Society* **27**, 2471 (2007).

[472] J. Ma, Y. Lin, C. W. Nan, *Journal of Physics D: Applied Physics* **43**, 012001 (2010).

[473] E. N. Moreira, M. H. Lente, J. M. Póvoa, J. A. Eiras, *Journal of the Korean Physical Society* **32**, S742 (1998).

[474] P. Hareesh, I. Misri, S. Yang, D. L. DeVoe, *Journal of Microelectromechanical Systems* **21**, 1513 (2012).

[475] H. Boukari, C. Cavaco, W. Eyckmans, L. Lagae, G. Borghs, *Journal of Applied Physics* **101**, 054903 (2007).

[476] K. Arai, C. Muranaka, M. Yamaguchi, *Magnetics, IEEE Transactions on* **30**, 916 (1994).

[477] M. Vopsaroiu, *et al.*, *Journal of Applied Physics* **109**, 066101 (2011).

[478] D. N. Astrov, *J. Exptl. Theoret. Phys. (U.S.S.R.)* **38**, 984 (1960).

[479] B. Liu, T. Sun, J. He, V. P. Dravid, *ACS Nano* **4**, 6836 (2010).

[480] Y. Wang, J. Hu, Y. Lin, C.-W. Nan, *NPG Asia Mater.* **2**, 61 (2010).

[481] M. Vopsaroiu, *et al.*, *Journal of Applied Physics* **109**, 066101 (2011).